MODELLING GAS EMISSION SUSCEPTIBILITY ON LAND COVER AND AIR QUALITY FROM CEMENT PLANT FACTORIES USING GAUSSIAN PLUME MODEL AND GIS

By

AJAJ QAYSSAR MAHMOOD AJAJ

Thesis Submitted to the School of Graduate Studies, Universiti Putra Malaysia, in Fulfilment of the Requirements for the Degree of Doctor of Philosophy

August 2024

FK 2024 60

Abstract of thesis presented to the Senate of Universiti Putra Malaysia in fulfilment of the requirement for the degree of Doctor of Philosophy

ESTIMATING THE SUSCEPTIBILITY OF GASES EMISSION ON LAND COVER AND AIR QUALITY FROM CEMENT PLANT FACTORY USING GAUSSIAN PLUMES MODEL AND GIS

By

AJAJ QAYSSAR MAHMOOD AJAJ

August 2024

Chairman : Associate Professor Helmi Zulhaidi bin Mohd Shafri, PhD
Faculty : Engineering

Emissions of gases from cement plants are considered to be environmental pollutants. It is significant to detect and monitor such emissions in the appropriate manner. These pollutants represent significant risks and consequences to human health, air quality, the growth of plantations, and the development of urbanised areas.

Various studies have been conducted to identify the pollutants that are released into the air by industrial sources and to assess their influence on air quality and land cover. One of the widely adopted method is Gaussian Plume Model for measuring the concentration of pollution from point sources. This model; however, has several significant limitations. Among these is its reliance on a single wind speed value, disregarding the spatial variations across the study area. The second issue is that the model although incorporates the Digital Elevation Model (DEM) to account for ground height variations, it fails to consider the impact of urban structures, forests, and complex terrain. Furthermore, the model assums linear pollutant transimission

neglecting the dynamic of wind patterns influenced by various atmospheric conditions. Moreover, the model does not take into account the effects of temperature and humidity on pollutant dispersion. Given these limitations, coupled with the environmental challenges posed by cement factory emissions and inadequate regulatory frameworks in the study area, there is a pressing need to develop a more comprehensive and efficient predictive model.

This research first extracted pollution concentration using Gaussian Plume Model implemented in QGIS considering parameters such as stability class based on wind speed values and solar radiation and terrain characteristics. Then, the study estimated pollutant concentration using the same model by incorporating the DEM of the study area and cross section of plume pathways by means of three-dimensional Gaussian Plume. The study further assessed the impact of temperature and specific humidity on pollution dispersion. Finally, the study developed a pollutant prediction model using deep learning methods. The spline interpolation was used to generate wind speed layers for four seasons 2020 from 11 NASA Meteorological stations in the study area. The land cover classes were extracted by applying the maximum likelihood (ML) classification on Landsat images. An Analytic Hierarchy Process (AHP) was used to do a comparison of the primary and secondary directions in terms of their potential exposure to cement plant emissions in the year 2020.

The wind speeds across the four seasons were between 3.07 and 4.35 meters per second. Sand, often known as barren ground, is the most frequent type of land, accounting for 75.75 percent of the area that was surveyed, followed by vegetation cover (13.35%) and urban areas (7.97%). The quantity of water is the smallest, making up only 4.67% of the total study area. Both the overall accuracy and the Kappa coefficient of ML were calculated to be 0.9736 and 98.2143%, respectively. According to the pollution risk assesmenr, four levels of severity were assigned to the effects of pollution risk: very high, high, medium, and low. The spring season records the maximum value of very high risk pollution, which ranges from 52.428 to 1264.332 g/m^3, while the winter season of 2020 records the lowest value of very high risk pollution, which ranges from 0 to 0.017 g/m^3. During the summer, 8.573 km^2 of urban areas had the highest levels of pollution. During the summer, 5 km^2 of plantation land contained the areas with the highest amounts of pollution. There were a total of 60,974 km^2 of polluted sand during the summer. During the summer, there were 2.667 km^2 of contaminated regions in water bodies. The results of 3D Gaussian Plume model indicated that the simulated pollutant concentration varied significantly by season, with higher concentrations observed in spring and summer, and lower concentrations observed in autumn and winter. The results were achieved via implementing the model to two important places surrounding the study area: Kirkuk City and the Laylan District. Pollutant concentrations in Kirkuk City are higher in autumn and winter than in spring and summer. As one gets farther away from the source, the concentration of pollutants rises progressively until it peaks at 500 meters. Currently, the maximum concentrations of pollutants are found in spring, summer, fall, and winter, with values ranging from 11.69 to 87.76 µg/m^3. With a maximum value of 87.65 µg/m^3 at 500 meters from the source, the data for Laylan District showed that the greatest concentration levels were recorded during the winter.

The maximum concentration of the pollutants increased with temperature adjustment and decreased with specific humidity correction, according to the results of the

Gaussian Plume Model with temperature and specific humidity corrections. The concentrations of the pollutants increased in the fall and winter after the temperature and specific humidity correction parameters were added. They peaked at 168.28 $\mu g/m^3$ and increased to 1677.84 $\mu g/m^3$ and 563.027 $\mu g/m^3$ for the fall season and 108.19 µg/m3 for the winter, which increased to 1418.7 $\mu g/m^3$ after temperature correction and 611.282 $\mu g/m^3$ after specific humidity correction. Results also showed that the model is effective in both the Allahabad and Laylan stations, with closer results for the data in the Laylan station, which is based on the Gaussian equation simulated data. Loss functions in Laylan range from 0.0221 for the CaO parameter to 0.0041 for the Fe_2O3 and MgO parameters, which corresponds to 0.038 for Xylene at the Allahabad station, and vice versa. The highest loss function value in Laylan is 4.466 for the AQI parameter.

Keywords: Deep Learning, Environmental Risk, Gaussian Plume Model, QGIS

SDG: GOAL 15: Life on Land

Abstrak tesis yang dikemukakan kepada Senat Universiti Putra Malaysia sebagai memenuhi keperluan untuk ijazah Doktor Falsafah

PENGANGGARAN KERENTANAN PELEPASAN SISA PEPEJAL KE ATAS LITUPAN TANAH DAN KUALITI UDARA DARIPADA KILANG LOJI SIMEN MENGGUNAKAN MODEL GAUSSIAN PLUMES DAN GIS

Oleh

AJAJ QAYSSAR MAHMOOD AJAJ

Ogos 2024

Pengerusi : Profesor Madya Helmi Zulhaidi bin Mohd Shafri, PhD
Fakulti : Kejuruteraan

Pelepasan gas dari kilang simen dianggap sebagai pencemar alam sekitar. Adalah penting untuk mengesan dan memantau pelepasan ini secara berkesan sesuai dengan matlamat kelestarian. Pencemar ini memberikan risiko dan kesan besar kepada kesihatan manusia, kualiti udara, pertumbuhan tanaman, dan pembangunan kawasan bandar.

Pelbagai kajian telah dijalankan untuk mengenal pasti pencemar yang dilepaskan ke udara oleh sumber industri dan menilai pengaruhnya terhadap kualiti udara dan penutupan tanah. Salah satu kaedah yang digunakan secara meluas ialah Model Gaussian Plume untuk mengukur kepekatan pencemaran dari sumber tertentu. Walau bagaimanapun, model ini mempunyai beberapa had yang ketara. Antaranya ialah pergantungannya pada satu nilai kelajuan angin, tanpa mengambil kira variasi spatial dalam kawasan kajian. Kedua, walaupun model ini menggunakan Model Ketinggian Digital (DEM) untuk mengambil kira variasi ketinggian tanah, ia tidak

mempertimbangkan kesan struktur bandar, hutan, dan kawasan beralun. Selain itu, model ini menganggap penghantaran pencemar secara linear dan mengabaikan dinamika corak angin yang dipengaruhi oleh pelbagai keadaan atmosfera. Tambahan pula, model ini tidak mengambil kira kesan suhu dan kelembapan terhadap penyebaran pencemar. Berdasarkan had ini, bersama dengan cabaran alam sekitar yang ditimbulkan oleh pelepasan kilang simen dan rangka kerja peraturan yang tidak mencukupi di kawasan kajian, terdapat keperluan mendesak untuk membangunkan model ramalan yang lebih menyeluruh dan cekap.

Kajian ini pertama sekali mengekstrak kepekatan pencemaran menggunakan Model Gaussian Plume yang dilaksanakan dalam QGIS dengan mempertimbangkan parameter seperti kelas kestabilan berdasarkan nilai kelajuan angin, sinaran matahari, dan ciri-ciri tanah. Kemudian, kajian ini menganggarkan kepekatan pencemaran menggunakan model yang sama dengan menggabungkan DEM kawasan kajian dan keratan rentas laluan wap pencemaran menggunakan Gaussian Plume tiga dimensi. Kajian ini juga menilai kesan suhu dan kelembapan tertentu terhadap penyebaran pencemaran. Akhirnya, kajian ini membangunkan model ramalan pencemar menggunakan kaedah pembelajaran mendalam. Interpolasi spline digunakan untuk menjana lapisan kelajuan angin untuk empat musim 2020 dari 11 stesen Meteorologi NASA di kawasan kajian. Kelas penutupan tanah diekstrak menggunakan klasifikasi kebolehjadian maksimum (ML) pada imej Landsat. Proses Hierarki Analitik (AHP) digunakan untuk membandingkan arah utama dan sekunder dari segi pendedahan mereka kepada pelepasan kilang simen pada tahun 2020.

Kelajuan angin sepanjang empat musim adalah antara 3.07 hingga 4.35 meter sesaat. Pasir, yang sering dikenali sebagai tanah tandus, merupakan jenis tanah yang paling kerap, meliputi 75.75 peratus kawasan yang dikaji, diikuti oleh penutup tumbuhan (13.35%) dan kawasan bandar (7.97%). Kuantiti air adalah yang paling kecil, hanya meliputi 4.67% daripada jumlah kawasan kajian. Ketepatan keseluruhan dan pekali Kappa ML masing-masing dikira sebagai 0.9736 dan 98.2143%. Berdasarkan penilaian risiko pencemaran, empat tahap keparahan telah diberikan kepada kesan risiko pencemaran: sangat tinggi, tinggi, sederhana, dan rendah. Musim bunga mencatatkan nilai maksimum risiko pencemaran yang sangat tinggi, iaitu antara 52.428 hingga 1264.332 g/m3, manakala musim sejuk 2020 mencatatkan nilai terendah bagi risiko pencemaran yang sangat tinggi, iaitu antara 0 hingga 0.017 g/m3. Semasa musim panas, kawasan bandar seluas 8.573 km^2 mencatatkan tahap pencemaran tertinggi. Selain itu, 5 km^2 tanah tanaman mengandungi kawasan dengan jumlah pencemaran tertinggi, sementara 60,974 km^2 pasir tercemar juga dikenal pasti. Kawasan air yang tercemar pada musim panas adalah 2.667 km^2.

Keputusan Model Gaussian Plume 3D menunjukkan bahawa kepekatan pencemaran yang disimulasikan berbeza dengan ketara mengikut musim, dengan kepekatan yang lebih tinggi diperhatikan pada musim bunga dan musim panas, dan kepekatan yang lebih rendah pada musim luruh dan musim sejuk. Hasil ini diperoleh melalui pelaksanaan model tersebut di dua tempat penting sekitar kawasan kajian: Bandar Kirkuk dan Daerah Laylan. Kepekatan pencemar di Bandar Kirkuk adalah lebih tinggi pada musim luruh dan musim sejuk berbanding musim bunga dan musim panas. Semakin jauh dari sumber, kepekatan pencemar meningkat secara progresif sehingga mencapai puncak pada 500 meter. Pada masa ini, kepekatan maksimum pencemar dicatatkan pada musim bunga, musim panas, musim luruh, dan musim sejuk, dengan nilai antara 11.69 hingga 87.76 µg/m3. Data untuk Daerah Laylan menunjukkan kepekatan tertinggi direkodkan semasa musim sejuk, dengan nilai maksimum 87.65 µg/m3 pada 500 meter dari sumber.

Kepekatan maksimum pencemar meningkat dengan pelarasan suhu dan menurun dengan pembetulan kelembapan tertentu, menurut keputusan Model Gaussian Plume. Kepekatan pencemar meningkat pada musim luruh dan musim sejuk selepas parameter pembetulan suhu dan kelembapan tertentu ditambah. Ia mencapai puncak pada 168.28 µg/m3 dan meningkat kepada 1677.84 µg/m3 dan 563.027 µg/m3 untuk musim luruh, serta 108.19 µg/m3 untuk musim sejuk, yang meningkat kepada 1418.7 µg/m3 selepas pembetulan suhu dan 611.282 µg/m3 selepas pembetulan kelembapan tertentu. Hasil juga menunjukkan bahawa model ini berkesan di stesen Allahabad dan Laylan, dengan hasil yang lebih hampir pada data di stesen Laylan, berdasarkan data simulasi persamaan Gaussian. Fungsi kehilangan di Laylan berkisar antara 0.0221 untuk parameter CaO hingga 0.0041 untuk parameter Fe2O3 dan MgO, yang sepadan dengan 0.038 untuk Xylene di stesen Allahabad, dan sebaliknya. Nilai fungsi kehilangan tertinggi di Laylan adalah 4.466 untuk parameter AQI.

Kata Kunci: Pembelajaran Mendalam, Risiko Alam Sekitar, Model Gaussian Plume, QGIS

SDG: MATLAMAT 15: Kehidupan di Darat

ACKNOWLEDGEMENTS

I thank ALLAH for his tremendous loving compassion, which has prompted us all to share and support one another, and who has dragged us out of the darkness into the light. All honor and respect to our holy prophet (Peace be upon him), who led us to the discovery of our creator. I also want to express my gratitude to all of my brothers and sisters who have responded to ALLAH's call and chosen to walk on ALLAH's straight path.

It is impossible to name everyone who has had an influence on this effort, but there are others whose spiritual support is much more essential. I am eternally grateful to my father (may God have mercy on him) and mother, who helped define my vision and taught me the important things in life. Their unfailing love and support have always been my greatest strengths. Their patience and sacrifice will be an inspiration to me for the rest of my life. I am also grateful to all of my family members for their never-ending inspiration.

My heartfelt thanks to my mother, my wife, my sons, my brothers and my sisters for their guidance and moral support. They always helped me out when I got any difficulties or queries regarding all the aspect of life.

I'd like to use this opportunity to present my heartfelt thanks to my thesis supervisor, Prof. Dr. Helmi Z. M. Shafri, for his exceptional guidance, monitoring, and continuous support during the duration of this thesis.

I am really grateful to my committee members, Prof. Dr. Mohammad Firuz Bin Ramli and Dr. Aimrun Wayayok, for the important information they provided in their respective studies. I am grateful for their assistance during my studies.

This thesis was submitted to the Senate of Universiti Putra Malaysia and has been accepted as fulfilment of the requirement for the degree of Doctor of Philosopy. The members of the Supervisory Committee were as follows:

Helmi Zulhaidi bin Mohd Shafri, PhD
Associate Professor
Faculty of Engineering
Universiti Putra Malaysia
(Chairman)

Mohammad Firuz bin Ramli, PhD
Associate Professor
Faculty of Forestry And Environment
Universiti Putra Malaysia
(Member)

Aimrun Wayayok , PhD
Associate Professor
Faculty of Engineering
Universiti Putra Malaysia
(Member)

ZALILAH MOHD SHARIFF, PhD
Professor and Dean
School of Graduate Studies
Universiti Putra Malaysia

Date: 13 March 2025

TABLE OF CONTENTS

				Page
ABSTRACT				i
ABSTRAK				v
ACKNOWLEDGEMENTS				ix
APPROVAL				xi
DECLARATION				xiii
LIST OF TABLES				xviii
LIST OF FIGURES				xx
LIST OF APPENDICES				xxiii
LIST OF ABBREVIATIONS				xxiv
CHAPTER				
1	**INTRODUCTION**			1
	1.1	Introduction		1
	1.2	Problem Statement		2
	1.3	Research Objectives		4
	1.4	Research Questions		5
	1.5	Scope of This Thesis		6
	1.6	Research Hypothesis		6
	1.7	Thesis Organization		7
2	**LITERATURE REVIEW**			9
	2.1	Introduction		9
	2.2	The Production of Cement		12
	2.3	Cement Industry Emissions		13
		2.3.1	Gases and Volatile Organic Compounds	13
		2.3.2	Dust	14
		2.3.3	Noise	15
		2.3.4	Bad Smell	15
	2.4	Air Pollution Models		15
		2.4.1	Dispersion Models	18
	2.5	Discussion		45
		2.5.1	AERMOD	46
		2.5.2	Gaussian Plume Model	52
		2.5.3	Hybrid Models	56
		2.5.4	Land Use Regression	60
		2.5.5	GIS Tools	61
	2.6	Deep learning Overview		65
	2.7	Summary		67
3	**MATERIALS AND METHODS**			69
	3.1	Introduction		69
	3.2	Overall Research Workflow		69
	3.3	Study Areas		72
		3.3.1	Main Study Area	72

	3.3.2	Specific Study Area	72
	3.3.3	Kirkuk Cement Plant	73
3.4	Data Used		74
	3.4.1	Source Information and Site Description	74
	3.4.2	Satellite Imagery (Landsat 8)	75
	3.4.3	Meteorological Conditions	75
	3.4.4	Gaussian Parameters	81
	3.4.5	Digital Elevation Model	82
3.5	Data Preprocessing		83
3.6	Land Cover Classes		84
	3.6.1	Classification Scheme	84
	3.6.2	Sampling and Training Data	85
	3.6.3	Digital Image Classification	86
	3.6.4	Accuracy Assessment	88
3.7	Interpolation		91
	3.7.1	Spline Interpolation	91
	3.7.2	Inverse Distance Weighting	92
	3.7.3	Kriging	93
3.8	Gaussian Plume Models (One Variable)		94
	3.8.1	1D Modelling	94
	3.8.2	1D Gaussian Modelling with Reality Wind Direction	102
3.9	Analytic Hierarchy Process		106
3.10	Risk Assessment		106
3.11	3D Gaussian Modelling (Three Variables)		107
3.12	Modelling with Temperature and Specific Humidity Effects		107
3.13	Validation and Verification Process		109
3.14	Deep Pollutant Prediction Model (DPPM)		110
	3.14.1	Dataset Description	110
	3.14.2	Methodology	111
	3.14.3	Data Splitting	113
	3.14.4	Data Normalization	113
	3.14.5	Architecture of DPPM	113
	3.14.6	Evaluation Metrics	116
3.15	Summary		116
4	**RESULTS AND DISCUSSIONS**		118
4.1	Classification Results		118
	4.1.1	Maximum Likelihood	118
	4.1.2	Support Vector Machine	120
	4.1.3	Accuracy Assessment	121
4.2	Wind Speed Maps Results		122
	4.2.1	Spline Interpolation Outcomes	123
	4.2.2	Inverse Distance Weighted Outcomes	124
	4.2.3	Kriging Outcome	127
4.3	Gaussian Plume Outcomes		128
	4.3.1	One Dimension Gaussian	128
4.4	AHP Outcomes		133
4.5	Risk Pollution Outcomes		134

	4.5.1	Risk Pollution of One Dimension Gaussian	134
4.6	Real Direction Of Gaussian Plume		138
	4.6.1	Spring Season	138
	4.6.2	Summer Season	140
	4.6.3	Autumn Season	142
	4.6.4	Winter Season	145
	4.6.5	3D Gaussian Plume Result	148
4.7	Results of the 3D Gaussian Plume Model Simulation		149
4.8	Impact of Over Serve Height (z)		156
4.9	Gaussian with Temperature and Relative Humidity		157
	4.9.1	Temperature Maps	157
	4.9.2	Specific Humidity Maps	160
4.10	Results and Discussion of DPPM		166
4.11	GJ001 Dataset Results		167
4.12	Simulated Output Results		168
4.13	Summary		168

5 CONCLUSION AND RECOMMENDATIONS 171

5.1	Overview	171
5.2	Contributions	172
5.3	Overall Findings	173
5.4	Conclusion	174
5.5	Recommendations for Future Work	178

REFERENCES 179
APPENDICES 206
BIODATA OF STUDENT 212
LIST OF PUBLICATIONS 213

LIST OF TABLES

Table		Page
2.1	The Pasquill-Gifford Stability Classification Based on Wind Speed Values	23
2.2	Nitrogen Dioxide and Statistics of Concentrations of Sulfur Dioxide Performance Assessment	48
2.3	Validation of AERMOD and CALPUFF Models with Statistical Indices	51
2.4	Common Spatial and Statistical Methods of Air Pollution Analysis	64
3.1	Source Information of Kirkuk Cement Plant	74
3.2	Landsat-8 OLI Satellite Data Used for the Study	75
3.3	Wind Speed Data Downloaded from RET Screen Program for 2020	76
3.4	Wind Directions of Study Region for All Seasons in 2020	78
3.5	Angles of Plume for Four Seasons Relative to Wind Speed Stability	78
3.6	The Temperature of 10 Locations Surrounding the Kirkuk Cement Plant for Four Seasons during 2020	80
3.7	The Specific Humidity of 10 Locations Surrounding the Kirkuk Cement Plant for Four Seasons during 2020	80
3.8	The Classification of Wind Speed Stability Based on Incoming Solar Radiation	81
3.9	The Coefficients (a, b, c, and d) Used in the Calculation of Crosswind Distance and Vertical Direction	82
3.10	Descriptions of Land Use/Land Cover Classes	85
3.11	Wind Direction Monitoring Sites around the Kirkuk Cement Plant for Four Seasons in 2020 with Different Period Per Day	105
3.12	Proposed Model Layers	114
4.1	The Overall Accuracy and Kappa Coefficient of the Classification Method on Satellite Image 2020	122
4.2	Weights and Importance of Primary and Secondary Direction around Kirkuk Cement Plant	134

4.3 The Areas of Exposed Land Cover Features to Pollution 2020 with Different Seasons and Real Directions 147

4.4 Seasonal Simulated Pollutant Concentration: Minimum, Maximum, Mean, and Standard Deviation 152

4.5 The Simulated Pollutant Concentration Values Obtained from the Gaussian Plume Model at Various Distances from the Emission Source with Different z Values 157

4.6 The Loss Error of DPPM for the GJ001 Dataset 167

4.7 The Loss Error of DPPM for Laylan District from (Simulated Output) 168

LIST OF FIGURES

Figure		Page
2.1	Cement Process Plan (Devi, 2018)	12
2.2	Template of Surface-Release Plume Dispersion	25
2.3	Concentration Levels at Any Height Are Describable Regarding Gaussian Distributions Formed by the Bell. True Calculations Can Be Significantly Deviating from Straight Curves (Venkatram and Modeling 2005)	26
2.4	Predicted and Observed SO_2 Statistics (Mean, RHC, Percentile Statistic, and Maximum) for All Sites (Jittra, Pinthong, and Thepanondh 2015)	49
2.5	CO Dispersion at Various Distances from the Cement Plant during the (a) Spring Season, (b) Summer Season, (c) Fall Season, and (d) Winter Season (Goudarzi et al. 2016)	55
2.6	(a) Comparing Simulated Daily PM_{10} Concentrations by the SCREEN3 and Gaussian Plume Models, and (b) Spearman r^2 Values (A.J. 2013)	55
2.7	For Stack 1, the Field and Simulated Data Are Plotted against the Downwind Distance (A.J. 2013)	56
2.8	Measured Data vs. Results of Three Utilized Models (Mohebbi A 2006)	59
3.1	Overall Methodology Flowchart	71
3.2	The Study Area (Laylan District and the Districts Surrounding it)	73
3.3	Seasonal Variation in Wind Speed across Multiple Locations in Iraq. The Graph Displays the Average Wind Speed in Meters Per Second (m/s) during Each Season of the Year, with Data Collected from Ten Different Locations across the Country	77
3.4	Separation Hyperplanes	88
3.5	Optimal Classifier	88
3.6	Flowchart of 1D Gaussian Plume Methodology	95
3.7	Flowchart of Real Direction with Gaussian Plume Methodology	104
3.8	Wind Direction Monitoring Sites around the Kirkuk Cement Plant	104
3.9	Flowchart of 3D Gaussian Plume Methodology	107

3.10	Flowchart of Gaussian Plume Model with Effect of Temperature and Specific Humidity	109
3.11	Flowchart of the Proposed Model	112
4.1	Land Cover Classes (Maximum Likelihood Classification Algorithm)	119
4.2	Land Cover Classes (Support Vector Machine Classification Algorithm)	121
4.3	Wind Speed Distribution Maps (Spline Interpolation) for Four Seasons of 2020 of the Whole Study Area. (a) Spring, (b) Summer, (c) Autumn, and (d) Winter Season	124
4.4	Wind Speed Distribution Maps (IDW Interpolation) for Four Seasons of 2020 of the Whole Study Area. (a) Spring, (b) Summer, (c) Autumn, and (d) Winter Season	126
4.5	Wind Speed Distribution Maps (Kriging Interpolation) for four Seasons of 2020 of the Whole Study Area. (a) Spring, (b) Summer, (c) Autumn, and (d) Winter Season	128
4.6	Pollution Risk of Kirkuk Cement Plant during the Spring 2020	130
4.7	Pollution Risk of Kirkuk Cement Plant during the Summer 2020	131
4.8	Pollution Risk of Kirkuk Cement Plant during the Autumn 2020	132
4.9	Pollution Risk of Kirkuk Cement Plant during Winter 2020	133
4.10	Land Cover Exposed to Pollution during Spring 2020	136
4.11	Land Cover Exposed to Pollution during the Summer of 2020	136
4.12	Land Cover Exposed to Pollution during Autumn 2020	137
4.13	Land Cover Exposed to Pollution during Winter 2020	137
4.14	Wind Direction for Four Time Periods on the First Day of April to Represent the Spring Season of 2020	139
4.15	Land Cover Exposed to Pollution during 1st April 2020 with Real Direction (Spring Season)	140
4.16	Wind Direction for Four Time Periods on the First Day of April to Represent the Summer Season of 2020	141
4.17	Land Cover Exposed to Pollution during 1st July 2020 with Real Direction (Summer Season)	142
4.18	Wind Direction for Four Time Periods on the First Day of September to Represent the Autumn Season of 2020	143

4.19 Land Cover Exposed to Pollution during 1st September 2020 with Real Direction (Autumn Season) 144

4.20 Wind Direction for Four Time Periods on the Second Day of January to Represent the Autumn Season of 2020 146

4.21 Land Cover Exposed to Pollution during 2nd January 2020 with Real Direction (Winter Season) 147

4.22 Topographic Map of the Study Area Prepared Based on ASTER GDEM Data 148

4.23 Seasonal Dispersion Maps of Pollutants from the Kirkuk Cement Plant Using Gaussian Plume Model: Simulated Concentration Contours for Winter, Spring, Summer, and Autumn Seasons 151

4.24 Selected Paths for Studying Pollutant Concentration Profiles from the Kirkuk Cement Plant Using Gaussian Plume Model: Kirkuk City Line and Laylan District Line 152

4.25 Pollutant Concentration Profiles and Wind Speed Comparison for Kirkuk City Line: Simulated Concentration vs. Distance from the Source, with Corresponding Wind Speed Data 153

4.26 Pollutant Concentration Profiles and Wind Speed Comparison for Laylan District Line: Simulated Concentration vs. Distance from the Source, with Corresponding Wind Speed Data 153

4.27 Seasonal Pollutant Concentration Profiles for (a) Kirkuk City Line and (b) Laylan District Line: Simulated Concentration vs. Distance from the Source for Winter, Spring, Summer, and Autumn Seasons 156

4.28 Seasonal Spatial Distribution Map of Temperature Over the Study Area in 2020 159

4.29 Seasonal Spatial Distribution of Specific Humidity Over the Study Area in 2020 161

4.30 Seasonal Dispersion Maps of Pollutants from the Kirkuk Cement Plant Using Gaussian Plume Model with Correction of Temperature for Spring, Summer, Autumn , and Winter Seasons 163

4.31 Seasonal Dispersion Maps of Pollutants from the Kirkuk Cement Plant Using Gaussian Plume Model with Correction of Specific Humidity for Spring, Summer, Autumn , and Winter Seasons 165

LIST OF APPENDICES

Appendix		Page
A	Source Information from Engineering Department of Kirkuk Cement Plant	206
B	1D Guassian Plume Model Plugin in QGIS	207
C	3D Guassian Plume Model Plugin in QGIS	208
D	The Designed Deep Learning Model (Deep Pollutant Prediction Model (DPPM))	209
E	The Emission of Pollutants from the Chimney of the Kirkuk Cement Plant	210
F	Validation of 3D Gaussian Plume Model	211

LIST OF ABBREVIATIONS

NO_2	Nitrogen dioxide
AAPD	Average Absolute Percent Deviation
ADMS	The Atmospheric Dispersion Modelling System
ANN	Neural Gas
BME	Space-Time Residuals
CALPUFF	The California Puff Model
CAR-FMI	Contaminants In The Air From a Road, Finnish Meteorological Institute
CC	Cubic Convolution
CFD	Computational Fluid Dynamic
CO	Carbon monoxide
CO_2	Carbon dioxide
DEM	Digital Elevation Model
EBK	Empirical Bayesian Kriging
EHF	Easy Hybrid Forecasting
ETM+	The Enhanced Thematic Mapper Plus
FAC2	Factor of Two
FB	Fractional Bias
FCC_S	False-Color Composites
FMEnv	Federal Ministry of Environment
GIS	Geographic Information System
GM	Gaussian Model
IDW	Inverse Distance Weight
IOA	Index of Agreement
ISC3	The Industrial Source Complex Dispersion Model

L1T	Level 1 Terrain-Corrected
$LPDM_S$	Lagrangian Particle Dispersion Models
LPGS	Level 1 Product Generation System
LSTM	Long short-Term Memory Networks
LUR	Land Use regression
MAE	Mean Absolute Error
MAPE	Mean Absolute Percentage Error
MG	Geometric Mean Bias
MLC	Maximum Likelihood
NAAQS	National Ambient Air Quality Standards
NAME	Numerical Atmospheric-Dispersion Modelling Environment
NASA	National Aeronautics and Space Administration
NIR	Near-Infrared
NMSE	Normalized Mean Square Error
NWS	National Weather Service
O_3	Ozone
OK	Ordinary kriging
OLI	Operational Land Imager
OSPM	The Operational Street Model
PLS	Partial Least Squares
QGIS	Quantum Geographic Information System
RNN	Recurrent Neural Network
SO_2	Sulphur oxides
SOM	
SVM	Support Vector Machine
SVM	Support Vector Machine

TOA	Top of Atmosphere
TSP	Total Suspended Particulates
UK	Universal Kriging
USGS	U.S. Geological Survey
UTM	Universal Transverse Mercator
VG	Geometric Variance
WGS	World Geodetic System
WHO	World Health Organization
WRF	Weather Research And Forecasting

CHAPTER 1

INTRODUCTION

1.1 Introduction

In today's world, gases emissions from cement plants are addressed as environmental pollutants, which would result in severe problems if not properly detected and monitored. These wastes have effects on human health, air, urbanization area expansion and plantation growth. The cement industry, as the primary producer of building materials, promotes rapid social and economic growth, but it also has heavy energy demand and severe air quality issues (J. Liu et al. 2020). The Cement factory of Laylan District in the governorate of Kirkuk City, Iraq pollutes all the area and the surrounding other districts. According to Environmental assessment of cement plants in Iraq prepared by the technical department of the Ministry of Environment, The Kirkuk Cement Plant raises solid waste about 700-750 tons per month. The plant also emits the gaseous wastes that are represented by the combustion gases, which are Nitrogen dioxide (NO_2), Carbon dioxide (CO_2), Sulphur oxides (SO_2), and Carbon monoxide (CO).

Several studies reported significant correlations between air pollution and certain diseases including shortness of breath, sore throat, chest pain, nausea, asthma, bronchitis and lung cancer (Abu-Allaban and Abu-Qdais 2011). It is a major contributor to dust, nitrogen oxides (NOx), sulphur oxides (SO_x), and carbon monoxide (CO) in metropolitan areas. Furthermore, it contributes about 5% of the global CO_2, the famous greenhouse gas (Worrell et al. 2001). Every industry is supposed to prevent any pollution before it creates more problems. One method of prevention in the study of public health is by using a spatial study to identify people living in the area with high dispersion pollution (E. A. Jayadipraja et al. 2016). Intermittent irregular sources of air pollution, when used in dispersion modelling, can exaggerate the acute health risk due to improbable coincidence of release with the worst-case meteorological conditions (Balter and Faminskaya 2017). According to the World Health Organization (WHO), approximately 800,000 deaths per year globally occur due to the respiratory and cardiovascular disease, and lung cancer caused by the air pollution (Khaniabadi, Hopke, et al. 2017).

Machine learning techniques use computational algorithms and statistical models to develop models without prior knowledge about data distribution (Al-Ruzouq et al. 2019). The combined use of air dispersion models and GIS (Geographic Information System) techniques is very common in research focusing on the effects produced by aerial pollutants on a regional-local scale (Heckel & Lemasters, (2011) & Teggi et al., (2018)) . Modules can be written by any third party in Python and added to the QGIS (Lawhead 2015). However, there are often serious problems due to the formats often adopted by GIS (vector objects) and the formats adopted by atmospheric dispersion models (tabulated text data) for the input/output data describing sources, receptors, concentrations and deposition fluxes (Teggi et al. 2018).

1.2 Problem Statement

Pollution has emerged as one of the most relevant global challenges to be addressed. The cement industry is one of the dangerous industries that many international environmental systems are concerned about due to the environmental and health risks posed by air pollution, particularly when it is located near residential areas. Some gaseous pollutants, such as nitrogen oxides, sulfur, carbon dioxide, and carbon monoxide, are emitted from cement plants, in addition to particles carried with combustion gases in the form of dust with small diameters.

Many studies have been carried out in order to identify pollutants emitted by industrial sources and to characterize the impact of this pollution on air quality and land cover patterns. However, there are several limits to the implementation of these investigations. Wind speed is an essential element in Gaussian Plume Model. When applying the model, single value of wind speed is substituted. However, in reality the wind speed variation over area of study (Rychlik and Mao 2019). Several factors affect the change in wind speed, including: vegetation roughness length, temperature, concentration of greenhouse gas (Bichet et al. 2012), variation of terrain (Emeksiz and Cetin 2019), wind direction, atmospheric pressure, and relative humidity (Yesilbudak, Sagiroglu, and Colak 2013). In addition, the assumption of uniform pollution dispersal is challenged by the turbulence caused by the terrain in Gaussian Plume Model. In other words, the presence of buildings, forests and high terrain in the area of study of the application of the model is neglected, although the collision with these obstacles leads to the dispersal and weakening of the pollutant dispersion, and this is not be taken into account in the application of the model. Moreover, the Gaussian model assumes that the mass of pollution emitted from a point source is transmitted in a straight line (Nikezić et al. 2017). However, the wind direction changes continually from one region to another due to variations in meteorological parameters (Zhanwei Li et al. 2020). Therefore, Gaussian Plume Model estimates the pollution within the straight line and not cover the area out of its path and this opposite to the truth.

This thesis proposes new ways to use Python and QGIS to map the concentrations of pollutants emitted by cement producers. The primary purpose of this research is to generate high-quality spatial maps that illustrate the concentration of toxins in regions affected by cement mill pollution. Furthermore, because these pollutants constitute a threat to humans, plants, and animals in these places, efforts should be taken to control them as well as to limit their sources. These maps may be used by the federal and local governments to develop the appropriate rules and recommendations to decrease pollution.

1.3 Research Objectives

The goal of this research is to create an advanced, multi-dimensional Gaussian Plume Model that accurately predicts pollution dispersion, particularly focusing on emissions from the Kirkuk Cement Plant. This study aims to improve the traditional Gaussian Plume Model by integrating detailed meteorological data, terrain features, and deep learning techniques. The objective is to develop a more reliable and precise tool for estimating pollutant concentrations, which will aid in better air quality management and environmental impact assessments in industrial regions. By incorporating real-world complexities and utilizing modern computational methods, this research seeks to connect theoretical models with practical applications in environmental monitoring and pollution control.

Specific objectives

1- Enhance the Gaussian Plume Model by incorporating weather factors like atmospheric stability, fluctuating wind speeds, solar radiation, and mass emission rates to better estimate pollution concentrations.

2- Modify the Gaussian Plume Model implementation to consider actual wind direction instead of assuming a straight path.

3- Expand the model to incorporate three-dimensional modeling by integrating Digital Elevation Model (DEM) data to account for terrain (z values) and implement cross-section analysis of plume paths to incorporate y-axis dispersion.

4- Develop the Gaussian Plume Model by studying and involving the corrections of temperature and specific humidity in Gaussian Equation.

5- Develop a prediction model for pollutants emitted from Kirkuk Cement Plant based on deep learning and simulated output Gaussian Plume Model of pollution concentration.

1.4 Research Questions

The following research questions are addressed in extensively in this thesis:

1. What is the significance of combining Python with QGIS to create high-resolution spatial maps of pollutant concentration?

2. How might the development of a new pollutant measuring plugin in QGIS aid in the study of environmental pollution emitted by cement plants, distinguishing it from other techniques of environmental analysis?

3. How does the introduction of the elements of heights and cross-sections of the plume improve the results of the concentration of constituents in the Gaussian equation?

4. What effect does adding new factors to the Gaussian equation, such as temperature and relative humidity, have on the outcomes of pollutant concentrations?

1.5 Scope of This Thesis

This study is carried out to develop a method for analyzing pollution concentration using Python Language and QGIS techniques for Gaussian Plume Equation in region suffers from environmental pollution which is Laylan District, Kirkuk City, Iraq. As well as applicability in other operating areas and other different areas by the change of the elements of the equation and other climatic elements. In this research, Python with QGIS were used for modelling Gaussian Plume equation and detecting pollutant concentration by mean of spatial distribution. Gaussian Plume Model througth Python and QGIS is applied in three ways. The first way is depended on one variable which is x- dimension which represents the distance from point source of release to any point around the cement plant. The second way is applied by mean of three dimension which are x, y, and z to identify the concentration of pollution at any points with any height from the ground. The third way is by using temperature and specific humidity as effected paramerters on Gaussian Plume Model. The Maximum Likelihood Classification is used to extract the land cover clsasses over the region of study. Analytical Heraracy Process is used for weighting the primary and secondary directions relative to their exposure times to cement plant emissions in all seasons. Thus, the land cover can be classified according to the number of times of exposure to pollution. The concentration of pollution with land covers are analyzed to detect the spatial risk of pollution over the study area.

1.6 Research Hypothesis

1. Developing a QGIS plugin to spatially apply the Gaussian Plume equation by the assumed straight direction and the real direction of the plume with

high precision in order to improve the representation of the risk of pollutants resulting from the cement plant.

2. Developing the Gaussian equation to give it is more logical by incorporating ground levels represented by DEM by mean of 3D Gaussian Plume Model as well as including the width of the area through which the plume travels along the path line using Python and QGIS

3. Developing the Gaussian Plume Model because temperature and specific humidity affect the properties of pollutant diffusion, it must be included into the Gaussian equation to reflect the true impact of pollution risk.

4. Designing a deep learning prediction model called the Deep Pollutant Prediction Model (DPPM) for the purposes of managing these pollutants by decision-makers

1.7 Thesis Organization

This thesis is organized into five chapters. The summary of each chapter is as follows:

(i) Chapter 1: Introduction

This chapter introduces the study's problem statement, aims, objectives, and scope. Moreover, this chapter emphasizes the research questions suggested for the thesis, as well as the significant contribution of new information and the thesis' overall structure.

(ii) Chapter 2: Literature Review

This section presents a summary of pollution diffusion from various sources, as well as past work on several models dealing with point, line, area, and volume sources. The chapter focuses on point source methodologies and models, namely from cement plants. The spatial analytic approaches were described immediately, as well as the traditional, experimental, and developing techniques for predicting pollution risk. Further to that, the characteristics and limitations of conventional models and current pollutant dispersion methods were examined. Finally, the validation procedures used to evaluate the accuracy of generated maps are summarized.

(iii) Chapter 3: Materials and Methodology

This chapter describes the characteristics of the study area followed by the following details in order: materials, data, methodology, land cover extraction using classification method, production of meteorological parameters using interpolation techniques, implementation of Gaussian Plume in QGIS through Python script for both one and three dimension, calculation of pollution risk on land cover, and various remote sensing techniques.

(iv) Chapter 4: Results and Discussion

This chapter focuses on the results of the study, which include the land cover classes, wind speed generation using satellite and meteorological data. Futhermore, outcomes of concentration of pollution from cement plant using Paython and QGIS. The concentration of pollution were estimated by three ways which are one dimension (x), three dimension (x,y,z), and with temperature and specific humidity parameters. Moreover, the findings of designed deep learning model named the Deep Pollutant Prediction Model (DPPM) . Lastly, the risk of pollution on land cover were determined and discussed for 1D Gaussian Plume. All results are supported by photos, tables, diagram and charts.

(v) Chapter 5: Conclusion and Future Work Recommendations

This chapter presents the study's general conclusion, recommendations, and future research for the area of study.

CHAPTER 2

LITERATURE REVIEW

2.1 Introduction

This chapter highlights the models used for have been applied to analyse and determine the effect of these emissions on the environment. Our study is focused on these analytical and statistical methods for analysing gaseous pollutant and particulate matter emissions from various pollution sources, especially cement plants.

Identifying the elements of emissions and the development stages of other authors' analysis methods allowed us to conduct the most precise report possible. Our study also depicts the determinants of these strategies and their advantages, limitations, and implementation variables. Additionally, it search on the frameworks utilised ranged from using a single model to two or more models, in order to compare or combine them. GIS was used as an additional tool to improve the model's functionality in several studies. Some authors utilized programming languages like Python and R to enhance the realism of their models.

Air pollution is responsible for the premature deaths of 3.7 million people each year, as reported by the World Health Organization (WHO) (Health Organization 2016). Among the various pollutants, particulate matter (PM) is often considered the most harmful according to several studies (Cohen et al. 2005; European Environment Agency (EEA) 2013; Anshumala Sharma, Massey, and Taneja 2018). Exposure to PM can result in numerous health issues, such as asthma, bronchitis, heart disease, and lung cancer (Anderson, Thundiyil, and Stolbach 2012; Massey, Habil, and Taneja

2016). Concerns about air pollution are widespread globally due to its detrimental impact on public health and overall well-being. Various health problems linked to air pollution have been documented, including shortness of breath, sore throat, chest discomfort, nausea, asthma, bronchitis, and lung cancer. Beyond health concerns, air pollution also poses a threat to plants, wildlife, forests, and natural ecosystems. Furthermore, metal, leather, rubber, and fabrics can suffer from cracking, soiling, rust, and degradation (Boubel, W. R., Fox, D. L., Turner, D. B., & Stern 1994).

Size and chemical composition are essential influent parameters in PM's potential to be unsafe (Harrison & Yin, 2000). Particles vary in size from micrometres to nanometres; PM_{10} (particulate matter with a diameter of less than 10 m) can penetrate the respiratory system and reach the lungs. The coarser particles, i.e. those with a diameter of 10–2.5 m ($PM_{10–2.5}$), reside in the upper respiratory tract, whilst the finer particles, i.e., those with a diameter of less than 2.5 m ($PM_{2.5}$), move directly to the lungs and are capable of entering the bloodstream. (Sánchez-Soberón et al. 2015). However, irregular, intermittent air pollution sources can cause the acute health risk used in dispersion modelling to be overstated, with respect to the improbable occurrence of emissions under the most severe weather conditions (Balter and Faminskaya 2017).

WHO estimates that about 800,000 fatalities worldwide occur annually as a result of respiratory and cardiovascular diseases, as well as air pollution-related lung cancer (Motesaddi Zarandi et al. 2015). Over the last few decades, extensive research has been conducted on long-term human exposure to nonlethal air pollution and the impact of emissions on regional and international atmospheric cycles. The pollutants that have earned special recognition include PM, ozone (O_3), total suspended particulates (TSP), nitrogen dioxide, sulphur dioxide, carbon monoxide, and lead, among others (Kirk, R. E., & Othmer 2007).

The cement industry's power usage is estimated to account for 2% of global energy use, with cement production accounting for 5% of global CO_2 emissions (Worrell et al. 2001). Mineral dust contains elevated amounts of certain metals that are thought to be toxic to plants, wildlife, and humans (Dubey and Bhopal 2013). It has been estimated that one kilogram of cement produced in Egypt produces approximately 0.07 kilograms of atmospheric dust (Hindy, Abdel Shafy, and Farag 1990).

Pollutant sources at manufacturing plants are mainly categorised into two categories: (1) point sources, which are piles exiting at manufacturing plants; and (2) volume sources, which are spaces within production facilities from which pollutants usually depart via controlled outlets (Abu-Allaban and Abu-Qdais 2011). The primary sources of global pollution emitted from cement manufacturing are gas and dust. The specific pollutants found in the gas are SO_2, NO_2, and CO; they can be classified under raw mill and kiln stack exit point source emissions. The specific pollutants found in the dust include TSP, PM_{10}, and $PM_{2.5}$; they are emitted from the clinker cooler and exit locations of cement mill stacks as point sources, and also from outlets through dust control devices as volume sources (Al Smadi, Al-Zboon, and Shatnawi 2009). By polluting the climate and posing health risks, the cement industry causes great environmental instability. Cement processing requires extensive use of natural raw materials and resources, resulting in atmospheric and soil emissions. The ability to control the cement manufacturing process and the degree of emissions can be a rewarding career (Madsen et al. 2004).

2.2 The Production of Cement

The cement production summary distinguishes three basic production steps (Figure 2.1) (Hendriks et al. 2003).

1. Mixing/homogenising, grinding, and preheating (drying) provides the raw meal.
2. Burning the raw meal forms cement clinker in the kiln, i.e., raw meal components react at high temperatures (900–1500 °C) in the precalciner and rotary kiln to produce cement clinker.
3. Clinkers are melted and combined with contaminants, i.e., the clinker is ground with additives after cooling.

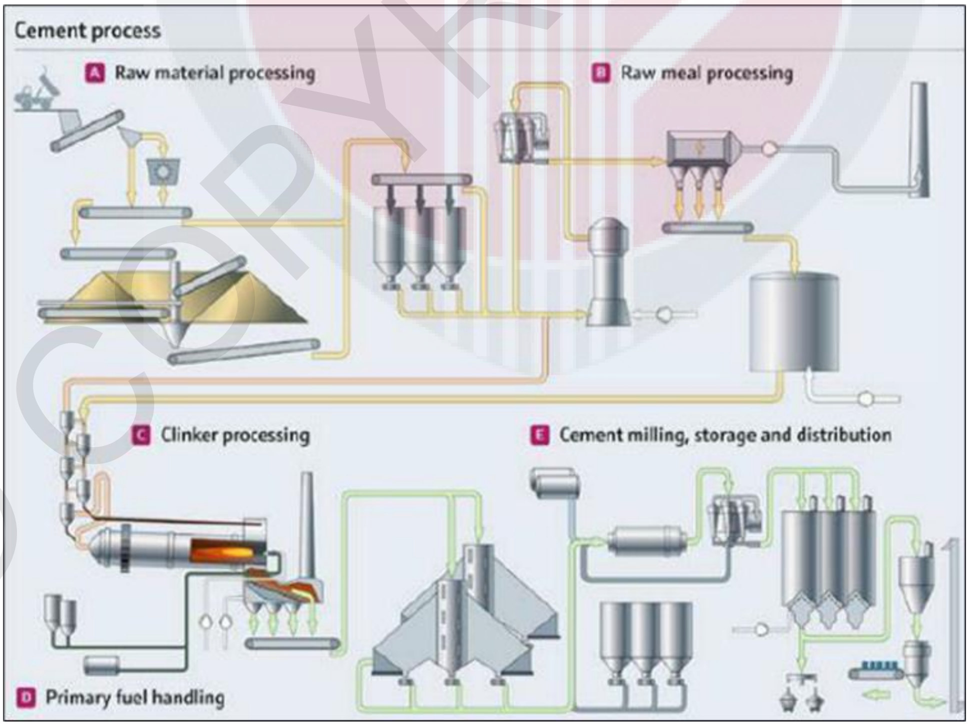

Figure 2.1 : Cement Process Plan (Devi, 2018)

2.3 Cement Industry Emissions

Cement manufacturing is a massive operation that necessitates a large amount of energy and resources, including raw materials, thermal fuels, and electrical power (Devi, Lakshmi, and Alakanandana 2017).

Cement plants emit various types of plumes, including detached plumes like steam and organic plumes (Miller, 2001). Plume dispersion models change as plant sizes increase, with coning being critical for smaller plants due to its higher frequency (Carpenter et al., 1971). Plume behaviors such as looping, meandering, and inversion trapping vary between flat and hilly terrains (Moore et al., 1988). Controlling flame shape and length is crucial for reducing fuel consumption and improving combustion efficiency in cement kilns (Tosunoglu, 2007). Air pollution dispersion from cement factories can be analyzed using both 2D and 3D models that take into account the dynamics of wind fields (Emetere & Akinyemi, 2013). The technologies for controlling particulate emissions in cement plants have advanced significantly to comply with stricter emission regulations (Biege et al., 1997). The use of fans is crucial for managing gas flow within these facilities (McKervey & Perry, 1993). Furthermore, recirculation fumigation technology has been introduced to enhance the fumigation process of concrete silos in the cement sector (Noyes et al., 2010).

The major environmental effects of cement production can be classed as follows.

2.3.1 Gases and Volatile Organic Compounds

Typical pollutants emitted into the air from the manufacture of cement include NO_x, SO_2, CO, CO_2, H_2S, volatile organic compounds (VOCs), dioxins, furans, and particulates (Mishra and Siddiqui 2014). It is possible to divide these major contaminants into two categories: gaseous and particulate. The combustion of fuel produces gaseous pollutants such as nitrogen oxides, sulphur oxides, carbon oxides, hydrogen sulphide, and volatile organic compounds. Quarrying is a source of PM in the form of dust and carbon particles, generated by fracking, blasting, transport, cement mills, petrol preparation, packing, road sweeping, and stacks (Al Smadi, Al-Zboon, and Shatnawi 2009), (Asuoha and Osu 2015), (Hesham G. Ibrahim, Aly Y. Okasha and Al-Meshragi 2012).

The amount of emissions generated is typically influenced by several factors, including oxygen, nitrogen, and combustion temperatures. The alkaline cement is replaced by reacting with sulphur dioxide and some nitrogen oxide (Devi, Lakshmi, and Alakanandana 2017).

VOCs are released directly into the air due to evaporation or some form of volatilisation. Further sources include stored petrol, solvents, and other raw compounds, and also some industrial processes. Failure to burn various fuels is also a significant source of VOC emissions into the atmosphere (Zimwara, Mugwagwa, and Chikowore 2012).

2.3.2 Dust

The cement industry is a significant emitter of mineral dust, with rotary kilns, raw mills, clinker coolers, and cement mills being the primary sources of dust pollution in the cement manufacturing process (Uliasz-Bocheńczyk 2019).

2.3.3 Noise

Another consequence of the cement industry is noise pollution. The stone crushers, frames, furnaces, cement transport systems, compressor chambers, and other machine operating sites generate significant levels of noise. In fact, in the cement industry, noise is a safety issue; long-term noise sensitivity can result in hearing loss (Arachchige 2019). Toure et al. (2023) developed an approach for risk assessment of noise pollution in a cement plant and studied the impact of noise pollution on workers. They suggested that the workers are mainly exposed to noise and have hearing problems. In addition, Awos (2024) found that the highest daily noise level result at the cement factory was below the NESREA regulatory standard in Ewekoro, Ogun State, Nigeria.

2.3.4 Bad Smell

A foul smell usually occurs during the chemical and discharge processes due to not cleaning before emissions are generated. However, the extensive washing required to prevent odour is challenging in factories where production machinery isn't properly maintained, with odorous ambient gases leaking into the atmosphere (Cheremisinoff 1992).

2.4 Air Pollution Models

Point source pollution dispersion models simulate the spread of pollutants from a single, identifiable source such as a smokestack or exhaust pipe. These models typically use Gaussian plume equations to calculate pollutant concentrations downwind based on emission rate, wind speed, atmospheric stability, and stack characteristics. They're relatively simple to use and computationally efficient, making them ideal for quick assessments and regulatory applications. While they can be useful, these models might oversimplify the complexities of different terrains and changing weather conditions. Point source models are typically employed for managing emissions from industries, power plants, and urban air quality. Recent research has aimed at enhancing the accuracy and applicability of point source pollution dispersion models. Gaussian dispersion models are still popular due to their straightforwardness and effectiveness (Singh, 2018; Sachdeva & Baksi, 2018). Researchers have created time-dependent models that take into account surface and inversion layer effects (Pal & Khan, 1990), along with models that feature variable wind speeds and constant removal rates (Verma, 2015). Numerical methods have also been investigated for modeling how pollutants disperse from point sources (Dvořák et al., 2008). Some studies highlight the importance of photochemical pollutant models that consider long-range transport and the influence of topography (Turner, 1979). There have been suggestions to modify the Pasquill-Gifford system to enhance point-source-plume modeling (Pasquill, 1979). Recent innovations include the integration of both integral and particle models to describe dispersion in aquatic environments (Johnsplass et al., 2021). These advancements are aimed at improving our understanding and forecasting of how pollutants disperse from point sources across different environmental settings.

Line source pollution dispersion models are created to simulate how pollutants spread from linear sources such as highways or busy streets. These models typically utilize a series of point sources or modified Gaussian plume equations to depict continuous emissions along a line. They take into account various factors, including traffic volume, types of vehicles, and the geometry of the road. Line source models are especially valuable for evaluating traffic-related air pollution and for urban planning purposes. While they can provide reliable estimates for pollutant concentrations near roads, their accuracy may decrease in complex street canyons or under significantly varying meteorological conditions along the line source. Recent research has aimed at enhancing these models for vehicular emissions. Several models based on the Gaussian method have been developed and assessed (Yang Fang, 2004; N. Sharma et al., 2004). The SLINE 1.0 model includes wind shear effects near the ground for both stable and unstable atmospheric conditions (Madiraju & Kumar, 2021). A three-phase turbulence model has been suggested to improve dispersion predictions (Madiraju & Kumar, 2022). Finite line source models, like GFLSM and R-Line, have been proposed as alternatives to infinite line source models in specific situations (Adak, 2020). Model intercomparison studies have been carried out using data from field experiments to assess the performance of various models, including ADMS-Roads, AERMOD, CALINE, and RLINE (Stocker et al., 2013). Additionally, there have been efforts to create computationally efficient models that are suitable for real-time traffic control applications (Damoiseaux & Schutter, 2021).

Area source pollution dispersion models are designed to simulate how pollutants spread from two-dimensional sources, such as landfills, urban areas, or large industrial complexes. These models typically break the area into a grid of smaller cells, treating each as a point or volume source. They often use more sophisticated algorithms to account for variations in emissions and meteorological conditions. Area source models are essential for regional air quality assessments and urban planning, as they can manage multiple pollutants and various source types at the same time. However, they demand more detailed input data and greater computational resources than point or line source models. The accuracy of these models can be affected by the resolution of the input data and the complexity of the terrain. Recent research has made strides in area source pollution dispersion modeling, tackling challenges in urban and industrial settings. Venkatram & Thiruvenkatachari (2023) introduced an efficient method for representing arbitrarily shaped area sources using line source models. Different models, including Gaussian plume dispersion, have been utilized in port areas (Milošević et al., 2020) and industrial contexts (Nebenzal et al., 2020). Atmospheric stability conditions play a crucial role in pollutant dispersion, with extremely stable conditions resulting in near-road concentrations that can be up to 12 times higher than those under neutral conditions (Huertas et al., 2021). The integration of dispersion models with GIS has enhanced exposure assessments in urban settings (An International Quarterly et al., 2022). Nonetheless, challenges persist in addressing indoor air pollution and the pathways between indoor spaces (de Ferreyro Monticelli et al., 2021). Advanced Gaussian plume models like ADMS and AERMOD have demonstrated comparable performance in simulating SO2 emissions and NOx chemistry (Patiño, 2020), serving as valuable tools for evaluating local air quality impacts from stationary sources.

2.4.1 Dispersion Models

Air pollution dispersion models play a vital role in predicting and managing air quality. These models vary from straightforward Gaussian plume models to more intricate computational fluid dynamics methods (Johnson, 2022; Leelőssy et al., 2014). They take into account factors like meteorological conditions, topography, and the characteristics of pollutants to estimate ground-level concentrations (Barratt, 2001;

Singh, 2018). Common types of models include Gaussian, Lagrangian, Eulerian, and CFD models, each offering unique advantages and limitations (Srivastava & Sinha, 2004; Leelőssy et al., 2014). Recent developments have introduced parallel computing and adaptive mesh refinement (Leelőssy et al., 2014). These models are essential for regulatory decision-making, environmental planning, and risk assessment (Srivastava & Sinha, 2004; Barratt, 2001). They can be utilized in various situations, from industrial emissions to accidental chemical releases (Sachdeva & Baksi, 2018; El-Harbawi, 2013). Despite significant improvements, challenges persist in accurately modeling complex atmospheric processes and validating the results (Chakraborty et al., 2019).

2.4.1.1 Gaussian Plume Models

Many decades have gone by since atmospheric dispersion models were created to explain how spontaneous and volatile substances are released into the air. The Gaussian plume model is often used for its simplicity; it represents a plume generated by a point source with a consistent wind direction. These simplifications enable the development of analytical solutions by introducing slight modifications to the model, making it more realistic, such as including specific vertical velocity changes caused by atmospheric layers.

Gaussian plume models respond quickly to new information. This model uses a straightforward formula for each data point, which greatly offsets the extra computational expense associated with turbulence. The model's duration can be shortened, especially in real-time and near real-time support applications (Brusca et al. 2016).

The Gaussian diffusion model was developed to help manage manufacturing operations and air pollution control under various circumstances, and also confront dangerous air pollution crises (Tang, McNabola, and Misstear 2020).

There are several different forms of pollution sources: a point, a volume, an area, an open pit, and a line. In general, Gaussian models can be used with more than one source by employing the superposition theorem. The Gaussian plume can be described as follows. First, we assume a Cartesian orthogonal reference system, where the origin represents the location of the pollution source. The x-axis is oriented perpendicular to the wind direction, while the y-axis is horizontal and perpendicular to the x-axis. The z-axis is vertical, indicating the height above the earth's surface (Brusca et al. 2016).

Goudarzi et al. (2017) and Fakinle et al. (2018) provided detailed equations for the fundamental formulation used to determine ground level concentration, as described by the Gaussian model (GM) in a downwind direction, represented by Equations 1 and 2:

$$x = \frac{Q}{2\pi u_s \sigma_y \sigma_z}\left\{exp\left[-0.5(\frac{z_r - h_e}{\sigma_z^2})^2\right] + exp\left[-0.5(\frac{z_r + h_e}{\sigma_z^2})^2\right] + A\right\} \tag{2.1}$$

$$A = \sum_{N=1}^{K}\left[exp\left(\frac{-0.5(z_r - h_e - 2Nz_i)}{\sigma_z}\right)^2 + exp\left(\frac{-0.5(z_r - h_e - 2Nz_i)}{\sigma_z}\right)^2 + exp\left(\frac{-0.5(z_r - h_e - 2Nz_i)}{\sigma_z}\right)^2 + exp\left(\frac{-0.5\ (z_r - h_e - 2Nz_i)}{\sigma_z}\right)^2\right] \tag{2.2}$$

where x is concentration in the downwind direction (μg·m^{-3}); Q is rate of pollutant emission (g·s^{-1}), u_s is the wind speed in the stack (m·s^{-1}); σ_y and σ_z are the standard deviations of lateral and vertical dispersion (m), respectively; vertical scattering (m);

z_r and z_i are the receptor height above ground level and the mixing height (m), respectively; and h_e is the height of the central plume (m).

The different measures to approximate CO concentrations in the downwind direction using wind speed are employed in Equations 3–11. Using Equation 3 as a reference, the air velocity at 10 m above ground level is converted into wind speed in the stack nozzle.

$$u = u_0 (\frac{H_s}{Z_0})^n \tag{2.3}$$

Where u and u_0 are the wind speed (m·s^{-1}), H_s is the stack height (m), Z_0 is the reference height (m), and n is an exponent of the wind profile.

Furthermore, to calculate the initial buoyancy flux (F_b), Equation 4 is used:

$$F_b = \frac{W_0 R_0^2 g}{T_{p0}(T_{p0} - T_{a0})} \tag{2.4}$$

Where W_0 is the initial gas flow velocity, R_0 is the stack radius, T_{p0} the temperature of the initial plume, and T_{a0} is the ambient temperature at stack height.

Moreover, the temperature is required to calculate the buoyant plume rise (dh), given by Equation 5 at stack high wind speeds:

$$dh = 38.71 \frac{F_b^{0.6}}{u_s} \tag{2.5}$$

Equation 5 received a buoyant increase of 55 m^4·s^{-3} in the Pasquill stability classes A–D; in this analysis, the F_b volume was calculated to be less than this figure.

The final plume rise (dh) in a stable atmosphere for classes E and F is given by Equation 6:

$$dh = 2.6(\frac{F_b}{u_s})^{\frac{1}{3}} \tag{2.6}$$

Stack height (h_s) plus plume rise (dh) equals the final effective height of the plume (H) in metres, given by Equation (7):

$$H = h_s + dh \tag{2.7}$$

For the rural process, Equations 8–10 (roughly in line with the Pasquill–Gifford curves) have been used to compute δ_y and δ_z:

$$\delta_y = 465.11628(x)\tan(TH) \tag{2.8}$$

$$\delta_z = ax^b \tag{2.9}$$

$$TH = 0.017452393[\mathrm{c} - \mathrm{d}\ln(x)] \tag{2.10}$$

Where parameter x is the downwind distance. The values of a, b, c, and d were calculated using Pasquill stability classes.

Meteorological information from either surface weather observation stations close to the cement factory or meteorological websites is required to evaluate the environmental impact assessment. The data and information required are listed as follows (Goudarzi et al. 2016):

1. Wind speed and direction, for drawing seasonal wind roses
2. Carbon monoxide samples, obtained from stacks in the cement plant
3. The temperature of gas flow
4. Exit gas velocity

5. The stack height for Electro and Kiln filters

6. The inner diameter of the stack, used for modelling dispersion

A.J. (2013) depended on Lodge (1995), and Rao (2006) classified and derived the average wind speed as illustrated in Table 1 below:

Table 2.1 : The Pasquill-Gifford Stability Classification Based on Wind Speed Values

Wind speed ($m.s^{-1}$) (at z=10m)	Day – time insolation			Night – time cloud cover	
	Strong	Moderate	Slight	>4/8 Cloud	<3/8 Cloud
< 2	A	A – B	B	–	–
2 – 3	A – B	B	C	E	F
3 – 5	B	B – C	C	D	E
5 – 6	C	C – D	D	D	D
>6	C	D	D	D	D

Where, A: Highly unstable, B: somewhat unstable, C: mildly unstable .E: Somewhat stable, F: stable.

2.4.1.2 AERMOD

The AERMOD model is AERMIC's scheme, including moist PM and gaseous deposition and source or plume depletion. The AERMOD model can be used in both rural and city settings, on flat and diverse land, ground and raised releases, and multiple outlets. Every effort was made to prevent discontinuities in model formulation, where significant differences in measured concentrations result from minor adjustments in parameters. This method was formulated to be physically practical and easy to execute. AERMOD does not require the definition of complex terrain regimes (WANG Hai-chao,JIAO Wen-ling 2010).

Given the height of the surface (Z_0), the wind direction, and the temperature, AERMOD only needs a single surface wind speed calculation (calculated between Z_0 and 100 m). The flow of data in AERMOD calculates the convective mix's height during the day (Kalhor and Bajoghli 2017). AERMOD can replace the ISC3 platform by operating using National Weather Service (NWS) data of a type that is readily available to stations. The parameters used by the meteorological guide inside AERMOD produce profiles of the meteorological variables required. Vertical depths of all available meteorological measurements are used to measure the wind level, wind direction, humidity, temperature, and temperature gradients (Jafarigol et al. 2016). AERMET's key objective is the measurement of maximum layer parameters for use in AERMOD.

Nonetheless, if a cloud obscures two vertical temperature measures (typically at 2 and 10 metres) and a solar radiation measurement (e.g., from the on-site monitoring program), they are replaced. AERMOD is programmed to operate on the bare minimum of observed weather parameters. To construct similarity profiles of corresponding PBL parameters, ground features (surface area, roughness, Bowen ratio, and albedo) are also required. Besides that, AERMET considers all meteorological measurements concerning AERMOD (Hoffnagle 2018).

A detailed explanation of the basic AERMOD dispersion model formula is given below. A dispersion model's actual implementation, such as AERMOD, can be demonstrated by developing a simple model for estimating concentrations at ground level linked to ground release, as shown in Figure 2.

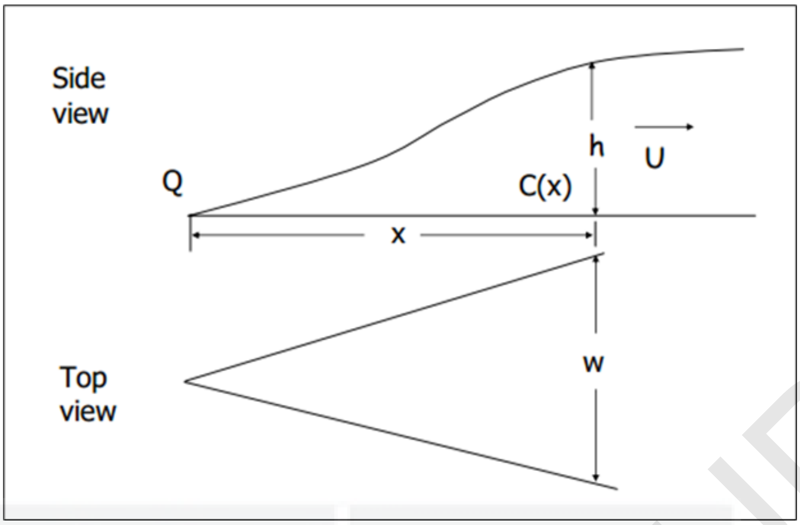

Figure 2.2 : Template of Surface-Release Plume Dispersion
(Venkatram and Modeling 2005)

Assuming the toxin release rate is Q (g·s^{-1}) for convenience, it is suggested the pollutant blends well around the plume's cross-sectional region, both horizontally and vertically. The height (*h*) multiplied by the width (*w*) equals the cross-sectional area on a line (*x*) from the source. The substance which moves through this region is then given by *C*(*x*) *hwu*, where *u* is held constant over the plume height. If we assume that the field does not absorb any material, then the emission rate (*Q*) must be equivalent to the material transfer through the plume cross section at any distance. The following the concentration expression is introduced as a result of this *C*(*x*):

$$C(x) = \frac{Q}{Uhw} \tag{2.11}$$

Although this is a highly simplified real-world model, it contains the basic aspects of regulatory dispersion models. Equation 1 multiplied by a constant provided the basis for Pasquill's proposed dispersion scheme in 1961. How can we determine the height and width of a plume when the concentration is not consistent across the plume's cross section? Observations reveal that the average time concentration has roughly Gaussian distributions both horizontally and vertically, as seen in Figure 3.

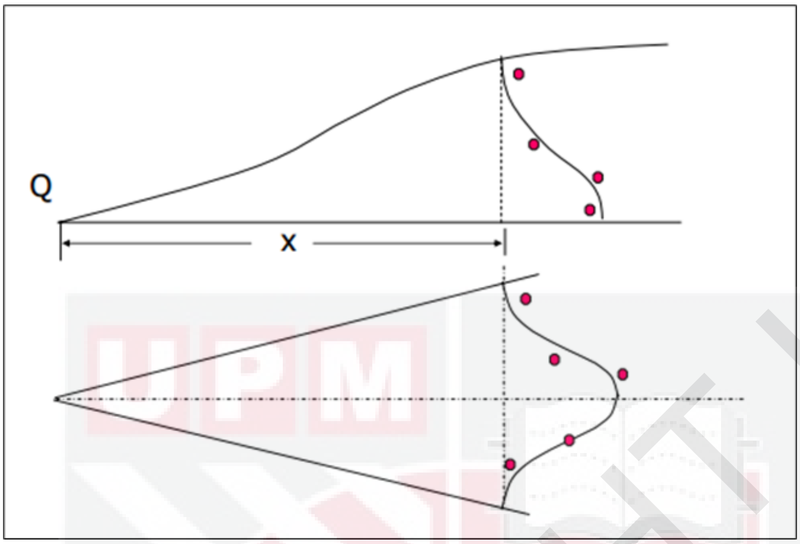

Figure 2.3 : Concentration Levels at Any Height Are Describable Regarding Gaussian Distributions Formed by the Bell. True Calculations Can Be Significantly Deviating from Straight Curves (Venkatram and Modeling 2005)

The distribution of concentration, *C*(*x*, *y*, *z*), can be represented for any height by:

$$C(x,y,z) = C(x,0,0)\exp\left(-\frac{y^2}{2\sigma_y^2}\right)\exp\left(-\frac{z^2}{2\sigma_z^2}\right) \quad (2.12)$$

Where y is the distance from the plume's centreline, as shown in Figure 3 as a dotted line; σ_y is the standard deviation of the Gaussian horizontal distribution; z is the height from the ground; and σ_z is the standard deviation of the Gaussian vertical distribution.

The plume's horizontal and vertical spreads are respectively compared to the distribution's standard deviations, σ_y and σ_z. Remember that individual concentration measurements can differ significantly from the formula's smooth curve (Venkatram and Modeling 2005).

Some notes regarding the emission process are as follows:

1. When the stack pollution concentration is below the acceptable level, long-term exposure will pollute the atmosphere and endanger people's health (E. A. Jayadipraja et al. 2016).

2. It is not common practice to use the full hourly time series of estimated concentrations in ISC / AERMOD; employing the series in its entirety induces randomness and accumulates in the desired direction (Avaliani et al., 2016).

3. These cement plants provided the data for estimating the emission factor, as did bibliographical research on comparable cement plants and the AP-42 guidelines. The most important information for calculating TSP pollution factors from these cement plants involves stacks; every cement plant has four active stacks to regulate emissions: the main kiln, the clinker cooler, the cement mill, and the raw mill, as well as bag filters (Abril et al. 2016).

4. Concentrations of released dust vary significantly during the cement manufacturing process, especially for fugitive sources, based on the local sources' quality and other considerations such as topography and overall climate conditions. Moreover, emitting events differ over time, and the information is always incomplete (Abril et al. 2016).

5. Gaussian ground level concentrations can be assessed in a specific study region within a non-uniform Descartes receptor network at a defined radius in kilometres from the sources (Amoatey et al. 2019).

6. The calibration equations previously mentioned could be used to change measured PM values. (Adeniran et al. 2018). The WolfPack® Compact Field System tracked all gaseous pollutants. Urban air control devices. It is embedded with a WinCE® operating system running GrayWolf's WolfSense® 2009 application software to view, register, and monitor critical parameters (Adeniran et al. 2019).

The AERMET model incorporates climate data such as wind speed and distance, temperature, cloud cover, and also surface data, including albedo, surface roughness, and Bowen ratio (Jayadipraja et al., 2016; Cimorelli et al., 2005).

To compute a representative terrain impact height, also referred to as terrain height, AERMAP uses grid elevation data. The AERMAP terrain data can be extracted from GTOPO30 (Seangkiatiyuth et al. 2011). AERMAP also accommodates topographic grid data derived from digital elevation models (DEMs) and receptor locations measured from mean sea level (MSL) (Jayadipraja et al., 2016; Cimorelli et al., 2005).

2.4.1.3 HIWAY-2 and CALINE-4

HIWAY-2 and CALINE-4 are the main models used to understand how pollutants diffuse along roads. The HIWAY-2 model classifies atmospheric stability into three categories: unstable, neutral, and stable, and it takes into account how mechanical turbulence affects diffusion during these stability conditions. On the other hand, the CALINE-4 model divides the highway into several segments, allowing for the measurement of pollutant distribution and variation within a 500 m range on either side of the highway, which helps in predicting pollutant concentration along the highway (Yu et al. 2019).

2.4.1.4 CAR-FMI

The CAR-FMI model (Contaminants in the Air from a Road, Finnish Meteorological Institute) is a Gaussian Plume model that utilizes the equations developed by Luhar and Patil (Luhar, 1989). This model measures the hourly concentrations of CO, NO, NO2, NOx, and PM2.5 emitted by automobiles. It also incorporates scaling of the boundary layer to describe atmospheric equilibrium. CAR-FMI, like other Gaussian models, has limited applicability to low wind conditions (Chimica and Tor 2006).

2.4.1.5 OSPM

The Operational Street Pollution Model (OSPM) is a functional, quick, and effective model of street pollution developed in Denmark that is now widely used around the world. In this model, the concentrations of engine exhaust emitted by road vehicles are measured by employing a plume model for direct contribution and a box model for street contaminant diffusion (Kakosimos et al. 2010).

2.4.1.6 AEROPOL

Tartu's air pollution modelling work began in the mid-1990s, leading to the development of the AEROPOL model.

The core features of AEROPOL 2.0 are as follows:

- Gaussian dispersion is included—the dry and wet fluxes, as well as concentrations, are measured.
- It contains dispersion parameters that depend on height and building effects.
- It considers both PM and gaseous pollutants.
- It considers point, line, and area sources of pollution.
- Its estimates are feasible for various meteorological conditions, time series, or temperature distributions.
- Modern Windows versions are available on PC.

Line sources include roads, which are shaped as segmented lines. Area sources include suburban traffic and domestic heating. Gridding is used for line and area sources, and every grid cell (usually 50–100 m) is viewed as a point source.

The AEROPOL model incorporates the following data:

- Stack data (coordinates, height, diameter, velocity and temperature of the gas, source pressure ($g \cdot s^{-1}$));
- Geometric data (buildings and obstacles);
- Admixture data (deposition velocity and washout coefficients (for gases), particle density and diameter);
- Meteorological data (wind speed and direction, temperature, cloudiness, date and time (dispersion parameters are calculated using Pasquill stability classes)) (Kimmel and Kaasik 2003).

2.4.1.7 UK-ADMS

The Atmospheric Dispersion Modelling System (ADMS) is a dispersion model which simulates bouncy, straightforwardly energetic particles and gasses in the atmosphere (DJ Carruthers, RJ Holroyd, JCR Hunt 1994). In its met pre-processor, the model can predict boundary layer structures (Bachtiar, V. S., & Davies 2018). The model uses a regular, unstable, and neutral Gaussian distribution (Chimica and Tor 2006). ADMS was developed by the UK government and industry consortium (Hanna et al. 2001).

2.4.1.8 SCREEN3

The Industrial Source Complex Dispersion Model (ISC3) is sampled in SCREEN3 (LIU et al. 2007). The SCREEN3 model utilises a Gaussian plume model that considers source-related factors and meteorological factors (S. Zhong, Zhou, and Wang 2011). In this model, it is assumed that the pollutant has no chemical reactions and that the feather during transport from the source does not work for other deletion methods, such as water or dry disposal (Brode 1995).

Box models

The box is the most essential mechanism for dispersion models, whereby the airshed is represented by a particular box or atmosphere volume. In these models, air contaminants in the box are spread uniformly and theory is used to estimate average levels of pollutants in the box. Nevertheless, while helpful, these models' capacity to predict air contaminant dispersal through an airshed is minimal since it assuming a homogenous distribution of pollutants does not accurately reflect reality (Oliveri Conti et al. 2017).

Computational fluid dynamic models

Computational fluid dynamic (CFD) models are used to predict wind and turbulence in a given setting and the transport and dispersal pollutants. They have become the community's preferred air quality model for understanding complex flow and the resulting dispersion behaviour. CFD models provide information about flow patterns that would be difficult or expensive to analyse using conventional experimental techniques. CFD models predict fluid flows in a qualitative and/or quantitative manner using mathematical formulas (partial differential equations), numerical techniques (discretisation and solutions), and software (solvers, pre-processing, and post-processing) [73, 74].

Given identical inputs, different CFD models demonstrate great agreement in the overall wind flow field but substantial variations in speed and turbulence. The discrepancy in wind tunnel information could be due to the various models' closing mechanisms (Gidhagen, L., C. Johansson 2004).

Lagrangian Models

Lagrangian particle dispersion models (LPDMs) can adapt approaches for simulating atmospheric gas, aerosol distribution, and turbulent mixing (Pisso et al. 2019). The Numerical Atmospheric-dispersion Modelling Environment (NAME) is an example of a Lagrangian model (Jones et al. 2007). Since the topography in a power plant's immediate surroundings is typically quite complex, LPDMs help to analyse pollutant flow, mainly using concentrations from the power plant's immediate environment (S. U. Park et al. 2016).

On the other hand, Lagrangian puff models are non-state, which implies that the model's input parameters change over time. Lagrangian models are frequently used to quantify the near-instantaneous impacts of a small number of high-resolution sources. In general, Lagrangian models are more stable but also more complex than Gaussian models. Many Lagrangian models are associated with gas and particle chemistry (Oliveri Conti et al. 2017).

2.4.1.9 CALPUFF

The California Puff Model (CALPUFF) was created by the California Air Science Board, funded by the Sigma Research Corporation. For case-by-case usage in various landscape and wind situations, CALPUFF is a receptor model recommended by the

U.S. EPA (Scire, Strimaitis, and Yamartino 2000). CALPUFF is a Lagrangian dispersion model, which is multi-layer, multi-species, and non-state. For isolated "puffs" released from models, dispersion is simulated. When dispersion, transfer, and elimination are measured, the puffs are monitored before the modelling domain is eliminated (USEPA 2004). A puff model opens emissions regularly (Silverman et al. 2007). CALPUFF was developed to model spaces 10–100 km from a source (Jittra, Pinthong, and Thepanondh 2015).

Statistical and Spatial Models

To enhance inventory accuracy and allow data management, a systematised emission inventory needs to be developed. The geographic information system (GIS) has sufficient storage capabilities, manipulating and processing digital data and delivering it to models appropriately. In the late 1980s, GIS was first widely used in transportation research (Thill 2000). However, it wasn't until the late 1990s that GIS was applied to modelling and managing air quality (Dalvi et al. 2006).

The spatial correspondence between air quality and disease statistics in the affected region can be reflected by GIS. The visualisation of information from various points of view categorises and reclassifies the information based on class breaks. In particular, GIS should investigate the following (Yerramilli, A., Dodla, V. B. R., & Yerramilli 2011):

- The relative spatial phenomenon of pollutant distribution in terms of position, extent, and time;
- The spatial scale and rate of pollutant dispersion below the impact zone at every geographical point;

- The socioeconomic characteristics of the populations impacted by these pollutants.

2.4.1.10 Interpolation Methods

Inverse distance weight (IDW), ordinary kriging (OK), and universal kriging (UK) are normal interpolation processes utilised to estimate air pollutant concentrations (H. Xu et al. 2019). GIS spatial interpolation technologies can interpolate successive air emission amounts based on distinct point values (Zou et al. 2010). Lawal and Asimiea (2017) used the Gaussian plume model following the geostatistical technique (empirical Bayesian kriging (EBK)) to estimate the potential spatial distribution of fugitive dust emitted from the Obajana Cement Plant in Nigeria.

Bhattacharjee and Chen (2020) used the kriging interpolation method to create a more accurate spatial prediction for $OCO\text{-}_2$ concentration measurements. According to the author, prior research has demonstrated that geostatistical interpolators, mainly multiple variants of kriging, are the most commonly used techniques for producing a full mapping of sparsely sampled data. Nonetheless, there is variation caused by many factors, such as the predictor smoothing factor, the available observed/sampled positions, and the category of auxiliary information. Geostatistical spatial interpolation and simulation techniques can produce raster grid-cell-based maps of soil pollutants and use spatial analysis to investigate differences in heavy metal emissions. Soil pollution maps allow for the separation of an area's natural baseline levels from anomalous increased levels due to human activity, as well as the identification of areas of polluted topsoil that require remedial action (Suh et al. 2017).

2.4.1.11 Spatial Proximity Models

Spatial proximity models are used based on the hypothesis that the emission source's spatial proximity is a proxy for exposure in the healthy human environment to establish associations between air environment and health consequences (Gupta 2018).

When the intensity of spatial monitoring stations is limited, GIS-based proximity models are among the essential tools for evaluating air pollution exposure (Zou et al. 2016). On the other hand, proximity models have some issues, including the fact that greater exposure is associated with smaller distances between receptors and sources of pollution. If the distance between a receptor and its nearest pollution source falls under a predetermined threshold, the receptor will assesses exposure levels in a "binary end mode" (Zou et al. 2009).

The spatial proximity method includes the transition of parameters from adjacent catchments to the unmanned catchment; since environment and catchment conditions can have similar spatial variations, catchments near each other are expected to behave similarly. This approach, being dependent on the density of the gas basin network, is intuitively attractive. Note that many improvements have been suggested for this procedure, such as reverse weighting of the donor catchments and the correction of the model's parameter values (Oudin et al. 2008).

2.4.1.12 Land Use Regression Models

LUR models play a vital role in understanding air pollution variations in urban areas. They effectively link easily obtainable land use data with pollutant measurements, making them a strong alternative to traditional methods. Like other air emission measurement techniques, LUR models depend on pollutant samples collected from specific sites to identify independent variables; however, they require less data (Gupta et al. 2018). Recently, there has been an excessive focus on this approach to grasp urban air dynamics, often integrating it with other algorithms to enhance prediction accuracy (M. M. Rahman et al. 2017).

Land use regression (LUR) models can be used to create maps showing air pollution concentrations and serve as a predictive tool available as a separate raster file. A script that relies on pollution levels can produce hazardous outcomes. The calculations for LUR models are demonstrated using raster Python (Schmitz et al. 2019).

The GIS-based regression mapping approach employed in their analysis provides an effective technique for generating maps of traffic-related contaminants like NO_2. These maps reliably estimate emission levels correctly at un-sampled sites. Nevertheless, as with any analytical strategy, regression mapping has some drawbacks; for instance, it potentially suffers from being case- and area-specific. When models are created exclusively through trial and error, a statistical optimisation process is particularly true. As the results for Amsterdam in this analysis suggest, the regression equations used cannot be true outside of that particular field of study. Nevertheless, when regression models are based on a basic underlying theory, as is the case in Prague and Huddersfield, the models can be more generalised (Briggs et al. 1997).

Based on previous conclusions, it is clear that the performance of the LUR models in different locations are considerably different because of the unique features of each site, the variability of impacts on pollutants examined for the predictor variables, and the choice of LUR models (M. M. Rahman et al. 2017).

2.4.1.13 Hybrid Models

Owing to the shortcomings of individual methods, multiple authors have opted to use the predictive validity of two or more air pollution models together. Lai et al. (2019) incorporated a wide range of models for air quality, such as the AERMOD and CMAQ diffusion models, using the leading meteorological Weather Research and Forecasting (WRF) model and benefitting from the advantages of a hybrid air quality model, which produces a more effective analysis of the required distribution of primary and secondary pollutants, as well as many other environmental data. Beckerman et al. (2013) developed a hybrid solution that combines two models: a LUR model selected by machine learning technology and LUR space-time residuals (BME) for LUR interpolation to measure PM smaller than 2.5 metres in the air. It can be inferred that combining the Support Vector Machine (SVM) and Partial Least Squares (PLS) in an urban environment provides a more convenient solution to time series forecasting for estimating Tehran's hourly and periodic atmospheric emissions (Yeganeh et al. 2012).

2.4.1.14 Additional Models

Given different criteria, accuracy, and available data, there are several other methods to measure the air pollution emitted from line, point, and area sources such as transportation and urban, industrial, and service areas. Examples of such models include the following: photochemical models (evaluating the efficacy of air pollution control policies provides valuable methods for regulatory research and demonstration) (Oliveri Conti et al. 2017), the WRF model (a musical numerical weather prediction method of the future for atmospheric science and operational forecasting) (Karl et al. 2015), and receptor models (receptor models play an essential role to identify specific pollutant sources and evaluate each source's quantitative contributions related to environmental data) (B. Yang et al. 2013).

2.4.1.14.1 Limitations of the Gaussian Plume Model

Several experiments have been performed to understand the limitations of Gaussian air pollution estimation approaches due to their susceptibility to inputs and questionable precision (Beychok 1979), and also their limited predictive capability (Carrascal, Puigcerver, and Puig 1993). The Pasquill–Gifford stability classification framework, which only considers the temperature gradient, is used for most Gaussian models. Other systems involve meteorological parameters, such as wind speed and direction, cosmic rays, gradients of accessible heat, etc. when categorising stability (Lapse Rate, Pasquill–Gifford, Turner, -, and Richardson Number). Moreover, plume rise formulas other than the Briggs equations were examined for their appropriateness within existing environmental conditions. As a result, a general kind of model is expected to combine various stability classification systems and plume rise configurations to deliver the best combination that balances the shortcomings of the Gaussian plume model with enhanced predictive capability (Awasthi, Khare, and Gargava 2006).

Plume models use steady-state approximations, which may not account for the time it takes for the pollutant to reach the receptor; this is a severe limitation of particle simulation dispersion models. (Chimica and Tor 2006).

There are many models associated with the Gaussian model, such as AERMOD, HIWAY-2, CALINE-4, CAR-FMI, OSPM, AEROPOL, UK-ADMS, SCREEN3, and CALPUFF (Chimica and Tor 2006).

2.4.1.14.2 Limitations of the Lagrangian Models

While Lagrangian models, including Lagrangian Particle Dispersion Models (LPDMs) and puff models like CALPUFF, are useful for simulating how pollutants spread in complex environments, they do come with some drawbacks. One major limitation is that Lagrangian models can be quite computationally intensive because they require tracking individual particles or puffs over time. This task becomes even more challenging when dealing with large-scale pollution events or long-term assessments, as monitoring each puff or particle through varying atmospheric conditions demands considerable processing power and memory.

Lagrangian models are complex, making them difficult to set up and use. They typically require more detailed meteorological data and terrain information compared to simpler models, such as Gaussian plume models. This added complexity can result in a steeper learning curve for users and a higher likelihood of errors during the model configuration process.

These models are also very sensitive to the quality and resolution of the input data, particularly meteorological parameters like wind speed, wind direction, and atmospheric turbulence. Any errors or uncertainties in these inputs can cause significant deviations in the predicted pollutant concentrations, which complicates the task of ensuring accuracy.

While Lagrangian models excel at near-instantaneous impacts and short-term simulations, their performance can degrade over longer time scales. Long-term simulations may accumulate small errors in the model, leading to less reliable results over extended periods, particularly when modeling regional or global transport of pollutants.

While certain Lagrangian models include gas and particle chemistry, they often find it challenging to accurately represent intricate chemical reactions in the atmosphere, especially over extended distances or timescales. This limitation can hinder their effectiveness in situations where understanding pollutant chemistry is essential, such as in the formation of secondary pollutants like ozone or particulate matter.

Lagrangian models can face boundary issues, particularly when applied to extensive areas. The model might struggle with accurately tracking pollutants near the edges of the modeling domain, making it challenging to follow puffs or particles. This can result in errors when pollutants either exit or enter the model's domain.

Lagrangian models typically work well for isolated or point sources, like power plants or industrial sites. However, they may struggle with area sources, such as traffic emissions across extensive road networks, or in complex urban settings, where the interactions among multiple sources and different atmospheric processes make modeling more difficult.

Even with these limitations, Lagrangian models such as CALPUFF are still effective tools, particularly in scenarios where intricate topography and changing weather conditions significantly influence how pollutants spread. Nonetheless, their application should be thoughtfully evaluated, especially for long-term or large-scale simulations, as other modeling approaches might provide more efficient or precise outcomes.

2.4.1.14.3 Limitations of the Statistical and Spatial Models

Statistical and spatial models, including GIS-based approaches, interpolation methods, spatial proximity models, and land use regression (LUR) models, are commonly employed to estimate air pollution and exposure levels. However, these models have certain limitations. They depend heavily on the availability of data, such as measurements from monitoring stations or land use information. In areas with limited data, such as rural or under-monitored regions, the accuracy of these models can be significantly affected. For instance, interpolation methods need a sufficient number of spatial data points to yield reliable results, and any gaps in the data can result in estimation errors.

Many of these models operate under the assumption that pollutant concentrations vary smoothly across different areas, which isn't always true. For instance, interpolation techniques like kriging rely on the idea of spatial autocorrelation, suggesting that nearby points tend to be more alike. However, this assumption can fail in regions with abrupt changes in pollution levels, such as those found near highways or industrial sites.

Spatial and statistical models frequently simplify the intricate atmospheric processes that impact how pollutants disperse. For instance, LUR models rely on land use characteristics as stand-ins for pollution sources, but they might miss crucial atmospheric elements such as wind patterns, temperature variations, and chemical transformations that play a significant role in pollutant behavior.

These models usually provide spatial estimates of pollutant concentrations, but they often have difficulty accounting for changes over time. For example, LUR models and spatial proximity models tend to offer static or average estimates, which makes it challenging to reflect short-term variations in air quality caused by factors such as traffic surges or shifts in weather conditions.

Statistical models, like LUR models, can experience overfitting if an excessive number of predictor variables are included. This often leads to models that accurately represent the training data but struggle to apply to different locations or time frames. Research has shown that models created for particular regions may not yield good results when used in other areas, largely because of variations in geography, pollution sources, and population density.

Statistical and spatial models, unlike dispersion models, frequently overlook the chemical reactions in the atmosphere that can create secondary pollutants, such as ozone or particulate matter. This oversight can result in an underestimation or misrepresentation of pollution levels in regions where these secondary pollutants play a major role in air quality problems.

Spatial proximity models typically consider exposure levels as binary, determined by the distance from a pollution source to a receptor (for instance, a receptor is deemed exposed if it falls within a specified distance from the source). However, this method oversimplifies actual exposure scenarios, which can fluctuate based on factors such as weather conditions or the arrangement of pollution sources.

Many statistical models, like LUR, are very specific to the cases they address. Their effectiveness relies on the unique features of the area in which they are used. Consequently, models designed for one city or region may not be suitable for another without considerable modifications, which limits their general applicability.

Statistical and spatial models often have difficulty addressing the impacts of complex terrain, including hills, valleys, and buildings, which can greatly affect how pollutants disperse. On the other hand, physically-based models, such as Lagrangian or Gaussian models, are more effective at representing these influences.

Even with these limitations, statistical and spatial models are still important for estimating air pollution in urban areas, especially in places where monitoring data is limited or hard to obtain. Nonetheless, it's crucial to interpret their results carefully, particularly in regions with complicated pollution patterns or insufficient data.

2.4.1.14.4 Validation of Model Results

Validation involves comparing the modeled performance with actual data (Paegelow and Olmedo 2008). Various statistical performance metrics are utilized to assess dispersion models, including mean, standard deviation, fractional bias (FB), geometric mean bias (MG), geometric variance (VG), index of agreement (IOA), factor of two (FAC2), and normalized mean square error (NMSE) (Kumar et al. 2006). Concentration should be statistically analysed because it is a random variable

(Lewellen and Sykes 1989). Furthermore, Kumar et al. (2006) suggested that in order to be applicable, every model should satisfy specific criteria. Time-series graphs of predicted and modelled TSP levels of concentration at both monitoring locations were given by Abril et al. (2016). Although the typical values sometimes did not match, average model values displayed similar trends to those found, and this was mirrored in the implementation of validity indices. It is critical to pay attention to the challenges of obtaining adequate PM validation results, taking into account the sources of emission number, the operation diversity of these sources (the majority of which are fugitive), and the uncertainties arising from the methodology of calculating emission factors.

Using statistical metrics, Amoatey et al. (2019) assessed the accuracies and reliability of the estimated daily SO_2 and NO_2 levels of CALPUFF and AERMOD with field concentrations. The five statistical metrics used to verify model performance according to USEPA guidelines included FB, NMSE, IOA, MG (Amoatey et al. 2019), as seen in Equations 13–17:

$$FB = \frac{2\,(\bar{C}_O - \bar{C}_P\,)}{\bar{C}_O + \bar{C}_P} \tag{2.13}$$

$$NMSE = \frac{(\overline{C_O - C_P}\,)^2}{\bar{C}_O \bar{C}_P} \tag{2.14}$$

$$IOA = 1 - \frac{\sum\,(C_P - \bar{C}_O\,)^2}{\sum(C_P - \bar{C}_O)\,\bar{C}_O \bar{C}_P} \tag{2.15}$$

$$MG = e(\overline{\mathrm{In}\,C_O}\; - \;\overline{In\,C_P}) \tag{2.16}$$

$$VG = e^{[(\overline{In\,C_O - In\,C_P})^2]} \tag{2.17}$$

The expected and monitored CP and CO, respectively, represent mean concentration values. The dimensionless value FB is utilised to test data sets with C values ranging from +2 to −2. Positive and negative FB values reflect under-predictions and over-predictions, respectively (J. C. Chang and Hanna 2004). Also, the NMSE equation computes the variance and dispersion between modelled and calculated data. Consequently, a complete model has FB and NMSE values equal to zero (Lee et al. 2014). Similarly, IOA is used to allocate a score of 0–1 for model accuracy. In an ideal world, IOA would be greater than 0 and less than 1. However, an IOA value of 0.5 is considered powerful (Sciences 2015). FB and NMSE are adaptive methods for calculating and modelling data sets with a narrow range of values. MG and VG are well suited for log transformation-based data set normalisation. MG and VG values are consistent across data sets, and a great model will incorporate those (Amoatey et al., 2019).

2.5 Discussion

The previous sections show that studies dealing with pollution from industrial regions are typically divided into two main parts: (1) managing these pollutants and providing solutions to reduce them, and (2) analysing the impact of pollutants on health and land cover spatially or statistically. This study discusses the spatial and statistical analysis of pollutants using the methods and models mentioned previously in the methods section. The results of the methods used differ according to the type of analysis method. Some are not intended be fit for purpose unless combined with secondary methods to give a spatial analysis that serves the study's objective. The spatial analysis represents the final important product through which it is possible to know the number of pollutant concentrations affecting the study area. As for the statistical analysis, its results can demonstrate the existence of risks without a spatial dimension. Table 3 summarises the studies of modelling the dust and gaseous pollutants emitted from different sources.

2.5.1 AERMOD

Assael and Kakosimo (2011) examined the impact of industrial PM emissions in the region of Thessaloniki, Greece. The results were checked by the available monitoring stations and achieved improved agreement. A comparison between AERMOD's estimated PM_{10} concentrations and those observed by the monitoring station showed fair agreement, according to the measured validation metrics such as FB = 0.17 (less than 0.3), MG = 1.17 (between 0.7 and 1.3) and VG = 1.07 (less than 1.6).

In an environmental risk analysis, the 12-receptor AERMOD model was implemented by Seangkiatiyuth, K., et al. , (2011) to assess the release of nitrogen dioxide (NO_2) from a cement complex. On the one hand, the results demonstrated a difference between AERMOD's simulations for the dry season and the wet season. The overall results from measuring and simulating NO_2 concentrations showed that the NO_2 concentration limit set by Thailand's National Ambient Air Quality Standards (NAAQS) was not exceeded. However, the AERMOD program was restricted to predicting air pollutants at a distance of 5 km from the reference point, especially in the wet season. AERMOD is a dispersion model without a reaction module, so NO_2 deposition reactions occur in wet and dry conditions.

Two models can be implemented in a comparative manner; for instance, Jittra et al. (2015) used two models (AERMOD and CALPUFF) in the Thailand industrial region of Maptaphut, to evaluate their success in forecasting NO_2 and SO_2. Data from 292 point sources in the field of research were collected. These measured data from 10 receptor sites were compared with the modelled findings. The researchers concluded that for both the NO_2 and SO_2 predictions, AERMOD produced more accurate results than CALPUFF. As far as the highest values are concerned, the highest total concentration study results show that AERMOD is more effective than CALPUFF to forecast the highest concentration. The results represented by Q-Q statistical plots and a tabular view, and the final comparison between AERMOD, CALPUFF, and site observations are shown in Figure 4 and Table 2 belo

Table 2.2 : Nitrogen Dioxide and Statistics of Concentrations of Sulfur Dioxide Performance Assessment

Monitoring site	No. of samples	Mean	Standard deviation	r^2	RMSE	IOA	fb	fs	RHC
Nitrogen dioxide concentration for all stations									
Observed	78800	39.8	82.01	-	-	-	-	-	63.91
AERMOD	78800	41.0	30.97	0.99	5.35	0.99	- 0.03	0.90	64.99
CALPUFF	78800	40.2	40.97	0.99	15.50	0.99	- 0.01	- 0.66	69.64
Nitrogen dioxide concentration for all stations									
Observed	50831	24.5	97.03		-	-	-	-	41.47
AERMOD	50831	36.8	29.10	0.98	13.88	0.99	- 0.40	1.07	62.67
CALPUFF	50831	38.6	49.14	0.98	27.24	0.97	- 0.44	0.65	66.93

Where, $r^{2:}$ correlation coefficient, IOA: agreement index, fb: fractional bias, fs: fractional variance and RHC: robust highest

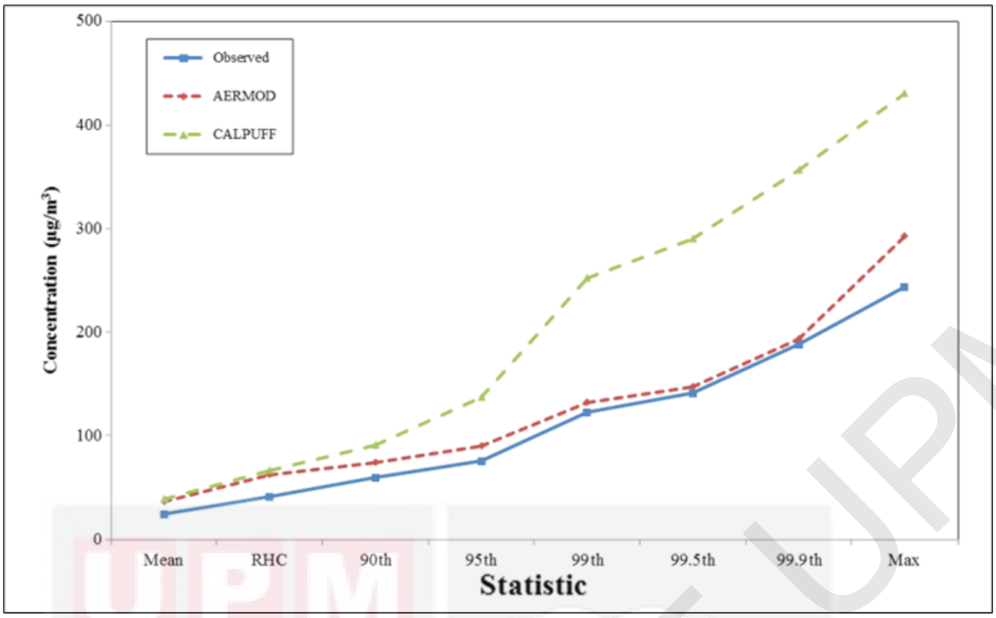

Figure 2.4 : Predicted and Observed SO_2 Statistics (Mean, RHC, Percentile Statistic, and Maximum) for All Sites (Jittra, Pinthong, and Thepanondh 2015)

Topographic influence can be taken into account in these procedures. E. Jayadipraja et al. (2016) used AERMOD to simulate SO_2 and NO_2 dispersion and measure the field of view of dispersion for PT Semen Tonasa in three districts in Indonesia. The highest hourly average and highest annual average of SO_2 and NO_2 values are based on meteorological and topographical data (SRTM30 satellite imagery) and analysis using AERMOD. Also, the authors noted that the west-to-east wind has a more significant impact because it does not run into any obstacles. Additionally, the wind is obstructed by the mountains' altitude diffusing the wind's force from the east. The average wind speed is 4.25 $m.s^{-1}$, with minimal variation.

Balter and Faminskaya (2017) identified a Monte Carlo algorithm for controlling the intermittent, erratic source emission timeline to obtain realistic estimates of the expected maximum hourly concentrations and the subsequent acute non-carcinogenic risk. Despite its comprehensiveness, this algorithm was only applicable to the

AERMOD simulation of air pollutant dispersion, which is very general and could cope with pollution from other habitats and other types of intermittent activity types. This study considered the risks caused by unreliable and intermittent sources of air pollution. From previous studies' debates [98, 99], the authors thought that this was a significant problem, but maybe not a critical one, since the examples given in these documents aimed at complying with short-term air quality requirements that were statistically based on continuous sources. However, the researchers' experiments with plants grown from intermittent sources indicate that it may be otherwise. The acute non-carcinogenic risk was critical in most risk management programs for the factory exclusion zone and the adjacent built-up areas. The feasibility of having an exclusion zone that omitted these areas largely depended on whether the significant sources' unusual presence had been taken into consideration.

Atabi and Nouri (2016) contrasted the predicted and observed atmospheric NO_2 concentrations in the fourth gas refinery in Asaluyeh. Land observations from nine gas refinery monitoring sites were included in the evaluation data, using receptors. The researchers concluded that all values calculated by statistical criteria demonstrated excellent modelling, and the predicted NO_2 concentrations agreed well with the measured evidence. In this simulation, all of the fourth gas refinery stacks were deemed to be the only sources of NO_2 pollution. This is the main reason for the slight variation in the results of the predicted and field measurements.

In this work, nine receptors were used to collect the field data, but this number of receptors is considered very small and causes weakness in evaluating the model's performance compared to the four stacks of the refinery. It should be noted here that the validity of the field measurements and the spatial distribution in the maps are understandable.

Amoatey et al. (2019) calculated possible impacts on communities and the atmosphere by estimating SO_2 and NO_2 concentrations in the refinery's immediate area. The findings showed that three metrics agreed with AERMOD, but four disagreed with CALPUFF. According to AERMOD, the levels of contaminants were within appropriate limits. Pollutants were measured over three seasons, each with different meteorological conditions. The concentrations differed slightly between the hot, dry wind and sea breeze but were substantial across the whole area. While there were many limitations to this project, AERMOD can reliably measure future health risks in the Tema area and the surrounding towns. This investigation could help solve the public health problem of pollution and pave the way for epidemiological studies within the city limits. Table 3 shows the acceptability of the AERMOD and CALPUFF models based on statistical indices such as FB, VG, NMSE, IOA, MG.

Table 2.3 : Validation of AERMOD and CALPUFF Models with Statistical Indices

	SO_2				
Model	**FB**	**NMSE**	**IOA**	**MG**	**VG**
CALPUFF	0.41	0.39	0.73	3.85	1.01
AERMOD	0.38	0.43	0.83	1.43	2.04
	NO_2				
Model	**FB**	**NMSE**	**IOA**	**MG**	**VG**
CALPUFF	0.36	1.34	0.36	3.45	2.61
AERMOD	0.52	0.62	0.87	1.64	1.04

The values shaded in green indicate the agreement

Adetayo et al. (2019) measured ambient air quality and used air pollution dispersion simulations to assess air quality at a major cement plant in Ibese, Ogun State, Nigeria. PM and gaseous pollutants ($PM_{2.5}$, PM_{10}, TSP, SO_2, NO_2, CO, and VOCS) were tested using 14 portable samplers and AERMOD. According to the findings, the SO_2 emissions cap from all fence points was maintained for 1 hour. The 1-hour NO_x levels met the cap in all regions, whereas the 24-hour CO and VOC levels were just under the limit. After 24 hours, the SO_2 and NO_x concentrations in specific locations exceeded their thresholds. Nevertheless, for the 1-hour NO_x emission levels, PM and gaseous pollutants from all point sources were below their local areas' limits. More systemic experiments should be conducted to investigate the emission and dynamics of NO_2 from this cement plant complex.

2.5.2 Gaussian Plume Model

Awasthi et al. (2006) built a general Gaussian plume model using Java and Visual Basic programming tools. The model had some limits, which are described as follows: the formula did not account for inversion, wet deposition, or terrain heterogeneity; GPD was evaluated by matching it to one analytic solution; the error from the numerical method was nil. The field experiments were conducted at four receptor locations around the Dadri power plant. The IOA value for all falsities was 0.471–0.519 (the equation to use is d = 0.522). The receptor at Khangora (R3) had significant inter- and intra-quantile variance, but its Q-Q plots indicated a firm agreement for all possible concentrations. However, checking the model against one dataset does not entirely validate the model.

Farhadi et al. (2017) utilised two models to assess cement dispersion in Doroud, Iran. The central dispersion of NO_x was to the southern plant. The concentrations for the C (slightly unstable) and D (neutral) stability classes were the greatest and smallest, respectively. The results from SCREEN3 and the Gaussian model corresponded close to the source; the estimated NO_x concentrations were above the NAAQ limits. This tells us that residents in the area will be affected by the nearby NO_x pollution from the cement factory. People and activities should not be situated closer than 650 m to the factory. The procedures suggested by the cement industry to measure emissions had worked. Both models provided valuable information for NO_x dispersion for predictive use; therefore, applying dispersion models should be encouraged. The outcomes of this study are not represented spatially; the statistical charts are limited by the distance from the source; and the author did not mention the impact of pollutants on land cover classes such as plantation, water, and soil.

Lawal and Asimiea (2017) examined the spatial distribution of fugitive dust (FD) emissions from the Obajana Cement Plant using the Gaussian plume model with interpolation techniques (EBK). The FD distribution across the study may have exceeded 15 $g \cdot m^{-1}$. Due to conservative assumptions, it was clear that two atmospheric conditions increased the risk of instability. Additionally, there was a high degree of FD exposure in the Harman period. When not all of the information is required, evaluating the effect a proposed pollution source or factory has on an area is done rapidly. It is possible to inform decision-makers about the uncertainty in the model results by creating probability maps. Based on the data and expectations, it seems that the Federal Ministry of Environment (FMEnv) guidelines may need to be updated. Even after considering the forecast and standard error, FD was still elevated in large sample regions. It was also clear that high FD was not restricted to the immediate vicinity. In light of the possible human health implications, efforts should be made to review the FMEnv guidelines.

They employed EBK as an additional tool for simulation, and applied the semivariogram to find expected semivariogram values and thus estimated priors, so weights, after which the Bayes' rule was applied to find the Bayes' posterior.

Goudarzi et al. (2017) examined the distribution of carbon monoxide (CO) from the stacks of a cement plant in Doroud. This study found that the most common direction for CO dispersion was southwest. Spring and fall were expected to have the highest and lowest maximum concentrations, respectively. However, the overall CO concentrations did not exceed NAAQS across the different seasons, so CO has no effect on human health in this region.

To obtain solid and improved predictive atmospheric studies, these findings highlight the importance of validating the operating dispersion model results with measured data; however, the authors did not work on the validity of the model used in their study. Figure 5 illustrates the concentration of CO over four seasons with a maximum distance of 4 km from the source, which considers a limited distance in order to cover the urban areas around the plant.

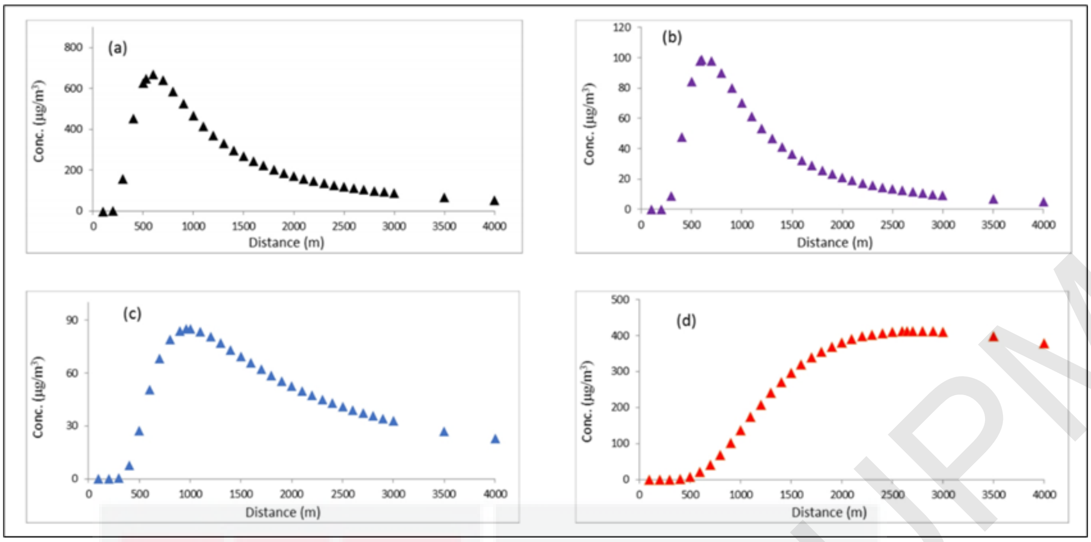

Figure 2.5 : CO Dispersion at Various Distances from the Cement Plant during the (a) Spring Season, (b) Summer Season, (c) Fall Season, and (d) Winter Season (Goudarzi et al. 2016)

De Marco (2018) identified and analysed the environmental dispersion of fine particles from the same cement plant in Doroud, Iran, using SCREEN3 and the Gaussian plume model. There was significant agreement between the measured and modelled findings, indicating that both models can be utilised to forecast PM concentrations downwind of a source, especially in regions far from the source of pollution, as seen in Figure 6. Even though the study demonstrates good validation of pollution results with in situ observations, the spatial representation is weak compared with statistical outcomes.

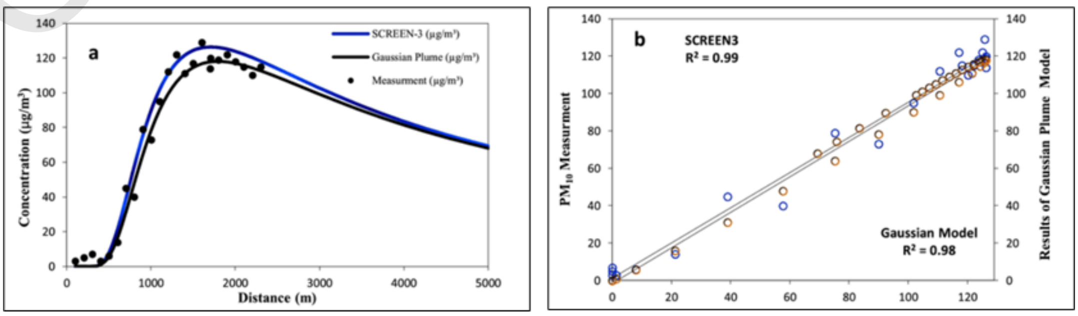

Figure 2.6 : (a) Comparing Simulated Daily PM_{10} Concentrations by the SCREEN3 and Gaussian Plume Models, and (b) Spearman r^2 Values (A.J. 2013)

A.J. (2013) developed a comprehensive dispersion model to calculate the PM concentration at every downwind distance from the cement factory stack, according to the Gaussian distribution equation.

Even though the statistical analysis showed promising results for the Gaussian model within a specified distance (100–200 m), where the conformity was at least 94% for all stacks, this can be attributed to additional emissions close to the emission sources in question, such as the parking lot, the homogenisation section, and the mixing storage. However, due to terrain variation, sedimentation, erosion, and the interception of trees and buildings in the region, the results for distances greater than 200 metres were poor. Additionally, all site measurements were taken within 5 km of the cement plant's stacks, as seen in Figure 7.

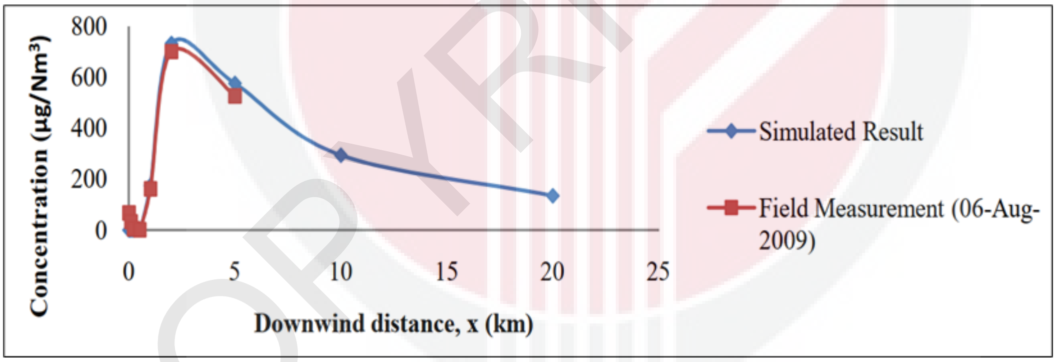

Figure 2.7 : For Stack 1, the Field and Simulated Data Are Plotted against the Downwind Distance (A.J. 2013)

2.5.3 Hybrid Models

Bougoudis et al. (2016) developed and applied a hybrid method, namely Easy Hybrid Forecasting (EHF), to predict air pollution without using sensor measurements or data from expensive software. Furthermore, the use of this model is flexible and accessible for observers. In this model, machine learning and computer languages such as Java and Python are key. The study was applied to four stations in Attica Prison, United States. The data included five gases: CO, NO, NO_2, O_3, and SO_2. The researchers used four unsupervised learning algorithms: SOM, Neural Gas ANN, Fuzzy C-means, and a SOM algorithm. For each of the algorithms, the most harmful pollutant values were used. Then, they compiled all of the data from the extreme clusters into four datasets, one for each algorithm. Although the researchers used several machine learning techniques, there was no spatial representation of the risk of pollution on the land cover, and the number of stations was minimal for a relatively small region.

A selection tool (the Partial Least Square (PLS) method) and predictor (the Support Vector Machine (SVM) model) were used as a hybrid model and compared with the SVM model by Yeganeh et al. (2012) to measure the CO concentration in Tehran, Iran. According to the analysis, the hybrid model outperformed the SVM model in CO concentration forecasting while using the same input parameters. Moreover, as opposed to SVM preparation and grid scan, the deployment of PLS for size reduction saved time. Even though PLS has consequences for both the daily and hourly prediction models' effectiveness, the PLS effectiveness for the daily estimation of CO concentration was better than the hourly estimation technique. In this study, the robustness of combining two models as a hybrid over the use of a single model was confirmed, but once again, the study did not present a risk map to represent the effect of CO concentration spatially.

Lai et al. (2019) merged various air quality models, including a diffusion model (AERMOD) and a grid model (CMAQ), to model air quality for the source apportionment of $PM_{2.5}$ in Taichung City, Taiwan. The hybrid model provided a comprehensive evaluation of the distribution of primary pollutants, secondary pollutants, and other environmental information. In comparison to monitoring station results, the hybrid model outperformed simple CMAQ simulation. This analysis selected two major delicate $PM_{2.5}$ events to evaluate the hybrid model's effectiveness, in order to examine the effect of traffic and the coal-fired Taichung Power Plant on $PM_{2.5}$ in the Taichung area.

According to the authors, although the hybrid model works better, there are some shortcomings in the new hybrid model's identification of primary and secondary pollutants. Furthermore, the modelled concentrations are meant to be solved in order to enhance the modular architecture.

Liu et al. (2019) designed a new hybrid model called EWT-MAEGA-NARX, which was formed by merging two models: the EWT, MAEGA, and NARX neural networks. The model was used to forecast four pollutants ($PM_{2.5}$, SO_2, NO_2, and CO) in Beijing, China, in order to verify the model. This study compared five selected models: VMD-MAEGA-NARX, EWTMAEGA-SVM, MAEGA-NARX, EWT-NARX, and EWT-ARIMA-NARX. The hybrid model demonstrated greater accuracy than the rest models, determined through the statistical calculation of errors (mean absolute error (MAE), mean absolute percentage error (MAPE), and root mean square error (RMSE)). In this study, the outcomes are restricted to calculations and statistical charts, without spatial distribution maps.

Mohebbi (2006) simulated and predicted PM_{10} in Kerman Cement Factory, United States, using three models: the Eulerian model, the Gaussian plume model, and an artificial neural network. The outputs of the models were compared to data that had been collected. The results of the Eulerian model, the Gaussian plume model and the artificial neural network had Average Absolute Percent Deviation (AAPD) values of 25.53%, 15.38%, and 5.91%, respectively, as shown in Figure 8 below (the x-axis represents the distance in metres and the y-axis represents the concentration of PM_{10} in $mg \cdot m^{-3}$).

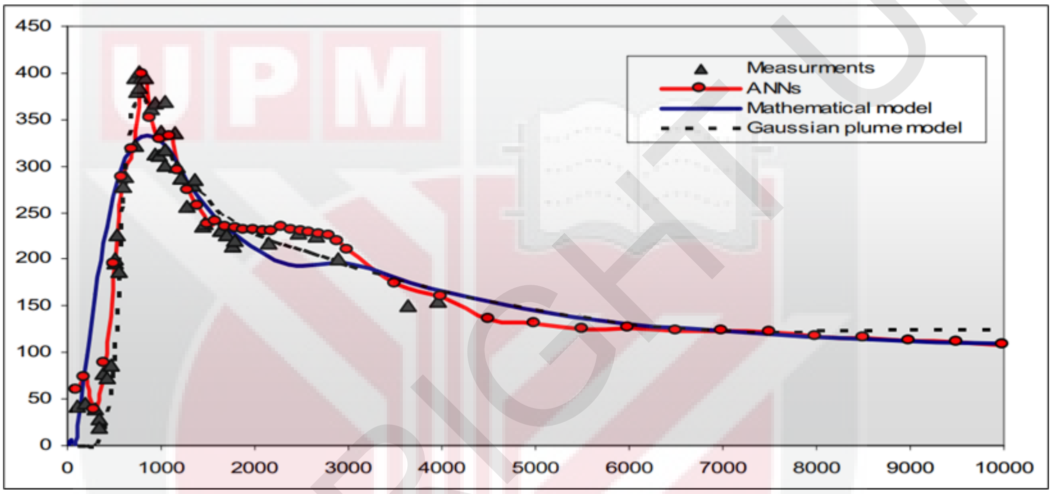

Figure 2.8 : Measured Data vs. Results of Three Utilized Models (Mohebbi A 2006)

Al-Dhurafi et al. (2018) proposed three approaches for modelling API qualities in Klang, Malaysia: traditional models, API structure models, and descriptive status models. According to the results, the API structure models are better for the classification and estimation of API. The suggested hybrid model is a superior, versatile type that is utilised in a variety of fields. The API data was represented well by the hybrid model as well. It could also be combined with other modules to estimate Klang API data for other regions and towns. The study was limited to comparing the approaches used with API without generating risk or forecast maps to determine pollution.

Carotenuto et al. (2018) employed two methods to analyse the intensity of CO_2 emissions from an industrial point source in Biganos, France. The first one was a mass balance method based on aircraft observed data, and the second was a dispersion simulation approach incorporating the CALMET diagnostic meteorological model and the CALPUFF puff dispersion model. The CALMET/CALPUFF model chain was run using WRF-modelled outputs from ECMWF reanalysis, WRF-modelled outputs from CFSR reanalysis, and local in situ measurements. The two methods compared had advantages and disadvantages, making an integrated system especially appealing. According to the development parameters, this method needs to be regularly updated in pace with the rapid development of airplanes and sensors.

2.5.4 Land Use Regression

LUR models were developed by Rahman et al. (2017) to estimate the concentrations of NO_2 and NO_x in the Brisbane Metropolitan Area (BMA), Australia, from 2009 to 2012. With leave-one-out cross-validation R2 values of 3–49% and 2–51%, the final models described 64% and 70% of spatial variation for NO_2 and NO_x, respectively. Distance from a major road or industrial area is a specific predictor for NO_2 and NO_x levels, implying that road traffic and industrial emissions play a significant role. The innovative modelling technique used in this study can also be applied to other cities. Despite the advantages of the model used, there are some limitations, including the number of field-measured sites being limited to 31 sites, and just one season of monitoring was performed at the short-term sites.

Ma et al. (2020) developed the PyLUR for LUR modelling and emission mapping. Using the Python platform-based GDAL/OGR library, it can create a LUR model and efficiently produce pollutant concentration maps. PyLUR's innovations and benefits include the ability to model more kinds of possible predictor variables; an automated regression modelling module; the ability to manage accurate GIS data and perform fine-resolution predictions easily and stably; and the fact that it is open-sourced, with the source code being accessible to researchers interested in LUR modelling or programming using GDAL/OGR. PyLUR's drawback is the lack of an advanced interface, such as that of RLUR. This can be resolved by doing separate GIS data exploration and displaying the output concentration maps in commercial GIS applications. PyLUR is currently available as PyLUR 1.0. The authors are working on a user-friendly PyLUR GUI and will update it soon to PyLUR 2.0.

2.5.5 GIS Tools

Table 2.4 presents the common spatial and statistical methods of air pollution analysis used in GIS. Wang and Huang (2014) used trend analysis methods to estimate the potential effects of pollutant emissions from point sources in Saskatchewan, Canada. The first method used was trend analysis, to show how the total number of point sources and their spatial distribution has changed over time. The second method used was IDW, to produce interpolation surfaces for the significant air contaminants emitted by industrial sources. The trend analysis showed that the overall number of facilities has been growing explosively, and most of the new facilities are in southern Saskatchewan, where most of the province's total population resides. Correspondingly, the findings from IDW showed that most emission hot spots are in the country's southern part. The methods used can estimate the pollution from new industrial projects built according to pre-determined requirements. Furthermore, the outcomes can assist with selecting a site and resident migration if necessary. Although

IDW interpolation performs well for points that are uniformly distributed, it is less effective for outliers; data clusters that are unevenly distributed can introduce errors (Azpurua and dos Ramos 2010).

Another GIS analysis was carried out by Teggi et al. (2018), who designed a new GIS-based Gaussian model named CAREA. Programmed using Python language, this model forecasts field concentrations and surface dry deposition fluxes from complex area sources. In particular situations, this model offers an some advantages over AERMOD and other similar models.

In the CAREA model, the amount of time can be accommodated, and large numbers of sources and receptors are possible, in contrast to AERMOD. A limitation of CAREA is that it only offers ground values; in general, it is only applicable to relatively simple terrain types and, unlike AERMOD, does not include pollution from stacks, lengths, open-pit, or wet deposition.

Ali et al. (2018) also used the IDW interpolation method to evaluate the concentration of PM_{10} over Kirkuk, Iraq. This study showed that significant fumes, solid particulates, and considerable vehicle emissions have been generated due to excessive amounts of these places. IDW perfectly represented the PM_{10} projected map. The PM_{10} emission level was appropriate for Iraq's proposed NAAQS, but not for WHO's guidelines.

Samad et al. (2020) investigated the air quality in a large cement factory's vicinity by looking for PM in the air. The results were assessed statistically using SEM photographs and spatially using GIS. It was found out that the average PM_{10} and $PM_{2.5}$

levels were considerably more significant than those permitted by the air quality standards established by numerous regulatory agencies. This statement is supported by the similarity between the SEM representations of particles captured in the analysis tool and those found in tree leaves and cement particles. The use of GIS to construct a visual view of the PM concentration distribution made it simpler to illustrate the study's hypotheses, even to a layperson. The spatial analysis interpolation approach was IDW combined with Quantum GIS.

Torres et al. (2020) used Python software to generate figures and plots of NO_2 concentration outcomes. Ma et al. (2020) described a LUR modelling and pollution visualisation software called PyLUR that uses Python-based GDAL/OGR libraries and can create a LUR model and produce efficient maps of pollutants concentration. Motyka et al. (2020) examined the air quality model SYMOS 97 in comparison to the bio-monitoring survey findings and vice versa; this model is also based on Python language programming.

Wyrwa (2015) used the πESA model to evaluate the concentration of $PM_{2.5}$. This model includes three components: TIMES-PL (an energy-economic model), Polyphemus (an air quality modelling system), and MAEH (a new module for environmental and health assessment). Polyphemus is based on the C++, FORTRAN 77, and Python programming languages.

More recently, Salih and Hassan (2023) developed a python-based implementation of Gaussian dispersion models to study the impact of urban trees on air pollution in the city of Kirkuk. They demonstrated the effect (size, type, and distribution) of urban trees on air pollution in Kirkuk, with a focus on simulating the dispersion of pollutants resulting from the oil refinery. In addition, Mushtaq and Farooq (2023) studied the use of geo-visualization tools in GIS and other plotting software including Python based packages for air pollution and environmental research. They found that such tools can offer valuable insights into the spatial patterns and trends of pollutants across various regions.

Table 2.4 : Common Spatial and Statistical Methods of Air Pollution Analysis

Objective	Data	Method	Source
Estimate the carbon monoxide (CO) delivery from Doroud cement industry stacks	In situ measurements of CO, parameters (stack, model, and receptors), and Meteorological	Gaussian Plume Model	(Goudarzi et al. 2016)
Distinguish and analyze fine particle dispersion in the environment from a cement plant stack in Doroud (Iran)	In situ measurements of PM_{10} and Meteorological data	SCREEN3 software and Gaussian plume model	(Khaniabadi et al. 2018)
Evaluate air pollution (PM_{10}, NO_2, and O_3) on cardiovascular mortality in Kermanshah, Iran, between 2014 and 2015.	Air quality data, Meteorological, and epidemiological parameters	The Air Quality Health Impact Assessment (AirQ2.2.3 model)	(Khaniabadi, Goudarzi, et al. 2017)
Utilizing outdoor air quality control and air pollution dispersion simulation to measure the air quality at a major cement plant in the Nigerian city of Ibese, Ogun State.	SO_2, NO, NO_2, CO, and VOCs site observations, all sources of pollutant emission in cement plant, and meteorological data.	AERMOD Model	(Adeniran et al. 2019)
Examine the effect of a cement factory on the atmosphere around the air forensically.	Terrain, Meteorological, and in situ PM observations	Spatial analyst using GIS	(Abdul Samad et al. 2020)
Display a new model of GIS-based Gaussian model for complex source areas named CAREA Model	Polygons for source areas, source emission rates, receptors, meteorology, concentrations, and deposition fluxes	CAREA Model and is coded by Python language	(Teggi et al. 2018)
present a scheme for predicting $PM_{2.5}$ concentrations using RNN and LSTM in Taiwan	Pollutants and meteorology data	Recurrent Neural Network (RNN) and Long Short-Term Memory networks ((LSTM)	(Tsai, Zeng, and Chang 2018)

Table 2.4 : Continued

Generate concentration maps for air pollutants	Pollutants monitoring in the site and variables of possible predictor	LUR Model and PyLUR software mapping of pollution	(X. Ma et al. 2020)
Observe the concentration of PM daily and nightly and compare between them over Bihar City, India	In situ observations of PM_1, $PM_{2.5}$, and PM_{10}	Statistical Charts	(Jena, Mishra, and Moharana 2020)

2.6 Deep learning Overview

Several gases, such as ozone (O3), carbon monoxide (CO), sulfur dioxide (SO2), and nitrogen oxides (NOx), along with suspended particles (PM), volatile organic compounds (VOCs), certain metals, and other pollutants released from various sources, have a harmful and direct effect on human health in urban areas (D. Zhu et al. 2018). Many cities globally experience elevated levels of air pollutants due to significant economic growth and development, making it essential to assess and predict these pollutants to understand the associated risks (J. Zhang and Ding 2017). Generally, methods for predicting air pollutants fall into two primary categories: statistical and deterministic methods (X. Li et al. 2017).

Artificial intelligence (AI) plays a significant role in creating effective prediction models across different scientific fields by helping to quickly identify optimal solutions (Oprea et al. 2017). Researchers have been focused on air quality prediction methods to enhance modeling through machine learning, especially deep learning, and data processing, aiming to deliver high-accuracy results and insights for decision-makers (Schürholz, Kubler, and Zaslavsky 2020).

Deep learning is a subset of machine learning that uses a network of neurons organized into layers, which include three types: input, output, and hidden (Mohsen et al. 2018). Deep learning (DL) encompasses a range of learning algorithms aimed at developing complex prediction models, including multi-layer neural networks with many hidden units (Emmert-Streib et al. 2020). Its ability to grasp contextual information from diverse data sources, along with the relationships between data, has led researchers to favor deep learning techniques for preference prediction challenges due to their promising capabilities (Z. Y. Khan et al. 2021).

Libraries are groups of pre-written code that programmers can use to enhance their work in various programming languages. Developers often rely on Python deep learning, AI, and machine learning libraries to tackle complex tasks (Davies 2018).

The prediction of air pollutants has been extensively studied and presents several challenges. This section discusses various research efforts from different countries that focus on predicting air pollutants using deep learning methods. The Convolutional Neural Network (CNN) model has demonstrated its effectiveness through input data testing. For instance, Mao & Lee (2019) successfully forecasted air quality by predicting the hourly concentrations of pollutants like ozone and PM2.5 using deep learning techniques. Additionally, Q. Zhang et al. (2020) proposed a hybrid deep learning model that predicts air quality at a high resolution by combining CNNs with Long Short-Term Memory (LSTM) networks. Furthermore, Ma et al. (2020) introduced a method that utilizes ambient concentrations of 18 chemical indicators to quickly evaluate the coefficients of air quality equations, leveraging data generated from a complex atmospheric chemical transport model. This approach incorporates deep learning techniques along with chemical indicators related to pollutant formation.

Whenever two or more models are integrated, a more efficient model can be generated by comparing the combined model (hybrid) to each individual model independently. Heydari et al., (2022) anticipated and analyzed Combined Cycle Power Plant air pollution by creating a novel hybrid intelligence model based on LSTM and MVO to. Bekkar et al., (2021) combined historical data on pollutants, meteorological information, and $PM_{2.5}$ concentrations at nearby stations to use CNN-LSTM to predict the hourly forecast of $PM_{2.5}$ concentrations in Beijing, China. Deep learning recently has been utilized for various types of pollutants prediction as Isam Drewil & Jabbar Al-Bahadili, (2021) indicate that the most of the researchers utilize more advanced and intelligent approaches to deal with the problem of air pollution detection in the early stages, while only a few researchers use basic strategies. Muthukumar et al., (2022) employed the advanced deep predictive Convolutional LSTM (ConvLSTM) model along with the cutting-edge Graph Convolutional Network (GCN) architecture to predict temporal and spatial hourly $PM_{2.5}$ in the Los Angeles City over time.

2.7 Summary

This study explores the methods and models used for analysing pollutants generated from sources of emissions (e.g., factories, urbanisation, and transport), how they function, and their limitations. The emphasis was on analytical models from factory sources, especially cement plants, as they negatively affected them. We found the following through a review of previous research:

1. Some researchers only used one statistical model for pollutant dispersion.
2. In other studies, two or three models were used independently and compared with site measurements, thereby determining which model is optimal.
3. Furthermore, the combination of two models (i.e., a hybrid model) has been used by several researchers to obtain a new model that provides better performance.
4. Moreover, several studies have used GIS as an additional tool to the model used, in order to support findings and analytical methods, such as interpolation, buffers, etc.
5. The final approach is to use languages such as Python and RNN to program the models, in order to provide GIS with a new tool that adds a qualitative analysis of the risks of air and land cover pollution.

The most effective model or system for measuring and estimating air pollution is one whose findings are very close to those obtained from field measurements. Furthermore, to validate the actual test model, it is preferable to take several samples at distances ranging from the sources nearest location to more remote areas. Furthermore, taking field measurements over more extended periods yields better results. Furthermore, classifying areas near the source into different forms of land cover can help demonstrate the effect of pollution on human health, plants, soil, and water bodies.

CHAPTER 3

MATERIALS AND METHODS

3.1 Introduction

This chapter states the characteristics and location of the study area. Materials and data used in this study have also been identified. The concentration of air pollution factors and their optimization are attended. A Gaussian Plume Equation based on Python program and QGIS is utilized in this chapter for identifying risk of pollutant on land cover and air that generated from cement plant. A developed Plugin in QGIS for modelling Gaussian Plume Equation through three stages of development to estimate the pollution distribution for areas surrounding cement plant has been dissected.

3.2 Overall Research Workflow

Multi-source data were used in this research, including in situ measurements, meteorological data, satellite images, main parameters for the Gaussian Equation, and pollution source data. Metrological data represented by wind speed which are downloaded from NASA climate stations that distributed within the study area through RETScreen program and wind direction for every day in 2020 was measured from a website https://www.ventusky.com/ for area of study. Two Landsat images Landsat-8 Operational Land Imager (OLI)) of the study area were downloaded from the Web site of the U.S. Geological Survey USGS (available online at http://glovis.usgs.gov/) and used to map land cover classes. Digital Elevation Model (DEM) was derived and modeled to represent the terrain of the study area. Gaussian parameters σ_y and σz are the normal parameters distribution in crosswind (y) and vertical direction (z) respectively were computed. Source information including Mass Emission Rate, Release height distribution of mass in vertical dimension (z), and distribution of mass in cross-wind dimension (y) were obtained. Figure 3.1 illustrates the flowchart of overall methodology for Estimating the susceptibility of solid and gases waste Emission on Land Cover and Air Quality from Cement Plant Using Gaussian Plumes Model and QGIS.

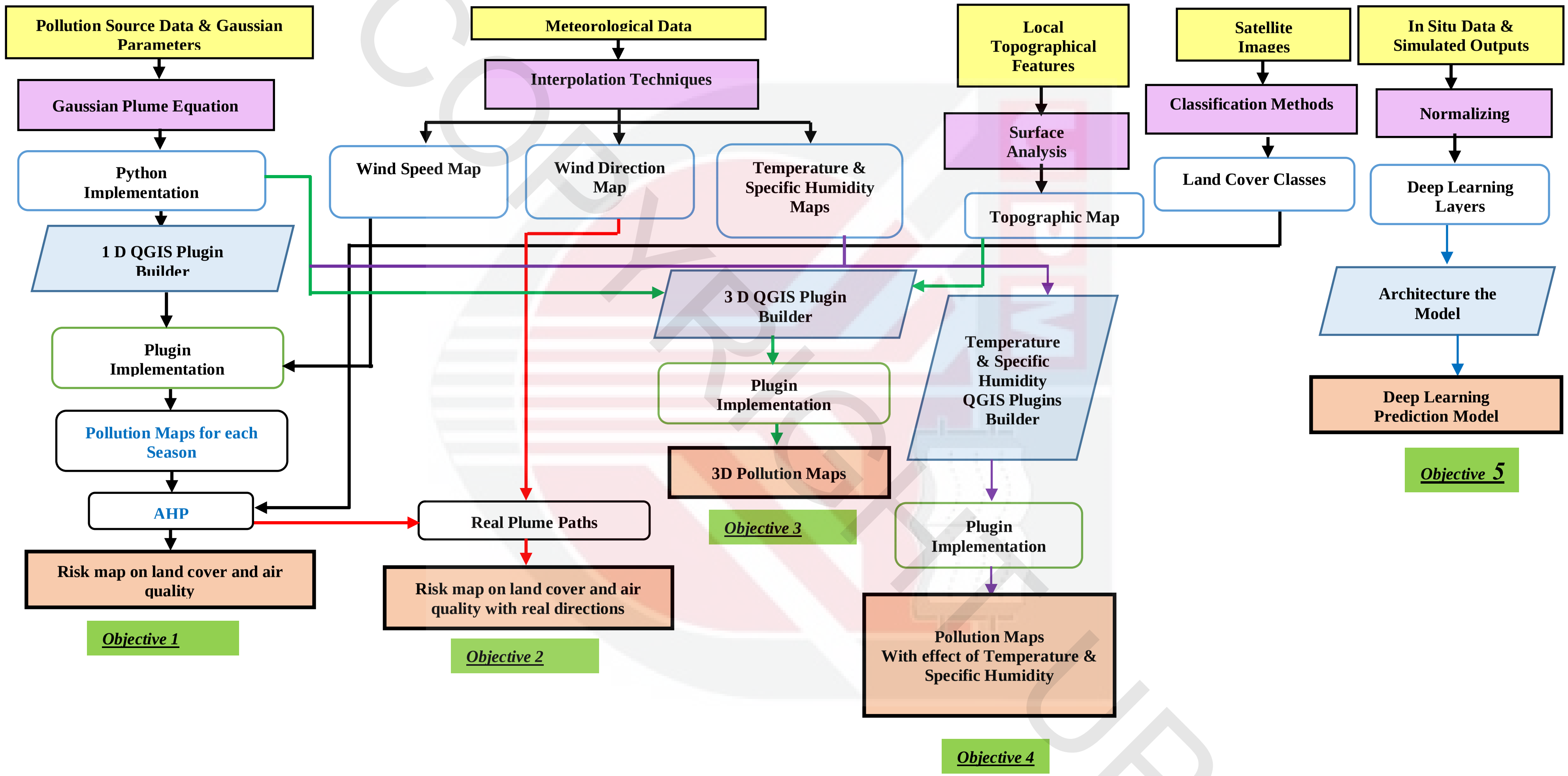

Figure 3.1 : Overall Methodology Flowchart

3.3 Study Areas

3.3.1 Main Study Area

Kirkuk City is located 286 kilometres north of Baghdad, Iraq's capital. This city is distinguished by its geographical position, which links Iraq's northern and center areas and lends it commercial prominence. The city is also rich in resources, particularly oil, as evidenced by the presence of many oil wells. Kirkuk City is also distinguished by its ethnic and cultural variety. The city also features many archaeological sites and the Al-Khassa River, which divides the city into two parts.

3.3.2 Specific Study Area

The specific study area is Laylan District which subordinates to the governorate of Kirkuk City. It is located 19 kilometres southeast of the city of Kirkuk. The boundary of Laylan ranged between longitudes 44˚ 20' and 44˚ 45' and latitudes 35˚ 09' and 35˚ 25' with total area about 691 km^2. Laylan district is a city with archaeological monuments in addition to its agricultural and industrial importance, represented by the Kirkuk Cement Factory. The population of Laylan is more than 16,000 people. Figure 3.2 states the study area of Laylan District and surrounding districts included Kirkuk City, Taza District, Kara-hingir District, and Daquq District.

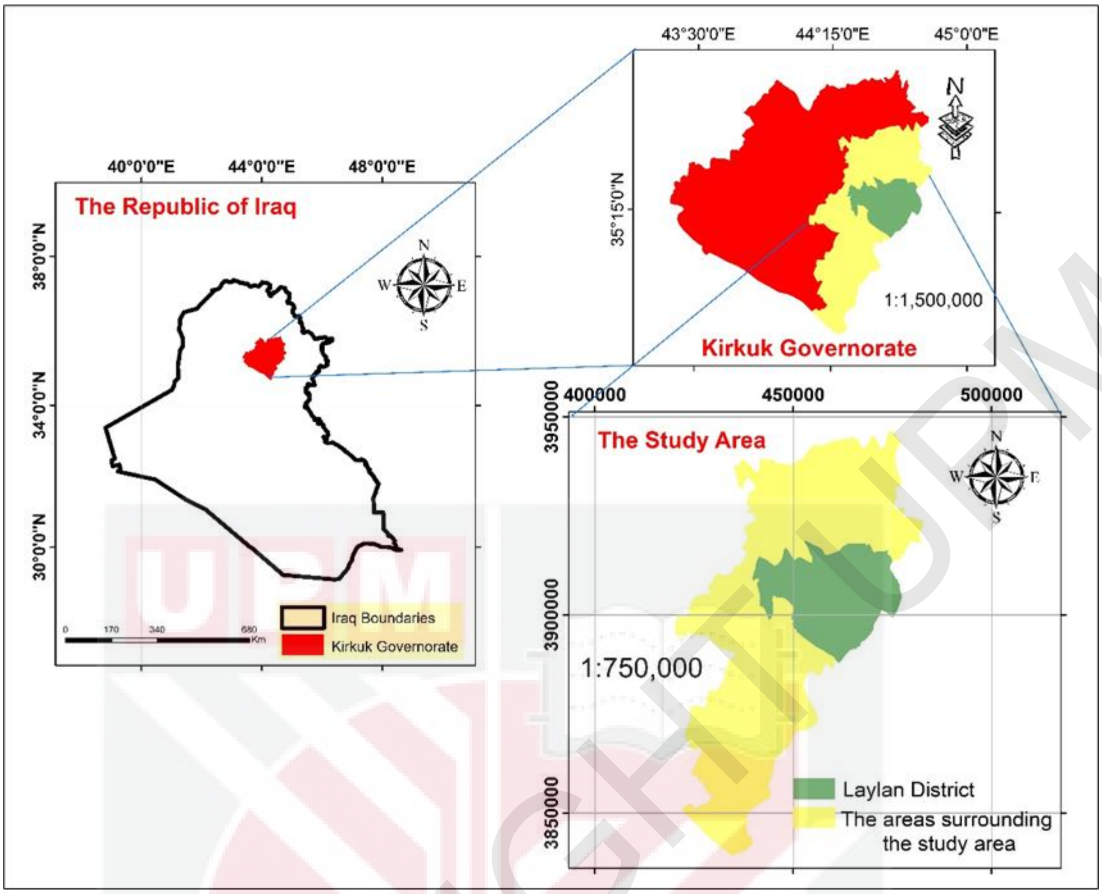

Figure 3.2 : The Study Area (Laylan District and the Districts Surrounding it)

3.3.3 Kirkuk Cement Plant

The factory is located in Kirkuk governorate, 2 km away from Laylan District (the nearest population center) in the direction of the prevailing wind. The location of the factory is considered in violation of the environmental legislation in force, as it is considered a class (A) polluting activity, it should be located at a distance (10 km) from the public design and about (5 km) the nearest population. The coordinates of the plant site are (452699 E, 3911170 N- UTM 38 S). The designed annual production capacity of the plant is (2,000,000 tons / year), while, the actual production capacity is (25,000 -30,000 tons / month) of Ordinary Portland cement. The plant is currently suffering from a significant shortage of electrical energy, as the plant needs (46 megawatts). To operate the two lines while the equipped one is (10 MW). The plant is currently using black oil as fuel with about (160 liters / ton of clinker). The type of production process used is the dry method. Raw materials quarries: Limestone from stone quarries, which is a distance of (85 km) In the Bazian area in the Sulaymaniyah Governorate, as for the quarries, they are surrounded by the factory.

3.4 Data Used

3.4.1 Source Information and Site Description

The source parameters needed for Gaussian Plume Model represented by Mass Emission Rate, Release height distribution of mass in vertical dimension (z), and distribution of mass in cross-wind dimension (y). All these data were reported by engineering office of Kirkuk Cement Plant and listed in table 3.1 below.

Table 3.1 : Source Information of Kirkuk Cement Plant

Parameters	Quantity
Mass emission rate	150 mg/Nm^3 = 22.5 grams/ second
Stack height	70 m
Stack diameter	4 m
Stack cross-sectional area (πr^2), r is the radius of the stack (half the diameter)	12.57 m^2
Velocity of the gases emitted from the stack ((4Q)/(πd2ρ)), Q is the mass emission rate (22.5 g/second), d is the diameter of the stack (4 m), and ρ is the density of the gas (which we will assume to be 1.2 kg/m3, a typical value for air).	3.57 m/second

The plume rise, Δh, is estimated employing the method proposed by Varma et al. (2014) presented in equation 3.1.

$$\Delta h = \frac{0.35 V_s d}{U} + 2.64 \frac{\sqrt{Q_h}}{U} \qquad (3.1)$$

3.4.2 Satellite Imagery (Landsat 8)

Two Landsat images Landsat-8 Operational Land Imager (OLI)) of the study area were downloaded from the Web site of the U.S. Geological Survey USGS (available online at http://glovis.usgs.gov/). All Landsat standard data products are processed using the Level 1 Product Generation System (LPGS) with the following parameters applied: Geo-Tiff format, Cubic Convolution (CC) resampling method, World Geodetic System (WGS) 84 datum, and Universal Transverse Mercator (UTM) map projection.

The two images Landsat-8 OLI for 2020 within WRS-2, (path 169 row 35, path 169 row 36) data sets were selected at very near anniversary acquisition data clearly in Table 3.2. Landsat-8 OLI sensor has two additional bands in the multispectral bands than landsat-7 ETM+, deep blue coastal / aerosol band and a shortwave-infrared cirrus bands with spatial resolution 30x30m, temporal resolution 16 day, and radiometric resolution 12-bits. The images merged through mosaic process in ENVI to cover the whole area of study.

Table 3.2 : Landsat-8 OLI Satellite Data Used for the Study

Image source	Acquisition Date	Path/Row	Map projection	Cloud cover
Landsat-8 OLI	2020-08-21	169/35	UTM/WGS84	0 %
Landsat-8 OLI	2020-08-21	169/36	UTM/WGS84	0 %

3.4.3 Meteorological Conditions

The wind speed and wind direction are needed as average for the study area, therefore, the wind data was collected for Kirkuk province. For comparison purposes, the Kirkuk data was compared to other Iraqi provinces. On the other hand, the relative humidity and temperature were acquired from several stations around the Kirkuk cement plant to capture the spatial variations of these two parameters. The following subsections describe these datasets in more detail.

3.4.3.1 Wind Speed

Wind speed considers the essential parameter in Gaussian Plume Model which were downloaded from NASA climate stations that distributed within the study area through. Table 3.3 and figure 3.3 show the wind speed data in m/s for four seasons 2020.

Table 3.3 : Wind Speed Data Downloaded from RET Screen Program for 2020

Station	Easting (m)	Northing	Spring	Summer	Autumn	Winter
Ramadi	341500.88	3700353.89	3.986	4.715	3.444	3.294
Baghdad	440563.74	3686147.3	3.470	4.176	3.067	2.911
Samaraa	395987.4	3784057.62	3.911	4.586	3.276	3.086
Mandali	551406.92	3734364.7	3.604	4.182	3.670	3.373
Khanaqin	536544.9291	3800465.699	3.377	3.884	3.250	3.050
Tuz	466424.82	3860693.25	3.482	4.101	3.353	3.154
Kirkuk	445744.63	3926280.56	3.479	4.016	3.379	3.246
Sulaimanya	537706.84	3935988.72	3.117	3.429	2.979	2.815
Erbil	410913.18	4005600.89	2.670	3.195	2.716	2.600
Mosul	332178.9	4023283.68	2.774	3.323	2.757	2.687

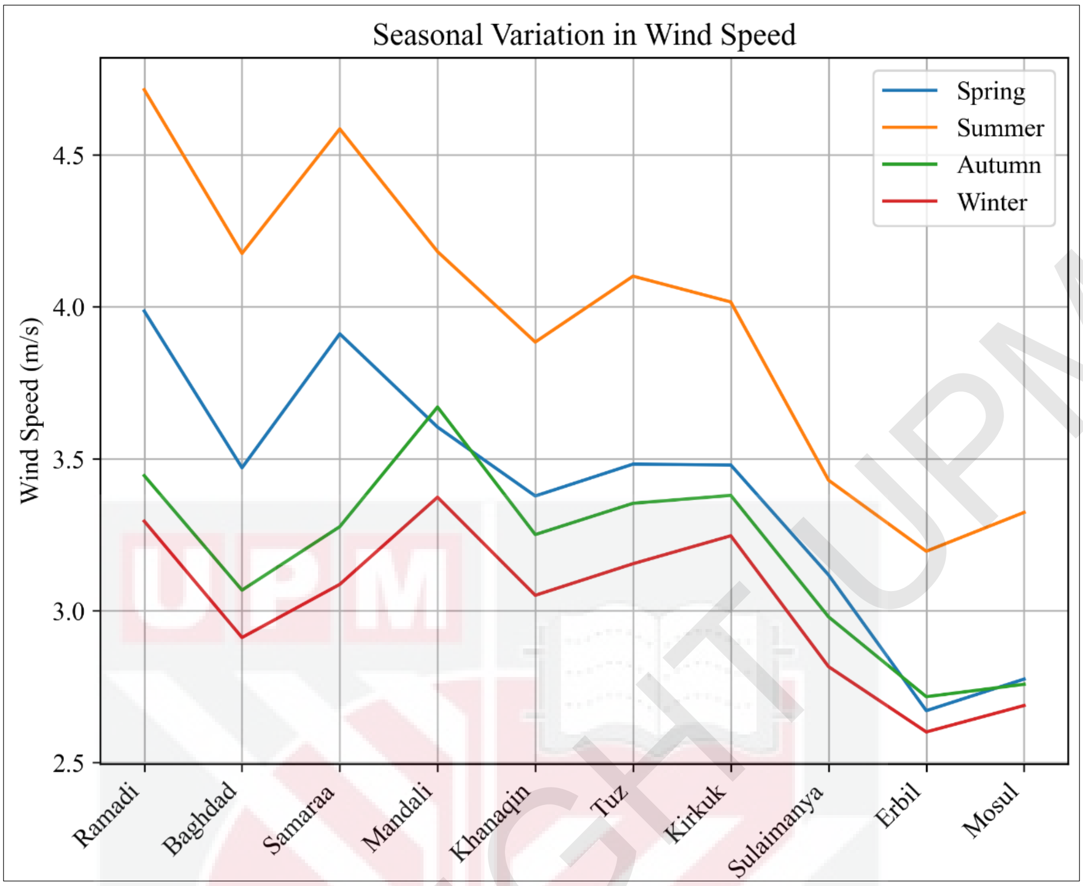

Figure 3.3 : Seasonal Variation in Wind Speed across Multiple Locations in Iraq. The Graph Displays the Average Wind Speed in Meters Per Second (m/s) during Each Season of the Year, with Data Collected from Ten Different Locations across the Country

3.4.3.2 Wind Direction

Wind direction for every day in 2020 were measured from a website https://www.ventusky.com for area of study. Thus, the wind direction is tabulated for all seasons of the year to indicate the areas most affected by the emissions of Kirkuk cement plant during 2020. Table 3.4 illustrates the seasons of 2020 with the frequent directions of wind. Except for factory holidays and days off due to special occasions, data were observed on all days of the year.

Table 3.4 : Wind Directions of Study Region for All Seasons in 2020

Season	Frequency of direction							
	N	NE	E	SE	S	SW	W	NW
Spring	3	0	0	2	8	14	14	4
Summer	0	0	3	17	21	23	10	4
Autumn	2	1	0	2	10	19	8	3
Winter	7	3	0	0	18	28	23	9

Based on tables 3.4, 3.8, and 3.9, the wind roses of all seasons could be drawn using the number of days for each season and the angle of the plume for 10 km which is calculated in table 3.5 and expressed in equations 3.2 and 3.3 as:

$$\theta_B = 0.017453293\ (c - d\ \ln(x)) \tag{3.2}$$

$$\theta_C = 0.017453293\ (c - d\ \ln(x)) \tag{3.3}$$

Table 3.5 : Angles of Plume for Four Seasons Relative to Wind Speed Stability

Distance (Km)	Angle of Plume θ_B	Angle of Plume θ_C
1	18° 19′ 58.80″	12° 30′ 00″
2	17° 04′ 43.25″	11° 44′ 50.82″
3	16° 20′ 41.83″	11° 18′ 26.05″
4	15° 49′ 27.70″	10° 59′ 41.64″
5	15° 25′ 15.80″	10° 45′ 09.48″
6	15° 05′ 26.28″	10° 33′ 16.87″
7	14° 48′ 42.05″	10° 23′ 14.37″
8	14° 34′ 12.15″	10° 14′ 32.46″
9	14° 21′ 24.85″	10° 06′ 52.10″
10	14° 09′ 58.97″	10° 00′ 00.30″

3.4.3.3 Temperature and Specific Humidity

Temperature is an indicator of matter in the universe thermal state and it represents the heart rate or coolness. It is a widely monitored quantity to quantify change in Weather because it impacts or controls other weather elements such as temperatures at the dew point, rainfall, humidity, cloudiness, and atmospheric pressure (Shrestha et al. 2019). Temperature can be extracted from satellite image , field observation , or by climate websites.

Specific humidity, defined as the ratio of moist air's water vapour mass to the overall mass of the system, has risen in reaction to rising temperatures (Majeed and Lee 2017).

Temperature and specific humidity both contribute to the composition of the air pollution mixture. One possible explanation for the closer relationships is that the size of particles may grow due to moisture absorption in more humid circumstances. Smaller particles may penetrate deeper into the lungs and into the circulation, altering the effect of the air pollution mixture. High temperatures and high levels of sunshine may hasten photochemical aging of particles, affecting the chemical characteristics of the air pollution mixture (Klompmaker et al. 2021).

Temperature and specific humidity for average seasons in 2020 were derived from https://power.larc.nasa.gov/data-access-viewer/ for 10 stations as illustrates in tables 3.6 and 3.7. The spline interpolation method is used to interpolate the temperature and specific humidity values at each grid point and product maps.

Table 3.6 : The Temperature of 10 Locations Surrounding the Kirkuk Cement Plant for Four Seasons during 2020

Station	E (m)	N (m)	Temperature at Spring (C°)	Temperature at Summer (C°)	Temperature at Autumn (C°)	Temperature at Winter (C°)
Laylan	456028.874	3907948.268	13.64	15.84	13.64	11.05
Daquq	449570.219	3888607.548	13.90	15.84	13.65	11.19
Kara Hinjir	467593.181	3927917.622	13.64	15.85	13.64	11.05
Chamchamal	485397.757	3931414.067	13.13	16.10	13.83	10.89
Tuz	466424.82	3860693.25	13.90	15.84	13.65	11.19
Kirkuk	445744.63	3926280.56	13.64	15.85	13.64	11.05
Sulaimanya	537706.84	3935988.72	12.97	16.93	14.25	10.63
Erbil	410913.18	4005600.89	13.44	16.03	13.63	11.08
Kifri	496334.8	3838373.366	13.89	15.77	13.77	11.20
Taqtaq	462535.204	3971589.935	12.97	15.88	13.36	10.50

Table 3.7 : The Specific Humidity of 10 Locations Surrounding the Kirkuk Cement Plant for Four Seasons during 2020

Station	E (m)	N (m)	Specific Humidity at Spring (g/kg)	Specific Humidity at Summer (g/kg)	Specific Humidity at Autumn (g/kg)	Specific Humidity at Winter (g/kg)
Laylan	456028.874	3907948.268	6.93	5.61	4.65	4.75
Daquq	449570.219	3888607.548	4.75	6.76	5.65	4.74
Kara Hinjir	467593.181	3927917.622	6.93	5.61	4.65	4.75
Chamchamal	485397.757	3931414.067	6.73	5.48	4.43	4.51
Tuz	466424.82	3860693.25	6.76	5.65	4.65	4.74
Kirkuk	445744.63	3926280.56	6.93	5.61	4.65	4.75
Sulaimanya	537706.84	3935988.72	6.70	5.68	4.39	4.35
Erbil	410913.18	4005600.89	7.37	6.14	4.88	4.70
Kifri	496334.8	3838373.366	7.10	5.44	4.54	5.05
Taqtaq	462535.204	3971589.935	7.06	5.78	4.68	4.58

3.4.4 Gaussian Parameters

σ_y and σz are the distribution of the normal parameters in a crosswind (y) and vertical direction (z) respectively which are listed in table 3.9. These parameters are also named coefficients of dispersion and the meter is the unit measure for them (Abdel-Rahman, 2008; Veigele & Head, 1978). To calculate the crosswind and vertical direction parameters, the class of wind speed should be stated. Since the Kirkuk cement plant operates five days a week and only during the day, the incoming solar radiation is taken into account when measuring the atmospheric stability classes of winds. All seasons during 2020 have wind speed between 3.5 and 3.8 and these case can be classes from B to C classes based on intensity of solar radiation as clear in table 3.8.

Table 3.8 : The Classification of Wind Speed Stability Based on Incoming Solar Radiation

Season	**Day – Incoming Solar Radiation**		
	Strong	**Moderate**	**Slight**
Spring	B		
Summer	B		
Autumn			C
Winter			C

Where, B: is somewhat unstable, C: mildly unstable.

Table 3.9 : The Coefficients (a, b, c, and d) Used in the Calculation of Crosswind Distance and Vertical Direction

Stability Classes of Pasquill	Downwind distance (x) in km	a	b	$\sigma_z = ax^b$	c	d	$\sigma_y = cx^d$
B	Less than 0.2	90.673	0.93198	20.23	18.333	1.8096	1.00
	0.21 – 0.4	98.483	0.98332	40.00			3.49
	More than 0.4	109.3	1.0971	638.94			337.36
	More than 5			5000			5000
C	Less than 0.2	61.141	0.91465	14.03	12.5	1.0857	2.18
	0.21 – 0.4			26.45			4.62
	More than 0.4			266.47			71.74
	More than 5			5000			
σ_y is being 5000 for a distance of more than 5 km							

(Janson et al. 2019)

3.4.5 Digital Elevation Model

Digital elevation models (DEMs) provide a three-dimensional representation (X, Y, Z) of bare ground in the study area. In other words, a DEM is "a regular matrix representation of continuous variations of space relief units" (Arseni et al. 2019). The DEM is one of the key geospatial datasets used in many engineering and science fields for countless applications (Caglar et al. 2018). However, the obtainability of some open-access DEMs products consequences in the confusion of researchers who choose different data for a definite application. The current investigation accomplished a practiced assessment of vertical and horizontal accuracies of a DEM derived from data from the (SRTM) Shuttle Radar Topography Mission, (ASTER) Advanced Spaceborne Thermal Emission and Reflection Radiometer, Cartosat 1, TanDEM-X, (ALOS) Advanced Land Observation Satellite, and Sentinel 1 InSAR with toposheet/elevation point (Devaraj and Yarrakula 2020). For the topographic mapping of Kirkuk, the ASTER GDEM data can be used to provide detailed elevation data for the area . The dataset can be accessed and downloaded from the NASA Earthdata website or from the ASTER GDEM website. The ASTER GDEM dataset is derived from data collected by the ASTER instrument aboard the Terra satellite, which is part of the NASA Earth Observing System (EOS). The instrument collects data in 14 different spectral bands, including visible, near-infrared, and thermal infrared. The data is used to create a digital elevation model by measuring the time it takes for the satellite to send a signal to the Earth's surface and receive it back, which is used to determine the distance to the surface. The ASTER GDEM dataset has a number of advantages for topographic mapping, including its global coverage, high resolution, and availability at no cost. However, it is important to note that the dataset has some limitations, including potential errors due to cloud cover, vegetation, and other factors, as well as potential inaccuracies in areas with steep terrain.

3.5 Data Preprocessing

For Landsat time series, a sequence of image pre-processing steps are necessary, including atmospheric corrections, cloud shadow detections, and composite-fusion metrics. To ensure that the time series are well aligned, most change detection algorithms only select Level 1 terrain-corrected (L1T) Landsat images as their inputs (Z. Zhu 2017).

In this study, we performed several data preprocessing steps on the Landsat time series to ensure the accuracy and quality of the data. First, atmospheric corrections were applied to convert top-of-atmosphere (TOA) radiance to surface reflectance, minimizing the impact of atmospheric interference. Geometric distortions were addressed through image-to-map rectification by matching ground control points with a reference map. Cloud and cloud shadow detection algorithms were applied to exclude noisy data, and a de-striping process was used to remove any striping artifacts present in the imagery. We also performed spatial subsetting to focus on the area of interest, reducing the processing load. Lastly, contrast stretching was applied to enhance image visibility, followed by mosaicking to combine multiple scenes into seamless composite images for more extensive area analysis. These preprocessing steps ensured that the dataset was well-aligned, consistent, and ready for further analysis.

3.6 Land Cover Classes

3.6.1 Classification Scheme

A classification scheme is a framework comprised of the organization and categorization of land use/land cover (LULC) classes extracted from an image. A suitable classification scheme includes the classes that are discernible in the available data and essential for the research at hand (Shareef, Ameen, and Ajaj 2020). The classification schemes are developed in remote sensing to classify remotely sensed images based on LULC with different levels of detail, and the essential level of aspect picks the spatial resolution of the data, which is the scale of the lowest angular or linear separation between two items to which the sensor is sensitive (Atharva Sharma et al. 2017). The classification scheme is organized into two hierarchical groups: The first group contains only LC classes, whereas the second group is a mix of LULC classes (Grippa et al. 2017). Both of these schemes contain multilevel LULC classifications;

classes of level I can be presented as maps from Landsat images, while the drawing out of info for levels II, III, and IV needs to practice high-, medium- and low-altitude aerial photos, respectively (Dewan and Corner 2014). This study modified the Anderson classification scheme and the National Land Cover Database 92 to achieve a suitable classification scheme for this research's study area. Four LULC types were recognized in the study: vegetation, water bodies, urban and barren land. The descriptions and identifying features of the above-mentioned land use/land cover classes are reported in Table 3.10.

Table 3.10 : Descriptions of Land Use/Land Cover Classes

No.	Class	Description
1	Barren	Dry salt flats, beaches, sandy areas other than beaches, barely exposed rock, strip mines, quarries, gravel pits, transitional areas, and mixed barren land.
2	Water bodies	All areas of open water, rivers, ponds, lakes, and lagoons.
3	Vegetation	Cropland and pastures, orchards, plantations, fallow plots, vegetable gardens, and areas of sparse vegetation cover, which include: cultivated land without crops and sand along rivers and beaches.
4	Urban	Residential areas, commercial areas, industrial areas, roads, and a small cluster of housing within a rural area.

3.6.2 Sampling and Training Data

The spectral pattern for each pixel of multispectral data can be utilized as a number for categorization in pixel-based classification (Mazzia, Khaliq, and Chiaberge 2020). Based on their spectral reflectance characteristic, each feature type has an unique combination of DNs (Okhrimenko, Coburn, and Hopkinson 2019). Pixel-based classification is based on statistical approaches of supervised or unsupervised classification (R. Sensing, List, and Factors 2016). In supervised classification, an analysis trains the computer by monitoring the pixel classification process and assigning the methods and numerical descriptions of the various land cover classes in the region (Sathya and Deepa 2017). A supervised classification's quality is determined by the quality of the training sites (J. Park et al. 2018). Defining of training sites, extraction of signatures, and classification of the Image are the fundamental steps in the supervised classification process (Rwanga and Ndambuki 2017).

3.6.3 Digital Image Classification

Two supervised classification algorithms were used for this research: support vector machine (SVM) and maximum likelihood (ML).

In this study, we used the ML classification method to classify the land cover classes of the study region based on satellite images and the ground truth of the region of interest. This method is characterized by normally distributed data, providing an individual understanding of the functions of classification intensity (Al-doski et al. 2013) as well as accurate, complicated, and traditional costing (M. Xu and Wei 2012). Additionally, this approach depends on Bayesian probability theory to compute the means and variances of the categories and use them to measure probability (Ajaj et al. 2017).

The following discriminant equation (3.4) for each pixel in the image are applied in ML classification (Richards and Jia 2006).

$$g_i(x) = \ln p\,(w_i) - \frac{1}{2}\ln|\sum i| - \frac{1}{2}\,(x - m_i)\ t \sum i^{-1}\,(x - m_i) \tag{3.4}$$

Where:

i = class

x = n-dimensional data (where n is the number of bands)

p (w_i) = probability that class w_i occurs in the image, assumed to be the same for all classes

$|\Sigma i|$ = determinant of the covariance matrix of the data in class w_i

$\sum i^{-1}$ = its inverse matrix

m_i = mean vector

On the other hand, SVMs provide a training approach using the pixels based on the neighbours of the separating hyperplanes, which are called the support pixel vectors. Supervised classification is performed on the image using an SVM to identify the class associated with each pixel (Helmi Zulhaidi M. Shafri, Maris, and Hadi 2011). Several recent studies have noted that SVMs generally deliver more accurate classification than other data classification approaches (Chidambaram and Srinivasagan 2019). The data are linearly separable and many hyperplanes can perform the separation. Figure 3.5 shows several decision hyperplanes that perfectly separate the input data set. Any hyperplane can be represented by w, x, and b, where w is a vector perpendicular to the hyperplane. Figure 3.6 shows the geometric representation of the quadratic programming problem showing H (the optimal separator) and hyperplanes H_1 and H_2 (Cervantes et al. 2020).

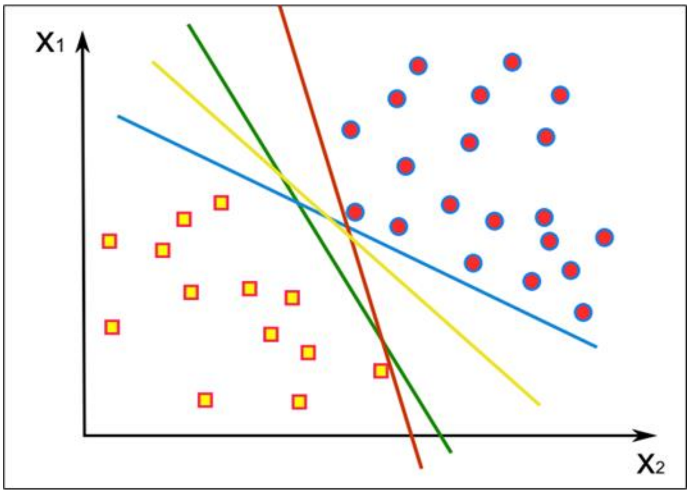

Figure 3.4 : Separation Hyperplanes

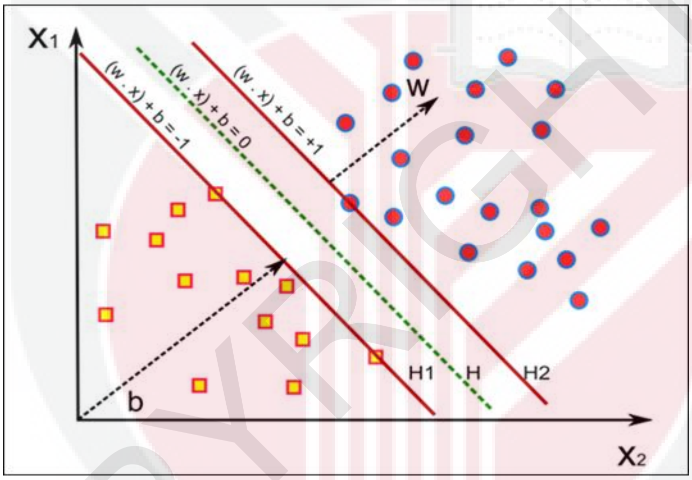

Figure 3.5 : Optimal Classifier

3.6.4 Accuracy Assessment

An accuracy assessment of the chosen sites in the mapped region is the relation between the map class expected and the actual field samples observed (Stehman, S. V., & Foody 2019). Accuracy assessment is usually used to indicate the extent to which a classification outcome is accurate (Huang et al. 2017). Accuracy is one of the most often used metrics of classification results, and it is defined as a ratio of properly classified samples to total number of samples (Tharwat 2018). The accuracy assessment is used to determine the efficiency of the classification, and many factors, including training sample size, the number of classes in the classification, the ability of the training data to adequately classify the classes being mapped, and the dimensionality of the data, can influence the outcomes of an accuracy assessment (Millard and Richardson 2015). As a result, if the reference data is significantly wrong, the assessment may reflect that the classification is poor even when it is actually an excellent classification (Russell G. Congalton and Kass Green 2019). I used the ENVI Classic program version 5.3 to apply accuracy assessment for the classification scheme through overall accuracy and kappa coefficient.

The foundation of accuracy assessment is the error matrix, also known as a confusion matrix. It is a square array of numbers arranged in rows and columns that represents the number of sample units (pixels, clusters of pixels, or polygons) assigned to a particular category relative to the actual category as verified by reference data.

Producer's accuracy measures the probability that a pixel in reference data is correctly classified. It is calculated for each class and indicates the error of omission (exclusion error).

$$PA = \frac{x_{ii}}{\sum_{j=1}^{n} x_{ji}} \times 100\backslash\%$$

where: x_{ii} is the number of correctly classified pixels for class i, $\sum x_{ji}$ is the column total (reference data total for class i).

User's accuracy measures the probability that a pixel classified as a certain class actually represents that class on the ground. It indicates the error of commission (inclusion error).

$$UA = \frac{x_{ii}}{\sum_{j=1}^{n} x_{ij}} \times 100\%$$

where: x_{ii} is the number of correctly classified pixels for class i, $\sum x_{ij}$ is the row total (classified data total for class i).

Overall accuracy represents the proportion of correctly classified pixels to the total number of validation pixels. While simple to calculate and interpret, it doesn't account for the distribution of errors among classes.

$$OA = \frac{\sum_{i=1}^{n} x_{ii}}{\sum_{i=1}^{n} \sum_{j=1}^{n} x_{ij}} \times 100\%$$

where: $\sum x_{ii}$ is the sum of diagonal elements, n is the number of classes, x_{ij} represents the elements in the error matrix.

The Kappa coefficient measures the agreement between classification and reference data while accounting for the agreement that occurs by chance. It ranges from -1 to 1, where: 1 represents perfect agreement, 0 represents agreement equal to chance, and Negative values represent agreement less than chance.

$$\kappa = \frac{N \sum_{i=1}^{n} x_{ii} - \sum_{i=1}^{n} (x_{i+} \times x_{+i})}{N^2 - \sum_{i=1}^{n} (x_{i+} \times x_{+i})}$$

where: N is the total number of observations, x_{ii} is the number of observations in row i and column i, x_{i+} is the marginal total of row i, x_{+i} is the marginal total of column i.

3.7 Interpolation

Interpolation is a technique for predicting the values of cells in areas where there are no sample points. Interpolation is founded on the theory of spatial autocorrelation, generally known as spatial dependence, which measures the degree of relational dependency between items based on their distance from each other (Ajaj et al. 2017).

Spatial interpolation is well-developed in geographic information systems (GIS), often used to predict the value at unknown locations using spatially sampled measurements. Over time, several popular spatial interpolation models have been thoroughly researched, including inverse distance weighting (IDW), shape functions, radial basis functions, spline interpolation, optimal interpolation, natural neighbors, trend surface analysis, and Kriging, model–data fusion (L. Li et al. 2016).

3.7.1 Spline Interpolation

This model uses mathematical functions to connect the examined data points, generating continuous elevation and grade surfaces while minimizing the curvature around the surface (Ikechukwu et al. 2017).

Polynomials that describe segments of a line or surface are fitted together seamlessly using the spline technique (Tan and Xu 2014). However, spline interpolation offers the best results with slowly varying surfaces; it is generally not appropriate when there are large fluctuations in the surface values within short horizontal distances (M. H. Rahman, Abu-Farsakh, and Jafari 2021).

The spline process forecasts $z(s)$ by minimizing a smooth function, g as clear in equation (3.5).

$$\sum_{i=1}^{n}(z\ (s_i - g\ (s_i))^2\ +\ \eta\ H_m\ (g) \tag{3.5}$$

where $H_m\ (g)$ is a measure of the spline function smoothness g, which is denoted as the mth degree derivative of g, and η referred to as the smooth parameter where its value is > 0.

When η = 0, the spline equation iterates over the data points, and as g approaches infinity, it approaches the least-squares polynomial (Hutchinson and Xu 2000). Equation 3.6 defines the function g. Generalized cross-validation can be used to determine the mth derivative and degree of smoothness (Meng, Liu, and Borders 2013).

$$g(s) = \sum_{k=0}^{k} a_k\, f_k\ (s) + \sum_{i=1}^{n} \lambda_i\, R\ (s - s_i) \tag{3.6}$$

where $f_k(s)$ is the order monomials k asset and $R\ (s- s_i)$ is the Euclidean distance scalar equation between s and s_i.

3.7.2 Inverse Distance Weighting

IDW, one of the most popular interpolation methods, takes a mechanical (deterministic) approach (Ajaj et al. 2018). The attribute values of any pair of points are related to one another, with their similarity inversely proportional to the distance between them (Bărbulescu, Șerban, and Indrecan 2021).

In equation (3.7), the unknown value $Z\ (S_o)$, at location S_o, is computed by the following equation (W. Yang et al. 2020):

$$Z\ (S_o) = \sum_{i=1}^{n} W_i\ Z\ (S_i) \tag{3.7}$$

where n is the monitoring station, $Z\ (S_i)$ is the value at the sampled locations S_i and W_i represents the weight of S_i, defined in equation (3.8) as:

$$W_i = \frac{\frac{1}{d_i^k}}{(\sum_{i=1}^{n} \frac{1}{d_i^k})} \qquad i = 1, 2, \dots, n \tag{3.8}$$

where d_i is the horizontal distance between the interpolation points and the points observed and k is the power of the distance.

3.7.3 Kriging

Kriging has become a popular metamodeling tool for resource-intensive computational experiments in recent years. Nevertheless, the quantity and distribution of the training points have a significant impact on the accuracy of the prediction (Fuhg, Fau, and Nackenhorst 2021).

Compared with other interpolation approaches, kriging offers several advantages. For example, it provides weights using a data-driven technique rather than an arbitrary algorithm, giving solitary points larger weights than points within a cluster (Amjady and Abedinia 2017).

The two types of kriging ordinary and universal equation (3.9) are the commonly used univariate kriging techniques, both of which are common linear regression models, $\hat{z}\ (s_0)$ is the point to be interpolated at position s_o. The sampled values are denoted by $z\ (s_i)$ and the weights to be allocated for all unsampled locations are denoted by λ_i, as determined by semivariogram modeling.

$$\hat{z}\ (s_0) = \sum_{i=1}^{n} \lambda_i z\ (s_i) \tag{3.9}$$

Typically, universal kriging expresses the spatial difference in z value has a drift or basic component which is determined by the difference in positions, where the information presence combined into the kriging progression. Dissimilar to ordinary kriging, which uses the stationary random function model to determine weights, universal kriging uses a non-stationary random function model to do the same (Meng, Liu, and Borders 2013).

3.8 Gaussian Plume Models (One Variable)

3.8.1 1D Modelling

The Gaussian plume is a uniform model that considers atmospheric disturbance as stationary and regular (Z. Yang et al. 2020). In this work, we have coded the Gaussian plume equation in QGIS via Python Language. Figure 3.7 states the overall methodology of 1D Gaussian Plume Modelling.

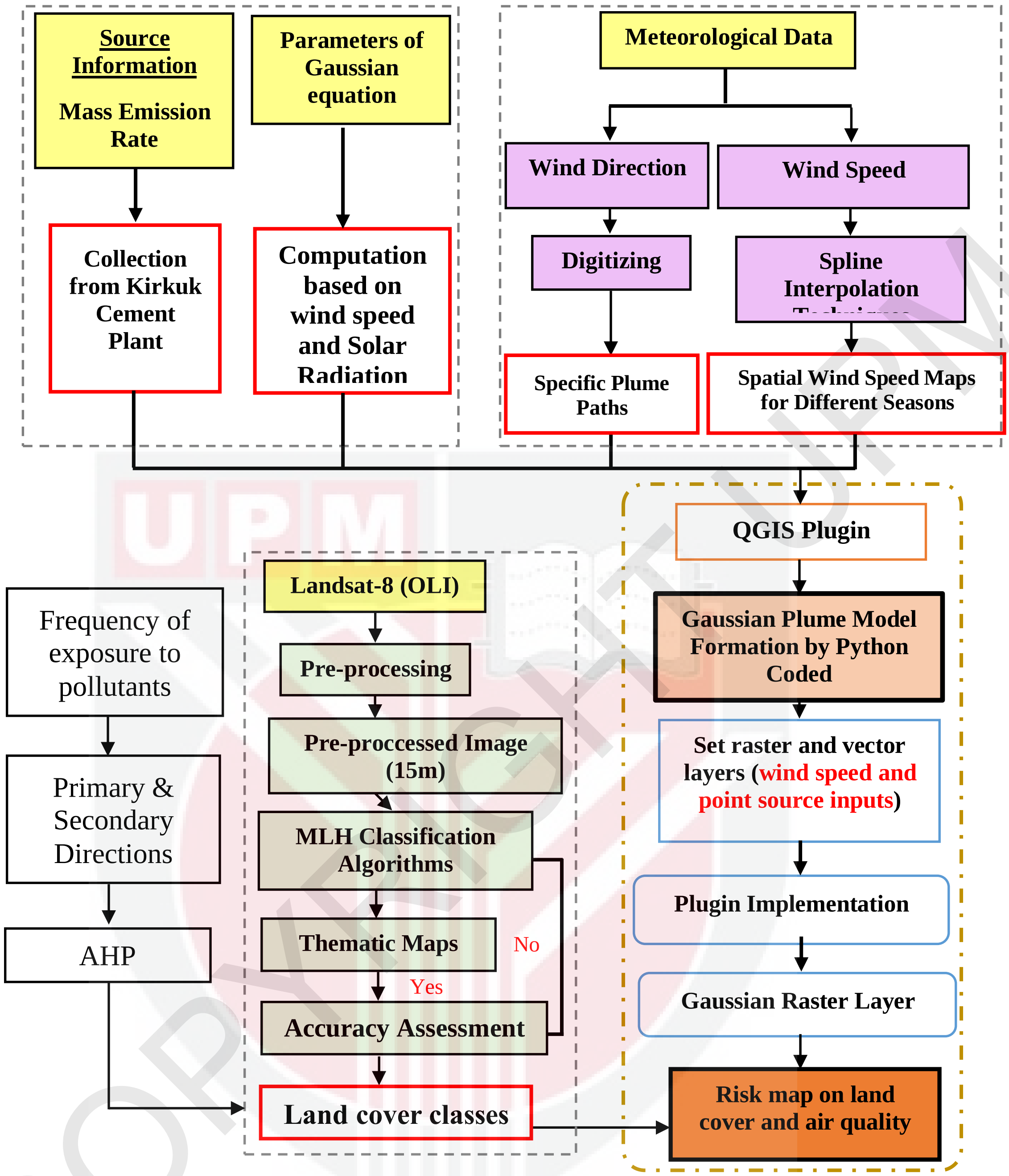

Figure 3.6 : Flowchart of 1D Gaussian Plume Methodology

The equation of Gaussian from point source expresses as:

$$C(x, y, z) = \frac{Q}{2\pi\, \sigma_y\, \sigma_z\, u} \exp\left(\frac{-y^2}{2\,\sigma_y^2}\right) \left[\exp\left(\frac{-(z-h)^2}{2\sigma_z^2}\right) + \exp\left(\frac{-(z+h)^2}{2\sigma_z^2}\right)\right] \qquad (3.10)$$

Where,

x, *y*, and *z* are the downwind, crosswind, and vertical coordinates (m),

h is the release height from the ground (m),

Q is source strength (g/s), u is wind speed (m/s),

y and z are the standard deviations of the distribution concentration in σ_y and σ_z axis (m).

All parameters and required measurements are prepared in a form proportional to the framework of the equation in Python.

The highest value is calculated at ground level (z = 0) and in the center line of the plume (y = 0). Thus, the concentration in equation (3.10) is reduced to the following (Lawal and Asimiea 2017) expressed in equation (3.11):

$$C(x, y = 0, z = 0) = \frac{Q}{2\pi\, \sigma_y\, \sigma_z\, u} \exp\left[-\frac{1}{2}\left(\frac{h}{\sigma_z}\right)^2\right] \tag{3.11}$$

3.8.1.1 Building QGIS Plugins

3.8.1.1.1 Building the Model with QGIS

QGIS is an important, open-source GIS software for spatial analysis development and planning (Kukulska et al. 2018) that provides several tools for visualizing and analyzing data (Dochev, Seller, and Peters 2019); it is mostly written in C++ code, but its functionality can be extended through APIs and plugins written in Python (Congedo 2021). The QGIS Processing toolbox is an object-oriented Python framework (Team 2016) that enhances the capabilities of the previous QGIS algorithms (Graser and Olaya 2015). The Processing toolbox also provides a graphical modeler for complex workflow management that automates the execution of algorithms (Sehra, Singh, and Rai 2017). PyQGIS is the QGIS open-source software library (Muenchow, Schratz, and Brenning 2017), the binding of which allows for easy integration of Python code with Qt libraries and eventually QGIS.

The Qt framework is widely used in application development for desktop environments. It is mainly used as a graphical user interface (GUI) tool with many graphical objects (Fedel et al. 2017). Qt facilitates easy object-to-object communication, which makes application development intuitive. Qt is also accompanied by Qt Designer, which is a graphical environment that allows users to create graphical applications without coding, just by dragging and dropping widgets (Fedel et al. 2017).

3.8.1.1.2 The QGIS Python Console

The QGIS Python Console is an interactive shell for Python commands. The Python Development Environment further allows for the automation of various tasks (S. Khan and Mohiuddin 2018).

The event data were contained in the Occurrence.txt file, whereas the request.txt contained paths to the environment variables and other configuration parameters such as the modeling algorithm. The plugin generated these files using the QGIS user interface. Copying all files to generate a text file allowed the corresponding request.txt file to be used as a parameter to execute om_console.exe and calculate the model (Becker et al. 2016).

Python was used to create the plugin. It was chosen because it is a language supported by the QGIS Application Programming Interface (API), it is platform-independent, and it is supported by a wide range of open-source geospatial libraries. To improve raster processing, the open-source graphical-based QGIS plugin was built using the (GDAL) Geo-spatial Data Abstraction Library and PyQt4 framework (Ndossi and Avdan 2016).

Processing generated a GUI for the script so its parameters could be configured automatically. Furthermore, processing scripts were used in the graphical modeler to create geoprocessing models. Finally, users can use standard PyQt classes to create their windows and dialog boxes to provide a sophisticated user interface for their Python scripts (Graser 2016).

3.8.1.1.3 The QGIS Python API

Several libraries were used in the plugin development. PyQGIS is a Python library for creating QGIS applications that enable the creation of custom plugins based on the QGIS API and Psycopg2, a library that allows Python to communicate with PostgreSQL. Psycopg2 also allows for the execution of SQL commands in Python while providing access to many PostgreSQL resources (Silveira, Camara, and Camboim 2018).

To avoid the time-consuming process of learning how spatial data should be represented in the modern C++ ecosystem, a simple GIS like QGIS helps to easily evaluate data and results during development. C++ provides many benefits in terms of efficiency and performance, as well as immediate technical support for shared memory multiprocessing, supercomputing, GPU computing (OpenACC, NVIDIA thrust), source code portability, elegance, library quality and support, and the ability to bind to a variety of low-profile languages, most notably R and Python (Werner 2019).

The coordinate reference system (CRS) definition is stored as a series of global characteristics in the files of models implemented in the QGIS plugin that was written in Python, although other models of weather metadata conventions demand that the CRS be expressed in a so-called grid mapping variable (Meyer and Riechert 2019).

The vector layers, relative densities, output raster resolution, and path are all inputs to the QGIS plugin interface (Mileu and Queirós 2018).

Using QGIS and additional QGIS plugin vector functionalities, such as a simple renaming of attribute values based on field calculations or exporting the labeled vector data into formats known by other applications, the vector layer can be modified in QGIS at the same time (Yudha and Purnama 2018).

Using the standard Database (DB) Manager Plugin, the layers are loaded into the database to the geom schema. The primary key id and the geometry field are named, and a spatial index is constructed to speed up access to vector features by naming the table to be generated in the same way that the layer would be named (Gritsenko, Senchenko, and Kalentiev 2020).

Furthermore, QGIS makes it easy to use third-party geo-algorithms by automatically converting vector and raster formats into a format supported by the third-party module (Muenchow, Schratz, and Brenning 2017).

The QQuake plugin is written in Python, with all spatial operations managed by the PyQGIS library and all graphical user components handled by the PyQt5 library. The workflow follows three steps: (i) filling the GUI with the constraint parameters that characterize each web service, (ii) issuing a remote request with these constraint parameters, and (iii) parsing the returned document and turning it into a standard QGIS map layer (Locati et al. 2021).

3.8.1.1.4 Creating QGIS Plugins

Because QGIS is open source and allows developer activities, it was used for all GIS operations in the research. The following were the primary goals of plugin development: Reducing processing time, removing the chance of user-induced error, standardization and rating, a subject-specific application tool, and being open source and developable are all advantages (Bediroglu 2021).

The following features highlight the work's innovation: (i) the literature analysis revealed that there is no GIS application available that specifically provides tree crown metrics; (ii) the methodology was developed and implemented in a new plugin, so users who are unfamiliar with the algorithms in the QGIS software can easily estimate the parameters with a simple tool; and (iii) the GIS application was developed in Python, a free programming language. Furthermore, we respect the freedoms of open-source software by using QGIS software, which allowed us to incorporate algorithms and functions from other software, and fractal analysis was only possible with an automatic implementation (Duarte, Silva, and Teodoro 2018).

Some ArcGIS features, such as 3D data, animations, and advanced network analysis, were not available in QGIS, according to researchers from the University of Vienna (Friedrich, 2014). However, QGIS now has these capabilities. The absence of user support in the form of user manuals and tutorials is another typical disadvantage of open-source software (Flenniken, Stuglik, and Iannone 2020).

Python uses a different approach to programming than earlier languages like Java and C++. However, this approach allows developers to accomplish more with less effort – often in just a few lines of code. Furthermore, Python's adaptability it to be used in a variety of settings, from web and mobile development to desktop applications and hardware programming (Saabith, AL Sayeth, M. M. M. Fareez 2019).

Plugin Builder is used in conjunction with the QGIS Plugin GUI to allow for the construction of plugins within QGIS. Within the QGIS directory, the new plugin is saved in a special directory. The plugin file resources are compiled for recognition by the QGIS interface when the OSGeo4w software is used. Furthermore, the plugins are written in Python, making QGIS, OpenDSS, and AIMMS integration easier. The plugin GUI (PGUI) is designed using Plugin Builder and Qt Designer. It is worth noting that Qt Designer is used only for PGUI development and is not considered part of the software integration. To match the requirements of power flow analysis, adjustments must be made to the PGUI as well as the tool's core functionality. Several options are available to customize the design of each element of the PGUI; e.g., Qt Widgets. Furthermore, buttons must be assigned to their appropriate functions so users may appropriately select the power flow analysis settings. This may be done with the help of Qt Designer, which makes the process easier. Additionally, PyQt5, a set of

Python bindings compatible with Qt-based applications, may be used to interact with the PGUI outside of Qt Designer. The uic and qtgui modules in the package allow you to transform and design graphical objects in Python (Custodio et al. 2019).

3.8.1.2 Using QGIS in the Gaussian Model

In this research, The Python language was used to model the Gaussian plume equation using a QGIS plugin. The QGIS API and PyQt4 API methods, modules, and classes were also utilized. This new plugin is a useful tool that allows users to automate several parameters and metrics of the model using spatial analysis tools, considering all parameters, such as wind speed and pollution source data.

QGIS can create maps with specified raster/vector layers of Gaussian parameters in a variety of map projections and formats (as supported by the GDAL/OGR libraries). Maps can be made in several formats and for many purposes. With both official and third-party plugins, QGIS has various open domain sources. As a turnkey package, these plugins provide a vast range of functionalities (Saxena, Mundra, and Jigyasu 2020).

3.8.2 1D Gaussian Modelling with Reality Wind Direction

The direction of plume in Gaussian Plume Model moves in straight line by mean of constant direction (Brusca et al. 2016). Due to various mesoscale weather phenomena, the wind direction in air boundary layers changes continuously (Stieren, Gadde, and Stevens 2021). Hence, the Gaussian Plume should be modeled with change of plume direction to achieve the reiality of pollution dispersion. In this study, I selected four days for different seasons in 2020 to present the reality of plume direction of Gaussain

Plume Model of pollution that emits from Kirkuk Cement Plant. The wind direction is exrtracted from https://www.ventusky.com/ . The direction of the wind is one of several variables that might affect the movement of a pollution plume released from a cement plant. The direction from which the wind is blowing is referred to as wind direction.

Wind speed, atmospheric stability, and terrain are additional variables that can impact how pollution plumes move in addition to wind direction.

For predicting and managing the impacts of cement plant emissions on the environment and human health, it is essential to comprehend the relationship between wind direction and the movement of pollution plumes.

In order to examine the changes in wind direction for each day and to represent the four seasons of the year 2020, four distinct days were selected. Winter Winds Day was observed on January 2nd, and Autumn Winds Day on October 1st. The first day of April as well as the first day of July were chosen to represent the spring and summer seasons' wind directions, respectively. As indicated in figure 3.9 and table 3.11 below, 15 locations around the Kirkuk Cement Plant used to have their wind direction measured. The wind direction data are analyzed in ArcMap GIS to produce wind direction map over the study area. The flowchart of real wind direction with Gaussian Plume Model is indicated in figure 3.8.

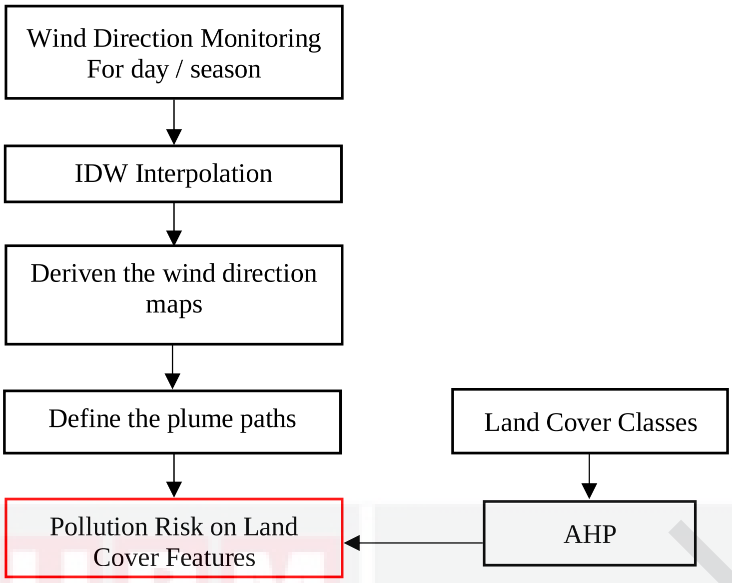

Figure 3.7 : Flowchart of Real Direction with Gaussian Plume Methodology

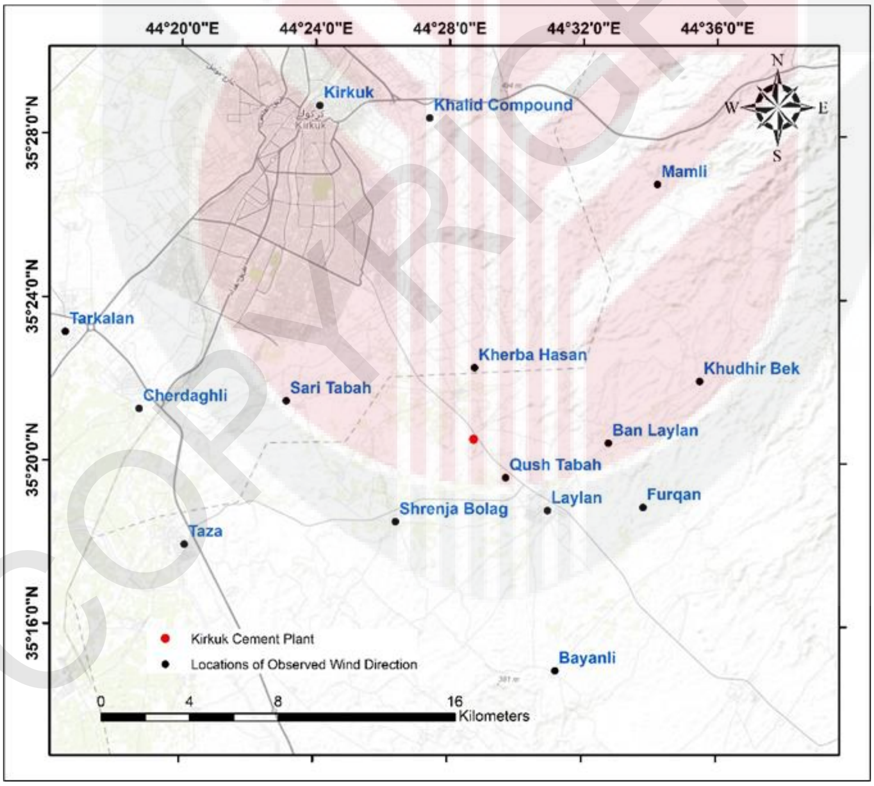

Figure 3.8 : Wind Direction Monitoring Sites around the Kirkuk Cement Plant

Table 3.11 : Wind Direction Monitoring Sites around the Kirkuk Cement Plant for Four Seasons in 2020 with Different Period Per Day

Location	E	N	Season	6 A.M	9 A.M	12 P.M	3 P.M
Kirkuk	445744.63	3926280.56	Spring	255	260	315	360
			Summer	225	45	30	20
			Autumn	260	270	315	15
			Winter	225	215	210	180
Sari Tabah	444221.412	3912916.491	Spring	260	270	315	355
			Summer	245	45	45	25
			Autumn	250	280	320	20
			Winter	235	190	200	165
Qush Tabah	454134.608	3909441.39	Spring	265	275	315	5
			Summer	225	50	35	25
			Autumn	240	275	315	20
			Winter	225	215	205	145
Laylan	456028.874	3907948.268	Spring	265	275	315	5
			Summer	225	45	35	25
			Autumn	230	270	310	20
			Winter	225	220	215	145
Kherba Hasan	452737.874	3914413.258	Spring	260	270	315	5
			Summer	225	50	45	30
			Autumn	250	270	310	25
			Winter	225	225	215	155
Cherdaghli	437575.233	3912570.334	Spring	260	265	315	355
			Summer	245	45	40	30
			Autumn	265	280	330	20
			Winter	225	185	210	170
Khudhir Bek	462916.142	3913785.374	Spring	255	270	315	5
			Summer	220	30	35	30
			Autumn	240	270	315	25
			Winter	225	225	190	125
Furqan	460354.309	3908090.272	Spring	260	275	315	5
			Summer	225	30	45	30
			Autumn	240	270	315	25
			Winter	225	225	190	125
Ban Laylan	458790.644	3910999.255	Spring	260	270	315	5
			Summer	225	45	45	25
			Autumn	240	270	315	25
			Winter	225	225	190	135
Tarkalan	434236.971	3916063.044	Spring	255	260	315	355
			Summer	226	50	45	25
			Autumn	270	275	330	15
			Winter	215	180	215	175
Taza	439607.238	3906431.938	Spring	165	270	315	355
			Summer	260	50	50	25
			Autumn	260	280	310	15
			Winter	215	190	215	155
Bayanli	456362.617	3900700.607	Spring	180	280	315	5
			Summer	225	40	50	25
			Autumn	250	280	310	20
			Winter	225	215	215	135
Mamli	461008.456	3922703.855	Spring	150	265	315	3
			Summer	225	45	50	30
			Autumn	250	275	315	20
			Winter	225	225	215	135
Shrenja Bolag	449162.913	3907444.764	Spring	180	270	315	360
			Summer	240	45	45	35
			Autumn	260	280	315	15
			Winter	235	190	210	195

Table 3.11 : Continued

Khalid Compound	450709.406	3925716.926	Spring	150	260	315	3
			Summer	225	50	40	25
			Autumn	265	275	315	15
			Winter	225	225	225	170

3.9 Analytic Hierarchy Process

The analytic hierarchy process (AHP) is a measuring concept and a conflict mechanism (Emrouznejad and Marra 2017). Saaty & Vargas, (1980) developed AHP to support decision-making in challenging and multi-criteria conditions (Singh and Nachtnebel 2016). Decision makers believe that the AHP is a highly effective decision-making tool since it is practical and simple to comprehend (Abdel-Basset, Mohamed, and Smarandache 2018). In this study, AHP was used to weigh the primary and secondary directions in terms of their exposure to cement plant emissions in 2020.

3.10 Risk Assessment

Cement plant emissions of gases and particles matter have a detrimental impact on public health and land cover. Cement industry air pollution has been identified as causing severe health hazards and adverse effects on crops, planting, and buildings (Dubey 2013). Dust deposited on the soil for long periods by cement plants contaminate the environment (Wróbel and Gołuchowska 2018). This man-made disaster considers a hazardous phenomenon that needs to know the size of the pollution that it produces and its impact on humans and the features around it. The concentration of pollution and land cover classes are the important factors to indicate the degree of susceptibility of each feature to the risk. These factors combine using spatial analyses utilizing raster calculation.

3.11 3D Gaussian Modelling (Three Variables)

The Gaussian model was used in this section to simulate the concentration of pollutants emitted by the Kirkuk Cement Plant for the surrounding areas. The model considered the three variables x, y, and z, resulting in a three-dimensional model. The equation (3.10) has been coded by Python to configure 3D Gaussian Model plugin in QGIS and the figure 3.10 illustrates the flowchart of methodology.

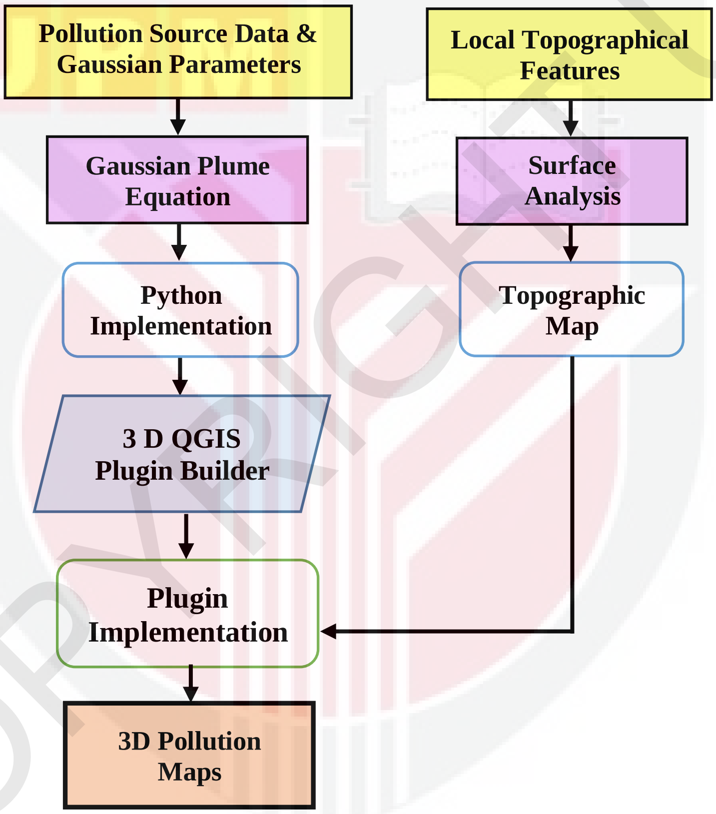

Figure 3.9 : Flowchart of 3D Gaussian Plume Methodology

3.12 Modelling with Temperature and Specific Humidity Effects

Meteorological elements such as atmospheric wind speed, wind direction, specific humidity, and temperature influence the concentration of air contaminants in the atmosphere (Jayamurugan et al. 2013). Because an increase in humidity causes particle adherence to it, which leads to the accumulation of its concentration and consequently sedimentation according to gravity, relative humidity causes a drop in dust concentration. Temperature, on the other hand, causes an increase in its concentration since it becomes dry and transportable in the atmosphere (Hernandez, G., Berry, T. A., Wallis, S. L., & Poyner 2017). In this study, the wind speed and wind direction are included in applying Gaussian Plume Model using Python in QGIS. However, the Gaussian Plume Model does not consider the temperature and specific humidity as effected parametres. Therefore, in order to develop the model, these parameters should be essential parameters in equation (3.12) for temperature effect and equation (3.13) for specific humidity effect to obtain real concentration of pollution. F(T) and F(SH) are the correction factores of temperature and specific humidity for Gaussian Plume Model respectively and express in equations (3.13) and (3.15). Figure 3.11 shows the overall methodology of Gaussian Plume Model with corrections of temperature and specific humidity.

$$C(x, y, z) = \frac{Q}{2\pi\, \sigma_y\, \sigma_z\, u} \exp\left(\frac{-y^2}{2\, \sigma_y^2}\right) \exp\left(-\frac{z^2}{2\sigma_z^2}\right) \exp\left(-\frac{ux}{v}\right)\, F(T) \tag{3.12}$$

$$F(T) = \left(\frac{T}{T_{ref}}\right)^{a-1} \tag{3.13}$$

Where T is the ambient air temperature, T_{ref} is a reference temperature (usually taken to be 20°C), alpha is the temperature exponent (usually taken to be 0.5), and ^(alpha-1) represents an exponential function.

$$C(x, y, z) = \frac{Q}{2\pi\, \sigma_y\, \sigma_z\, u} \exp\left(\frac{-y^2}{2\, \sigma_y^2}\right) \exp\left(-\frac{z^2}{2\sigma_z^2}\right) \exp\left(-\frac{ux}{v}\right)\, F(SH) \tag{3.14}$$

$$F(SH) = \left(\frac{SH}{SH_{ref}}\right)^{a-1} \tag{3.15}$$

where SH is the specific humidity at a given location, SH_{ref} is a reference relative humidity (usually taken to be 50%), and beta is the specific humidity exponent (usually taken to be 0. 5).

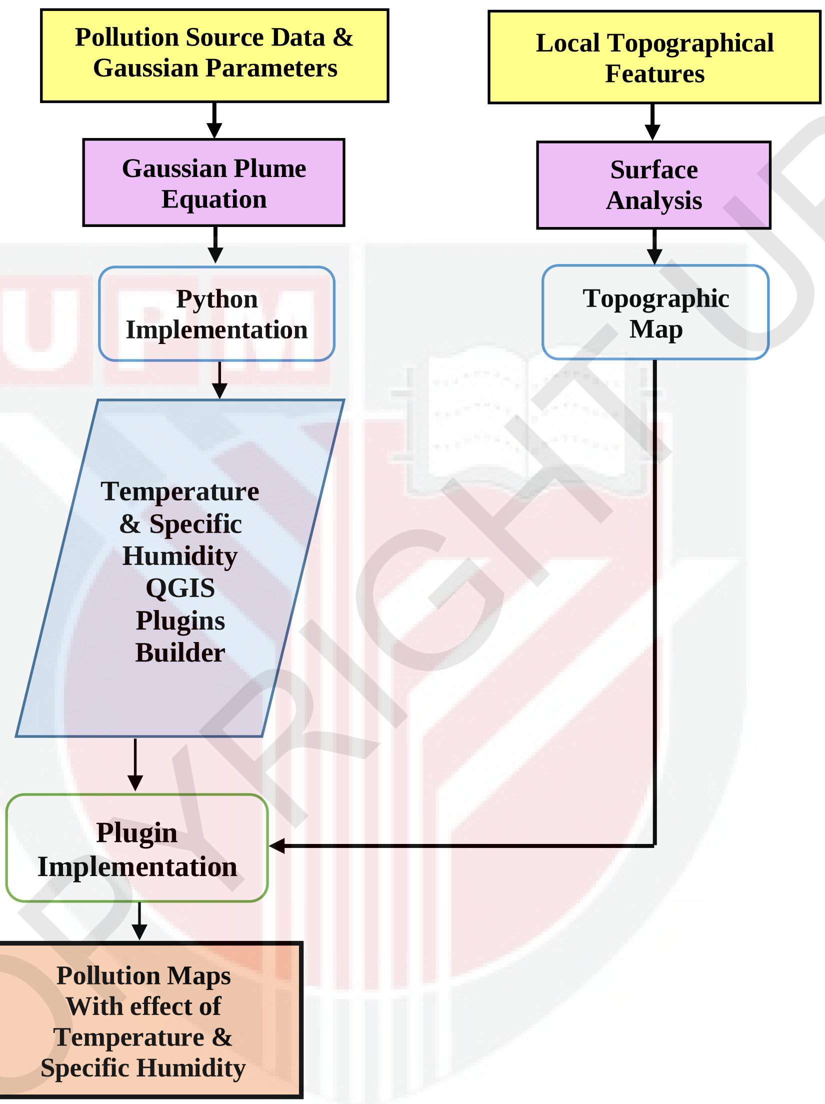

Figure 3.10 : Flowchart of Gaussian Plume Model with Effect of Temperature and Specific Humidity

3.13 Validation and Verification Process

Validation measures the model's performance by comparing its output with known information (Paegelow & Olmedo, 2008). The mean, standard deviation, fractional bias (FB), geometric mean bias (GM), index of agreement (IOA), the factor of two

(FAC2), and normalized mean square root error (NMSRE) are statistical performance measurements applied to assess dispersion models (Kumar et al., 2006).Validation of mathematical results using model outputs is an iterative process that entails refining the model depending on validation results (Eldin, Abd-Elhady, and Kandil 2016). This study is comapared the mathematical calculation results with the outputs of Gaussian Plume Model that coded using Python in QGIS plugin.

3.14 Deep Pollutant Prediction Model (DPPM)

This section describes the parts of the proposed method for building a smart model based on deep learning to predict air pollutants, as follows:

3.14.1 Dataset Description

Because the study area lacked long-term pollution data, the proposed model was applied to a dataset from the Institute of Mental Health in Ahmedabad City, India (GJ001). The GJ001 pollution dataset contains 12 parameters which are PM_{10}, PM, NO, NO_2, CO, SO_2, O_3, Benzene, Toluene, and Xylene, Air Quality Index (AQI), and compounds for 2009 observed days. Initially, this dataset was processed using the statistical missing values approach in order to accommodate the suggested deep learning model. However, simulated data of Laylan District using the proposed Gaussian Plume models. The simulated data were calculated for three years 2019, 2020, and 2021. The simulated data include 7 parameters which are Calcium Carbonate ($CaCO_3$), Silicon dioxide (SiO_2), Aluminum oxide (Al_2O_3), Iron (III) Oxide (Fe_2O_3), Calcium oxide (CaO), Magnesium oxide (MgO), and Sulfur trioxide (SO_3). These emissions are components of cement material, which are released in various amounts from the stack of the cement plant.

3.14.2 Methodology

Building the suggested model is a crucial procedure since the model must be successfully represented, which has a significant effect on the success of the planned model when implemented applications. The suggested model is designed to predict pollution components emitted from cement plants in a short time and with reliable data. Figure 3.12 shows the overall procedures of DPPM model.

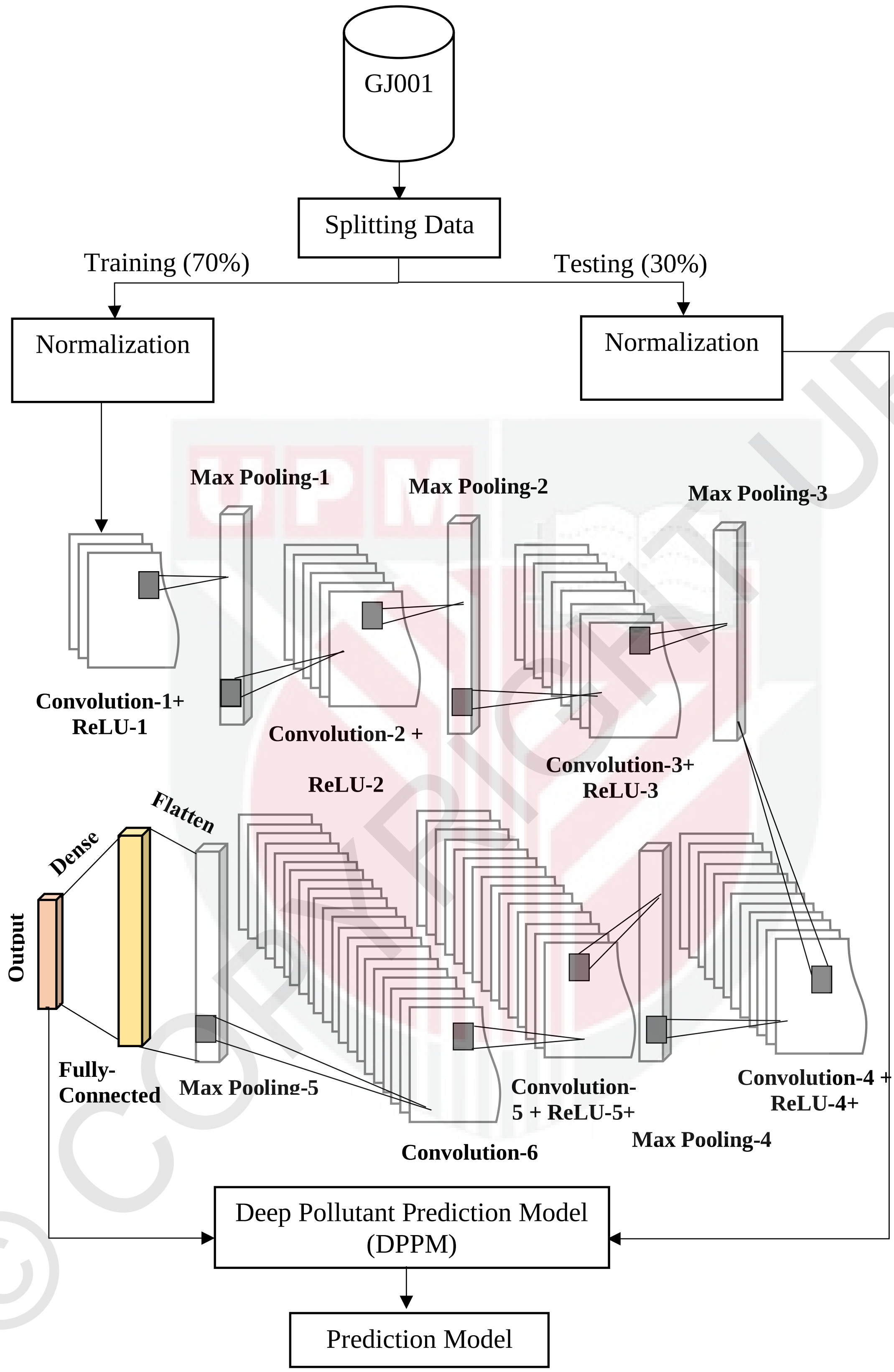

Figure 3.11 : Flowchart of the Proposed Model

3.14.3 Data Splitting

Data splitting is a key step for model validation since it splits a given dataset into training and testing sets. The training data is then used to fit and evaluate statistics and machine learning models. If it Hold-out a set of data for validation separate from the training set, it may analyze and compare the accuracy of multiple models' predictions without being worried about potential overfitting of the training set. The dataset is split into 70% for training and 30% for testing in this model.

3.14.4 Data Normalization

Normalization is the process of modifying data in order to compare statistics from various measures accurately by reducing artifactual biases in the source observations (Weiss et al. 2017). Feature normalization is an essential process of data preprocessing for applying machine learning and deep learning to multiple datasets (Ferreira, P., Le, D. C., & Zincir-Heywood 2019). Data normalization could be effective in the data processing stage despite requiring a significant increase in processing and memory capability (Pires et al. 2020). In this study, we used StandardScaler to normalize the dataset. Standard Scaler provides standard data by eliminating the mean and scaling to unit variance (Towfek El-Kenawy 2019).

3.14.5 Architecture of DPPM

Deep learning has increasingly acquired popularity as a consequence of its capacity to scale to big data, perform feature engineering from beginning to end, and provide accuracy in learning supervised and unsupervised data (Dargazany, Stegagno, and Mankodiya 2018). Deep learning is a subset of machine learning that is based on artificial neural networks. Learning is possible in a supervised, semi-supervised, or unsupervised environment (Bagherzadeh and Asil 2019). The DPPM consists of 13 layers as follows:

- ***Convolutional neural network (CNN)*** (6) layers.
- ***Max Pooling*** (5) layers.
- ***Flatten*** (1) layer
- ***Dense*** (1) layer.

Table (3.12) explains these layers in some detail.

Table 3.12 : Proposed Model Layers

NO.	Layer Type	Filters	Size/Stride	Activation
1	Convolutional	16	3/1	ReLU
2	Max Pooling	–	1/1	–
3	Convolutional	32	3/1	ReLU
4	Max Pooling	–	1/1	–
5	Convolutional	64	3/1	ReLU
6	Max Pooling	–	1/1	–
7	Convolutional	128	3/1	ReLU
8	Max Pooling	–	1/1	–
9	Convolutional	265	3/1	ReLU
10	Convolutional	512	3/1	ReLU
11	Max Pooling	–	1/1	–
12	Flatten	–	–	–
13	Dense	–	–	Softmax

To modify the data (reducing the error rate and adjusting the weights) from the associated errors, the Adam optimizer was used. Recently, the Adam optimization algorithm—an adaptation of the Stochastic Gradient Descent algorithm—has seen widespread use in deep learning applications, particularly in computer vision and natural language processing.

The learning rate used in the model was (0.001) and the learning rate affects the convergence of the improvement process as it balances the effect of the curvature of the cost function. When the learning rate is very small then the update will be small and the optimization is slow especially when the cost curve is low and the update is likely to settle at the local minimum. And when the learning rate is very large then the upgrading will be large and the improvement varies especially when the curvature of the cost function is high. If the learning rate is chosen well, the updates will be appropriate and the optimization will converge to a good set of parameters.

The activation function of deep neural networks has a significant influence on the training procedure's performance (Hayou, Doucet, and Rousseau 2019). The kernel allows natural methods to manage learning capacity and reduce overfitting (Mairal 2016). The kernel size and number of filters have a substantial influence on network accuracy (Agrawal and Mittal 2020). When a large amount of information and a more complicated kernel are employed, the strides influence how a convolution process works with a kernel (Mureşan and Oltean 2018).

The validity of the model is evaluated by the value of the loss functions which play an important role in statistical models. Loss functions specify a target by which the performance of the model is evaluated and the parameters used by the model are determined by reducing the chosen loss function. The loss function denotes the degree of disagreement between the model's predicted and true values (Y. Zhong and Zhao 2020).

3.14.6 Evaluation Metrics

The system has been evaluated using two metrics. These metrics are explained in this section as follows:

3.14.6.1 Matching Rate

It is defined as the probability that any value in that class has been properly predicted. Equation (3.16) yields the following result:

$$Matching\ Rate = \frac{Number\ of\ tests\ is\ correct}{Total\ number\ of\ tests} \tag{3.16}$$

3.14.6.2 Loss Function

This value is computed as shown in Equation (3.17) as follows:

$$Loss = \frac{Number\ of\ tests\ is\ wrong}{Total\ number\ of\ tests} \tag{3.17}$$

3.15 Summary

The following details are summarized for the methodology of developing the Gaussian Plume model in QGIS using the Python language and the design of a deep learning model for the management of pollutants caused by the Kirkuk cement plant:

- The land cover of the study area was classified using the Maxim Likelihood method, in addition different interpolation techniques were used to generate maps of temperature, specific humidity and wind speed for their importance in the Gaussian model.
- A Gaussian Plume Model was developed in Python to create a plugin in QGIS for one variable (x), which indicates the horizontal distance from the point source of the Kirkuk cement plant (chimney hole) to any point in the

plant's surrounding areas, in order to assess the pollutant risk on the land cover.

- The real wind direction was derived for four days (one day for each season in 2020) to determine the true their path of the plume instead of the Gaussian model's assumed straight direction and thus the risk of pollutants on the land cover.
- Another plugin for Gaussian Plume Model was developed through Python in QGIS for three variables x, y (the perpendicular dimension on x at any distance from source point), and z (the vertical coordinates which substituted in different heights).
- Another plugin was developed to represent the Gaussian model with the influence of two climate parameters, specifically temperature and specific humidity, in order to correct the pollutant concentrations produced by the Gaussian model.
- A highly efficient deep learning model was designed to predict the risk of pollutants emitted from the Kirkuk Cement Plant to be presented to the decision-making authorities to reduce the risk resulting from the emitted pollutants.

CHAPTER 4

RESULTS AND DISCUSSIONS

4.1 Classification Results

In this study, pixel-based classification was used to create land cover maps for the study area in 2020 by applying two supervised classification algorithms, Maximum Likelihood (MLC) and Support Vector Machine (SVM), and choosing the proper result. Whereas the Maximum Likelihood method was more efficient in classifying land cover, the Support Vector Machine method was inefficient in classifying land cover because it had many mix-classifications, particularly between urban and some types of barren lands. To obtain more reliable results from classification algorithm suitability analysis, it is critical to choose a well-distributed and sufficient number of training samples for each class. As a result, training samples were collected for each class while considering the study area's well distribution. The study used the Maximum Likelihood Classification method in this research because the nature of study area is non homogeneous and Maximum Likelihood is very suitable for this type of area.

4.1.1 Maximum Likelihood

Figure 4.1 states the land cover classes that are produced from the classification process. The majority class is the barren land that accounts for approximately 75.75% of the study region with 2435.3253 km^2. The water class, on the other hand, has the lowest area about 150.2145 km^2, with rivers and lakes accounting for 4.67 % of the study area. Vegetation accounted for about 13.35 % of the whole area, covering about

429.2145 km^2. Finally, the same graph depicts the urban class, which accounts for 6.22 % of the sample area and covers 199.99 km^2.

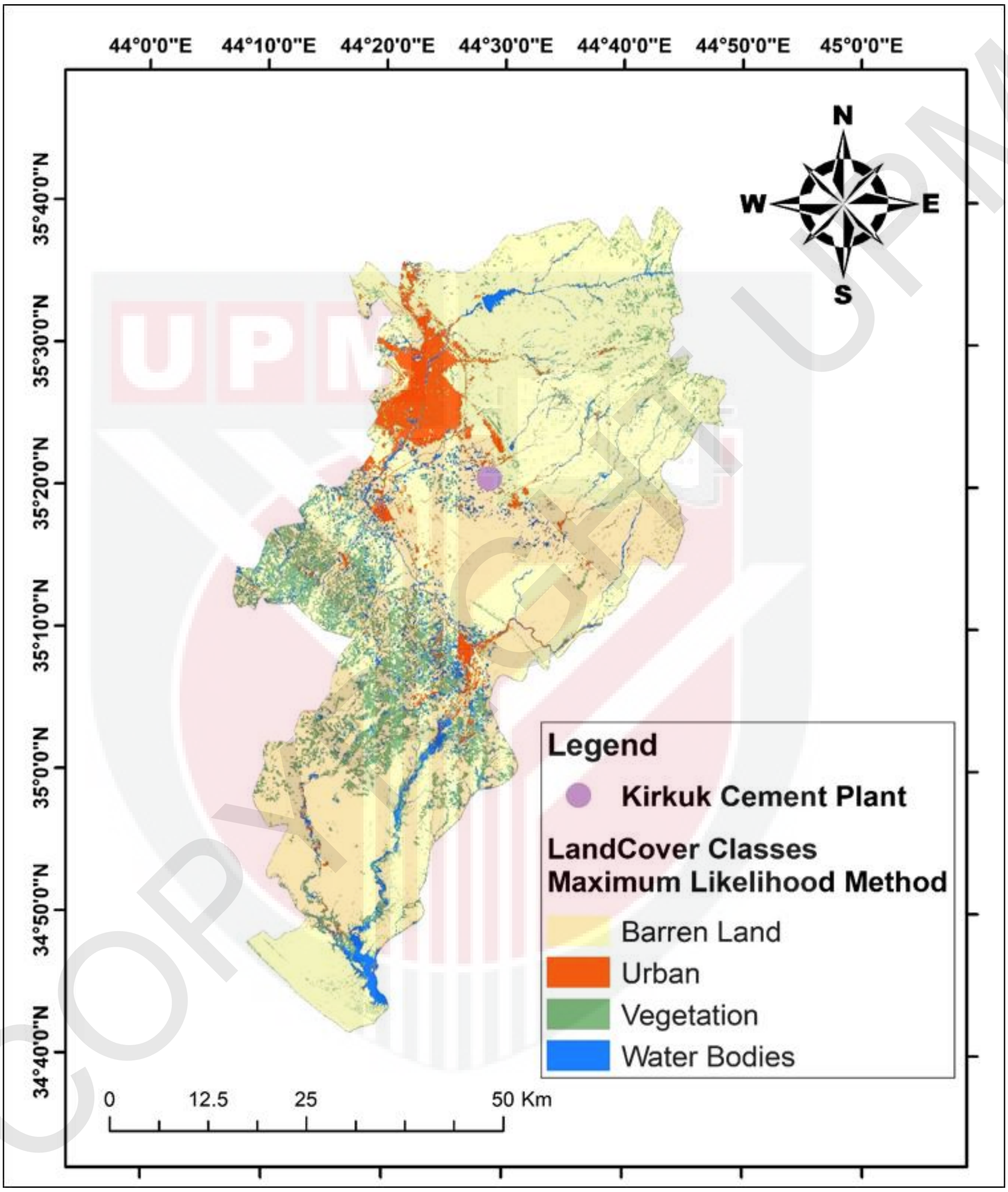

Figure 4.1 : Land Cover Classes (Maximum Likelihood Classification Algorithm)

4.1.2 Support Vector Machine

Figure 4.2 depicts the land cover classes that are created from SVM classification method. The majority class is barren land, which covers approximately 75.75% of the study area (2435.1939 km^2). The water class, on the other hand, has the smallest area, covering approximately 149.6484 km^2, with rivers and lakes accounting for 4.66% of the studied area. The vegetation covered around 419.0409 km^2 and accounted for approximately 13.03% of the total area. Finally, the urban class is depicted on the same graph, accounting for 6.56% of the sample area and covering 210.8646 km^2.

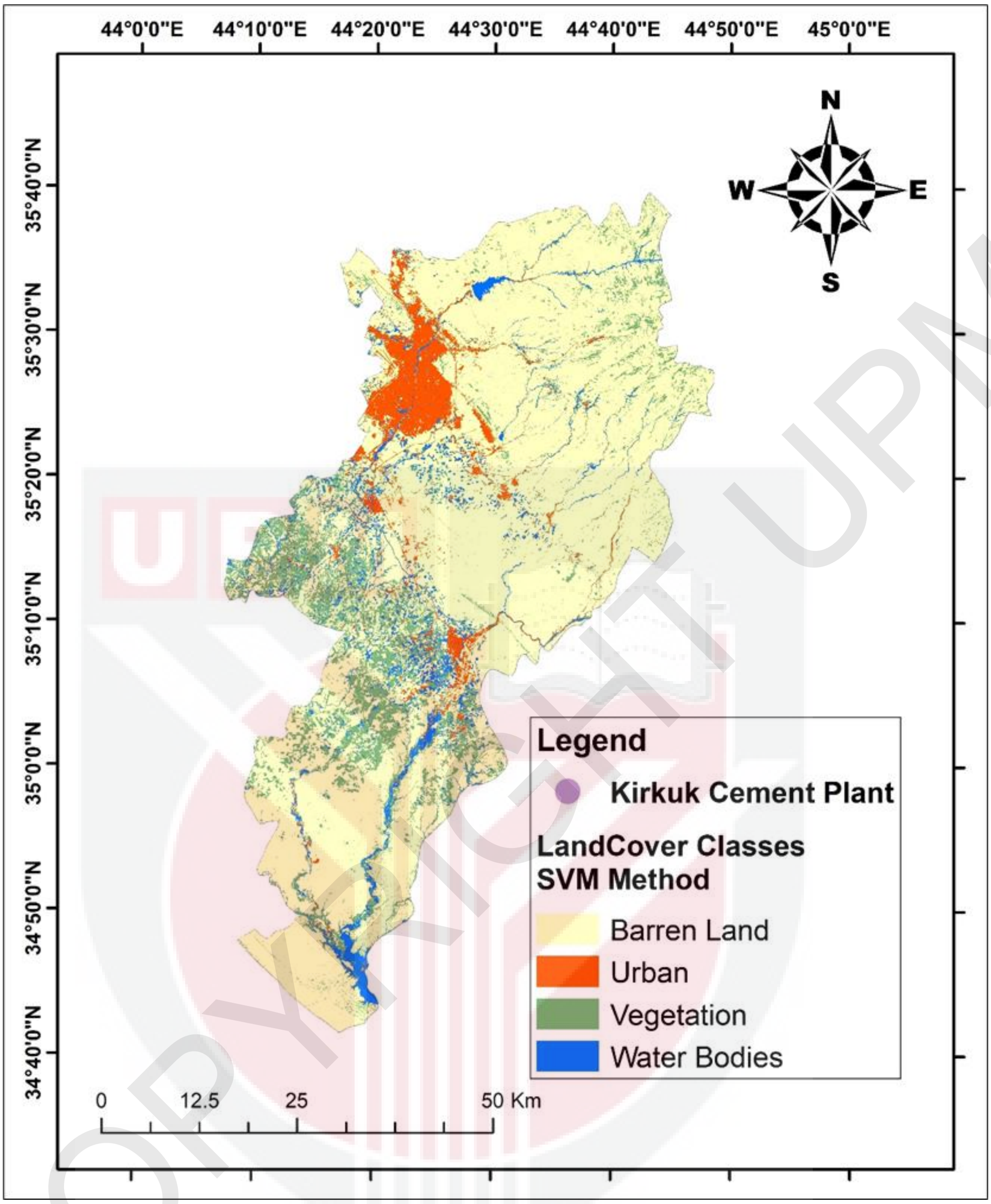

Figure 4.2 : Land Cover Classes (Support Vector Machine Classification Algorithm)

4.1.3 Accuracy Assessment

The Landsat images 2020 were classified using the mentioned techniques. There were four classes identified: barren land, urban, vegetation, and water bodies. The confusion matrix was used to compute the overall accuracy, kappa coefficient, and producer and user accuracies after applying the two classification algorithms to each picture. The confusion matrix method is frequently used to evaluate land-cover classification findings. The confusion matrices were created by manually comparing predicted classes to ground truths (Ren et al. 2019). The confusion matrix was used in this study to evaluate the outcomes of the classification approach applied to Landsat-8 OLI data. Table 4.1 shows the results of the overall accuracy assessment and the Kappa coefficient.

Many studies in the literature have indicated that the best classification model depends on the nature of the study area and the dataset characteristics (Mondal et al. 2012, Chowdhury 2024). Generally, simpler models such as MLC performs better in areas with mixed land use and overlapping pixels unless the more complex models such as SVM is carefully fine-tunned (Chepkochei 2014). The results of the current study showed that the MLC perfomed better than the SVM.

Table 4.1 : The Overall Accuracy and Kappa Coefficient of the Classification Method on Satellite Image 2020

Classes	MLC		SVM	
	Produce's accuracy percent	User's accuracy percent	Produce's accuracy percent	User's accuracy percent
Urban	99.24	100.00	98.48	100.00
Vegetation	100.00	95.65	100.00	100.00
Barren land	100.00	97.66	100.00	72.25
Water bodies	85.71	96.77	82.86	96.67
Overall accuracy	98.2143%		84.5238%	
Kappa coefficient	0.9736		0.7604	

4.2 Wind Speed Maps Results

Thh study used 10 monitoring stations to create the wind speed raster maps using interpolation methods. Due to the lack of monitoring stations, it is required to test several interpolation methods. This study evaluated three different methods including Spline, IDW, and Kriging. It was not sufficient to divide the stations into development and testing stations for statistical validation and evealuation of the interpolation methods. As a result, the evaluation was based on qualitative assessment. The results indicated that the Spline is more effective due to its smoothness.

4.2.1 Spline Interpolation Outcomes

Figure 4.3 indicates the wind speed distribution maps by Spline interpolation method for the four seasons of 2020 of the study area including Laylan City and other cities around it. The wind speed distribution map for the summer and spring seasons is almost similar, as the wind speed increases as it heads to the south of the study area. However, in summer the wind speed is greater than in spring, as it starts from 3.74 to 3.91(m/s) and ends from 4.23 to 4.35 (m/s), with five classes. Whereas in the spring the wind speed for the region starts from 3.28 to 3.4 (m/s) and ends from 3.6 to 3. 69 (m/s) with five classes as well.

On the other hand, the wind speed distribution in winter and autumn is somewhat similar, with a slight increase in the autumn season compared to winter. Where the highest wind speed is in the center of the study area, and it decreases whenever we head toward the external boundaries. As the wind speed starts in the winter from 3.07 to 3. 15 (m/s) and ends from 3.26 to 3.29 (m/s) in the fifth class. Whereas in the fall, it starts from 3.21 to 3.29 (m/s) and ends from 3.41to 3.44 (m/s) with five varieties as well.

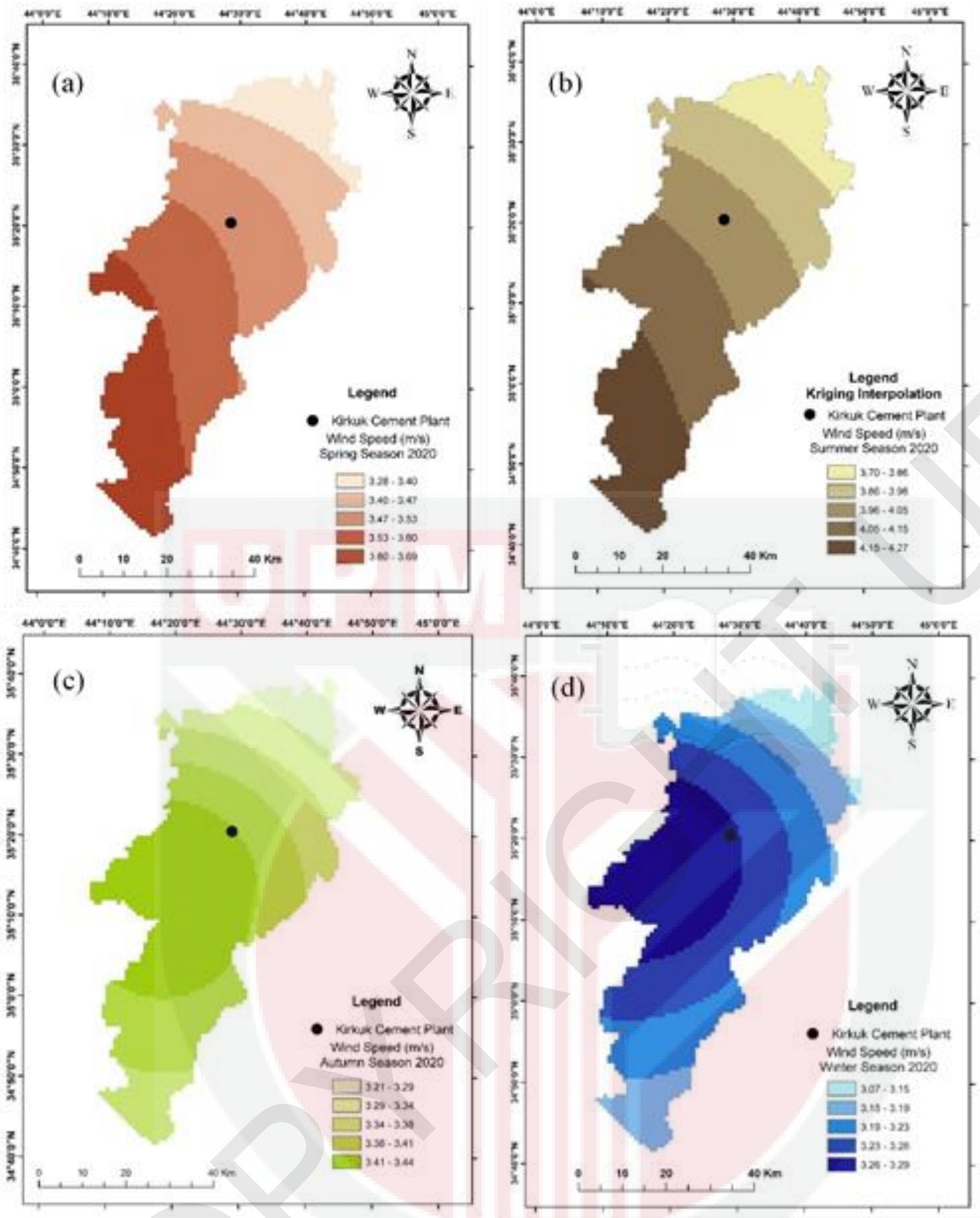

Figure 4.3 : Wind Speed Distribution Maps (Spline Interpolation) for Four Seasons of 2020 of the Whole Study Area. (a) Spring, (b) Summer, (c) Autumn, and (d) Winter Season

4.2.2 Inverse Distance Weighted Outcomes

Figure 4.4 depicts wind speed distribution maps using the IDW interpolation method for the four seasons of 2020 in the research region, which includes Laylan City and other nearby cities. The geographical distribution of wind speed in the spring season is represented by five classes, with the maximum value distributed in the extreme south of research area, with values ranging from 3.48 to 3.51 m/s. The lowest wind speed value of spring season is dispersed in a very limited region at the north-east of the study area, with values ranging from 3.34 to 3.40 m/s. The other classes are distributed as follow: the second class with values from 3.4 to 3.43 m/s is extended from north to northeast, adjacent to the first class, and a small part of it is distributed in the west of the study area, the third class is concentrated in the center of the study area and extends to parts of the north and east and takes the largest area of the study area and its value ranges from 3.43 to 3.45 m/s, and the last class is the fourth class which is distributed at the middle south and northeast of the study area near the cement factory, and its value ranges from 3.45 to 3.48 m/s. The spatial distribution of wind speed in the summer, which consists also of five classes, is that the high wind speeds are distributed in the south of the study area and gradually begin to decline towards the north and north-east of the study area, as the highest values in the south range between 4.05 to 4.11 m/s, while the lowest values of wind speed are in the north and northeast of the study area, which ranges between 3.85 to 3.93 m/s. The rest classes are spread between the highest and lowest values of wind speed, specifically in the middle of the study area.

The geographical distribution of wind speed in autumn and winter is slightly similar. In the winter, the highest value ranges from 3.21 to 3.24 m/s, distributed in the northwest with a semi-circular area, and gradually begins to decline in a radial manner, moving away from the rest of the directions, until it reaches its lowest value, ranging from 3.08 to 3.12 m/s, in small parts in the north and northeast and other parts in Southwest. As for the rest of the categories, they are graded between the highest and lowest value of the wind speed, as it extends from north to east, south and southeast.

The geographical distribution of wind speed in the autumn season resembles that of the winter season in some aspects, with the exception that the highest value, which varies from 3.34 to 3.37 m/s, is distributed mostly in the northwest and to a smaller extent in the southwest. The regional distribution of the remaining wind speed classes is comparable to that of the winter season and has a lower value ranging from 3.22 to 3.27 m/s.

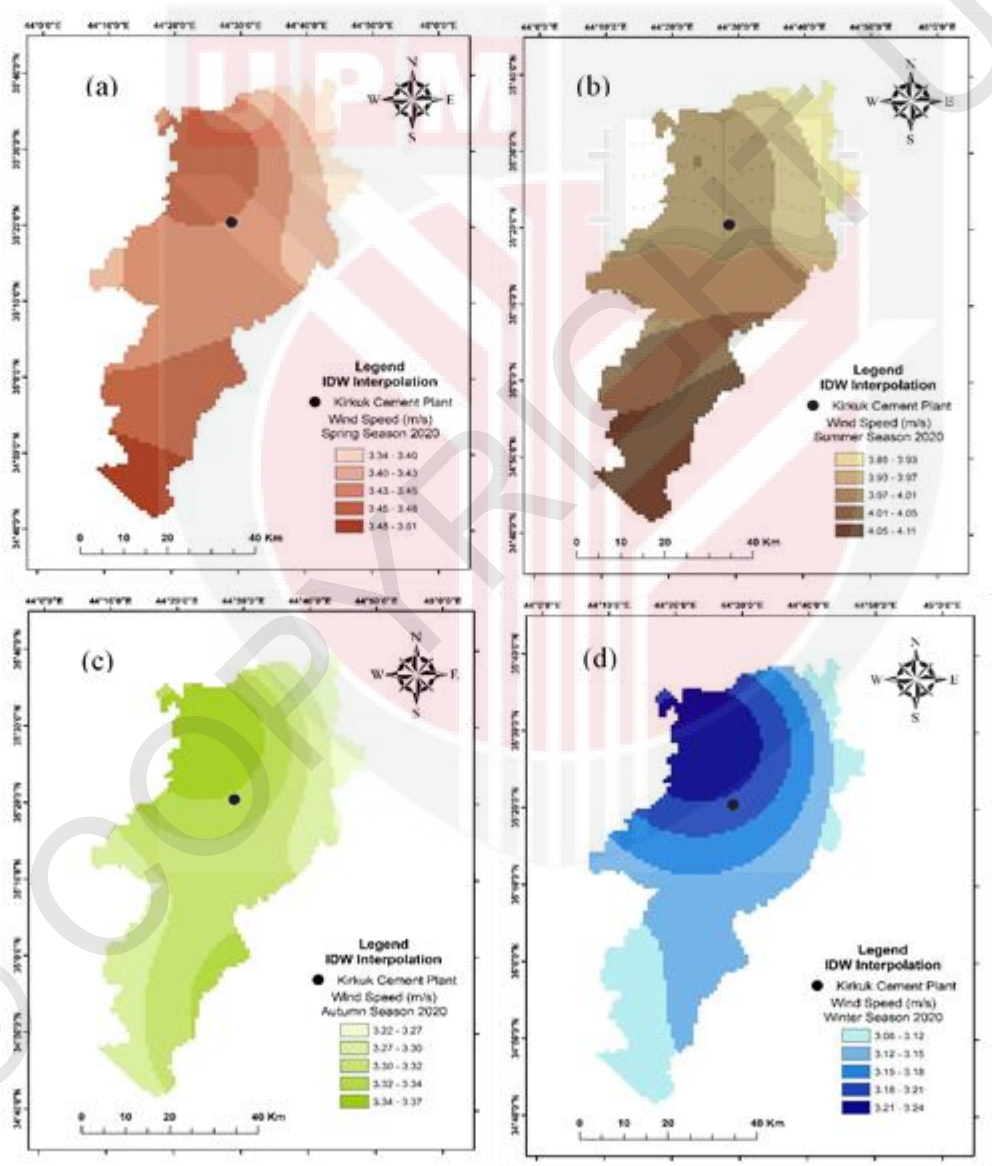

Figure 4.4 : Wind Speed Distribution Maps (IDW Interpolation) for Four Seasons of 2020 of the Whole Study Area. (a) Spring, (b) Summer, (c) Autumn, and (d) Winter Season

4.2.3 Kriging Outcome

Figure 4.5 illustrates wind speed distribution maps created using the Kriging interpolation method for the four seasons of 2020 in the study area, which includes Laylan City and other nearby cities. The geographical distribution of wind speed in the Kriging interpolation method is fairly similar, with all of the high values of wind speed dispersed in the south of the research region and the other classes gradually distributed towards the north as the speed decreases. In the spring season, the highest value of wind speed varies from 3.54 to 3.63 m/s, while the lowest value ranges from 3.24 to 3.25 m/s. The highest value of wind speed in the summer season ranges from 4.15 to 4.27 m/s, while the lowest value extends from 3.70 to 3.86 m/s. Wind speed records the highest value, ranging from 3.29 to 3.32 m/s, and the lowest value, ranging from 3.13 to 3.19 m/s, in the autumn season. Finally, the highest value of wind speed in winter season is between 3.10 and 3.12 m/s, while the lowest value is between 2.97 and 3.02 m/s.

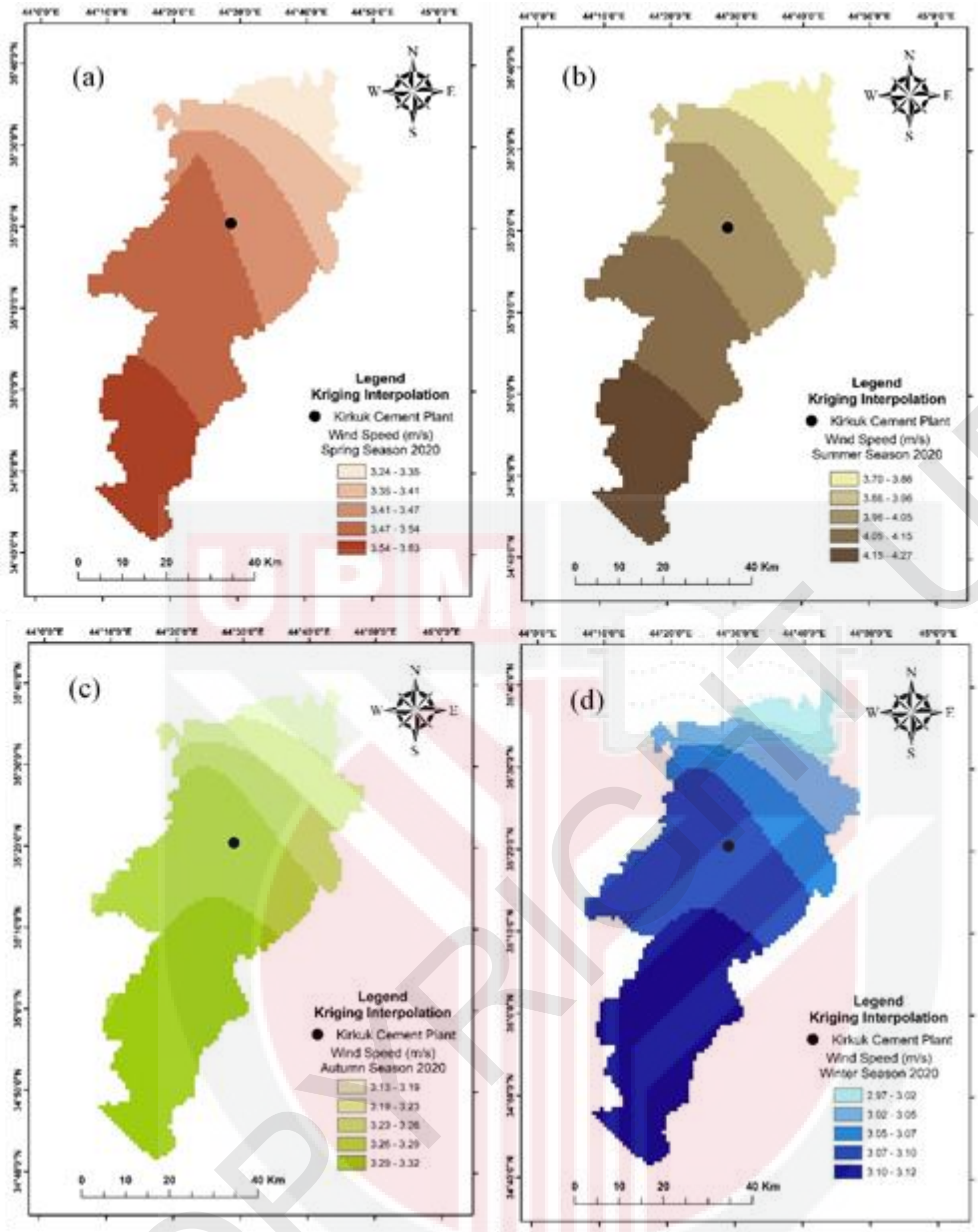

Figure 4.5 : Wind Speed Distribution Maps (Kriging Interpolation) for four Seasons of 2020 of the Whole Study Area. (a) Spring, (b) Summer, (c) Autumn, and (d) Winter Season

4.3 Gaussian Plume Outcomes

4.3.1 One Dimension Gaussian

The developed plugin, which was developed based on the Gaussian equation, was used to examine the concentration of pollutants from the Kirkuk cement plant. As indicated in Figures 4.6, 4.7, 4.8, and 4.9 the risk of pollutants during spring, summer, winter, and autumn in 2020 respectively. The plume of pollutant is spread and bounded according to the primary directions of north, east, south, and west, as well as secondary directions of northeast, southeast, southwest, and northwest.

Pollutant concentrations are classified into four risk levels. The summer and spring seasons are similar in the spatial distribution of pollutants due to the close wind speed values in these seasons while the winter and autumn are different. The pollution dispersion is calculated for 10 km around the cement plant. In the mentioned figures, the red color represents the highest concentration of pollutants (very high-risk pollution), with a value, ranging between 52.428 to 1264.332 µg/m^3 for spring, and from 43.899 to 1058.651 µg/m^3 in summer, 137.736 to 125.703 µg/m^3 for winter, and between 153.412 to 166.819 µg/m^3 for the autumn season. The yellow color symbolizes the high effect of pollutants (high-risk pollution) which is the second class, with a value of 27.727 to 52.428 µg/m^3 for spring and from 23.216 to 43.899 µg/m^3 in summer seasons, 0.035 to 137.736 µg/m^3 for winter, and ranged between 0.042 to 153.412 µg/m^3 for autumn. The third class is medium-risk pollution which indicates by green color, with a value ranging between 0.041 to 27.727 µg/m^3 for the spring season and 0.034 to 23.216 µg/m^3 in summer, for winter the medium-risk pollution is ranged between 0.017 to 0.035 µg/m^3 and ranged between 0,021 to 0,042 µg/m^3 for the autumn season. Whilst blue color shows the fourth class which is classified as the lowest risk of pollutants compared to the rest of the areas, with a value ranging between 0 to 0.041 µg/m^3 for spring and 0 to 0.034 µg/m^3 for summer seasons, between 0 to 0.017 µg/m^3 for the winter season, and ranged between 0 to 0.021 µg/m^3

for the autumn season. The classification is based on natural breaks classification included in GIS.

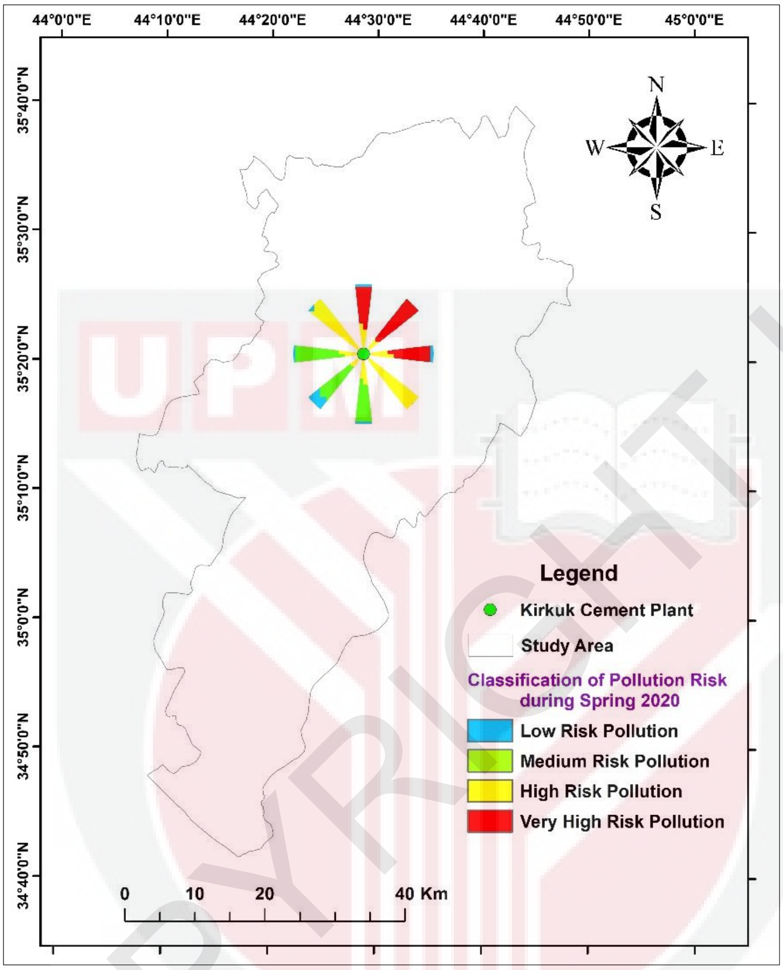

Figure 4.6 : Pollution Risk of Kirkuk Cement Plant during the Spring 2020

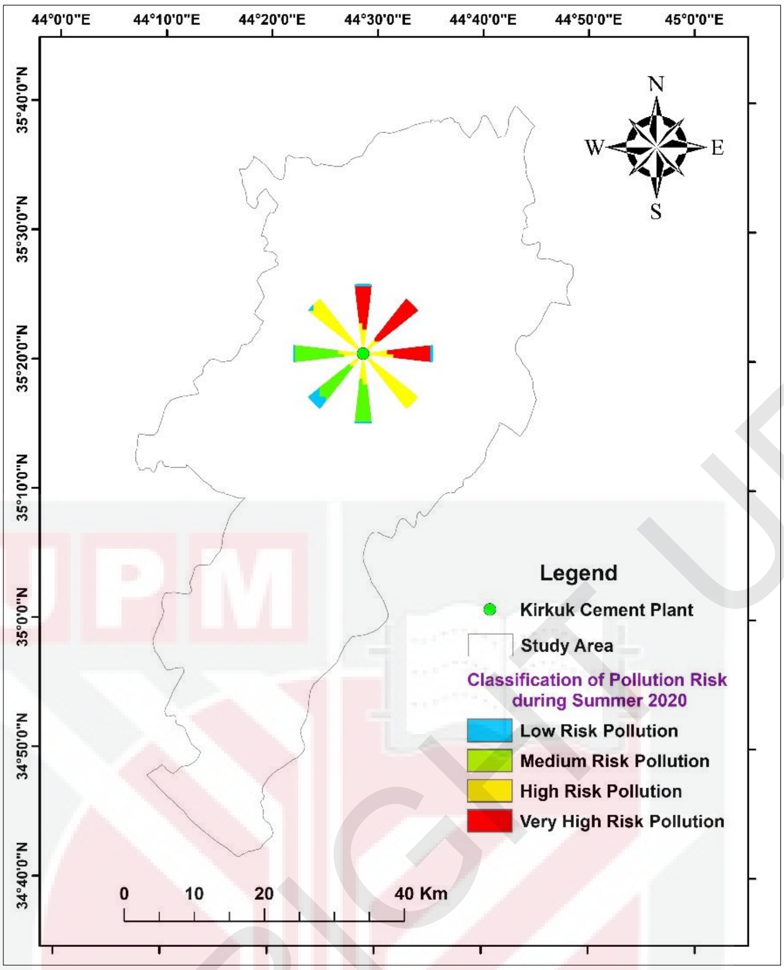

Figure 4.7 : Pollution Risk of Kirkuk Cement Plant during the Summer 2020

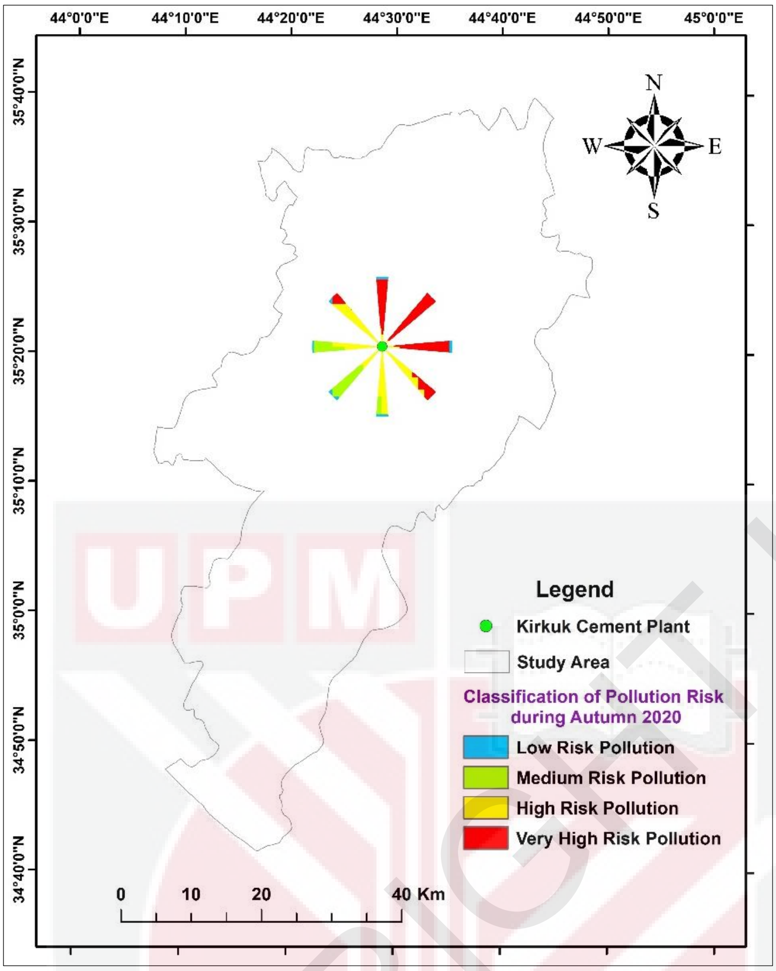

Figure 4.8 : Pollution Risk of Kirkuk Cement Plant during the Autumn 2020

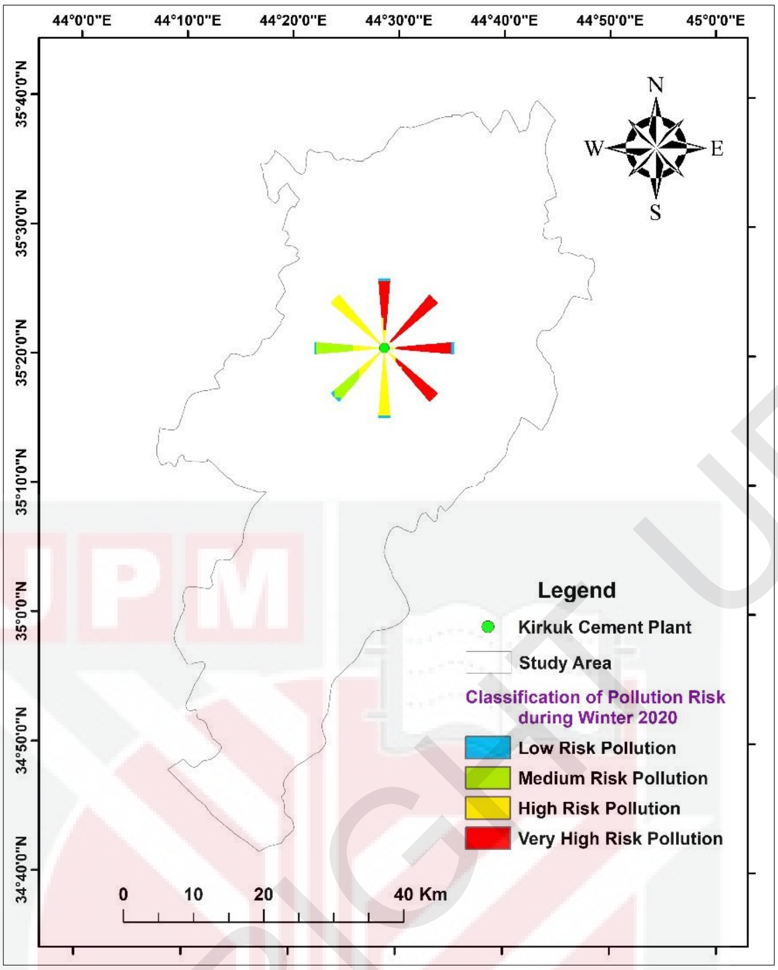

Figure 4.9 : Pollution Risk of Kirkuk Cement Plant during Winter 2020

4.4 AHP Outcomes

The weights that were calculated from the pairwise and normalize AHP are indicated in Table 4.2. Where the greatest importance was given to the direction that was exposed to the plume of emitted pollution in the most number of days in 2020.

Table 4.2 : Weights and Importance of Primary and Secondary Direction around Kirkuk Cement Plant

Direction	Importance	Weight
SW	1	0.326763962
S	2	0.227339521
W	3	0.156853872
SE	4	0.10766222
NW	5	0.073403637
N	6	0.049795778
NE	7	0.034015286
E	8	0.024165724

4.5 Risk Pollution Outcomes

Pollutants emitted from the Kirkuk Cement Plant have a hazardous impact on the metropolitan regions where the population lives, leading to respiratory diseases (Morshed et al. 2022). Pollution also harms agricultural regions, as it decreases the number of ants, yields, and damages plant leaves (Baciak et al. 2015). Plant pollution also threatens to exhaust the topsoil improvement and impair its suitability for agriculture, since there is a detrimental change in the qualities of the soil. Flying dust from the cement plant also pollutes surrounding water bodies, harming humans and animals that drink or utilize the water for various purposes. All of these dangerous substances are referred to as air pollution, which is one of the most serious issues facing humans as a result of the rise of industries and the inadequacy of some of them to achieve environmental safety requirements.

4.5.1 Risk Pollution of One Dimension Gaussian

Figures 4.10, 4.11, 4.12, and 4.13 depict the affected land cover areas in various directions around the plant, classified according to the number of exposures throughout the year 2020, as given in Table 3.4. Where weights were assigned with different percentages based on AHP, as indicated in Table 4.2. Three colors red, orange, and rose quartz represent the urban areas affected by the pollutants generated by the cement plant and are classified into high exposure, medium exposure, and not exposure respectively. The areas of urban regions exposed to the most pollution were 8.573 km^2 in the summer and 8.402 km^2 in the spring seasons, 7.889 km^2 in the fall, and 6.25 km^2 in the winter. The plantation regions impacted by pollution are shown in three colors: dark green, medium green, and light green, and are categorized as high exposure, medium exposure, and not exposure, respectively. The most polluted plantation areas were 5 km^2 in the summer and 4.761 km^2 in the spring seasons, 4.341 km^2 in the autumn, and 3.992 km^2 in the winter. The sand feature influenced by pollution is represented by three colors: olivenite, medium yellow, and light yellow, and is classed as high exposure, medium exposure, and not exposure. The most polluted sand areas were 60.974 km^2 in the summer and 48.88 km^2 spring seasons, 48.999 km^2 in the autumn, and 42.832 km^2 in the winter. The colors blue, medium blue, and sky blue indicate the polluted water bodies, which are categorized as high exposure, medium exposure, and not exposed, respectively. The most polluted regions of water bodies were 2.667 km^2 in the summer and 2.256 km^2 spring seasons, 1.849 km^2 in the autumn, and 1.126 km^2 in the winter.

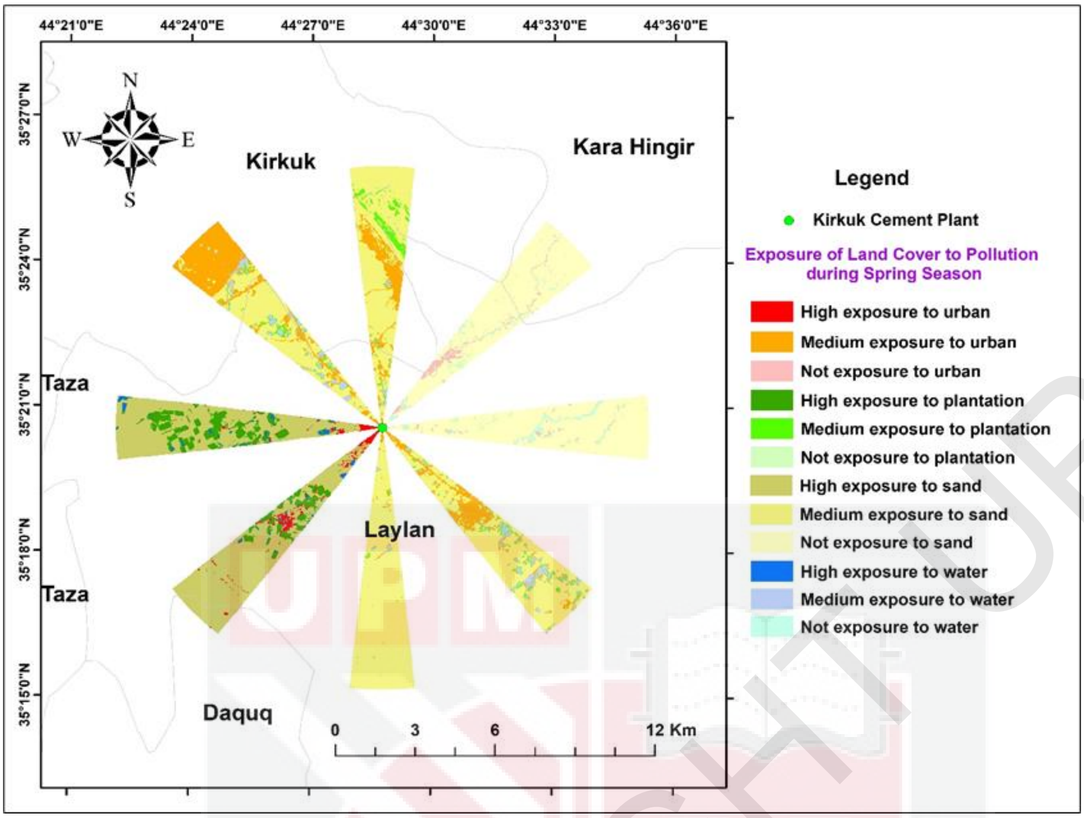

Figure 4.10 : Land Cover Exposed to Pollution during Spring 2020

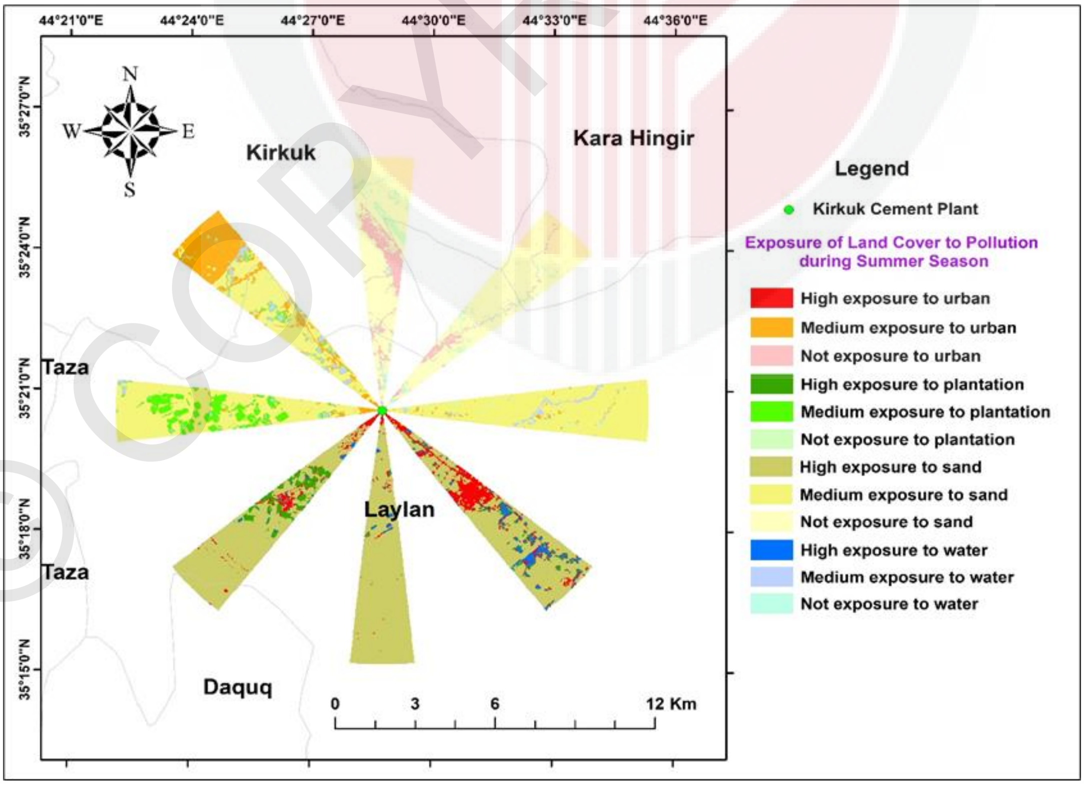

Figure 4.11 : Land Cover Exposed to Pollution during the Summer of 2020

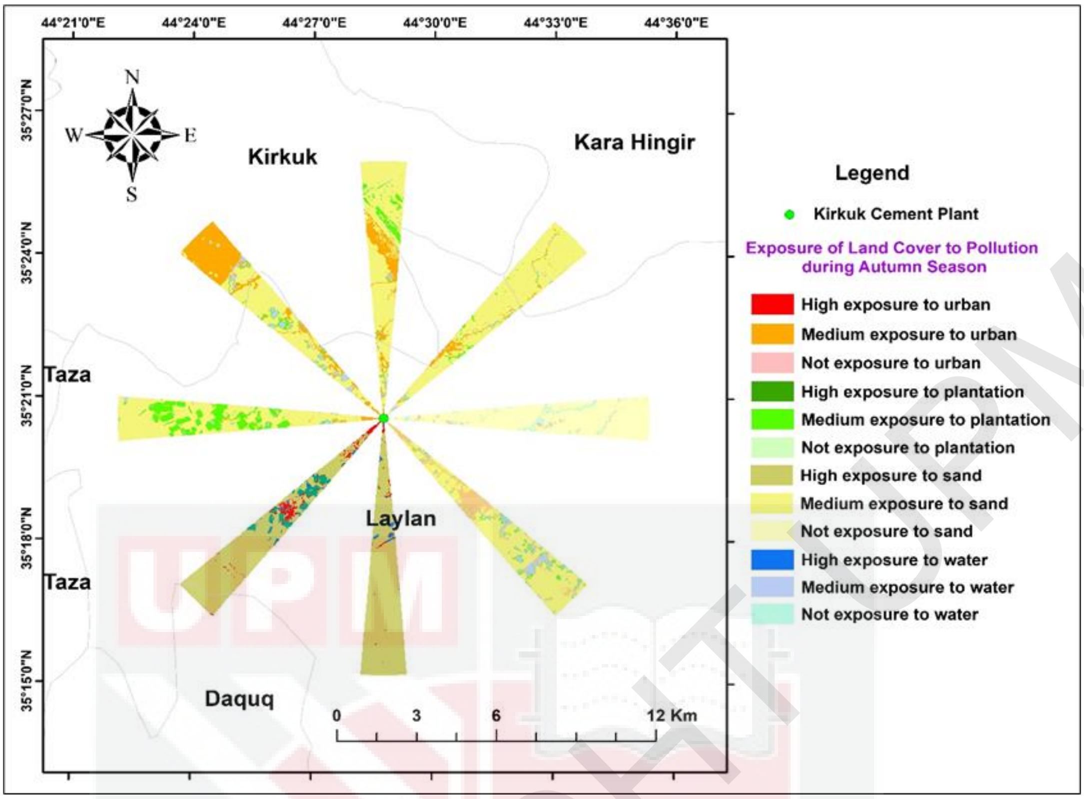

Figure 4.12 : Land Cover Exposed to Pollution during Autumn 2020

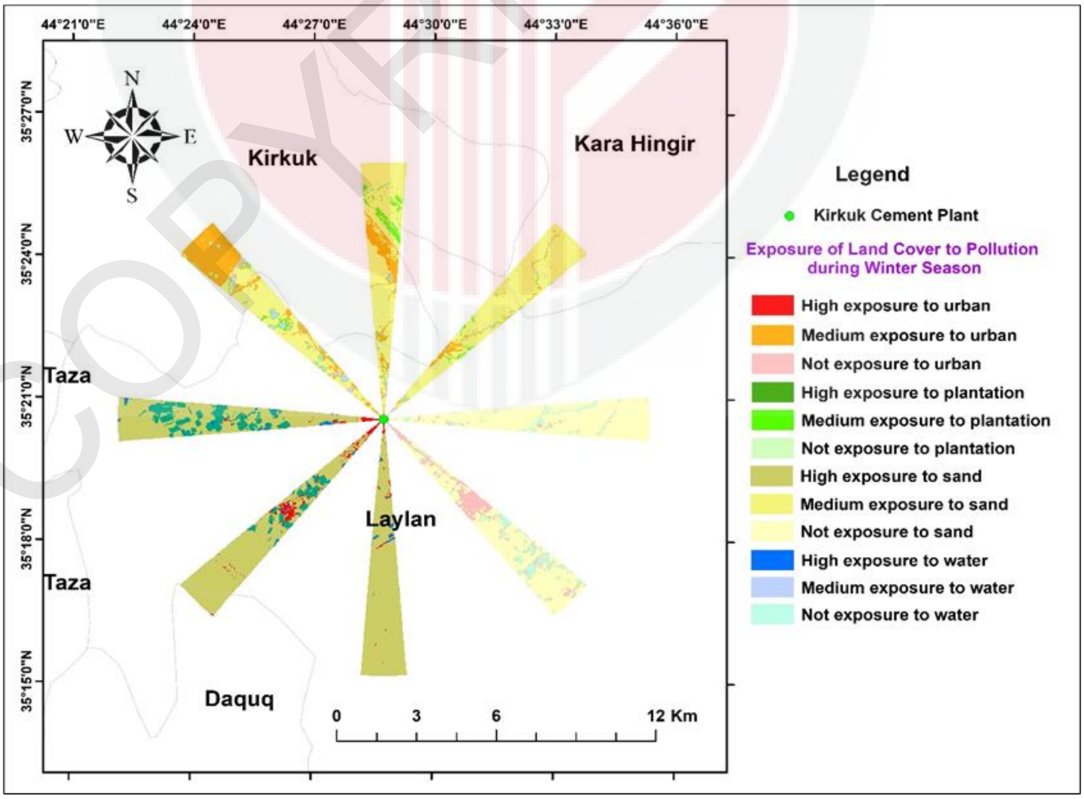

Figure 4.13 : Land Cover Exposed to Pollution during Winter 2020

4.6 Real Direction Of Gaussian Plume

The plume path of the pollutants emitted from the Kirkuk Cement Factory was identified for each season during 2020 from direction maps, and the results according to each season were as follows:

4.6.1 Spring Season

Figure 4.14 shows the wind direction in 1st April 2020 (spring season) for four period times and four interval distances from point source of pollution. At 6 a.m. and within interval distance (0 to 2500 m), the wind direction was (250˚). Then, at 9 a.m. within interval distance (2500 to 5000 m), the wind direction changed 25˚ to be (275˚). After that, the wind direction turned to (315˚) at 12 p.m. within interval distance of (5000 to 7500 m). Finally, the wind direction at 3 p.m. was (350˚) within the interval distance (7500 to 10000 m).

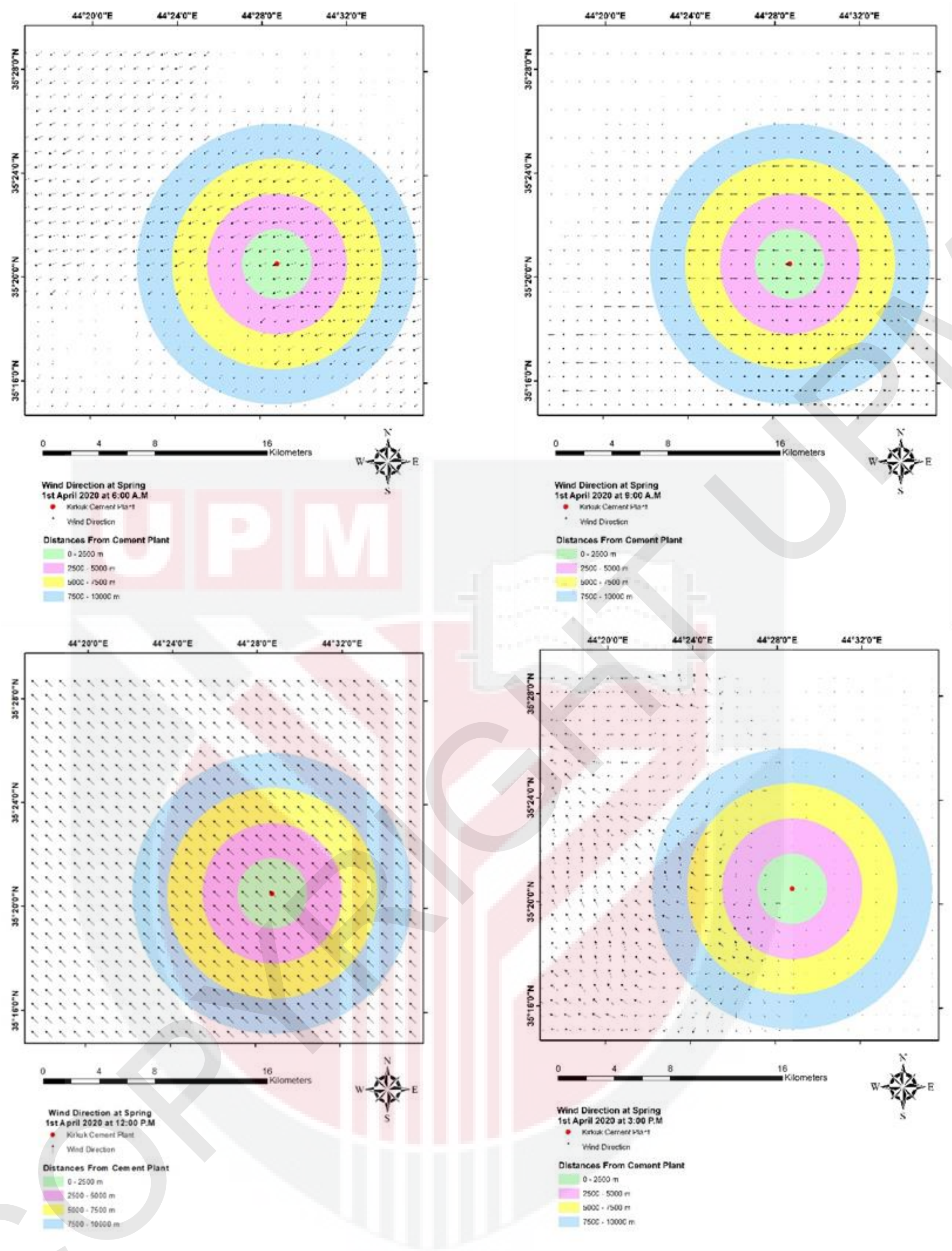

Figure 4.14 : Wind Direction for Four Time Periods on the First Day of April to Represent the Spring Season of 2020

Figure (4.15) depicts the degree of risk in each region in terms of exposure to pollutants emitted by the cement plant and actual the emissions during the spring season based on wind direction. Because of the extensive spread of pollutants, barren lands are the most affected, with a total covered area of 15.2298 km^2. With a total area of 2.6802 km^2, urban areas are likewise very vulnerable to pollution. Similarly, vegetation-covered regions have a vast area of pollution exposure with a total area of 2.7585 km^2. With a total area of 1.647 km^2, water areas are the smallest to be covered and are least polluted.

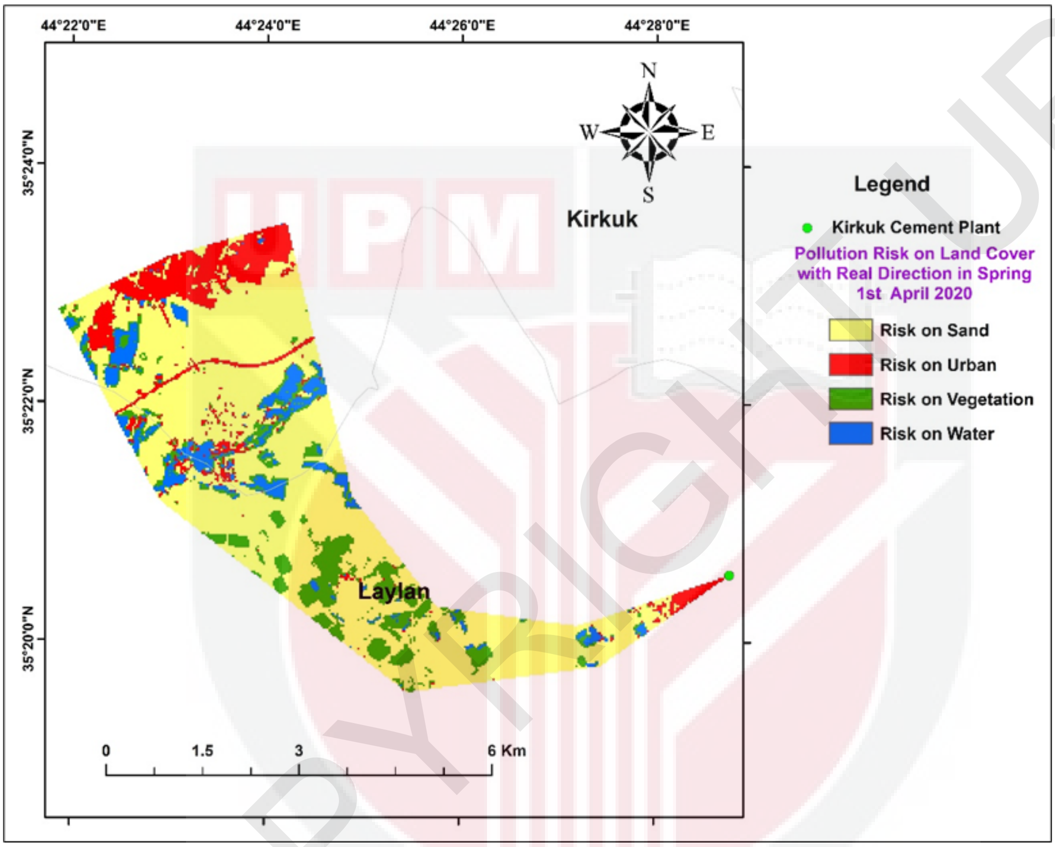

Figure 4.15 : Land Cover Exposed to Pollution during 1st April 2020 with Real Direction (Spring Season)

4.6.2 Summer Season

Figure 4.16 depicts the wind direction for four period times and four interval distances from a point source of pollution on 1st July, 2020 (summer season). The wind was blowing in a (255˚) direction at 6 a.m. and within an interval of 0 to 2500 m. The wind direction was then (45˚) at 9 a.m. at interval distance (2500 to 5000 m). Following that, the wind remained in the same direction which is (45˚) around 12 p.m. within an interval of (5000 to 7500 m). At 3 p.m., the wind was blowing in a direction of (10˚) within the interval range of 7500 to 10000 m.

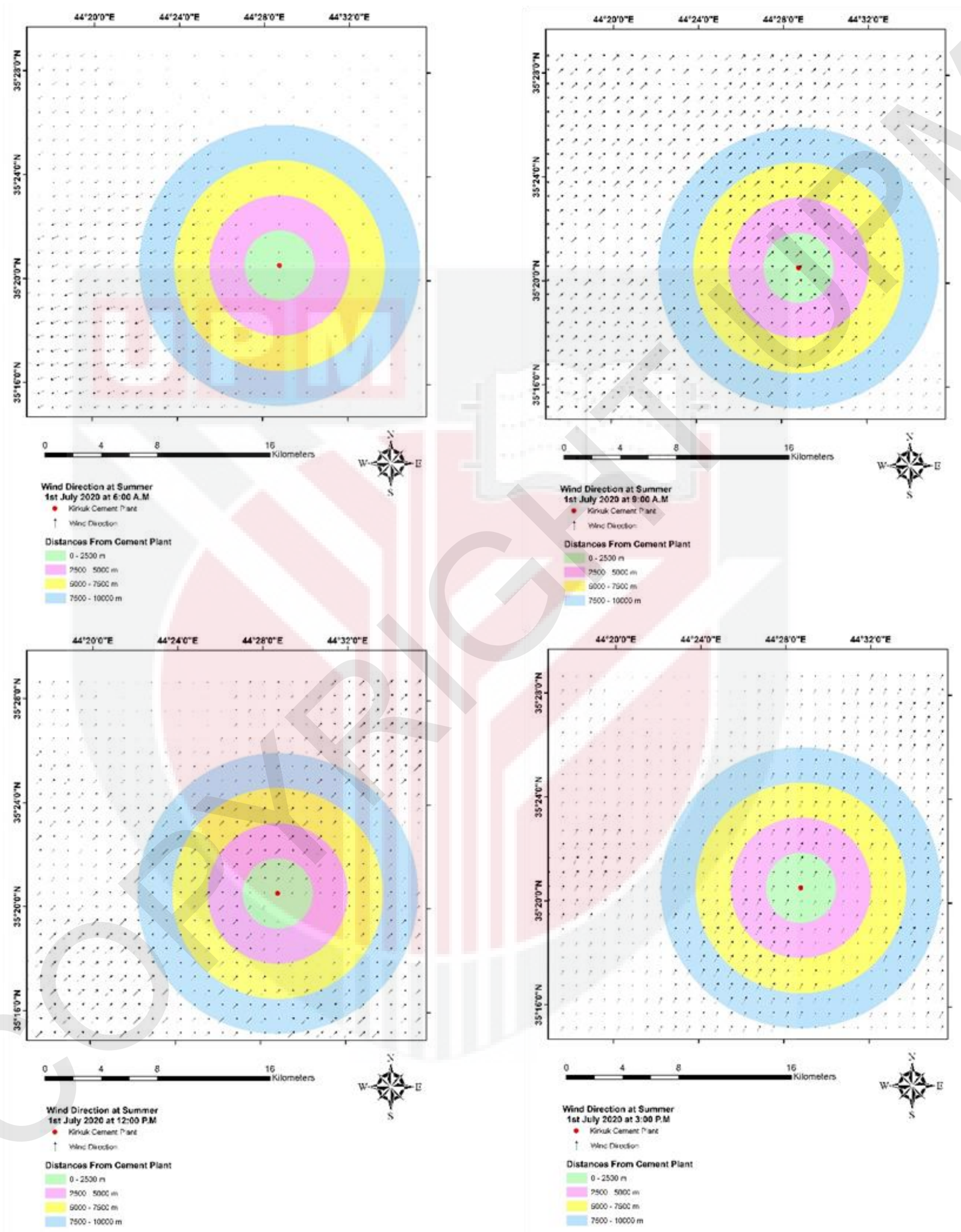

Figure 4.16 : Wind Direction for Four Time Periods on the First Day of April to Represent the Summer Season of 2020

Figure 4.17 illustrates the risk of pollutants emitted from the cement plant, the real direction of plume emission in the summer season. Where the area of barren lands exposed to the risk of pollutants is 10.8621 km^2, which is the most exposed area to pollutants. While the area of the urban areas is 0.6786 km^2, which is less exposed in the summer due to the direction of the winds. Green areas come in second place in terms of exposure to pollutants, with an area of 1.3023 km^2. As for the water areas, the area at risk of pollutants is 0.0647 km^2, and the least exposed area.

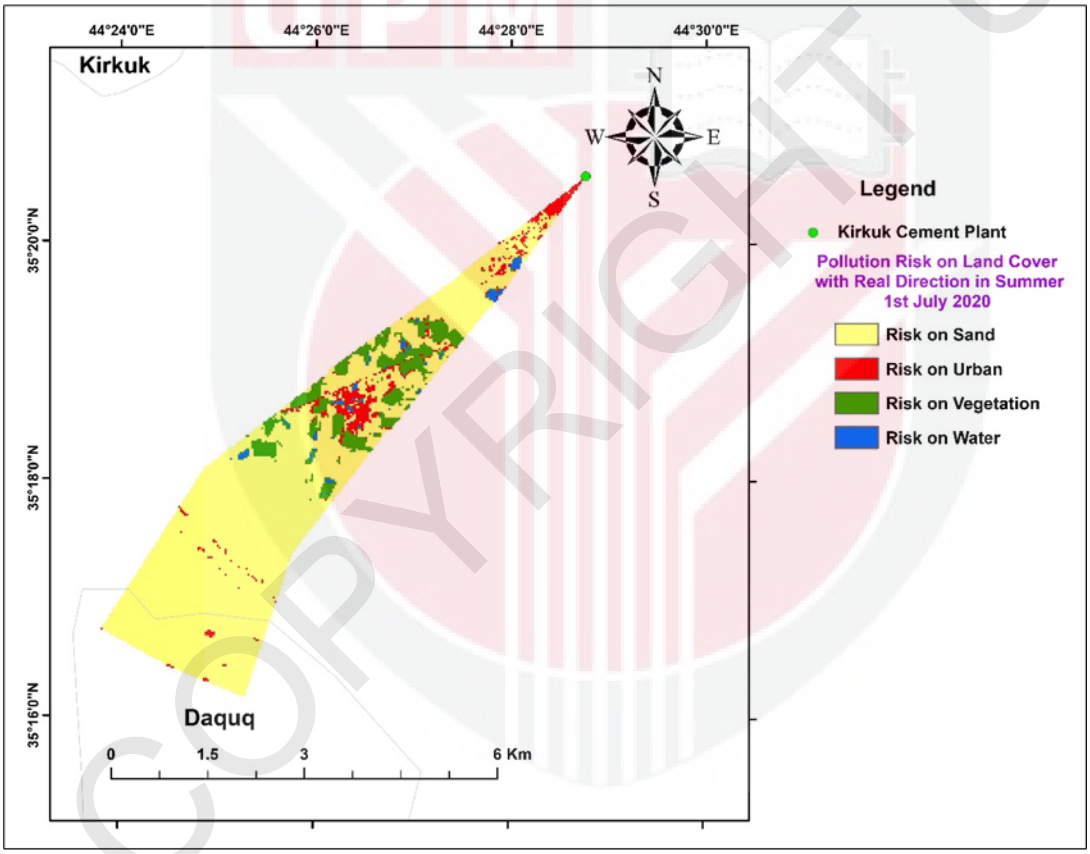

Figure 4.17 : Land Cover Exposed to Pollution during 1st July 2020 with Real Direction (Summer Season)

4.6.3 Autumn Season

Figure 4.18 displays the wind direction for four period times and four interval distances from a point source of pollution on 1st September, 2020 (autumn season).

The wind was blowing in a (245˚) direction at 6 a.m. and within an interval of 0 to 2500 m. The wind direction was then (275˚) at 9 a.m. at interval distance (2500 to 5000 m). Following that, the wind direction changed to (315˚) around 12 p.m. within an interval of (5000 to 7500 m). At 3 p.m., the wind was blowing in a direction of (70˚) within the interval range of 7500 to 10000 m.

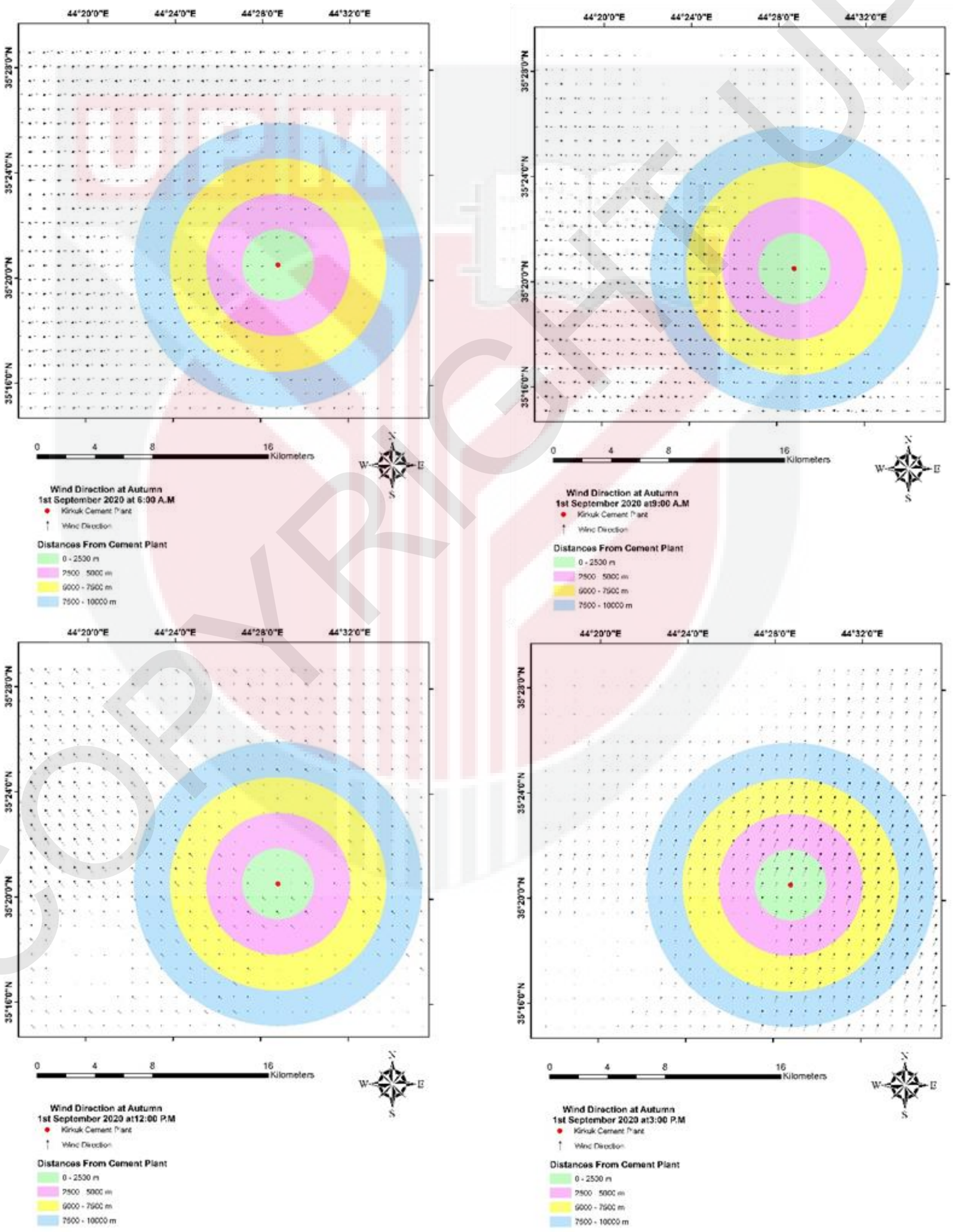

Figure 4.18 : Wind Direction for Four Time Periods on the First Day of September to Represent the Autumn Season of 2020

Figure (4.19) shows us the amount of the risk pollutants emitted from the cement factory, the real direction of plume emissions in the autumn season over the areas shown. Where the sand areas exposed to pollution from pollutants emitted from the source of pollution with an area of 7.0083 km^2. As for the urban areas exposed to pollution in the autumn season, it is the largest area due to the direction of the winds in the autumn season, as it occupies an area of 4.1841 km^2. As for the vegetation spaces, the area exposed to pollution is 1.3401 km^2. Likewise, the water areas that are exposed to pollution are few in the autumn season, with an area of 0.5877 km^2.

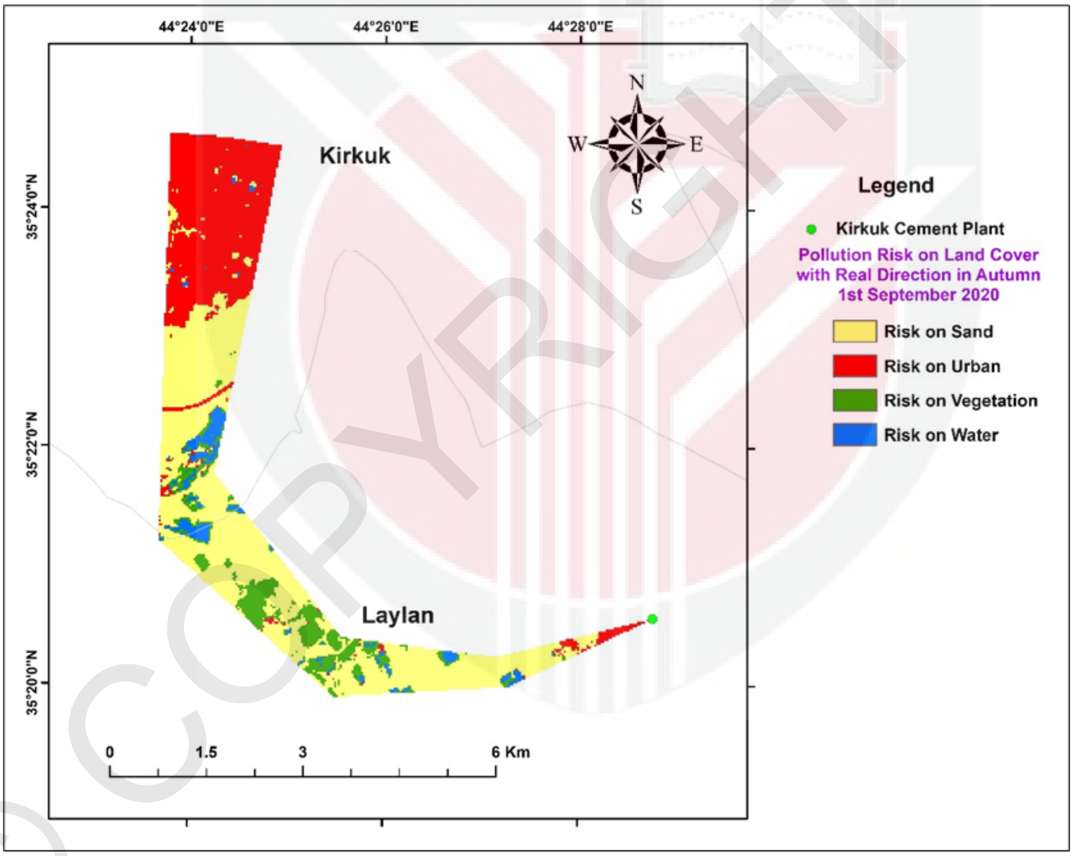

Figure 4.19 : Land Cover Exposed to Pollution during 1st September 2020 with Real Direction (Autumn Season)

4.6.4 Winter Season

Figure 4.20 illustrates the wind direction for four period times and four interval distances from a point source of pollution on 2nd January, 2020 (winter season). The wind was blowing in a (225˚) direction at 6 a.m. and within an interval of 0 to 2500 m. The wind direction was then (205˚) at 9 a.m. at interval distance (2500 to 5000 m). After that, the wind direction stilled in same direction to be (205˚) around 12 p.m. within an interval of (5000 to 7500 m). At 3 p.m., the wind was blowing in a direction of (170˚) within the interval range of 7500 to 10000 m.

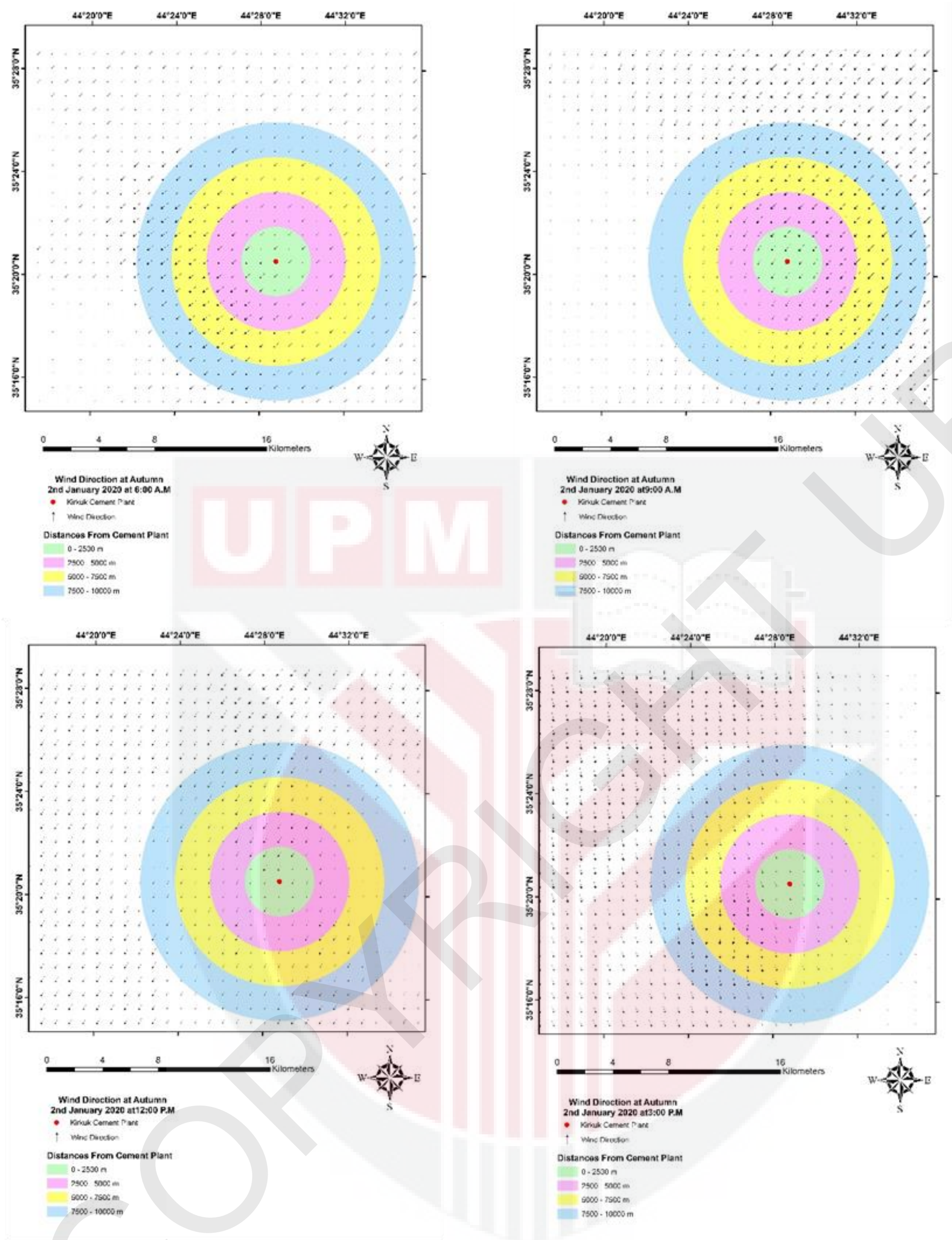

Figure 4.20 : Wind Direction for Four Time Periods on the Second Day of January to Represent the Autumn Season of 2020

Figure 4.21 indicates each region with its exposure to pollutants emitted in the winter from the cement plant, in the real direction of plume emission in the winter. The barren areas are more exposed to other areas with an area of 8.8722 km^2. The urban areas exposed to pollution have an area of 0.4923 km^2. As well as green areas, the amount of exposure to pollutants emitted from the cement factory is 0.7857 km^2. As for water areas, they are less exposed to pollutants, as the exposure area is 0.0711 km^2 in winter.

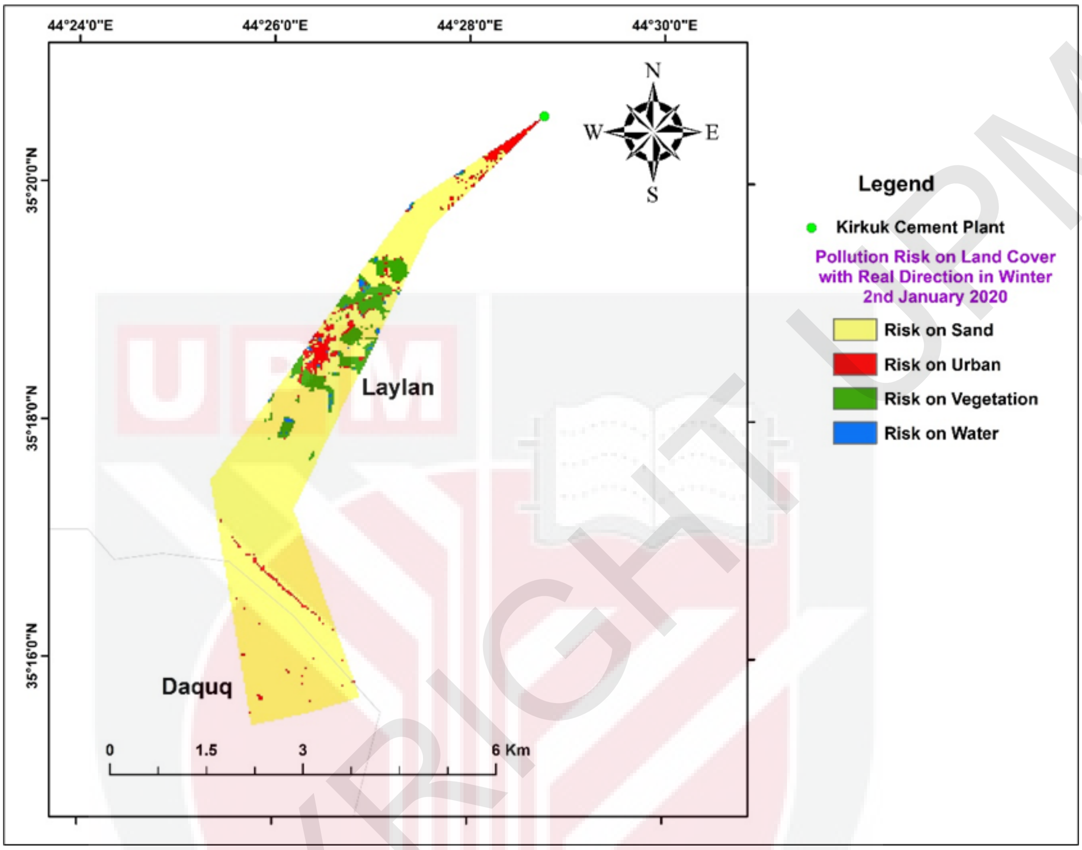

Figure 4.21 : Land Cover Exposed to Pollution during 2nd January 2020 with Real Direction (Winter Season)

Overall, the table shows the areas of items exposed to the risk of pollutants emitted from the Kirkuk cement factory in square kilometers for four seasons during 2020.

Table 4.3 : The Areas of Exposed Land Cover Features to Pollution 2020 with Different Seasons and Real Directions

Classes	Area in Km^2			
	Spring	Summer	Autumn	Winter
Sand	15.2298	10.8621	7.0083	8.8722
Urban	2.6802	0.6786	4.1841	0.4923
Vegetation	2.7585	1.3023	1.3401	0.7857
Water	1.647	0. 0647	0.5877	0.0711

4.6.5 3D Gaussian Plume Result

4.6.5.1 Digital Elevation Model DEM

Figure 4 represents the topography of the ground in the research area, with the level gradient ranging from 106m to 998m above sea level. The northern portions of the study area have very high values, indicated by the white color, and decreases gradually to the south and west of the study area, to the lowest value, represented by the light green color. The ground level of the Kirkuk Cement plant is 333 meters, and the surrounding lands rises gradually above 400 meters to the north and northeast of the plant, while it lowers to less than 300 meters to the south and west of the facility.

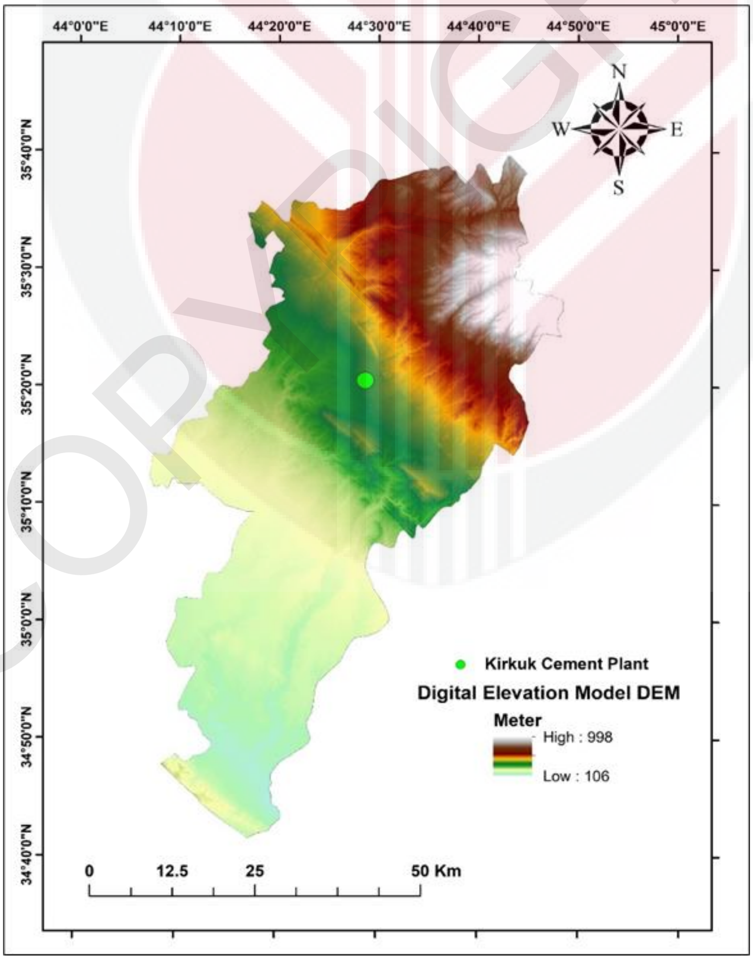

Figure 4.22 : Topographic Map of the Study Area Prepared Based on ASTER GDEM Data

4.7 Results of the 3D Gaussian Plume Model Simulation

The Gaussian plume model is used to predict the dispersion of pollutants from a point source (Kirkuk Cement Plant). The model assumes that the pollutant concentration can be described by a Gaussian distribution in the vertical and horizontal directions. The key parameters in the model are the effective plume height (*H*), the standard deviations of the plume in the vertical (*sigma_z*) and horizontal (*sigma_y*) directions, and the wind speed. Therefore, the pollutant concentration is highly dependent on the effective plume height (H) and the values of the standard deviations in the crosswind and vertical directions. These parameters are used to describe the shape and size of the pollutant plume, which in turn affect the rate of dispersion and dilution of pollutants in the atmosphere.

Figure 4.23 shows the maps of seasonal pollutant concentration within the study area. It can be seen that the pollutant concentration is highest near the source and gradually decreases as it is transported by the wind. The highest concentration is found within the first few hundred meters downwind from the source, after which it decreases more slowly. This is because the pollutant plume initially rises due to buoyancy effects before being dispersed by the wind. The pollutant concentrations are highest during autumn and winter and lowest during spring and summer. This is likely due to the meteorological conditions during each season, such as wind patterns and temperature inversions, which can affect the dispersion of pollutants in the air. At the source point, the pollutant concentration is zero for all seasons except for autumn, where it is non-zero but very low. At larger distances from the source, the pollutant concentrations gradually increase, with the highest concentrations being observed at 500-1000 meters. Beyond 1000 meters, the concentrations gradually decrease.

Table 4.4 indicates that the simulated pollutant concentration varies by season, with different minimum, maximum, mean, and standard deviation values for each season. The highest maximum values are observed in spring and summer, with concentrations as high as 177.82 and 168.28 μg/m^3, respectively. In contrast, the lowest maximum values are observed in autumn and winter, with concentrations of 108.19 and 113.10 μg/m^3, respectively. The lowest minimum values are observed in summer, with a concentration of 0.078 μg/m^3, while the highest minimum value is observed in autumn, with a concentration of 0.114 μg/m^3. The mean values for all seasons are relatively low, with the highest mean observed in winter at 0.73 and the lowest mean observed in summer at 0.35. The standard deviation values indicate the variability of the data. The highest standard deviation values are observed in spring and winter, with values of 3.20 and 5.85, respectively. In contrast, the lowest standard deviation values are observed in summer, with a value of 2.96. Overall, it appears that the simulated pollutant concentration varies significantly by season, with higher concentrations observed in spring and summer and lower concentrations observed in autumn and winter. It is important to note that these values are simulated and may not necessarily reflect actual pollutant concentrations in the environment.

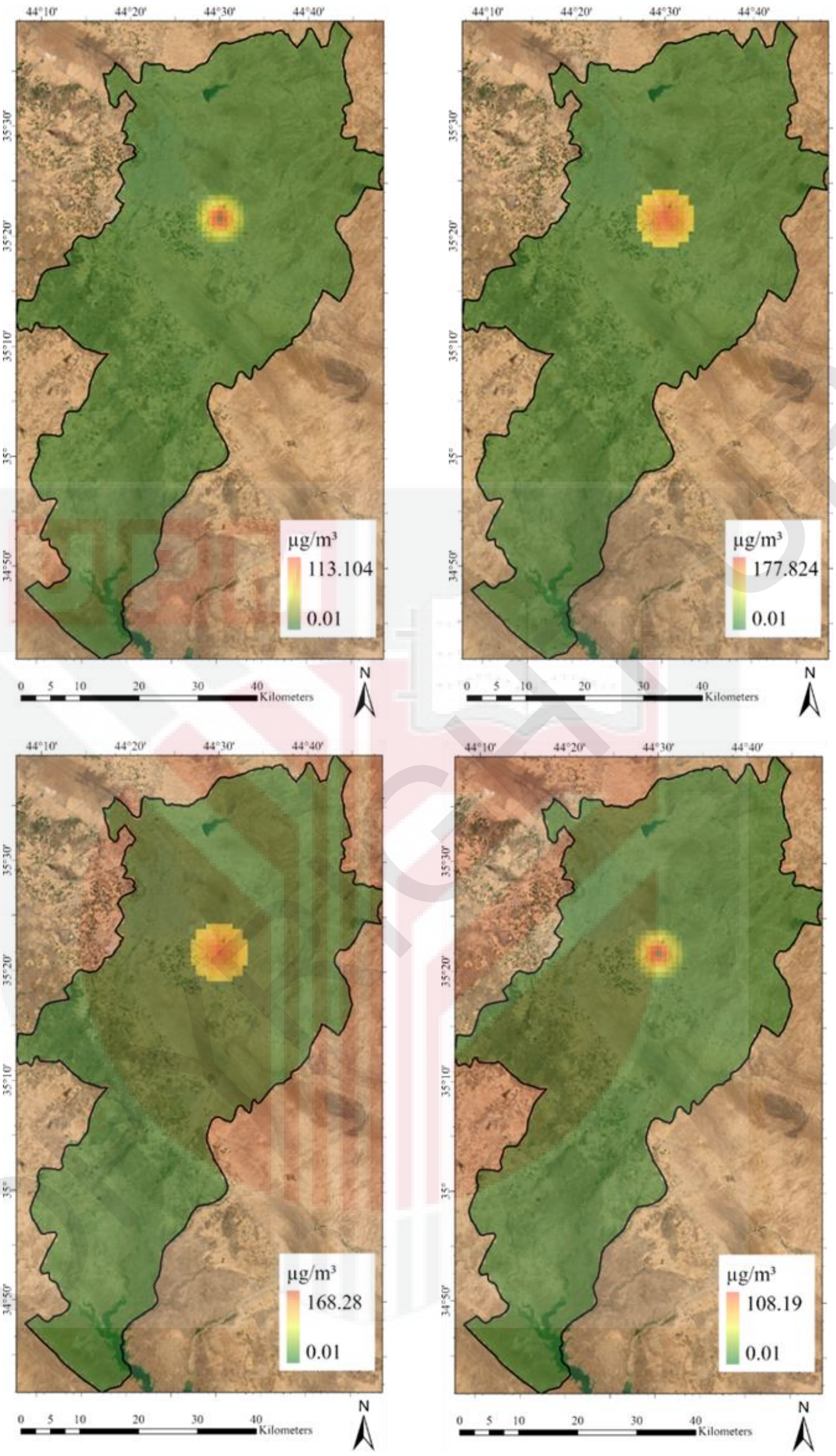

Figure 4.23 : Seasonal Dispersion Maps of Pollutants from the Kirkuk Cement Plant Using Gaussian Plume Model: Simulated Concentration Contours for Winter, Spring, Summer, and Autumn Seasons

Table 4.4 : Seasonal Simulated Pollutant Concentration: Minimum, Maximum, Mean, and Standard Deviation

Season	Minimum	Maximum	Mean	Standard Deviation
Winter	0.119	113.10	0.73	5.85
Spring	0.092	177.82	0.40	3.20
Summer	0.078	168.28	0.35	2.96
Autumn	0.114	108.19	0.70	5.60

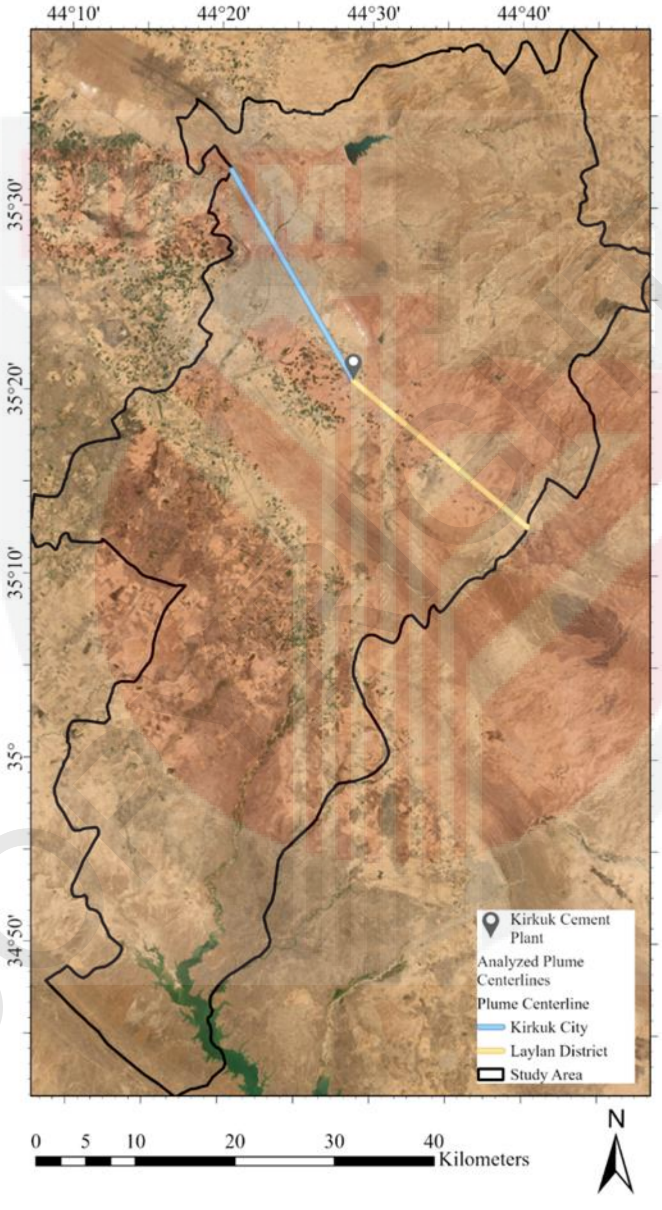

Figure 4.24 : Selected Paths for Studying Pollutant Concentration Profiles from the Kirkuk Cement Plant Using Gaussian Plume Model: Kirkuk City Line and Laylan District Line

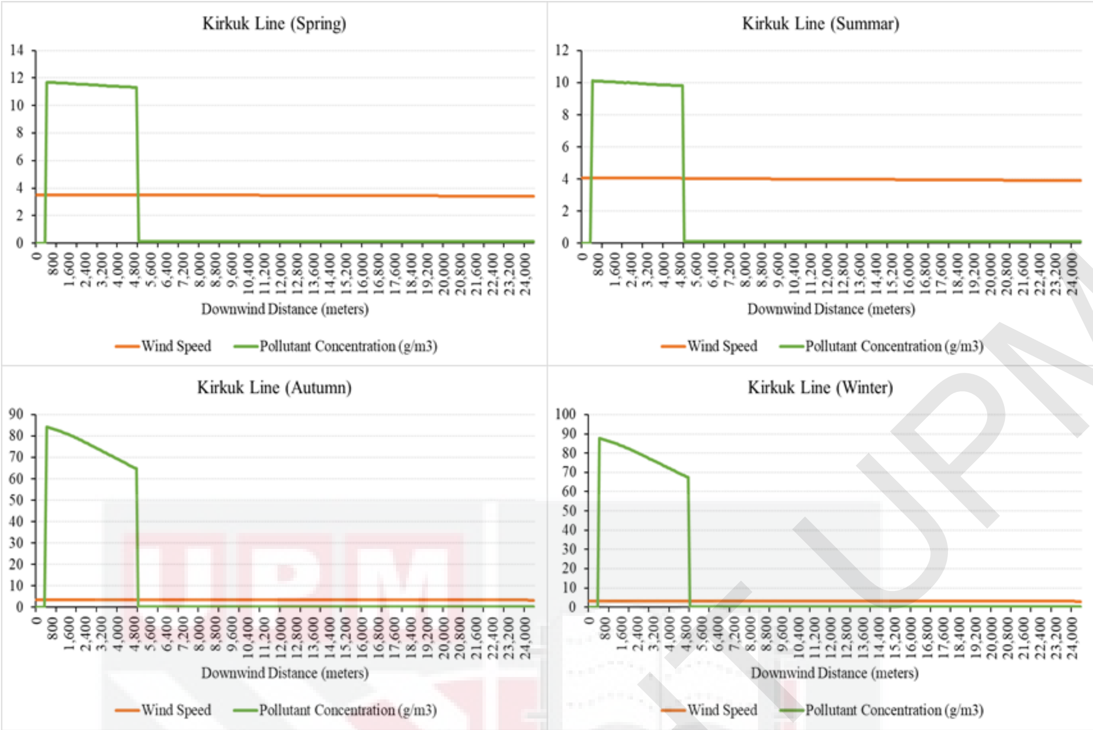

Figure 4.25 : Pollutant Concentration Profiles and Wind Speed Comparison for Kirkuk City Line: Simulated Concentration vs. Distance from the Source, with Corresponding Wind Speed Data

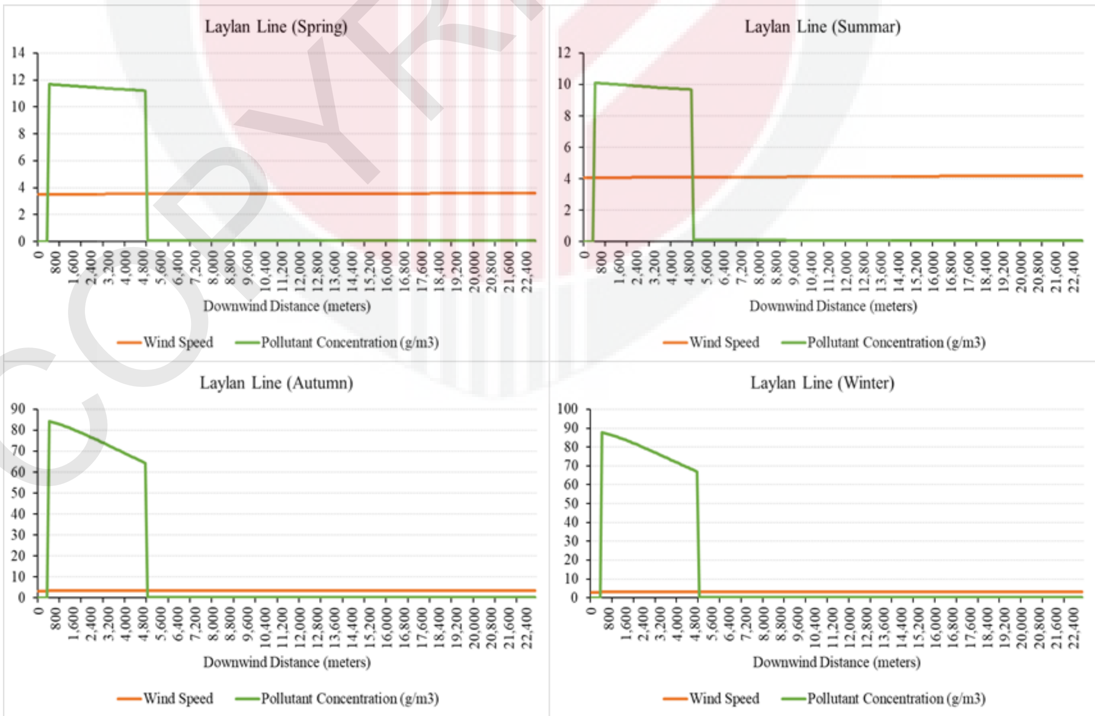

Figure 4.26 : Pollutant Concentration Profiles and Wind Speed Comparison for Laylan District Line: Simulated Concentration vs. Distance from the Source, with Corresponding Wind Speed Data

Simulating pollutant dispersion is an important task for understanding and mitigating the environmental impact of industrial facilities. In this study, the researchers focused on simulating the dispersion of pollutants from the Kirkuk cement plant in different seasons using numerical modeling.

Figure 4.27 shows the simulated pollutant concentration along the path of Kirkuk city from the source in different seasons. As expected, the concentration of pollutants is higher in winter and autumn compared to spring and summer. At the source of the pollutant emission, the concentration is negligible, with values ranging from 7.57×10^{-256} μg/m^3 to 1.21×10^{-253} μg/m^3 in winter and autumn, respectively. As the distance from the source increases, the concentration of pollutants gradually increases until it reaches a peak at 500 meters. At this point, the concentration of pollutants is the highest, with values ranging from 11.69 to 87.76 μg/m^3 in spring, summer, autumn, and winter. Beyond 500 meters, the concentration of pollutants gradually decreases as it spreads further away from the source. At a distance of 1000 meters, the concentration of pollutants is lower than the peak, with values ranging from 10.08 to 82.82 μg/m^3 in spring, summer, autumn, and winter. At larger distances, the concentration of pollutants decreases even further, with values ranging from 0.104 to 0.124 μg/m^3 at distances of 5000 meters and beyond. The results of this study provide valuable insights into the dispersion of pollutants from the Kirkuk cement plant. By understanding how pollutants disperse, measures can be taken to reduce their impact on the environment and public health. Additionally, the modeling approach used in this study can be applied to other industrial facilities to evaluate their environmental impact and optimize their operations.

Figure 4.27 represents the simulated concentration of pollutants at various distances from the source, along the Laylan district path. The concentration values were obtained for different seasons: spring, summer, autumn, and winter. The results show that the highest concentration values were recorded during the winter season, with a maximum value of 87.65 μg/m^3 at a distance of 500 meters from the source. The concentration values decrease as the distance from the source increases. However, it is noteworthy that the concentration values for spring and summer are negligible, with the values ranging from 0 to 11.67 μg/m^3, indicating that the dispersion of pollutants during these seasons is minimal. This could be due to factors such as wind patterns, atmospheric stability, and temperature, which may affect the dispersion of pollutants. In contrast, the concentration values during autumn and winter are relatively higher, with the values ranging from 1.21E-253 to 87.65 μg/m^3, indicating that the dispersion of pollutants during these seasons is more significant. Another interesting observation is that the concentration values of pollutants at a distance of 5000 meters from the source and beyond are minimal, with values ranging from 0.088 to 0.102 μg/m^3. This suggests that the pollutants emitted from the Kirkuk cement plant do not have a significant impact on the air quality in the distant areas.

In conclusion, the simulation results suggest that the dispersion of pollutants from the Kirkuk cement plant is relatively higher during autumn and winter seasons, with the concentration values decreasing as the distance from the source increases. The results also indicate that the impact of the pollutants on the air quality in distant areas is minimal. However, further research is needed to validate the simulation results and to provide a better understanding of the factors affecting the dispersion of pollutants in the region.

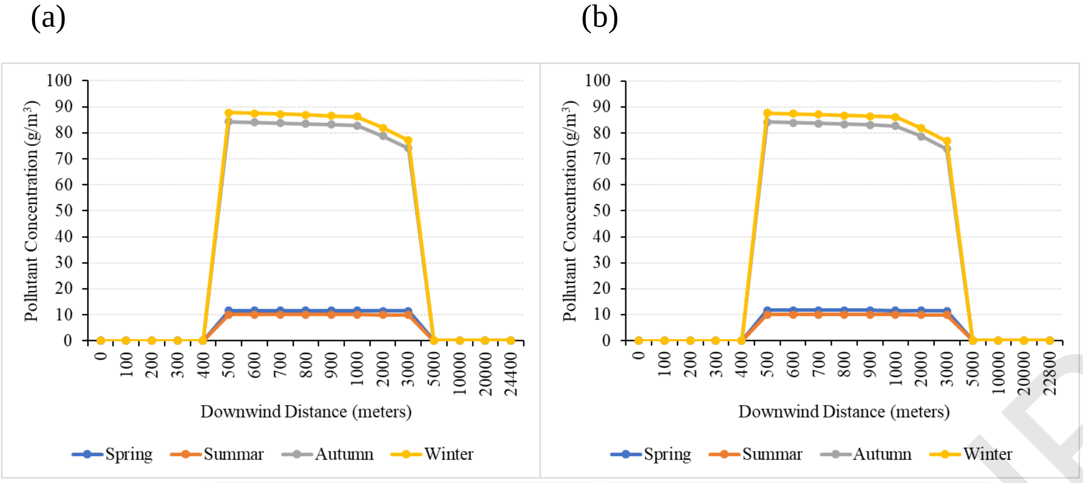

Figure 4.27 : Seasonal Pollutant Concentration Profiles for (a) Kirkuk City Line and (b) Laylan District Line: Simulated Concentration vs. Distance from the Source for Winter, Spring, Summer, and Autumn Seasons

4.8 Impact of Over Serve Height (z)

The results of the study show that as the value of Z increases, the pollutant concentration at ground level decreases. This is due to the fact that as the height of the emission source increases, the pollutant plume is subjected to more atmospheric mixing, which leads to more dilution and dispersion of the pollutants. This is evident from the decreasing values of pollutant concentrations at increasing values of Z (Table 4.5). However, it is also important to note that this effect is not uniform across all distances. The rate at which the pollutant concentration decreases with increasing Z depends on the distance from the source. At closer distances (e.g. 100-500m), the decrease in pollutant concentration is more rapid as the height of the source increases. However, at further distances (e.g. 500-2000m), the decrease is less pronounced, indicating that the effect of atmospheric mixing is less significant at these distances.

Overall, the results of this study demonstrate the importance of considering the height of the emission source when predicting the dispersion of pollutants using the Gaussian plume model. The model can be used to estimate the likely concentration of pollutants at different distances from the source for different values of Z, which can be useful in assessing the potential impacts of pollutant emissions on human health and the environment.

Table 4.5 : The Simulated Pollutant Concentration Values Obtained from the Gaussian Plume Model at Various Distances from the Emission Source with Different z Values

X	Z						
	1	**2**	**5**	**10**	**25**	**50**	**75**
0	0.00	0.00	0.00	0.00	0.00	0.00	10602.76
100	0.00	0.00	0.00	0.00	0.00	0.00	8794.30
200	0.00	0.00	0.00	0.00	0.00	0.00	6052.52
300	0.00	0.00	0.00	0.00	0.00	0.00	5316.46
400	0.00	0.00	0.00	0.00	0.00	0.00	4563.55
500	10.12	10.12	10.13	10.13	10.11	10.03	9.90
600	10.11	10.11	10.12	10.12	10.10	10.02	9.89
700	10.10	10.11	10.11	10.11	10.09	10.02	9.89
800	10.09	10.10	10.10	10.10	10.08	10.01	9.88
900	10.09	10.09	10.09	10.09	10.08	10.00	9.87
1000	10.08	10.08	10.08	10.08	10.07	9.99	9.86
2000	10.00	10.01	10.01	10.01	9.99	9.92	9.79
3000	9.93	9.93	9.94	9.94	9.92	9.84	9.72
4000	9.86	9.86	9.87	9.87	9.85	9.77	9.65
5000	0.09	0.09	0.09	0.09	0.09	0.09	0.09
6000	0.09	0.09	0.09	0.09	0.09	0.09	0.09
7000	0.09	0.09	0.09	0.09	0.09	0.09	0.09
8000	0.09	0.09	0.09	0.09	0.09	0.09	0.09
9000	0.09	0.09	0.09	0.09	0.09	0.09	0.09
10000	0.09	0.09	0.09	0.09	0.09	0.09	0.09
15000	0.09	0.09	0.09	0.09	0.09	0.09	0.09
20000	0.09	0.09	0.09	0.09	0.09	0.09	0.09
24400	0.09	0.09	0.09	0.09	0.09	0.09	0.09

4.9 Gaussian with Temperature and Relative Humidity

4.9.1 Temperature Maps

Figure 4.28 indicates the temperature distribution in the study area for the four seasons in 2020. In the summer, the average temperature in the study region and all adjacent cities is high, reaching 16.032 degrees Celsius. In contrast, the average temperature in winter is relatively low, reaching a low of 10.919 degrees Celsius. While the average temperatures in the spring and autumn seasons are roughly identical, the highest average in the spring is 13.905 degrees Celsius, the lowest average is 13.296 degrees Celsius, and the average temperatures in the autumn season are somewhere in between.

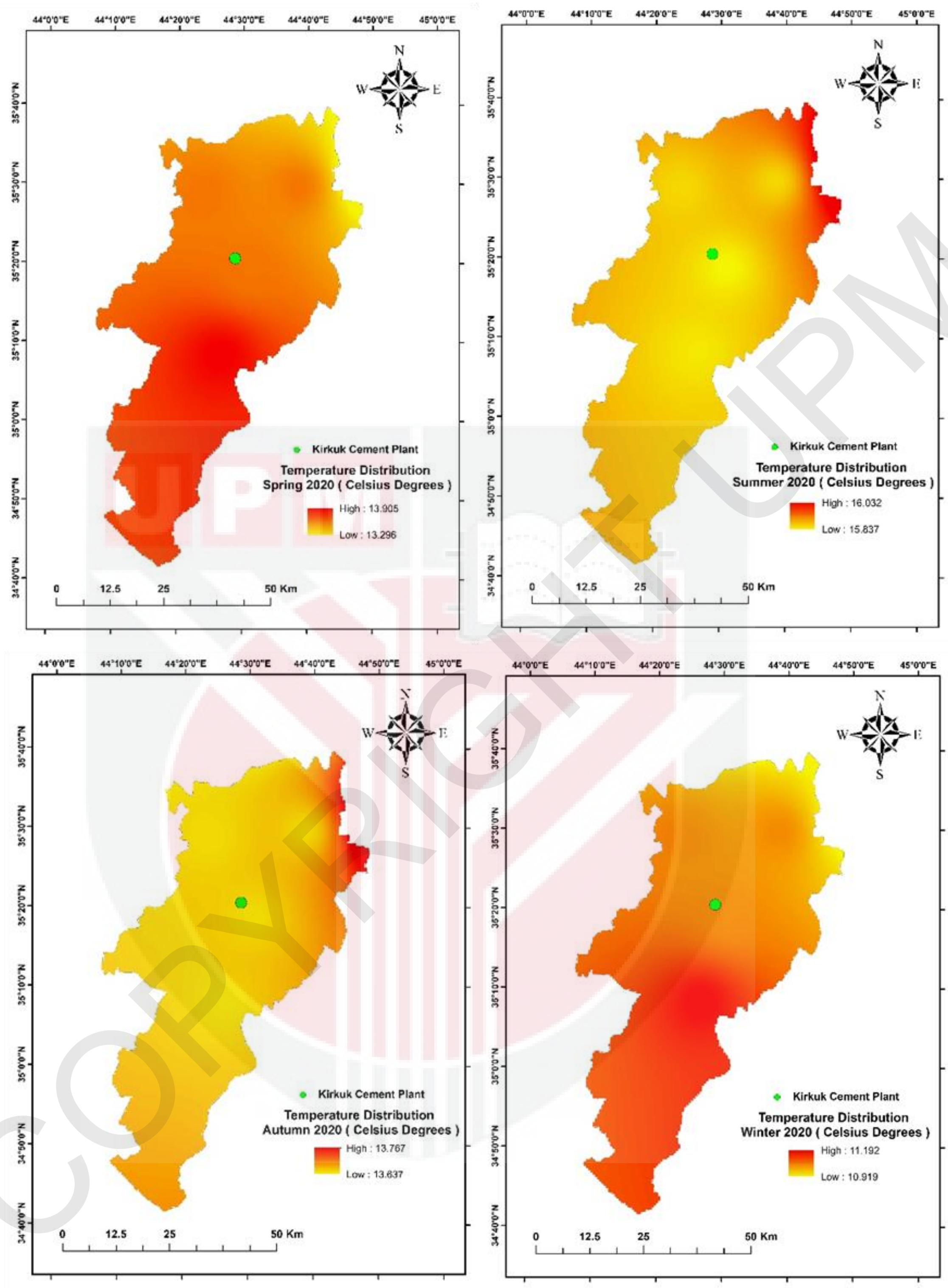

Figure 4.28 : Seasonal Spatial Distribution Map of Temperature Over the Study Area in 2020

4.9.2 Specific Humidity Maps

Figure 4.29 depicts the specific humidity distribution in the study region in 2020. The highest values of specific humidity are in the summer, reaching 6.76 g/kg and concentrated in the south of the study region, and gradually decrease to the north and south, where ranged between 5.79 and 6.06 g/kg for the cement plant area and nearby locations. In contrast, the lowest specific humidity rates are in the winter season, ranging from 4.59 to 4.76 g/kg, and in the cement plant and surrounding regions, ranging from 4.73 to 4.76 g/kg. The specific humidity levels likewise remain high in the spring, with the lowest average being 4.75 and rising to 6.93 g/kg in the cement plant area. In terms of season, the specific humidity values are higher than the winter season and lower than the summer and spring seasons, resulting in the lowest rate of 4.52 g/kg in the cement plant area and surrounding regions, and the maximum average of 5.65 in the the cement plant area.

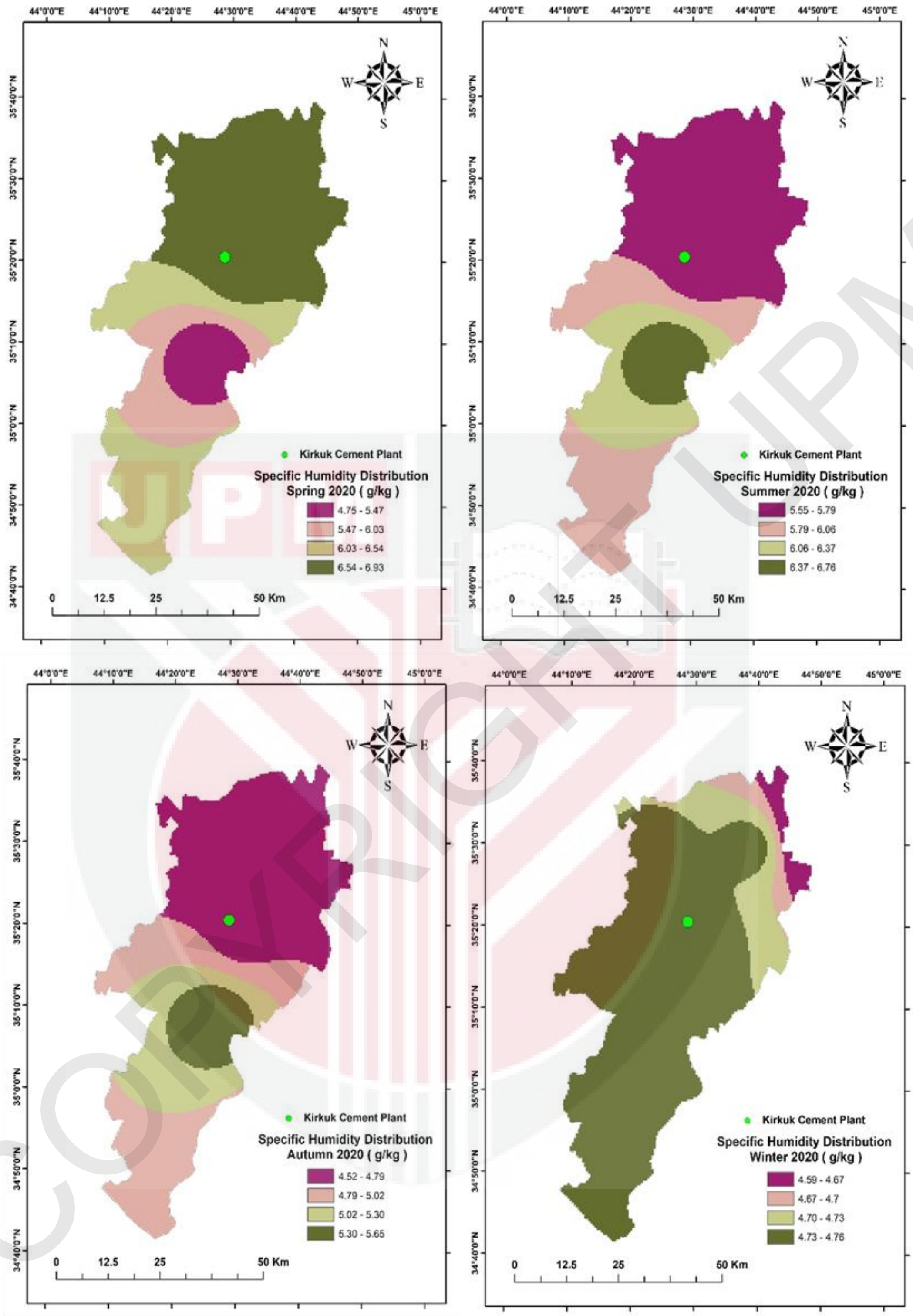

Figure 4.29 : Seasonal Spatial Distribution of Specific Humidity Over the Study Area in 2020

Pollution Concentration with Temperature

Figure 4.30 presents the seasonal pollutant concentration maps produced by the Gaussian equation after applying the seasonal temperature correction within the study region at a radius of 10 km in all directions from the Kirkuk Cement Plant. The pollutant concentration is highest near the source and progressively declines as it is carried by wind. The concentration is highest in the first several hundred meters downwind from the source, then gradually decreases. This is caused by the fact that the pollutant column rises due to buoyancy effects before being dispersed by wind. Pollutant levels are highest in the fall and winter, and lowest in the spring and summer. This is most commonly related to seasonal meteorological situations such as wind patterns, temperature inversions, and atmospheric pressure, all of which can impact the dispersion of pollutants in the air. Because of the height of the stack above the ground cover, the pollutant concentration at the source location is very low in all seasons. Pollutant concentrations grow progressively with distance from the source, with the maximum concentrations as 161.552 μg/m^3 in spring, 162.753 μg/m^3 in summer, 1677.84 μg/m^3 in autumn, and 1418.7 μg/m^3in winter reported between 500-1000 meters. The concentrations steadily decrease outside 1000 meters.

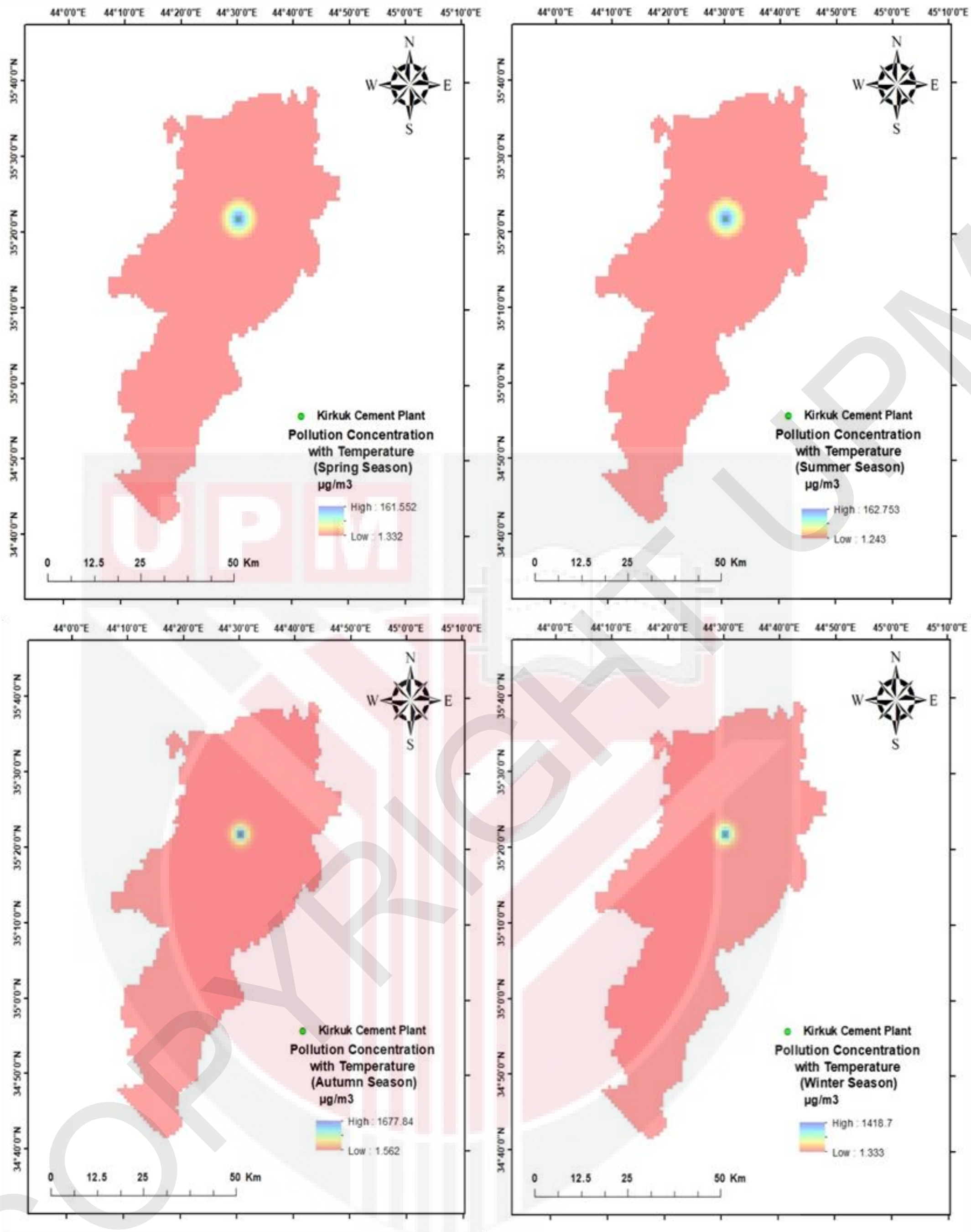

Figure 4.30 : Seasonal Dispersion Maps of Pollutants from the Kirkuk Cement Plant Using Gaussian Plume Model with Correction of Temperature for Spring, Summer, Autumn , and Winter Seasons

Pollution Concentration with Specific Humidity

Figure 4.31 depicts seasonal pollutant concentration maps derived from the Gaussian equation by including the seasonal specific humidity correction within the study area at a distance of 10 km in all directions from the Kirkuk Cement Plant. The pollutant concentration is highest near the source and progressively declines as it is carried by wind. The concentration is highest in the first several hundred meters downwind from the source, then gradually goes down. This is result of the reality that the pollutant column rises due to buoyant forces before being dispersed by wind. Pollutant levels are highest in the fall and winter, and lowest in the spring and summer. This is likely due to weather conditions during each season which can affect the dispersion of pollutants in the air. At the source point, the pollutant concentration is very low in all seasons due to the height of the stack above the ground cover. At greater distances from the source, pollutant concentrations increase progressively, with the highest concentrations observed at 500 –1000 meters to be 84.648 $\mu g/m^3$ in spring, 56.693 $\mu g/m^3$ in summer, 563.027 $\mu g/m^3$ in autumn, and611.282 $\mu g/m^3$ in winter. After 1000 meters, the concentrations gradually decrease, except for the spring season, when the concentration is high for a distance of 3500 meters, after which it begins to gradually decrease.

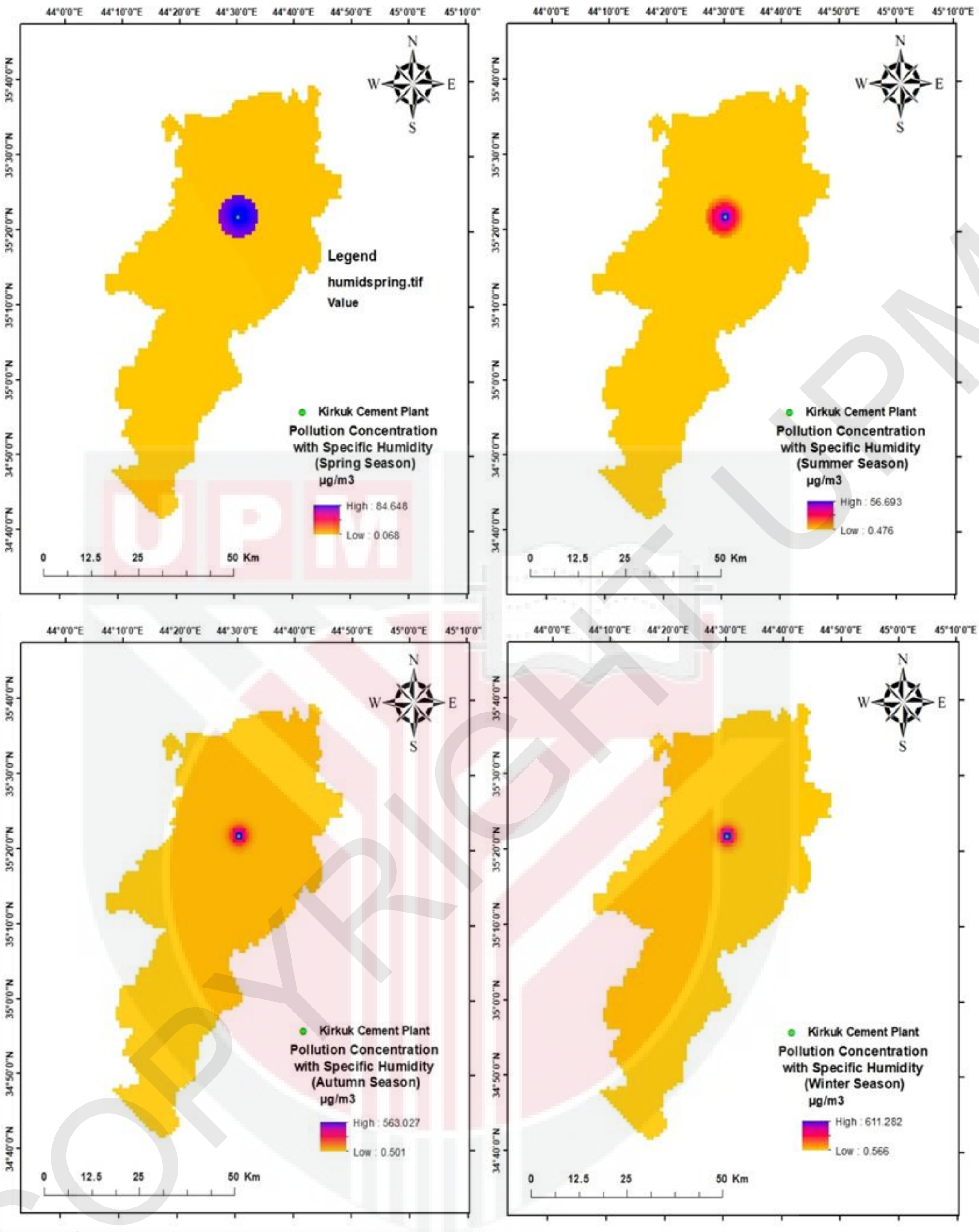

Figure 4.31 : Seasonal Dispersion Maps of Pollutants from the Kirkuk Cement Plant Using Gaussian Plume Model with Correction of Specific Humidity for Spring, Summer, Autumn , and Winter Seasons

Recent studies on air pollution modeling in Iraqi cities, particularly Kirkuk, have employed various approaches including the Gaussian plume model. Research has focused on assessing the impact of cement plant emissions on land cover and air quality (Salih & Hassan, 2023). Studies have utilized GIS, remote sensing, and programming languages like Python to enhance model functionality and accuracy (Jumaah et al., 2023). Air quality assessments in multiple Iraqi cities have revealed concerning levels of particulate matter, often exceeding WHO standards (Abbas & Abbas, 2021; Jumaah et al., 2023). The cement industry has been identified as a significant contributor to CO_2 emissions and air pollution in Iraq (Hason et al., 2020; Al-Kasser, 2021). Researchers have emphasized the need for improved air quality control measures and the potential role of urban trees in mitigating pollution (Salih & Hassan, 2023; Ajayi et al., 2021). These studies provide valuable insights for evidence-based decision-making to improve air quality in Iraqi cities.

Temperature, humidity, and wind speed were considered in some studies (S. A. Saleh et al., 2014; O. Ajayi et al., 2021). The AERMOD model was applied to assess pollutant dispersion from cement factory stacks (Noorpoor & Rahman, 2015). Additionally, research has examined air quality and health impacts in multiple Iraqi cities, including Kirkuk, using the AirQ+ model (Abbas and Abbas, 2021).

4.10 Results and Discussion of DPPM

To assess the validity of the proposed model (Deep Pollutant Prediction Model), data from the GJ001 station in Allahabad City, as well as simulated data from Laylan City retrieved from the Gaussian Plume Model, were utilized. The loss function index was used in this work to evaluate the performance of the DPPM.

4.11 GJ001 Dataset Results

Despite the reality that the data for Allahabad are noisy and unstable, as shown in figure F, DPPM demonstrated high efficiency in the prediction process for xylene and benzene parameters, with loss functions of 0.038 and 0.051, respectively. The $PM_{2.5}$, NO_2, NO_X, CO, SO_2, O_3, and Toluene parameters have excellent DPPM efficiency, with loss functions less than 1%, as shown in table G. The loss functions for the BM10 and NO parameters are quite similar and indicate very good outcomes, with 1.41 and 1.4, respectively. The one parameter with a massive loss function relative to the others is the AQI, which is evident by the fact that it is mathematically dependent on the sum of several other parameters, including O_3, particulate matter ($PM_{2.5}$ and BM_{10}), CO, SO_2, and NO_2.

Despite the inconstancy of the measured values in the station and the missing values procedures done on the data preprocessing, these findings assessed the effectiveness of DPPM. Table (2) illustrates the loss function error of DPPM for each parameter included in the GJ001 dataset.

Table 4.6 : The Loss Error of DPPM for the GJ001 Dataset

Parameters	Loss Function testing 30%	Matching Percentage
$PM_{2.5}$	0.668	99.332
PM_{10}	1.141	98.859
NO	1.140	98.86
NO_2	0.575	99.425
NO_X	0.470	99.53
CO	0.220	99.78
SO_2	0.548	99.452
O_3	0.388	99.612
Benzene	0.051	99.949
Toluene	0.275	99.725
Xylene	0.038	99.962
AQI	4.466	95.534

4.12 Simulated Output Results

The Gaussian output (simulated data) results demonstrate the high efficiency of DPPM with very low function loss. Table (3) shows the output of the Gaussian equation with the loss functions and their matching percentage for each parameter. The findings are relatively constant with little or no significant vacillation, which contributes to the effectiveness of the model. The smallest loss function was 0.0041 for the elements Fe_2O_3 and MgO, while the loss function close to them, which is 0.0042 for Al_2O_3 and 0.0045 for SO_3, as well as the loss function for SiO_2 was 0.0073. While the largest values of the loss functions were 0.0174 and 0.0221 for $CaCO_3$ and CaO respectively, they express the efficiency of DPPM due to its smallness values.

Table 4.7 : The Loss Error of DPPM for Laylan District from (Simulated Output)

Parameters	Loss Function testing 30%	Matching Percentage
$CaCO_3$	0.0174	99.9826
SiO_2	0.0073	99.9927
Al_2O_3	0.0042	99.9958
Fe_2O_3	0.0041	99.9959
CaO	0.0221	99.9779
MgO	0.0041	99.9959
SO_3	0.0045	99.9955

4.13 Summary

In chapter 4, the concentrations of pollution emitted from Kirkuk Cement Plant using Gaussian Plume Model as a tool through Python in QGIS were calculated. In addition to the pollution prediction using deep learning techniques were found. The following results are summarized:

1. The supervised Maximum Likelihood method performed better than Support Vector Machine method in extracting the land cover classes with overall accuracy (98.2143%) and kappa coefficient (0.9736).

2. Spline interpolation method was effential than other interpolation methods in producing the wind speed maps. Since there were only 10 meteorological stations from which the wind speed was derived, which is considered a small proportion to the area over which the stations are distributed, Spline interpolation method was employed. Spline interpolation provides the best results with slowly varying surfaces; it is generally not appropriate when there are large fluctuations in the surface values within short horizontal distances.

3. 1D Gaussian Plume Model in QGIS provided spatial maps of the pollutants concentration with high efficiency for whole study area, as well as maps of the risk of these pollutants on the land cover with the support of AHP.

4. 1D Gaussian Plume Model in QGIS with real direction of plumes provided spatial maps of the pollutant concentrations with high efficiency for whole study area, as well as maps of the risk of these pollutants on the land cover with the support of AHP.

5. 1D Gaussian Plume Model in QGIS with real direction of plumes generated high accurate spatial maps of the pollutant concentrations , as well as produced a pollution risk maps on the land cover with AHP assistance.

6. The results of 3D Gaussian Plume Model in QGIS presented the maps of seasonal pollutant concentration within the study area. The results highlited that the pollutant concentration is highest near the source and gradually decreases as it is transported by the wind. The highest concentration is found within the first few hundred meters downwind from the source, after which it decreases more slowly. The pollutant concentrations are highest during autumn and winter and lowest during spring and summer.

7. The findings of the 3D Gaussian Plume Model with temperature and specific humidity corrections in QGIS displayed maps of seasonal pollutant

concentrations within the research region. The modifications impacted the concentration of contaminants in all seasons in 2020. The concentration raised with temperature correction and receded with specific humidity correction during the spring season. The concentration of contaminants decreased in temperature and specific humidity corrections over the summer. Pollutant concentrations raised with temperature and specific humidity correction in the autumn and winter seasons.

8. The results of the loss functions for all the parameters in the Deep Pollutant Prediction Model (DPPM) findings for the Laylan station proved that data continuity and non-volatility produce excellent outcomes. Where elements Fe_2O3 and MgO had the lowest loss function value of 0.0041, and element CaO had the greatest loss function value of 0.0221.

CHAPTER 5

CONCLUSION AND RECOMMENDATIONS

5.1 Overview

Generally, the Gaussian Plume Model was developed using Python in the QGIS plugin to analyze the risks of cement plant emissions to air and land cover. The model was applied in three stages or forms, the first of which is the general Gaussian equation with all required parameters. The second form was created by incorporating the natural ground levels into the model and extracting them from the Digital Elevation Model, as well as the plum cross down distance (cross-section of the plume). The third form showed the direct impact of new parameters, such as temperature and relative humidity, on emissions. Due to the successful analysis of the GIS tool, Python has been utilized with QGIS to increase the logic and quality of risk map outputs to the environment.

Two classification algorithms, Maximum Likelihood and Support Vector Machine, were used to produce the land cover classes. Three different interpolation methods were used to generate the wind speed maps: Spline, IDW, and Kriging. Kirkuk Cement Plant in Laylan sub-district of Kirkuk City, Iraq was the case of this study. In situ observations of gases and suspended particles matter present in the emissions were used to test the validation of the model.

Cement plant emissions are a threat to human health, plants, water bodies, soil, and even livestock in the research region. The factory uses outdated and underdeveloped technologies, and there is no filter for the factory's chimney, which has a significant impact on the air quality and the surrounding urban areas. This phenomenon is one of the industrial disasters that affect the quality of the environment appropriate for life, thus its hazard must be identified and controlled appropriately to prevent the pollution from continuing to be emitted.

The advancement of spatial analysis utilizing QGIS and the Python programming language improves the real identification of these risks. This innovative approach can be used in other regions to evaluate the degree of industrial pollution in areas where environmental regulation is absent.

5.2 Contributions

This thesis primarily contributes to the development of new Gaussian Plume Model tools in QGIS in different stages. Furthermore, build a new deep learning model to predict the pollutants released by the Kirkuk Cement Plant.

1. A new Gaussian Plume Model tool in QGIS using Python including one variable (x) in equation to calculate the concentration of pollution emitted by Kirkuk Cement Plant and estimate the risk on land cover features with straight direction hypothesis for plume in Gaussian and with real direction of plume.

2. A new Gaussian Plume Model tool in QGIS using Python including three variable (x, y, and z) in equation to calculate the concentration of pollution emitted by Kirkuk Cement Plant by mean of three dimention.

3. A new Gaussian Plume Model tool in QGIS using Python including three variable (x, y, and z) in equation and including the correction of climate parameters which are temperature and specific humidity to calculate the concentration of pollution emitted by Kirkuk Cement Plant.

4. Design a new deep learning model to pridect the concentration of pollution as a requirement to manage pollutants in order to reduce it.

5.3 Overall Findings

The overall finding of the research can be summarized by the following points addressing the objectives of this research:

1. Gaussian Plume Model with QGIS and Python demonstrated the risk of pollutants on the land cover of urban, agricultural areas, water bodies, and soil by evaluating the spatial concentration of pollutants emitted from a cement plant for all points around the plant and by using the essential variable in the equation, wind speed, as a raster.

2. Using a real direction of plume offered a true values of pollution risk on land cover Instead of the straight line hypothesis adopted by the Gaussian equation and as a process to develop the Gaussian tool in QGIS.

3. Three dimentional Gaussian Plume Model indicates the importants of using the x, y, and z variables to give more accurate concentration of pollution with different heights and different terrain elevations.

4. The correction of climate parameters (temperature and specific humidity) in Gaussian Plume Model considered an evolution of the Gaussian tool in QGIS, which gave more realism to the concentration of pollutants due to the importance of climate elements in the pollution diffusion equations.

5. The results of the designed deep learning model (Deep Pollutant Prediction Model) proved that data continuity and non-volatility produce and this refered to hight affecincy of the model.

5.4 Conclusion

The following points address the research objectives and describe the conclusions of the current research:

1. Addressing the first objective, The significance of analyzing the risk of environmental contaminants contributes to advancing decision-makers to take proper measures to minimize environmental risk and health disasters. The land cover classes were extracted from Landsat images 2020 using the Maximum Likelihood Classification technique, with overall accuracy and kappa values of 98.2143% and 0.9736, respectively. Wind speed maps for the four seasons of 2020 were created using the Spline interpolation method and NASA data for 10 virtual stations located inside and around the research area. Wind speeds ranged from 3.07 to 4.35 meters per second (m/s) throughout the year. The wind speed propagation map is nearly comparable in the summer and spring seasons because the wind speed varies as it moves south of the sample field. The wind speed is higher in the summer than it is in the spring. On another side, in winter and autumn, the wind speed distribution is slightly comparable, with a slight increase over winter during the autumn season. Where in the middle of the study the maximum wind speed becomes, then decreases as far as due to the external boundaries. Source information was collected from Kirkuk Cement Plant and other coefficients of the Gaussian equation were computed using stability classes of Pasquill and their equations. Very high-risk pollution has a maximum value of 52.428 to 1264.332 $\mu g/m^3$ in the spring season and a minimum value of 0 to 0.017 $\mu g/m^3$ in the winter season of 2020. The pollutant was riskier in the summer season, where the results have shown that the most polluted urban areas, sand, plantation, and water bodies were 8.573 km^2, 60.974 km^2, 5 km^2, and 2.667 km^2 respectively.

2. Addressing the second objective, by using the real direction of blume related to the Gaussian model, the pollution risks values that emitted on the land cover can be calculated the area of classes more realistically and with accurate results. In all seasons, the barren lands (sand class) are the most areas

affected by pollution risk where the areas were 15.2298 km^2, 10.8621 km^2, 7.0083 km^2, and 8.8722 km^2 for the spring, summer, autumn, and winter seasons, respectively. In contrast, the water class was the smallest areas exposed to risk of pollution by 1.647 km^2, 0. 0647 km^2, 0.5877 km^2, and 0.0711 km^2 for the seasons of spring, summer, autumn, and winter, respectively **.**The vegetation class comes in the second rank as exposed areas to the risk of pollution after barren lands expect in the autumn season which the urban class was in the second rank. Where the green spaces areas were 2.7585 km^2 in the spring season, 1.3023 km^2 in the summer season, 1.3401km^2 in the fall season, and 0.7857 km^2 in the winter. Finally, the areas of urban class that exposed to the risk of pollution were as follows: 2.6802 km^2 in spring season, 0.6786 km^2 in summer season, 4.1841 km^2 in autumn season, and 0.4923 km^2 in winter season.

3. Addressing the third objective, the results of 3D Gaussian Plume tool provided important insights into the wind speed distribution, pollutant concentration, and dispersion patterns in the Kirkuk city area. The results indicated that the wind speed distribution varies by season, with higher wind speeds and greater variability observed in summer, and lower wind speeds and greater stability observed in winter. The simulated pollutant concentration also varied significantly by season, with higher concentrations observed in spring and summer, and lower concentrations observed in autumn and winter. As expected, for Kirkuk City the concentration of pollutants is higher in winter and autumn compared to spring and summer. At the source of the pollutant emission, the concentration is negligible, with values ranging from 7.57E-256 to 1.2133E-253 in winter and autumn, respectively. As the distance from the source increases, the concentration of pollutants gradually increases until it reaches a peak at 500 meters. At this point, the concentration of pollutants is the highest, with values ranging from 11.69 to 87.76 in spring, summer, autumn, and winter. Beyond 500 meters, the concentration of pollutants gradually decreases as it spreads further away from the source. At a distance of 1000 meters, the concentration of pollutants is lower than the peak, with values ranging from 10.08 to 82.82 in spring, summer, autumn, and winter. At larger distances, the concentration of

pollutants decreases even further, with values ranging from 0.104 to 0.124 at distances of 5000 meters and beyond. For Laylan District, the results show that the highest concentration values were recorded during the winter season, with a maximum value of 87.65 at a distance of 500 meters from the source. The concentration values decrease as the distance from the source increases. However, it is noteworthy that the concentration values for spring and summer are negligible, with the values ranging from 0 to 11.67, indicating that the dispersion of pollutants during these seasons is minimal. This could be due to factors such as wind patterns, atmospheric stability, and temperature, which may affect the dispersion of pollutants. In contrast, the concentration values during autumn and winter are relatively higher, with the values ranging from 1.21E-253 to 87.65, indicating that the dispersion of pollutants during these seasons is more significant. Another interesting observation is that the concentration values of pollutants at a distance of 5000 meters from the source and beyond are minimal, with values ranging from 0.088 to 0.102. The study also showed that the height of the emission source affects the pollutant concentration at ground level, with higher emissions leading to more dilution and dispersion of pollutants. Moreover, the results of this study demonstrate the importance of considering the height of the emission source when predicting the dispersion of pollutants using the Gaussian plume model. The model can be used to estimate the likely concentration of pollutants at different distances from the source for different values of Z, which can be useful in assessing the potential impacts of pollutant emissions on human health and the environment.

These findings have important implications for understanding the environmental impact of industrial facilities and can inform strategies to mitigate the impact on air quality and public health.

4. Addressing the fourth objective, After introducing the temperature and specific humidity corrections to the Gaussian model, it was found that the concentrations of pollutants differs in the spring season, as the concentration increased with the temperature correction and decreased with the specific

humidity correction. Where the highest concentration without correction was 113.104 μg/m^3, it increased to be 161.552 μg/m^3 with correction for temperature and decreased to be 84.648 μg/m^3 with correction for specific humidity. In the summer, the highest concentration of pollutants without correction parameters was 177.824 μg/m^3, and it decreased in temperature and specific humidity corrections to become 162.783 and 56.693 μg/m^3, respectively. In the autumn and winter seasons, the concentrations of pollutants increased after adding the correction parameters of the temperature and specific humidity, where the highest concentration of the pollutants without the corrections was 168.28 μg/m^3 and became 1677.84 μg/m^3 due to the temperature correction and 563.027 μg/m^3 due to the specific humidity correction for the autumn season. As for the winter season, the highest concentration of pollutants was 108.19 μg/m^3, and it became 1418.7 μg/m^3 due to the temperature correction and 611.282 μg/m^3 due to the correction of specific humidity in the winter season.

5. Addressing the fifth objective, the designed Deep Pollutant Prediction Model (DPPM) has an efficient and high precision structure and it is containing from six layers of CNN with filter sizes of 16, 32, 64, 128, 256, and 512 with kernel size equal to (3). The strides and padding of CNN layers are the same and equal to (1). The activation function of CNN is the ReLU function and the input shape is equal to the number of items in the data. Furthermore, it has five Maxpooling layers, one Flatten layer, and one Dense layer. Despite the reality that the data are noisy and unstable which is effect on model, DPPM demonstrated high efficiency in the prediction process. Seven parameters were used in the implementation of DPPM for the Laylan station which are $CaCO_3$, SiO_2, Al_2O_3, Fe_2O_3, CaO, MgO, and SO_3. These parameters are the simulated data of Gaussian Plume Model outputs. The loss functions for all the parameters in the DPPM findings for the Laylan station were precise. Where elements Fe_2O_3 and MgO had the lowest loss function value of 0.0041, and element CaO had the greatest loss function value of 0.0221.

5.5 Recommendations for Future Work

From the research, the following recommendations are made for future work:

1. In this research, the pollutant concentrations were detected in combination, which includes all solid elements, dust, and gases. As a result, in future research, it may be preferable to determine the concentration of each element or gas independently, using either measuring the mass emission rate from the combustion process within the plant or by inserting sensors in the external aperture of the chimney.

2. Countries that have a deficit in following up the pollution sources and do not work for reducing pollution need to intensify scientific research in this field to identify risks to humans, plants , and animals and rely on scientific research to provide advice through analysis of these risks and design reliable models in predicting and controlling pollutants

3. This study dealt with adding the correction of temperatures and specific humidity to the Gaussian equation. In future, this research can be improved by adding corrections of all climate parameters such as relative humidity, atmospheric pressure, and participition that influence reducing or increasing the concentration of pollutants emitted from the cement plant.

4. The real wind direction was driven for each season in this study using an interpolation approach and GIS analysis. In the future, it is extremely important to include an automatic technique in the developed plugin to save time and acquire more accurate results.

REFERENCES

A.J., Otaru,. 2013. “Model Prediction of Particulate Dispersion from a Cement Mill Stack: Case Study of a Cement Plant In Nigeria.” *IOSR Journal of Environmental Science, Toxicology and Food Technology* 3(2): 63–76.

Abd, Abbas M., and Suhad M. Abd. 2017. “Modelling the Strength of Lightweight Foamed Concrete Using Support Vector Machine (SVM).” *Case Studies in Construction Materials* 6: 8–15. http://dx.doi.org/10.1016/j.cscm.2016.11.002.

Abdel-Basset, Mohamed, Mai Mohamed, and Florentin Smarandache. 2018. “An Extension of Neutrosophic AHP-SWOT Analysis for Strategic Planning and Decision-Making.” *Symmetry* 10(4).

Abdel-Rahman, Aa. 2008. “On the Atmospheric Dispersion and Gaussian Plume Model.” In *... Proceedings of the 2nd International Conference on ...*, , 31–39. http://www.wseas.us/e-library/conferences/2008/corfu/wwai/wwai04.pdf.

Abdul Samad, Muhammed Siddik et al. 2020. “Environmental Forensic Investigation of the Air Pollution from a Cement Manufacturing Unit.” *Environmental Forensics* 21(1): 37–47. https://doi.org/10.1080/15275922.2019.1694094.

Abril, Gabriela A., Sebastián C. Diez, María L. Pignata, and Javier Britch. 2016. “Particulate Matter Concentrations Originating from Industrial and Urban Sources: Validation of Atmospheric Dispersion Modeling Results.” *Atmospheric Pollution Research* 7(1): 180–89.

Abu-Allaban, Mahmoud, and Hani Abu-Qdais. 2011. “Impact Assessment of Ambient Air Quality by Cement Industry: A Case Study in Jordan.” *Aerosol and Air Quality Research* 11(7): 802–10.

Adeniran, Jamiu Adetayo, Adeniyi Saheed Aremu, Yusuf Olatunji Saadu, and Rafiu Olasunkanmi Yusuf. 2018. “Particulate Matter Concentration Levels during Intense Haze Event in an Urban Environment.” *Environmental Monitoring and Assessment* 190(1).

Adeniran, Jamiu Adetayo, Rafiu Olasunkanmi Yusuf, Bamidele Sunday Fakinle, and Jacob Ademola Sonibare. 2019. “Air Quality Assessment and Modelling of Pollutants Emission from a Major Cement Plant Complex in Nigeria.” *Atmospheric Pollution Research* 10(1): 257–66.

Agrawal, Abhinav, and Namita Mittal. 2020. “Using CNN for Facial Expression Recognition: A Study of the Effects of Kernel Size and Number of Filters on Accuracy.” *Visual Computer* 36(2): 405–12. https://doi.org/10.1007/s00371-019-01630-9.

Ajaj, Qayssar Mahmood et al. 2018. “GIS Based Spatial Modeling to Mapping and Estimation Relative Risk of Different Diseases Using Inverse Distance Weighting (IDW) Interpolation Algorithm and Evidential Belief Function

(EBF) (Case Study: Minor Part of Kirkuk City, Iraq).” *International Journal of Engineering and Technology(UAE)* 7(4): 185–91.

Ajaj, Qayssar Mahmood, Biswajeet Pradhan, Abbas Mohammed Noori, and Mustafa Neamah Jebur. 2017. “Spatial Monitoring of Desertification Extent in Western Iraq Using Landsat Images and GIS.” *Land Degradation and Development* 28(8): 2418–31.

Al-Dhurafi, Nasr Ahmed, Nurulkamal Masseran, Zamira Hasanah Zamzuri, and Muhammad Aslam Mohd Safari. 2018. “Modeling the Air Pollution Index Based on Its Structure and Descriptive Status.” *Air Quality, Atmosphere and Health* 11(2): 171–79.

Al-doski, Jwan, Shattri B Mansor, Helmi Zulhaidi, and Mohd Shafri. 2013. “Image Classification in Remote Sensing.” 3(10): 141–48.

Al-Ruzouq, Rami et al. 2019. “Dam Site Suitability Mapping and Analysis Using an Integrated GIS and Machine Learning Approach.” *Water (Switzerland)* 11(9).

Alhayani, Bilal S.A., and Haci llhan. 2021. “Visual Sensor Intelligent Module Based Image Transmission in Industrial Manufacturing for Monitoring and Manipulation Problems.” *Journal of Intelligent Manufacturing* 32(2): 597–610. https://doi.org/10.1007/s10845-020-01590-1.

Ali, Fadi. 2015. “Urban Classification by Pixel and Object-Based Approaches for Very High Resolution Imagery.”

Ali, Sabah H, Mohamed A Najemaden, and Rehab T Ahmed. 2018. “Using GIS Techniques for Mapping the Pollution of Particulate Materials in Kirkuk.” 3(2): 1–8.

Amjady, Nima, and Oveis Abedinia. 2017. “Short Term Wind Power Prediction Based on Improved Kriging Interpolation, Empirical Mode Decomposition, and Closed-Loop Forecasting Engine.” *Sustainability (Switzerland)* 9(11).

Amoatey, Patrick, Hamid Omidvarborna, Hannah A. Affum, and Mahad Baawain. 2019. “Performance of AERMOD and CALPUFF Models on SO2 and NO2 Emissions for Future Health Risk Assessment in Tema Metropolis.” *Human and Ecological Risk Assessment* 25(3): 772–86. https://doi.org/10.1080/10807039.2018.1451745.

Anderson, Jonathan O., Josef G. Thundiyil, and Andrew Stolbach. 2012. “Clearing the Air: A Review of the Effects of Particulate Matter Air Pollution on Human Health.” *Journal of Medical Toxicology* 8(2): 166–75.

Arachchige, Udara. 2019. “Environmental Pollution by Cement Industry.” *International Journal of Research* 06(08): e-ISSN: 2348-6848 p-ISSN: 2348-795X. https://journals.pen2print.org/index.php/ijr/.

Arseni et al. 2019. “Testing Different Interpolation Methods Based on Single Beam Echosounder River Surveying. Case Study: Siret River.” *ISPRS International*

Journal of Geo-Information 8(11): 507.

Ashish, B. K., A. Kumar, and P. K. Padhy. 2011. "Satellite Image Processing Using Discrete Cosine Transform and Singular Value Decomposition." *Communications in Computer and Information Science* 205 CCIS(August 2015): 277–90.

Asuoha, Adaku N, and Charles I Osu. 2015. "Seasonal Variation of Meteorological Factors on Air Parameters and the Impact of Gas Flaring on Air Quality of Some Cities in Niger Delta (Ibeno and Its Environs)." *African Journal of Environmental Science and Technology* 9(3): 218–27.

Awasthi, Seema, Mukesh Khare, and Prashant Gargava. 2006. "General Plume Dispersion Model (GPDM) for Point Source Emission." *Environmental Modeling and Assessment* 11(3): 267–76.

Azpurua, M., and K. dos Ramos. 2010. "A Comparison of Spatial Interpolation Methods for Estimation of Average Electromagnetic Field Magnitude." *Progress In Electromagnetics Research M* 14(August): 135–45.

Bachtiar, V. S., & Davies, F. 2018. "Limitation of A Dispersion Model on Prediction the Boundary Layer Height in An Urban Area."

Bagherzadeh, Jamshid, and Hasan Asil. 2019. "A Review of Various Semi-Supervised Learning Models with a Deep Learning and Memory Approach." *Iran Journal of Computer Science* 2(2): 65–80. https://doi.org/10.1007/s42044-018-00027-6.

Balter, B. M., and M. V. Faminskaya. 2017. "Irregularly Emitting Air Pollution Sources: Acute Health Risk Assessment Using AERMOD and the Monte Carlo Approach to Emission Rate." *Air Quality, Atmosphere and Health* 10(4): 401–9. http://dx.doi.org/10.1007/s11869-016-0428-x.

Bărbulescu, Alina, Cristina Șerban, and Marina Larisa Indrecan. 2021. "Computing the Beta Parameter in Idw Interpolation by Using a Genetic Algorithm." *Water (Switzerland)* 13(6).

Becker, Daniel, Christian Willmes, Georg Bareth, and Gerd-Christian Weniger. 2016. "A Plugin To Interface Openmodeller From Qgis for Species' Potential Distribution Modelling." *ISPRS Annals of Photogrammetry, Remote Sensing and Spatial Information Sciences* III–7(July): 251–56.

Bediroglu, Sevket. 2021. "Developing GIS Interface for the Automated Analysis and Assessment of Livable and Sustainable City Criterion Sets." *Arabian Journal of Geosciences* 14(12).

Bekkar, Abdellatif, Badr Hssina, Samira Douzi, and Khadija Douzi. 2021. "Air-Pollution Prediction in Smart City, Deep Learning Approach." *Journal of Big Data* 8(1): 1–21. https://doi.org/10.1186/s40537-021-00548-1.

Bernardo, Nariane, Fernanda Watanabe, Thanan Rodrigues, and Enner Alcântara. 2017. "Atmospheric Correction Issues for Retrieving Total Suspended Matter Concentrations in Inland Waters Using OLI/Landsat-8 Image." *Advances in Space Research* 59(9): 2335–48.

Beychok, M. R. 1979. "How Accurate Are Dispersion Predictions. Hydrocarbon Process." *Gulf Publishing* 59.

Bhandari, A. K., A. Kumar, S. Chaudhary, and G. K. Singh. 2017. 28 Multidimensional Systems and Signal Processing *A New Beta Differential Evolution Algorithm for Edge Preserved Colored Satellite Image Enhancement*. Springer US.

Bhattacharjee, Shrutilipi, and Jia Chen. 2020. "Prediction of Satellite-Based Column CO_2 Concentration by Combining Emission Inventory and LULC Information." *IEEE Transactions on Geoscience and Remote Sensing* 58(12): 8285–8300.

Bichet, A., M. Wild, D. Folini, and C. Schr. 2012. "Causes for Decadal Variations of Wind Speed over Land: Sensitivity Studies with a Global Climate Model." *Geophysical Research Letters* 39(11): 4–9.

Boubel, W. R., Fox, D. L., Turner, D. B., & Stern, A. C. 1994. "Sources of Air Pollution. Fundamentals of Air Pollution." *Journal of medical toxicology* 8: 166–175.

Briggs, David J. et al. 1997. "Mapping Urban Air Pollution Using Gis: A Regression-Based Approach." *International Journal of Geographical Information Science* 11(7): 699–718.

Brode, R. W. 1995. "SCREEN3 Model User's Guide." *NASA 19980015351* EPA-454(B-95-004. U.S.).

Brusca, S. et al. 2016. "Theoretical and Experimental Study of Gaussian Plume Model in Small Scale System." In *Energy Procedia*, The Author(s), 58–65. http://dx.doi.org/10.1016/j.egypro.2016.11.008.

Caglar, Bayik, K. Becek, C. Mekik, and M. Ozendi. 2018. "On the Vertical Accuracy of the ALOS World 3D-30m Digital Elevation Model." *Remote Sensing Letters* 9(6): 607–15.

Carrascal, M. D., M. Puigcerver, and P. Puig. 1993. "Sensitivity of Gaussian Plume Model to Dispersion Specifications." *Theoretical and Applied Climatology* 48(2–3): 147–57.

Cervantes, Jair, Farid Garcia-Lamont, Lisbeth Rodríguez-Mazahua, and Asdrubal Lopez. 2020. "A Comprehensive Survey on Support Vector Machine Classification: Applications, Challenges and Trends." *Neurocomputing* (408): 189–215. https://doi.org/10.1016/j.neucom.2019.10.118.

Chang, J. C., and S. R. Hanna. 2004. “Air Quality Model Performance Evaluation.” *Meteorology and Atmospheric Physics* 87(1–3): 167–96.

Chang, Ni Bin, Sanaz Imen, and Benjaminr Vannah. 2015. “Remote Sensing for Monitoring Surface Water Quality Status and Ecosystem State in Relation to the Nutrient Cycle: A 40-Year Perspective.” *Critical Reviews in Environmental Science and Technology* 45(2): 101–66.

Chen, Lajiao et al. 2015. “A Review of Parallel Computing for Large-Scale Remote Sensing Image Mosaicking.” *Cluster Computing* 18(2): 517–29. http://dx.doi.org/10.1007/s10586-015-0422-3.

Chen, Tong et al. 2016. “Emission and Distribution of PCDD/Fs and CBzs from Two Co-Processing RDF Cement Plants in China.” *Environmental Science and Pollution Research* 23(12): 11845–54. http://dx.doi.org/10.1007/s11356-016-6403-0.

Cheremisinoff, Paul N. 1992. “Industrial Odour Control.” *Butterworth-Heinemann Ltd. Oxford* (9): 222.

Chidambaram, S., and K. G. Srinivasagan. 2019. “Performance Evaluation of Support Vector Machine Classification Approaches in Data Mining.” *Cluster Computing* 22: 189–96. https://doi.org/10.1007/s10586-018-2036-z.

Chimica, Dipartimento, and Roma Tor. 2006. “A Review of Dispersion Modelling and Its Application to the Dispersion of Particles.” *Atmospheric Environmen* 7: 1046–72.

Cohen, Aaron J. et al. 2005. “The Global Burden of Disease Due to Outdoor Air Pollution.” *Journal of Toxicology and Environmental Health - Part A* 68(13–14): 1301–7.

Congedo, Luca. 2021. “Semi-Automatic Classification Plugin: A Python Tool for the Download and Processing of Remote Sensing Images in QGIS.” *Journal of Open Source Software* 6(64): 3172.

Corumluoglu, Ozsen, Alaaddin Vural, and Ibrahim Asri. 2015. “Determination of Kula Basalts (Geosite) in Turkey Using Remote Sensing Techniques.” *Arabian Journal of Geosciences* 8(11): 10105–17.

Custodio, Guilherme, F. C.L. Trindade, Kyriacos Petrou, and Luis F. Ochoa. 2019. “An Advanced GIS-Based Tool for the Analysis of Future Distribution Networks.” *2019 IEEE PES Conference on Innovative Smart Grid Technologies, ISGT Latin America 2019* (October).

Dalvi, Mohit et al. 2006. “A GIS Based Methodology for Gridding of Large-Scale Emission Inventories: Application to Carbon-Monoxide Emissions over Indian Region.” *Atmospheric Environment* 40(16): 2995–3007.

Dargazany, Aras R., Paolo Stegagno, and Kunal Mankodiya. 2018. “WearableDL: Wearable Internet-of-Things and Deep Learning for Big Data Analytics -

Concept, Literature, and Future.” *Mobile Information Systems* 2018(Dl).

Davies, E.R. 2018. Computer Vision “Face Detection and Recognition.”

Devaraj, Suresh, and Kiran Yarrakula. 2020. “Evaluation of Sentinel 1–Derived and Open-Access Digital Elevation Model Products in Mountainous Areas of Western Ghats, India.” *Arabian Journal of Geosciences* 13(20).

Devi, K Syamala, V Vijaya Lakshmi, and A Alakanandana. 2017. “Impacts of Cement Industry on Environment-an Overview.” *Asia Pacific Journal of Research ISSN* (February): 2347–4793. www.apjor.com.

Dewan, Ashraf M., and Robert J. Corner. 2014. “Monitoring and Prediction of Land-Use and Land-Cover (LULC) Change.” In *Dhaka Megacity: Geospatial Perspectives on Urbanisation, Environment and Health*, Springer, Dordrecht., 75–97.

DJ Carruthers, RJ Holroyd, JCR Hunt, WS Weng. 1994. “UK-ADMS: A New Approach to Modelling Dispersion in the Earth’s Atmospheric Boundary Layer.” *Journal of Wind Engineering and Industrial Aerodynamics* 52: 139–53.

Dochev, Ivan, Hannes Seller, and Irene Peters. 2019. “Spatial Aggregation and Visualisation of Urban Heat Demand Using Graph Theory. An Example from Hamburg, Germany.” *International Journal of Sustainable Energy Planning and Management* 24: 115–24.

Duarte, Lia, Pedro Silva, and Ana Cláudia Teodoro. 2018. “Development of a QGIS Plugin to Obtain Parameters and Elements of Plantation Trees and Vineyards with Aerial Photographs.” *ISPRS International Journal of Geo-Information* 7(3): 14–19.

Dubey, Anita, and Govt M L B College Bhopal. 2013. “Studies on the Air Pollution Around Cement and Lime Factories.” *Journal of Environment and Earth Science* 3(9): 191–95.

Eldin, S. A.Sharaf, M. S. Abd-Elhady, and H. A. Kandil. 2016. “Feasibility of Solar Tracking Systems for PV Panels in Hot and Cold Regions.” *Renewable Energy* 85: 228–33. http://dx.doi.org/10.1016/j.renene.2015.06.051.

Emeksiz, Cem, and Tugce Cetin. 2019. “In Case Study: Investigation of Tower Shadow Disturbance and Wind Shear Variations Effects on Energy Production, Wind Speed and Power Characteristics.” *Sustainable Energy Technologies and Assessments* 35(June): 148–59. https://doi.org/10.1016/j.seta.2019.07.004.

Emmert-Streib, Frank et al. 2020. “An Introductory Review of Deep Learning for Prediction Models With Big Data.” *Frontiers in Artificial Intelligence* 3(February): 1–23.

Emrouznejad, Ali, and Marianna Marra. 2017. "The State of the Art Development of AHP (1979–2017): A Literature Review with a Social Network Analysis." *International Journal of Production Research* 55(22): 6653–75. https://doi.org/10.1080/00207543.2017.1334976.

EPA. 2011. "Additional Clarification Regarding Application of Appendix w Modeling Guidance for the 1-h NO2 National Ambient Air Quality St a n Da Rd." *U S Epa*.

European Environment Agency (EEA). 2013. *Air Quality in {Europe} — 2013 Report*. http://www.eea.europa.eu/publications/air-quality-in-europe-2013.

Fakinle, B. S., A. A. Oki, and J. A. Sonibare. 2018. "DISPERSION MODELING OF AIR EMISSIONS FROM ALL CEMENT PLANT IN NIGERIA." *International Journal of Mechanical Engineering and Technology* 9(13): 1155–71.

Fantaye, Y, M Motuma, and G Tsegaye. 2017. "Land Use Land Cover Change Analysis Using Geospatial Tools in Case of Asayita District, Zone One, Afar Region, Ethiopia." *Journal of Resources …* 29: 10–15. https://www.researchgate.net/profile/Gebrie_Tsegaye/publication/334575950_Land_use_land_cover_change_analysis_using_Geospatial_tools_in_case_of_Asayita_district_zone_one_Afar_region_Ethiopia/links/5d35a97a92851cd0467b9aa2/Land-use-land-cover-change-analys.

Fedel, GS, DB Beniz, LP Do Carmo, and JR Piton LNLS. 2017. "Python for User Interfaces at Sirius; Python for User Interfaces at Sirius." : 1091–97.

Ferreira, P., Le, D. C., & Zincir-Heywood, N. 2019. "Exploring Feature Normalization and Temporal Information for Machine Learning Based Insider Threat Detection." In *2019 15th International Conference on Network and Service Management (CNSM)*, , (pp. 1-7). IEEE.

Flenniken, Jeffry M., Steven Stuglik, and Basil V. Iannone. 2020. "Quantum GIS (QGIS): An Introduction to a Free Alternative to More Costly GIS Platforms." *Edis* 2020(2): 7.

Fuhg, Jan N., Amélie Fau, and Udo Nackenhorst. 2021. 28 Archives of Computational Methods in Engineering *State-of-the-Art and Comparative Review of Adaptive Sampling Methods for Kriging*. Springer Netherlands. https://doi.org/10.1007/s11831-020-09474-6.

Gidhagen, L., C. Johansson, et al. 2004. "Simulation of NOx and Ultrafine Particles in a Street Canyon in Stockholm, Sweden." *Atmospheric Environment* 38(14): 2029–44.

Goudarzi, Gholamreza et al. 2016. "Modeling of CO Dispersion from the Stack of an Iranian Cement Plant." *J Adv Environ Health Res* 4(4): 199–205. http://jaehr.muk.ac.ir/.

Graser, Anita. 2016. *Learning Qgis*. mumbai, India: Packt Publishing Ltd. Mumbai, India.

Graser, Anita, and Victor Olaya. 2015. “Processing: A Python Framework for the Seamless Integration of Geoprocessing Tools in QGIS.” *ISPRS International Journal of Geo-Information* 4(4): 2219–45.

Grippa, Taïs et al. 2017. “An Open-Source Semi-Automated Processing Chain for Urban Object-Based Classification.” *Remote Sensing* 9(4).

Gritsenko, Yury B., Pavel V. Senchenko, and Konstantin A. Kalentiev. 2020. “Development of a Geographic Information System for Managing University Campus.” *14th IEEE International Conference on Application of Information and Communication Technologies, AICT 2020 - Proceedings*: 1–6.

Gupta, Shivam. 2018. “Spatial Modelling of Air Pollution for Open Smart Cities.”

Gupta, Shivam, Edzer Pebesma, Jorge Mateu, and Auriol Degbelo. 2018. “Air Quality Monitoring Network Design Optimisation for Robust Land Use Regression Models.” *Sustainability (Switzerland)* 10(5): 1–27.

Hall, Dolly L. et al. 2020. “Using Near-Road Observations of CO, NOy, and CO2 to Investigate Emissions from Vehicles: Evidence for an Impact of Ambient Temperature and Specific Humidity.” *Atmospheric Environment* 232(x): 117558. https://doi.org/10.1016/j.atmosenv.2020.117558.

Hamel, R., Paine, R., Heinold, D., Kumar, N., & Knipping, E. 2012. “An Emissions Variability Processor for Modeling Applications.” *Air and Waste Management Association Annual Meeting* 105(1): 873–86.

Hanna, Steven R., Bruce A. Egan, John Purdum, and Jen Wagler. 2001. “Evaluation of the ADMS, AERMOD, and ISC3 Dispersion Models with the OPTEX, Duke Forest, Kincaid, Indianapolis and Lovett Field Datasets.” *International Journal of Environment and Pollution* 16(1–6): 301–14.

Hayou, Soufiane, Arnaud Doucet, and Judith Rousseau. 2019. “On the Impact of the Activation Function on Deep Neural Networks Training.” In *36th International Conference on Machine Learning, ICML 2019*, , 4746–54.

Health Organization, World. 2016. “Ambient Air Pollution: A Global Assessment of Exposure and Burden of Disease.” *Clean Air Journal* 26(2): 6.

Heckel, Pamela Funderburg, and Grace K. Lemasters. 2011. “The Use of AERMOD Air Pollution Dispersion Models to Estimate Residential Ambient Concentrations of Elemental Mercury.” *Water, Air, and Soil Pollution* 219(1–4): 377–88.

Hendriks, C A et al. 2003. “Emission Reduction of Greenhouse Gases from the Cement Industry.” *Greenhouse gas control technologies conference*: 1–11.

Hernandez, G., Berry, T. A., Wallis, S. L., & Poyner, D. 2017. "Temperature and Humidity Effects on Particulate Matter Concentrations in a Sub-Tropical Climate During Winter." In *International Proceedings of Chemical, Biological and Environmental Engineering*, , 41–49.

Hesham G. Ibrahim, Aly Y. Okasha, Mokhtar S. Elatrash, and and Mohamed A. Al-Meshragi. 2012. "Emissions of SO2, NOx and PMs from Cement Plant in Vicinity of Khoms City in Northwestern Libya,." 1: 287–92.

Heydari, Azim et al. 2022. "Air Pollution Forecasting Application Based on Deep Learning Model and Optimization Algorithm." *Clean Technologies and Environmental Policy* 24(2): 607–21. https://doi.org/10.1007/s10098-021-02080-5.

Hindy, K. T., H. I. Abdel Shafy, and S. A. Farag. 1990. "The Role of the Cement Industry in the Contamination of Air, Water, Soil and Plant with Vanadium in Cairo." *Environmental Pollution* 66(3): 195–205.

Hoffnagle, Gale F. 2018. "EPA Making 2018 Air Permit Modeling Even More Uncertain." *Natural Gas & Electricity* 34(7): 21–24.

Huang, Dongmei et al. 2017. "Accuracy Assessment Model for Classification Result of Remote Sensing Image Based on Spatial Sampling." *Journal of Applied Remote Sensing* 11(04): 1.

Hutchinson, Michael F., and Tingbao Xu. 2000. "ANUSPLIN Version 4.3." *Centre for Resource and Environmental Studies, Australian National University* (August): 1–52.

Ikechukwu, Maduako Nnamdi, Elijah Ebinne, Ufot Idorenyin, and Ndukwu Ike Raphael. 2017. "Accuracy Assessment and Comparative Analysis of IDW, Spline and Kriging in Spatial Interpolation of Landform (Topography): An Experimental Study." *Journal of Geographic Information System* 09(03): 354–71.

Isam Drewil, Ghufran, and Riyadh Jabbar Al-Bahadili. 2021. "Multicultural Education Forecast Air Pollution in Smart City Using Deep Learning Techniques: A Review." *Multicultural Education* 7(5): 38–47.

Jafarigol, F., F. Atabi, F. Moattar, and J. Nouri. 2016. "Predicting Ambient Concentrations of NO2 in a Gas Refinery Located in South Pars Gas Complex." *International Journal of Environmental Science and Technology* 13(3): 897–906.

Janson, Jeyleenny Ranty et al. 2019. "A Study on the Atmospheric Dispersion of Radionuclide Released from TRIGA MARK II Reactor Using Gaussian Plume Model." *Sains Malaysiana* 48(9): 2021–28.

Jawak, Shridhar D., Prapti Devliyal, and Alvarinho J. Luis. 2015. "A Comprehensive Review on Pixel Oriented and Object Oriented Methods for Information Extraction from Remotely Sensed Satellite Images with a Special Emphasis on

Cryospheric Applications.” *Advances in Remote Sensing* 04(03): 177–95.

Jayadipraja, Erwin Azizi, Anwar Daud, Alimuddin Hamzah Assegaf, and Maming. 2016. “APPLYING SPATIAL ANALYSIS TOOLS IN PUBLIC HEALTH: THE USE OF AERMOD IN MODELING THE EMISSION DISPERSION OF SO2 AND NO2 TO IDENTIFY AREA EXPOSED TO HEALTH RISKS.” *Public Health of Indonesia* 2(1): 20–27.

Jayadipraja, Erwin, Anwar Daud, Alimuddin Assegaf, and Maming Maming. 2016. “The Application of the AERMOD Model in the Environmental Health to Identify the Dispersion Area of Total Suspended Particulate from Cement Industry Stacks.” *International Journal of Research in Medical Sciences* (October 2020): 2044–49.

Jayamurugan, Ramasamy, B. Kumaravel, S. Palanivelraja, and M. P. Chockalingam. 2013. “Influence of Temperature, Relative Humidity and Seasonal Variability on Ambient Air Quality in a Coastal Urban Area.” *International Journal of Atmospheric Sciences* 2013: 1–7.

Jena, Madhab Chandra, Sarat kumar Mishra, and Himanshu Sekhar Moharana. 2020. “Air Pollution from Cement Plants: Case Study on Particulate Matter in Bihar, India.” *Environmental Claims Journal* 32(3): 221–32. https://doi.org/10.1080/10406026.2020.1714200.

Jin, Hong Sung, and Dongyeob Han. 2017. “Multisensor Fusion of Landsat Images for High-Resolution Thermal Infrared Images Using Sparse Representations.” *Mathematical Problems in Engineering* 2017.

Jing, Weipeng, Shuaiqi Huo, Qiucheng Miao, and Xuebin Chen. 2017. “A Model of Parallel Mosaicking for Massive Remote Sensing Images Based on Spark.” *IEEE Access* 5: 18229–37.

Jittra, Nattawut, Nattaporn Pinthong, and Sarawut Thepanondh. 2015. “Performance Evaluation of AERMOD and CALPUFF Air Dispersion Models in Industrial Complex Area.” *Air, Soil and Water Research* 8(2): 87–95.

John R. Jensen. 2015. *INTRODUCTORY DIGITAL IMAGE PROCESSING A Remote Sensing Perspective*. 4th editio. Pearson Education.

Jones, Andrew, David Thomson, Matthew Hort, and Ben Devenish. 2007. “The U.K. Met Office’s Next-Generation Atmospheric Dispersion Model, NAME III.” *Air Pollution Modeling and Its Application XVII* (January): 580–89.

Kakosimos, Konstantinos E., Ole Hertel, Matthias Ketzel, and Ruwim Berkowicz. 2010. “Operational Street Pollution Model (OSPM) - A Review of Performed Application and Validation Studies, and Future Prospects.” *Environmental Chemistry* 7(6): 485–503.

Kalhor, Mostafa, and Mehrshad Bajoghli. 2017. “Comparison of AERMOD, ADMS and ISC3 for Incomplete Upper Air Meteorological Data (Case Study: Steel Plant).” *Atmospheric Pollution Research* 8(6): 1203–8.

http://dx.doi.org/10.1016/j.apr.2017.06.001.

Karl, M. et al. 2015. “Modelling Atmospheric Oxidation of 2-Aminoethanol (MEA) Emitted from Post-Combustion Capture Using WRF-Chem.” *Science of the Total Environment* 527–528: 185–202.

Khan, Shafat, and Khalid Mohiuddin. 2018. “Evaluating the Parameters of ArcGIS and QGIS for GIS Applications.” *Int. J. Adv. Res. Sci. Eng* 7(3): 582–94.

Khan, Zahid Younas, Zhendong Niu, Sulis Sandiwarno, and Rukundo Prince. 2021. 54 Artificial Intelligence Review *Deep Learning Techniques for Rating Prediction: A Survey of the State-of-the-Art*. Springer Netherlands. https://doi.org/10.1007/s10462-020-09892-9.

Khaniabadi, Yusef Omidi, Philip K. Hopke, et al. 2017. “Cardiopulmonary Mortality and COPD Attributed to Ambient Ozone.” *Environmental Research* 152(1): 336–41. http://dx.doi.org/10.1016/j.envres.2016.10.008 (October 21, 2022).

Khaniabadi, Yusef Omidi, Gholamreza Goudarzi, et al. 2017. “Exposure to PM10, NO2, and O3 and Impacts on Human Health.” *Environmental Science and Pollution Research* 24(3): 2781–89. http://dx.doi.org/10.1007/s11356-016-8038-6.

Khaniabadi, Yusef Omidi et al. 2018. “Modeling of Particulate Matter Dispersion from a Cement Plant: Upwind-Downwind Case Study.” *Journal of Environmental Chemical Engineering* 6(2): 3104–10.

Kimmel, Veljo, and Marko Kaasik. 2003. “Assessment of Urban Air Quality in South Estonia by Simple Measures.” *Environmental Modeling and Assessment* 8(1): 47–53.

Kirk, R. E., & Othmer, D. F. 2007. “Chemical Technology and the Environment.” *Wiley-Interscience* 2.

Klompmaker, Jochem O. et al. 2021. “Air Pollution and Cardiovascular Disease Hospitalization – Are Associations Modified by Greenness, Temperature and Humidity?” *Environment International* 156: 106715. https://doi.org/10.1016/j.envint.2021.106715.

Kukulska, Anita, Tomasz Salata, Katarzyna Cegielska, and Marta Szylar. 2018. “Methodology of Evaluation and Correction of Geometric.” *Acta Scientiarum Polonorum* 17(1): 137–50.

Kumar, Ashok et al. 2006. “Evaluation of the AERMOD Dispersion Model as a Function of Atmospheric Stability for an Urban Area.” *Environmental Progress* 25(2): 141–51.

Lawal, Olanrewaju, and Aminanyanaba Onari Asimiea. 2017. “Modelling of the Potential Pattern and Concentration of Fugitive Dust Around a Cement Plant.” *Environmental Research, Engineering and Management* 73(1): 48–68.

Lawhead, Joel. 2015. *Learning Geospatial Analysis with Python*. mumbai, India: Packt Publishing Ltd. Mumbai, India.

Lee, Hyung Don et al. 2014. "Evaluation of Concentrations and Source Contribution of PM10 and SO2 Emitted from Industrial Complexes in Ulsan, Korea: Interfacing of the WRF-CALPUFF Modeling Tools." *Atmospheric Pollution Research* 5(4): 664–76.

Lewellen, W. S., and R. I. Sykes. 1989. "Meteorological Data Needs for Modeling Air Quality Uncertainties." *Journal of Atmospheric and Oceanic Technology* 6(5): 759–68.

Li, Lixin, Xiaolu Zhou, Marc Kalo, and Reinhard Piltner. 2016. "Spatiotemporal Interpolation Methods for the Application of Estimating Population Exposure to Fine Particulate Matter in the Contiguous U.S. and a Real-Time Web Application." *International Journal of Environmental Research and Public Health* 13(8).

Li, Xiang et al. 2017. "Long Short-Term Memory Neural Network for Air Pollutant Concentration Predictions: Method Development and Evaluation." *Environmental Pollution* 231: 997–1004.

Li, Zhanwei et al. 2020. "Aerodynamic and Aeroelastic Characteristics of Flexible Wind Turbine Blades under Periodic Unsteady Inflows." *Journal of Wind Engineering and Industrial Aerodynamics* 197(December).

Li, Zhiqiang, and Chengqi Cheng. 2019. "A CNN-Based Pan-Sharpening Method for Integrating Panchromatic and Multispectral Images Using Landsat 8." *Remote Sensing* 11(22).

Liang, Dong et al. 2016. "Comparison and Fusion of Multispectral and Panchromatic IKONOS Images Using Different Algorithms." *Communications in Computer and Information Science* 569: 504–13.

Lisani, Jose Luis et al. 2016. "An Inquiry on Contrast Enhancement Methods for Satellite Images." *IEEE Transactions on Geoscience and Remote Sensing* 54(12): 7044–54.

LIU, Gang jun et al. 2007. "A Framework of Environmental Modelling and Information Sharing for Urban Air Pollution Control and Management." *Journal of China University of Mining and Technology* 17(2): 172–78.

Liu, Hui et al. 2019. "An Intelligent Hybrid Model for Air Pollutant Concentrations Forecasting: Case of Beijing in China." *Sustainable Cities and Society* 47(February): 101471. https://doi.org/10.1016/j.scs.2019.101471.

Liu, Jun et al. 2020. "Carbon and Air Pollutant Emissions from China ' s Cement Industry 1990-2015 : Trends , Evolution of Technologies and Drivers." *Atmospheric chemistry and physics* 21(3): 1–39.

Liu, Yaolin et al. 2017. "Analysis of Coastline Extraction from Landsat-8 OLI Imagery." *Water (Switzerland)* 9(11): 1–26.

Locati, Mario, Roberto Vallone, Matteo Ghetta, and Nyall Dawson. 2021. "QQuake, a QGIS Plugin for Loading Seismological Data From Web Services." *Frontiers in Earth Science* 9(February): 1–8.

Lodge, J. P. 1995. "Fundamentals of Stack Gas Dispersion." *3rd Edition, Irvin, California*.

López-Serrano, Pablito M. et al. 2016. "Evaluation of Radiometric and Atmospheric Correction Algorithms for Aboveground Forest Biomass Estimation Using Landsat 5 TM Data." *Remote Sensing* 8(5): 1–19.

M. J. Assael, K. E. Kakosimo+, A.S. Katsarou. 2011. "Application and Evaluation of AERMOD on the Assessment of Particulate Matter Pollution Caused by Industrial Activities in the Greater Thessaloniki Area." *Environmental Technology* 32(6): 593–608.

Ma, Mingyuan et al. 2020. "Deep Learning for Prediction of the Air Quality Response to Emission Changes." *Environmental science & technology* 54(14): 8589–8600.

Ma, Xuying et al. 2019. "A Site-Optimised Multi-Scale GIS Based Land Use Regression Model for Simulating Local Scale Patterns in Air Pollution." *Science of the Total Environment* 685(May): 134–49.

Ma, Xuying, Ian Longley, Jennifer Salmond, and Jay Gao. 2020. "PyLUR: Efficient Software for Land Use Regression Modeling the Spatial Distribution of Air Pollutants Using GDAL/OGR Library in Python." *Frontiers of Environmental Science and Engineering* 14(3).

Madsen, Henrik, Poul Thyregod, Florin Popentiu, and Grigore Albeanu. 2004. "Computer Aided Modeling and Pollution Control in Cement Plants." *Fourth Annual Meeting of ENBIS* (June 2014): 1–11.

Mairal, Julien. 2016. "End-to-End Kernel Learning with Supervised Convolutional Kernel Networks." *Advances in Neural Information Processing Systems* (Nips): 1407–15.

Majeed, Haris, and Jonathan Lee. 2017. "The Impact of Climate Change on Youth Depression and Mental Health." *The Lancet Planetary Health* 1(3): e94–95. http://dx.doi.org/10.1016/S2542-5196(17)30045-1.

Mao, Yushun, and Shiejue Lee. 2019. "Deep Convolutional Neural Network for Air Quality Prediction." *Journal of Physics: Conference Series* 1302(3): 032046.

Massey, David D., Mahima Habil, and Ajay Taneja. 2016. "Particles in Different Indoor Microenvironments-Its Implications on Occupants." *Building and Environment* 106: 237–44. http://dx.doi.org/10.1016/j.buildenv.2016.06.036.

Maurya, Khushbu, Seema Mahajan, and Nilima Chaube. 2021. “Remote Sensing Techniques: Mapping and Monitoring of Mangrove Ecosystem—a Review.” *Complex & Intelligent Systems* 7(6): 2797–2818. https://doi.org/10.1007/s40747-021-00457-z.

Mazzia, Vittorio, Aleem Khaliq, and Marcello Chiaberge. 2020. “Improvement in Land Cover and Crop Classification Based on Temporal Features Learning from Sentinel-2 Data Using Recurrent-Convolutional Neural Network (R-CNN).” *Applied Sciences (Switzerland)* 10(1): 1–23.

Meng, Qingmin, Zhijun Liu, and Bruce E. Borders. 2013. “Assessment of Regression Kriging for Spatial Interpolation - Comparisons of Seven GIS Interpolation Methods.” *Cartography and Geographic Information Science* 40(1): 28–39.

Meyer, D., and M. Riechert. 2019. “Open Source QGIS Toolkit for the Advanced Research WRF Modelling System.” *Environmental Modelling and Software* 112: 166–78.

Mileu, Nelson, and Margarida Queirós. 2018. “Development of a QGIS Plugin to Dasymetric Mapping.” *QGIS Plugin to Dasymetric Mapping OSGeo Journal* 18(2): 9. https://scholarworks.umass.edu/foss4g/vol18/iss1/9.

Millard, Koreen, and Murray Richardson. 2015. “On the Importance of Training Data Sample Selection in Random Forest Image Classification: A Case Study in Peatland Ecosystem Mapping.” *Remote Sensing* 7(7): 8489–8515.

Mishra, Shraddha, and Nehal Anwar Siddiqui. 2014. “A Review On Environmental and Health Impacts Of Cement Manufacturing Emissions.” *International Journal of Geology, Agriculture and Environmental Sciences* 2(3 June 2014): 2. www.woarjournals.org/IJGAES.

Mohebbi A, Baroutian S. A. 2006. “A Detailed Investigation of Particulate Dispersion from Kerman Cement Plant.” *Iranian Journal of Chemical Engineering* 3(3): 65–74.

Mohsen, Heba, El-Sayed A. El-Dahshan, El-Sayed M. El-Horbaty, and Abdel-Badeeh M. Salem. 2018. “Classification Using Deep Learning Neural Networks for Brain Tumors.” *Future Computing and Informatics Journal* 3(1): 68–71. https://doi.org/10.1016/j.fcij.2017.12.001.

Motesaddi Zarandi, Saeed et al. 2015. “Long-Term Trends of Nitrogen Oxides and Surface Ozone Concentrations in Tehran City, 2002-2011.” *Journal of Environmental Health Science and Engineering* 13(1): 1–6. http://dx.doi.org/10.1186/s40201-015-0218-7.

Motyka, Oldřich et al. 2020. “Moss Biomonitoring and Air Pollution Modelling on a Regional Scale: Delayed Reflection of Industrial Pollution in Moss in a Heavily Polluted Region?” *Environmental Science and Pollution Research* 27(26): 32569–78.

Muenchow, Jannes, Patrick Schratz, and Alexander Brenning. 2017. "RQGIS: Integrating R with QGIS." *The R Journal* 9(2): 409–28. https://cran.r-project.org/package=RQGIS.

Muhsin, I. J., Salih, K. H., & Fadhel, E. 2015. "Augment the Spatial Resolution of Multispectral Image Using PCA Fusion Method and Classified It's Region Using Different Techniques." *International Journal of Engineering Trends and Technology* 26(3): 152–57.

Mureşan, Horea, and Mihai Oltean. 2018. "Fruit Recognition from Images Using Deep Learning." *Acta Universitatis Sapientiae, Informatica* 10(1): 26–42.

Muthukumar, Pratyush et al. 2022. "Predicting PM2.5 Atmospheric Air Pollution Using Deep Learning with Meteorological Data and Ground-Based Observations and Remote-Sensing Satellite Big Data." *Air Quality, Atmosphere and Health* 15(7): 1221–34.

Natya, S, and V Rehna. 2016. "Land Cover Classification Schemes Using Remote Sensing Images: A Recent Survey." *British Journal of Applied Science & Technology* 13(4): 1–11.

Ndossi, Milton Isaya, and Ugur Avdan. 2016. "Application of Open Source Coding Technologies in the Production of Land Surface Temperature (LST) Maps from Landsat: A PyQGIS Plugin." *Remote Sensing* 8(5).

Nikezić, Dušan P. et al. 2017. "Modeling Air Concentration of Fly Ash in Belgrade, Emitted from Thermal Power Plants TNTA and TNTB." *Process Safety and Environmental Protection* 106(June): 274–83.

Okhrimenko, Maxim, Craig Coburn, and Chris Hopkinson. 2019. "Multi-Spectral Lidar: Radiometric Calibration, Canopy Spectral Reflectance, and Vegetation Vertical SVI Profiles." *Remote Sensing* 11(13).

Oliveri Conti, Gea et al. 2017. "A Review of AirQ Models and Their Applications for Forecasting the Air Pollution Health Outcomes." *Environmental Science and Pollution Research* 24(7): 6426–45.

Oprea, Mihaela, Marian Popescu, Sanda Florentina Mihalache, and Elia Georgiana Dragomir. 2017. "Data Mining and ANFIS Application to Particulate Matter Air Pollutant Prediction. A Comparative Study." *ICAART 2017 - Proceedings of the 9th International Conference on Agents and Artificial Intelligence* 2(Icaart): 551–58.

Oudin, Ludovic et al. 2008. "Spatial Proximity, Physical Similarity, Regression and Ungaged Catchments: A Comparison of Regionalization Approaches Based on 913 French Catchments." *Water Resources Research* 44(3): 1–15.

Paegelow, Martin, and María Teresa Camacho Olmedo. 2008. Environmental Science and Engineering (Subseries: Environmental Science) *Modelling Environmental Dynamics: Advances in Geomatic Solutions*.

Park, Jongchan, Joon Young Lee, Donggeun Yoo, and In So Kweon. 2018. "Distort-and-Recover: Color Enhancement Using Deep Reinforcement Learning." In *Proceedings of the IEEE Computer Society Conference on Computer Vision and Pattern Recognition*, , 5928–36.

Park, Soon Ung, In Hye Lee, Jae Won Ju, and Seung Jin Joo. 2016. "Estimation of Radionuclide (137 Cs) Emission Rates from a Nuclear Power Plant Accident Using the Lagrangian Particle Dispersion Model (LPDM)." *Journal of Environmental Radioactivity* 162–163(April 2011): 258–62. http://dx.doi.org/10.1016/j.jenvrad.2016.05.033.

Pelton, Joseph N., Scott Madry, and Sergio Camacho-Lara. 2013. "Handbook of Satellite Applications." *Handbook of Satellite Applications* 1–2: 1–1228.

Pires, Ivan Miguel et al. 2020. "Homogeneous Data Normalization and Deep Learning: A Case Study in Human Activity Classification." *Future Internet* 12(11): 1–14.

Pisso, Ignacio et al. 2019. "The Lagrangian Particle Dispersion Model FLEXPART Version 10.4." *Geoscientific Model Development* 12(12): 4955–97.

Rahman, Md Habibur, Murad Y. Abu-Farsakh, and Navid Jafari. 2021. "Generation and Evaluation of Synthetic Cone Penetration Test (Cpt) Data Using Various Spatial Interpolation Techniques." *Canadian Geotechnical Journal* 58(2): 224–37.

Rahman, Md Mahmudur et al. 2017. "Development of a Land Use Regression Model for Daily NO2 and NOx Concentrations in the Brisbane Metropolitan Area, Australia." *Environmental Modelling and Software* 95: 168–79.

Rao, C. S. 2006. "Environmental Pollution Control Engineerin." *Revised 2nd edition, Chemical Engineering – Birla Institute of Technology and Science, Pilani. New Age International (P) Limited Publishers, New Delhi*.

Ratnaparkhi, Nayana S. 2020. "Satellite Image Pre-Processing For Interactive Image Interpretation." 7(1): 961–65.

Ren, Chao et al. 2019. "Assessment of Local Climate Zone Classification Maps of Cities in China and Feasible Refinements." *Scientific Reports* 9(1): 1–11.

Richards, John A., and Xiuping Jia. 2006. Remote Sensing Digital Image Analysis: An Introduction *Remote Sensing Digital Image Analysis: An Introduction*.

Russell G. Congalton and Kass Green. 2019. 1 CRC Press *Assessing the Accuracy of Remotely Sensed Data Principles and Practices, Third Edition*.

Rwanga, Sophia S., and J. M. Ndambuki. 2017. "Accuracy Assessment of Land Use/Land Cover Classification Using Remote Sensing and GIS." *International Journal of Geosciences* 08(04): 611–22.

Rychlik, Igor, and Wengang Mao. 2019. “Spatio-Temporal Modelling of Wind Speed Variations and Extremes in the Caribbean and the Gulf of Mexico.” *Theoretical and Applied Climatology* 135(3–4): 921–44.

Saabith, AL Sayeth, M. M. M. Fareez, and T. Vinothraj. 2019. “PYTHON CURRENT TREND APPLICATIONS- AN OVERVIEW.” *International Journal of Advance Engineering and Research Development* 6(10): 6–12.

Saaty, Thomas L, and Luis G Vargas. 1980. “Hierarchical Analysis of Behavior In.” *Behavioral Science* 25: 180–91.

Sánchez-Soberón, Francisco et al. 2015. “Main Components and Human Health Risks Assessment of PM10, PM2.5, and PM1 in Two Areas Influenced by Cement Plants.” *Atmospheric Environment* 120: 109–16. http://dx.doi.org/10.1016/j.atmosenv.2015.08.020.

Santellani, E., E. Maset, and A. Fusiello. 2018. “Seamless Image Mosaicking Via Synchronization.” *ISPRS Annals of the Photogrammetry, Remote Sensing and Spatial Information Sciences* 4(2): 247–54.

Sathya, P., and Baby V. Deepa. 2017. “Analysis of Supervised Image Classification Method for Satellite Images.” *International Journal of Computer Science Research (IJCSR)* 5(2): 16–19. https://www.academia.edu/33546348/Analysis_of_Supervised_Image_Classification_Method_for_Satellite_Images.

Saxena, Vivek, Priyanka Mundra, and Divyani Jigyasu. 2020. “Efficient Viewshed Analysis as QGIS Plugin.” *Proceedings - IEEE 2020 2nd International Conference on Advances in Computing, Communication Control and Networking, ICACCCN 2020*: 957–61.

Schmitz, Oliver et al. 2019. “Data Descriptor: High Resolution Annual Average Air Pollution Concentration Maps for the Netherlands.” *Scientific Data* 6: 1–12. http://dx.doi.org/10.1038/sdata.2019.35.

Schürholz, Daniel, Sylvain Kubler, and Arkady Zaslavsky. 2020. “Artificial Intelligence-Enabled Context-Aware Air Quality Prediction for Smart Cities.” *Journal of Cleaner Production* 271: 121941. https://doi.org/10.1016/j.jclepro.2020.121941.

Sciences, Allied. 2015. “Numerical Simulation of Dispersion of Emissions from Tema Oil Refinery in Ghana.”

Scire, J.S., D.G. Strimaitis, and R.J. Yamartino. 2000. “A User’s Guide for the CALPUFF Dispersion Model. Version 5, Earth Tech Inc., Lowell.” *Eearth Tech. Inc* (January): 521.

Seangkiatiyuth, Kanyanee, Vanisa Surapipith, Kraichat Tantrakarnapa, and Anchaleeporn W. Lothongkum. 2011. “Application of the AERMOD Modeling System for Environmental Impact Assessment of NO 2 Emissions from a Cement Complex.” *Journal of Environmental Sciences* 23(6): 931–40.

http://dx.doi.org/10.1016/S1001-0742(10)60499-8.

Sehra, Sukhjit Singh, Jaiteg Singh, and Hardeep Singh Rai. 2017. "Assessing Openstreetmap Data Using Intrinsic Quality Indicators: An Extension to the QGIS Processing Toolbox." *Future Internet* 9(2).

Sensing, Advanced Remote, and Second Edition. 2020. "Atmospheric Correction of Optical Imagery." *Advanced Remote Sensing*: 131–56.

Sensing, Remote, Journal List, and Impact Factors. 2016. "A Meta-Analysis of Remote Sensing Research on Supervised Pixel-Based Land-Cover Image Classification Processes: General Guidelines for Practitioners and Future Research." *Remote Sensing of Environment,* 77: 89–100.

Shafri, Helmi Zulhaidi M., Nisfariza Mohd Noor Maris, and Basharudin Abdul Hadi. 2011. "An Assessment on the Performance of Support Vector Machine over Traditional Parametric and Non-Parametric Techniques for Satellite Image Classification." *32nd Asian Conference on Remote Sensing 2011, ACRS 2011* 3(Mlc): 1504–9.

Shafri, Helmi Zulhaidi Mohd, Affendi Suhaili, and Shattri Mansor. 2007. "The Performance of Maximum Likelihood, Spectral Angle Mapper, Neural Network and Decision Tree Classifiers in Hyperspectral Image Analysis." *Journal of Computer Science* 3(6): 419–23.

Shareef, Muntadher Aidi, Mohammed Hashim Ameen, and Qayssar Mahmood Ajaj. 2020. "Change Detection and Gis-Based Fuzzy Ahp to Evaluate the Degradation and Reclamation Land of Tikrit City, Iraq." *Geodesy and Cartography (Vilnius)* 46(4): 194–203.

Sharma, Anshumala, David D. Massey, and Ajay Taneja. 2018. "A Study of Horizontal Distribution Pattern of Particulate and Gaseous Pollutants Based on Ambient Monitoring near a Busy Highway." *Urban Climate* 24(August): 643–56. http://dx.doi.org/10.1016/j.uclim.2017.08.003.

Sharma, Atharva, Xiuwen Liu, Xiaojun Yang, and Di Shi. 2017. "A Patch-Based Convolutional Neural Network for Remote Sensing Image Classification." *Neural Networks* 95: 19–28. http://dx.doi.org/10.1016/j.neunet.2017.07.017.

Shrestha, Arun Kumar, Arati Thapa, and Hima Gautam. 2019. "Solar Radiation, Air Temperature, Relative Humidity, and Dew Point Study: Damak, Jhapa, Nepal." *International Journal of Photoenergy* 2019.

Silveira, Flávia, Gabriele Silveira Camara, and Silvana Philippi Camboim. 2018. "Simbology for Small Scale Reference Mapping: Automation and Sharing of Symbols." *Proceedings of the Brazilian Symposium on GeoInformatics* 2018-Decem: 36–45.

Silverman, Keith C., Joan G. Tell, Edward V. Sargent, and Zeyuan Qiu. 2007. "Comparison of the Industrial Source Complex and AERMOD Dispersion Models: Case Study for Human Health Risk Assessment." *Journal of the Air* *and Waste Management Association* 57(12): 1439–46.

Singh, Rana Pratap, and Hans Peter Nachtnebel. 2016. "Analytical Hierarchy Process (AHP) Application for Reinforcement of Hydropower Strategy in Nepal." *Renewable and Sustainable Energy Reviews* 55: 43–58. http://dx.doi.org/10.1016/j.rser.2015.10.138.

Al Smadi, Bashar M., Kamel K. Al-Zboon, and Khaldoun M. Shatnawi. 2009. "Assessment of Air Pollutants Emissions from a Cement Plant: A Case Study in Jordan." *Jordan Journal of Civil Engineering* 3(3): 265–82.

Stehman, S. V., & Foody, G. M. 2019. "Key Issues in Rigorous Accuracy Assessment of Land Cover Products Stephen V. Stehman." *Remote Sensing of Environment* 231(111199).

Stieren, Anja, Srinidhi N. Gadde, and Richard J.A.M. Stevens. 2021. "Modeling Dynamic Wind Direction Changes in Large Eddy Simulations of Wind Farms." *Renewable Energy* 170: 1342–52. https://doi.org/10.1016/j.renene.2021.02.018.

Stirnberg, Roland et al. 2020. "Meteorology-Driven Variability of Air Pollution (PM1) Revealed with Explainable Machine Learning." *Atmospheric Chemistry and Physics* (January 2016): 1–35.

Suh, Jangwon, Sung Min Kim, Huiuk Yi, and Yosoon Choi. 2017. "An Overview of GIS-Based Modeling and Assessment of Mining-Induced Hazards: Soil, Water, and Forest." *International Journal of Environmental Research and Public Health* 14(12).

Sun, Rui, Tamer M. Ismail, Xiaohan Ren, and M. Abd El-Salam. 2016. "Influence of Simulated MSW Sizes on the Combustion Process in a Fixed Bed: CFD and Experimental Approaches." *Waste Management* 49: 272–86. http://dx.doi.org/10.1016/j.wasman.2015.12.019.

Suresh, Shilpa, Shyam Lal, Chintala Sudhakar Reddy, and Mustafa Servet Kiran. 2017. "A Novel Adaptive Cuckoo Search Algorithm for Contrast Enhancement of Satellite Images." *IEEE Journal of Selected Topics in Applied Earth Observations and Remote Sensing* 10(8): 3665–76.

Tan, Qulin, and Xiao Xu. 2014. "Comparative Analysis of Spatial Interpolation Methods: An Experimental Study." *Sensors and Transducers* 165(2): 155–63.

Tang, Jiayi, Aonghus McNabola, and Bruce Misstear. 2020. "The Potential Impacts of Different Traffic Management Strategies on Air Pollution and Public Health for a More Sustainable City: A Modelling Case Study from Dublin, Ireland." *Sustainable Cities and Society* 60: 102229. https://doi.org/10.1016/j.scs.2020.102229.

Team, Q. D. 2016. "QGIS Geographic Information System." *Open source geospatial foundation project*.

Teggi, Sergio et al. 2018. "A GIS-Based Atmospheric Dispersion Model for Pollutants Emitted by Complex Source Areas." *Science of the Total Environment* 610–611: 175–90. http://dx.doi.org/10.1016/j.scitotenv.2017.07.196.

Teodoro, Ana Claudia Moreira, and Norma Beltrão. 2018. "Evaluating the Potential of Sentinel-2 MSI and Landsat-8 OLI Data Fusion for Land Cover Mapping in Brazilian Amazon." (October 2018): 7.

Tharwat, Alaa. 2018. "Classification Assessment Methods." *Applied Computing and Informatics* 17(1): 168–92.

Thill, Jean Claude. 2000. "Geographic Information Systems for Transportation in Perspective." *Transportation Research Part C: Emerging Technologies* 8(1): 3–12.

Torres, Javier Martínez et al. 2020. "A Functional Data Analysis Approach for the Detection of Air Pollution Episodes and Outliers: A Case Study in Dublin, Ireland." *Mathematics* 8(2).

Towfek El-Kenawy, El-Sayed M. 2019. "A Machine Learning Model for Hemoglobin Estimation and Anemia Classification." *International Journal of Computer Science and Information Security (IJCSIS)* 17(2). https://sites.google.com/site/ijcsis/.

Tsai, Yi Ting, Yu Ren Zeng, and Yue Shan Chang. 2018. "Air Pollution Forecasting Using Rnn with Lstm." In *Proceedings - IEEE 16th International Conference on Dependable, Autonomic and Secure Computing, IEEE 16th International Conference on Pervasive Intelligence and Computing, IEEE 4th International Conference on Big Data Intelligence and Computing and IEEE 3*, IEEE, 1068–73.

Uliasz-Bocheńczyk, Alicja. 2019. "Chemical Characteristics of Dust from Cement Kilns." *Gospodarka Surowcami Mineralnymi / Mineral Resources Management* 35(2): 87–102.

USEPA. 2004. "'User's Guide for the AMS/EPA Regulatory Model–AERMOD.'"

Veigele, W. M.J., and James H. Head. 1978. "Derivation of the Gaussian Plume Model." *Journal of the Air Pollution Control Association* 28(11): 1139–40.

Venkatram, Akula, and Dispersion Modeling. 2005. "Introduction to Aermod." : 1–24.

Wakjira, T, A Tamene, and T Dawud. 2016. "Land Use Land Cover Change Analysis Using Multi Temporal Landsat Data in Gilgel Gibe, Omo Gibe Basin, Ethiopia." *International Journal of Science and Technology* 5.

WANG Hai-chao,JIAO Wen-ling, ZOU Ping-hua. 2010. "Development of AERMOD Dispersion Model." *Environmental Science & Technology* 11.

Weiss, Sophie et al. 2017. "Normalization and Microbial Differential Abundance Strategies Depend upon Data Characteristics." *Microbiome* 5(1): 1–18.

Werner, Martin. 2019. "GIS++: Modern C++ for Efficient and Parallel in-Memory Spatial Computing." *Proceedings of the 1st ACM SIGSPATIAL International Workshop on Geospatial Data Access and Processing APIs, SpatialAPI 2019 - In conjunction with the 27th International Conference on Advances in Geographic Information Systems, ACM SIGSPATIAL 2019*.

Wiele, Siamak Khorram • Cynthia F. van der, Frank H. Koch • Stacy A. C. Nelson, and Matthew D. Potts. 2016. *Principles of Applied Remote Sensing*.

Worrell, Ernst et al. 2001. "Carbon Dioxide Emissions from the Global Cement Industry." *Annual Review of Energy and the Environment* 26: 303–29.

Wróbel, Radosław, and Beata Gołuchowska. 2018. "Magnetic Susceptibility Spatial Distribution as an Indicator of Soil Pollution in the Area of Opole City." *Ecological Chemistry and Engineering. A* 25(2): 167.

Wyrwa, Artur. 2015. "An Optimization Platform for Poland's Power Sector Considering Air Pollution and Health Effects." *Environmental Modelling and Software* 74: 227–37. http://dx.doi.org/10.1016/j.envsoft.2015.04.017.

Xiuquan Wanga and Guohe Huang. 2014. "Impacts Assessment of Air Emissions from Point Sources in Saskatchewan, Canada — A Spatial Analysis Approach." *Environmental Progress & Sustainable Energy* 34(1): 304–13.

Xu, Hao et al. 2019. "National PM2.5 and NO2 Exposure Models for China Based on Land Use Regression, Satellite Measurements, and Universal Kriging." *arXiv* (2): 1–32.

Xu, Mengxi, and Chenglin Wei. 2012. "Remotely Sensed Image Classification by Complex Network Eigenvalue and Connected Degree." *Computational and Mathematical Methods in Medicine* 2012: 1–9.

Yang, Bing et al. 2013. "Source Apportionment of Polycyclic Aromatic Hydrocarbons in Soils of Huanghuai Plain, China: Comparison of Three Receptor Models." *Science of the Total Environment* 443: 31–39.

Yang, Wenjie et al. 2020. "Using Principal Components Analysis and Idw Interpolation to Determine Spatial and Temporal Changes of Surfacewater Quality of Xin'Anjiang River in Huangshan, China." *International Journal of Environmental Research and Public Health* 17(8): 1–14.

Yang, Zijiang et al. 2020. "Modification and Validation of the Gaussian Plume Model (GPM) to Predict Ammonia and Particulate Matter Dispersion." *Atmospheric Pollution Research* 11(7): 1063–72. https://doi.org/10.1016/j.apr.2020.03.012.

Ye, Yuanxin, Jie Shan, Lorenzo Bruzzone, and Li Shen. 2017. "Robust Registration of Multimodal Remote Sensing Images Based on Structural Similarity." *IEEE Transactions on Geoscience and Remote Sensing* 55(5): 2941–58.

Yeganeh, B., M. Shafie Pour Motlagh, Y. Rashidi, and H. Kamalan. 2012. “Prediction of CO Concentrations Based on a Hybrid Partial Least Square and Support Vector Machine Model.” *Atmospheric Environment* 55: 357–65.

Yerramilli, A., Dodla, V. B. R., & Yerramilli, S. 2011. “Air Pollution, Modeling and GIS Based Decision Support Systems for Air Quality Risk Assessment.” *Advance air pollution*: 295–324.

Yesilbudak, Mehmet, Seref Sagiroglu, and Ilhami Colak. 2013. “A New Approach to Very Short Term Wind Speed Prediction Using K-Nearest Neighbor Classification.” *Energy Conversion and Management* 69: 77–86. http://dx.doi.org/10.1016/j.enconman.2013.01.033.

Yossif, M H. 2017. “Change Detection of Land Cover and Salt Affected Soils at Siwa Oasis, Egypt.” *Alexandria Science Exchange Journal: An International Quarterly Journal of Science Agricultural Environments* 38(July-September): 446–62.

Young, Nicholas E. et al. 2017. “A Survival Guide to Landsat Preprocessing.” *Ecology* 98(4): 920–32.

Yu, Quan, Rui Liang, Zengzeng Guo, and Xiaofei Zhu. 2019. “Law of Spatial Distribution of Particles at the Intersection of Urban Roads.” *Beijing Gongye Daxue Xuebao/Journal of Beijing University of Technology* 45(5): 485–92.

Yudha, G. D., and S. M. Purnama. 2018. “Analysis of Dissemination Methods for Remote Sensing Information in Maritime Field to Support the Local Government.” *IOP Conference Series: Earth and Environmental Science* 162(1).

Zhang, Jiangshe, and Weifu Ding. 2017. “Prediction of Air Pollutants Concentration Based on an Extreme Learning Machine: The Case of Hong Kong.” *International Journal of Environmental Research and Public Health* 14(2): 1–19.

Zhang, Qi, Jacqueline CK Lam, Victor OK Li, and Yang Han. 2020. “Deep-AIR: A Hybrid CNN-LSTM Framework ForFine-Grained Air Pollution Forecast.” In *ArXiv Preprint ArXiv:2001.11957*, , 1–7. http://arxiv.org/abs/2001.11957.

Zhong, Shengjun, Legang Zhou, and Zhufang Wang. 2011. “Software for Environmental Impact Assessment of Air Pollution Dispersion Based on ArcGIS.” *Procedia Environmental Sciences* 10(PART C): 2792–97. http://dx.doi.org/10.1016/j.proenv.2011.09.433.

Zhong, Yong, and Ming Zhao. 2020. “Research on Deep Learning in Apple Leaf Disease Recognition.” *Computers and Electronics in Agriculture* 168(August 2019): 105146. https://doi.org/10.1016/j.compag.2019.105146.

Zhu, Dixian, Changjie Cai, Tianbao Yang, and Xun Zhou. 2018. “A Machine Learning Approach for Air Quality Prediction: Model Regularization and Optimization.” *Big Data and Cognitive Computing* 2(1): 1–15.

Zhu, Zhe. 2017. "Change Detection Using Landsat Time Series: A Review of Frequencies, Preprocessing, Algorithms, and Applications." *ISPRS Journal of Photogrammetry and Remote Sensing* 130: 370–84.

Zimwara, D., L. Mugwagwa, and T. R. Chikowore. 2012. "Air Pollution Control Techniques for the Cement Manufacturing Industry: A Case Study for Zimbabwe." *Proceedings of International Conference on Computers and Industrial Engineering, CIE* 1(July): 121–33.

Zou, Bin et al. 2016. "An Optimized Spatial Proximity Model for Fine Particulate Matter Air Pollution Exposure Assessment in Areas of Sparse Monitoring." *International Journal of Geographical Information Science* 30(4): 727–47.

Zou, Bin, F. Benjamin Zhan, J. Gaines Wilson, and Yongnian Zeng. 2010. "Performance of AERMOD at Different Time Scales." *Simulation Modelling Practice and Theory* 18(5): 612–23. http://dx.doi.org/10.1016/j.simpat.2010.01.005.

Zou, Bin, J. Gaines Wilson, F. Benjamin Zhan, and Yongnian Zeng. 2009. "Air Pollution Exposure Assessment Methods Utilized in Epidemiological Studies." *Journal of Environmental Monitoring* 11(3): 475–90.

Miller, F.M. (2001). Management of detached plumes in cement plants. IEEE-IAS/PCA 2001 Cement Industry Technical Conference. Conference Record (Cat. No.01CH37150), 301-311.

Carpenter, S.B., Montgomery, T.L., Leavitt, J.M., Colbaugh, W.C., & Thomas, F.W. (1971). Principal Plume Dispersion Models: TVA Power Plants. Journal of the Air Pollution Control Association, 21, 491-495.

Moore, G.E., Milich, L., & Liu, M. (1988). Plume behaviors observed using lidar and SF6 tracer at a flat and hilly site. Atmospheric Environment, 22, 1673-1688.

Tosunoglu, M. (2007). Optimising calciner burners: Theoretical treatment of turbulent diffusion jets in cross flow. 2007 IEEE Cement Industry Technical Conference Record, 129-139.

Emetere, M.E., & Akinyemi, M.L. (2013). MODELING OF GENERIC AIR POLLUTION DISPERSION ANALYSIS FROM CEMENT FACTORY.

Biege, N.W., Pretti, H., & Pirwitz, W.W. (1997). Emerging and competing technologies for particulate control in cement plants. 1997 IEEE/PCA Cement Industry Technical Conference. XXXIX Conference Record (Cat. No.97CH36076), 321-344.

McKervey, G., & Perry, B. (1993). Fan applications in the cement industry. [1993] Record of Conference Papers 35th IEEE Cement Industry Technical, 467-476.

Noyes, R.T., Plullips, T.W., Cuperus, G.W., & Bonjour, E.L. (2010). Advances in recirculation fumigation technology U . S . A . in the.

Johnsplass, J., Winger, A.C., Bjørgesæter, A., Kleven, M., & Jensen, J.D. (2021). Combined integral and particle model for describing the dispersion, dilution, terminal layer formation and influence area from a point source discharge into a water body. Environmental Fluid Mechanics, 21, 1009 - 1034.

Pasquill, F. (1979). Atmospheric Dispersion Modeling. Journal of the Air Pollution Control Association, 29, 117-119.

Turner, D.B. (1979). Atmospheric dispersion modeling. a critical review.

Dvořák, R., Zboril, F., Kapoun, M., & Masek, I. (2008). Modeling of Atmospheric Dispersion from Point Source. 2008 Second UKSIM European Symposium on Computer Modeling and Simulation, 46-51.

Verma, V.S. (2015). A Mathematical Model on Dispersion of Air Pollutants.

Pal, D., & Khan, S.K. (1990). A time dependent mathematical model for dispersion of air pollutants from point sources. International Journal of Environmental Studies, 35, 197-208.

Sachdeva, S., & Baksi, S. (2018). Air Pollutant Dispersion Models: A Review.

Singh, K. (2018). Air pollution modelling. International Journal of Advance Research, Ideas and Innovations in Technology, 4, 951-959.

Damoiseaux, M., & Schutter, B.D. (2021). An Efficient Dispersion Model for Control of Emission Levels in the Vicinity of Freeways. 2021 IEEE International Intelligent Transportation Systems Conference (ITSC), 2455-2462.

Stocker, J., Heist, D.K., Hood, C., Isakov, V., Carruthers, D.J., Perry, S.G., Snyder, M.G., Venkatram, A., & Arunachalam, S. (2013). H15-78: Road source model intercomparison study using new and existing datasets.

Adak, P. (2020). A brief discussion on near-surface finite line source models: GFLSM and R-Line.

Madiraju, S.V., & Kumar, A. (2022). Examination of the Performance of a Three-Phase Atmospheric Turbulence Model for Line-Source Dispersion Modeling Using Multiple Air Quality Datasets. J.

Madiraju, S.V., & Kumar, A. (2021). Development and Evaluation of SLINE 1.0, a Line Source Dispersion Model for Gaseous Pollutants by Incorporating Wind Shear Near the Ground under Stable and Unstable Atmospheric Conditions. Atmosphere.

Sharma, N., Chaudhry, K., & Rao, C. (2004). Vehicular pollution prediction modelling: a review of highway dispersion models. Transport Reviews, 24, 409 - 435.

Fang, Y. (2004). Review of Emission Dispersion Models Based on Gaussian Line-Source Model. Environmental Protection In Transportation.

Patiño, W. (2020). A review on short-range dispersion modelling of gaseous pollutants released from stationary sources.

de Ferreyro Monticelli, D., Santos, J.M., Goulart, E.V., Mill, J.G., Kumar, P., & Reis, N.C. (2021). A review on the role of dispersion and receptor models in asthma research. Environmental pollution, 287, 117529 .

Quarterly, A.I., Journal, S., Tech., N.E., & Wagh, N.D. (2022). A Review on Atmospheric Dispersion System for Air Pollutants Integrated with GIS in Urban Environment. Nature Environment and Pollution Technology.

Huertas, J.I., Martínez, D.S., & Prato, D.F. (2021). Numerical approximation to the effects of the atmospheric stability conditions on the dispersion of pollutants over flat areas. Scientific Reports, 11.

Nebenzal, A., Fishbain, B., & Kendler, S. (2020). Model-based dense air pollution maps from sparse sensing in multi-source scenarios. Environ. Model. Softw., 128, 104701.

Milošević, T., Kranjčević, L., Pilicic, S., Čavrak, M., Kegalj, I., & Traven, L. (2020). Air Pollution Dispersion Modeling in Port Areas. Journal of Maritime & Transportation Science.

Venkatram, A., & Thiruvenkatachari, R.R. (2023). Accounting for Area Sources in Air Pollution Models. International Journal of Environmental Research and Public Health, 20.

Salih, A. S., & Hassan, N. D. (2023). The Impact of Urban Trees on Air Pollution in Kirkuk City: A Gaussian Dispersion Model Approach. NTU Journal of Engineering and Technology, 2(4).

Mushtaq, F., & Farooq, M. (2023). Significance of Geo-Visualization Tools for Pollution Monitoring. In Geospatial Analytics for Environmental Pollution Modeling: Analysis, Control and Management (pp. 353-384). Cham: Springer Nature Switzerland.

Toure, H., Baïla, D. B., Amadou, T. C., & Diatta, A. E. R. (2023). Risk Assessment of Noise Pollution in a Cement Plant: Perspectives and Recommendations. Medicine & Community Health Archives, 1(03), 70-77.

Awos, A. (2024). Environmental assessment and impact of air, water and noise levels near a cement factory in Ewekoro, Ogun State, Nigeria.

Monojit Chakraborty, M.C., Sangeeta Bansal, S.B., Renu Masiwal, R.M., & Amit Awasthi, A.A. (2019). Air-Pollution modelling aspects: an overview. Air pollution: sources, impacts and controls.

El-Harbawi, M. (2013). Air quality modelling, simulation, and computational methods: a review. Environmental Reviews, 21, 149-179.

Sachdeva, S., & Baksi, S. (2018). Air Pollutant Dispersion Models: A Review.

Srivastava, S., & Sinha, I.N. (2004). CLASSIFICATION OF AIR POLLUTION DISPERSION MODELS: A CRITICAL REVIEW.

Singh, K. (2018). Air pollution modelling. International Journal of Advance Research, Ideas and Innovations in Technology, 4, 951-959.

Barratt, R. (2001). Atmospheric Dispersion Modelling: An Introduction to Practical Applications.

Leelőssy, Á., Molnár, F., Izsák, F., Havasi, Á., Lagzi, I., & Mészáros, R. (2014). Dispersion modeling of air pollutants in the atmosphere: a review. Central European Journal of Geosciences, 6, 257-278.

Johnson, J.B. (2022). An Introduction to Atmospheric Pollutant Dispersion Modelling. ECAS 2022.

Baciak, M., Warmiński, K., & Bęś, A. (2015). The effect of selected gaseous air pollutants on woody plants.

Morshed, S. M., Ardeni, A. A., & Laylani, S. (2022). Effect of Exposure to Cement Dust of Residents in Vicinity of Kirkuk Cement Factory on Kidney Parameters. Kirkuk University Journal for Scientific Studies, 17(4).

Chepkochei, L. C. (2014). Urban tree species classification on pixel and object level with worldview-2 image, using maximum likelihood classifier and support vector machine (Master's thesis, University of Twente).

Chowdhury, M. S. (2024). Comparison of accuracy and reliability of random forest, support vector machine, artificial neural network and maximum likelihood method in land use/cover classification of urban setting. Environmental Challenges, 14, 100800.

Mondal, Arun, Sananda Kundu, Surendra Kumar Chandniha, Rituraj Shukla, and P. K. Mishra. "Comparison of support vector machine and maximum likelihood classification technique using satellite imagery." International Journal of Remote Sensing and GIS 1, no. 2 (2012): 116-123.

Salih, A. S., & Hassan, N. D. (2023). The Impact of Urban Trees on Air Pollution in Kirkuk City: A Gaussian Dispersion Model Approach. NTU Journal of Engineering and Technology, 2(4).

Abbas, T. R., & Abbas, R. R. (2021, February). Assessing health impact of air pollutants in five Iraqi cities using AirQ+ model. In IOP conference series: materials science and engineering (Vol. 1094, No. 1, p. 012006). IOP Publishing.

Jumaah, H. J., Jasim, A., Rashid, A., & Ajaj, Q. (2023). Air Pollution Risk Assessment Using GIS and Remotely Sensed Data in Kirkuk City, Iraq. Journal of Atmospheric Science Research, 6(3), 41-51.

Ajayi, O. O., Ngene, B. U., & Ogbiye, S. A. (2021, March). Plume Model: A Simple Approach to Air Quality Control. In IOP Conference Series: Materials Science and Engineering (Vol. 1036, No. 1, p. 012017). IOP Publishing.

Al-Kasser, M. K. (2021, June). Air pollution in Iraq sources and effects. In IOP Conference Series: Earth and Environmental Science (Vol. 790, No. 1, p. 012014). IOP Publishing.

Hason, M. M., Al-Sulttani, A. O., Abbood, I. S., & Hanoon, A. N. (2020, November). Emissions investigating of carbon dioxide generated by the iraqi cement industry. In IOP Conference Series: Materials Science and Engineering (Vol. 928, No. 2, p. 022041). IOP Publishing.

Noorpoor, A., & Rahman, H. R. (2015). Application of AERMOD to local scale diffusion and dispersion modeling of air pollutants from cement factory stacks (Case study: Abyek Cement Factory). Pollution, 1(4), 417-426.

APPENDICES

Appendix A

Source Information from Engineering Department of Kirkuk Cement Plant

Kirkuk Cement Company Ltd. — شركة سمنت كركوك المحدودة

Information	Unit	Quantity	المعلومات
The height of the chimney	m	70	ارتفاع مدخنة المعمل
Diameter of stack	m	4	قطر المدخنة
Position of stack		Raw material Grinding department	موقع المدخنة
Contaminant emission rate		150 mg /Nm^3	معدل انبعاث المواد الغازية والصلبة
The number of operating hours for the plant per day	h	24 h	عدد ساعات التشغيل للمعمل في اليوم الواحد
Production capacity of the plant / hour	ton	3200 ton clinker/day for one Line	الطاقة الانتاجية للمعمل بالساعة
Chemical components of the released material		SiO_2 Al_2O_3 Fe_2O_3 Cao Mgo SO_3	العناصر والمركبات الكيميائية للمواد المنبعثة

شركة ليلان لتاهيل و تشغيل واستثمار معامل الاسمنت المحدودة
LAYLAN
COMPANY FOR REHABILTATION OPERATION AND INVESTMENT OF CEMENT PLANTS LTD

Appendix B

1D Guassian Plume Model Plugin in QGIS

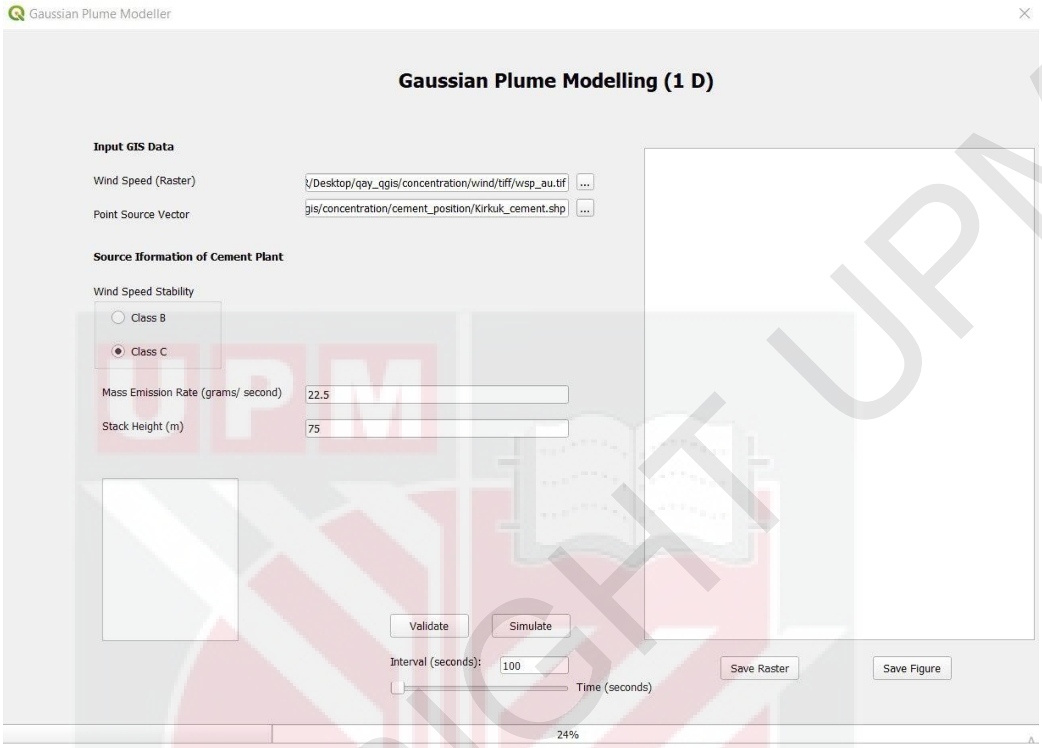

Appendix C

3D Guassian Plume Model Plugin in QGIS

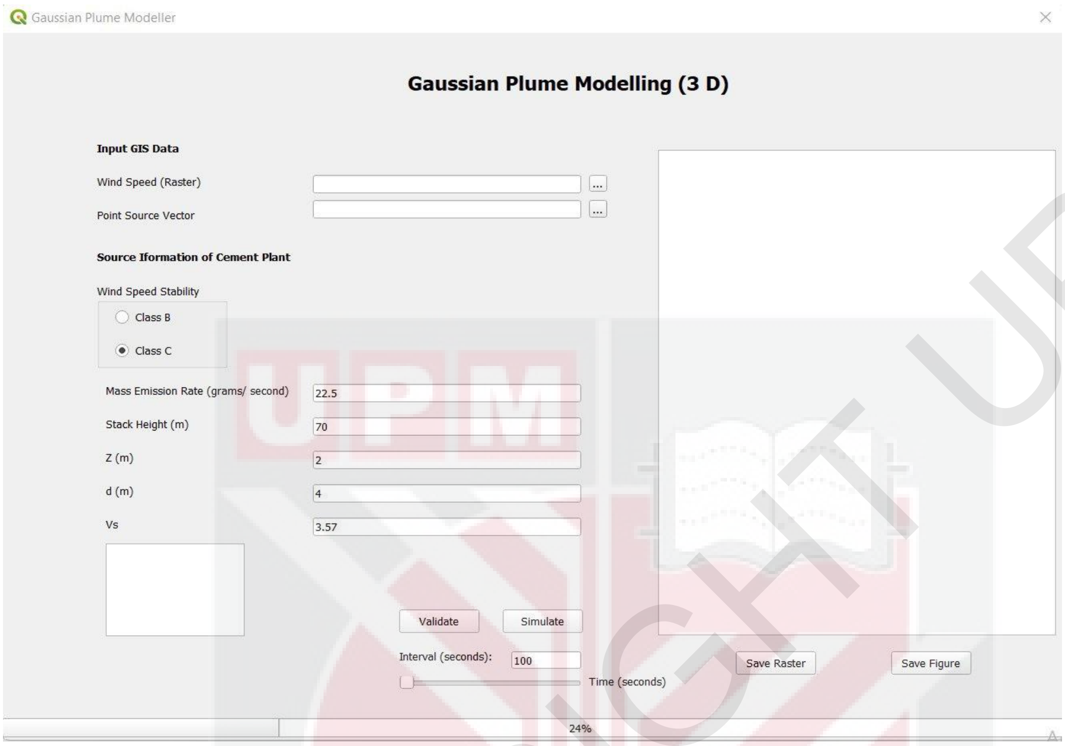

Appendix D

The Designed Deep Learning Model (Deep Pollutant Prediction Model (DPPM))

deep1.py - D:\deep1.py

File Edit Format Run Options Windows Help

```
__author__ = '3D'
__author__ = '3D'

__author__ = '3D'

import numpy as np
import pandas as pd
import seaborn as sns
import keras
import tensorflow as tf

from keras.models import Sequential
from keras.layers import Conv1D,MaxPooling1D,Flatten
from keras import optimizers
from keras.layers import Dense

from sklearn.preprocessing import StandardScaler, LabelBinarizer
from sklearn.model_selection import train_test_split

import warnings
warnings.simplefilter("ignore")


inpdata = pd.read_csv("cement.csv")

df_norm = inpdata[inpdata.columns[0:12]]

target = inpdata[['SO3']]
df = pd.concat([df_norm, target], axis=1)



#'CaCO3','SiO2','Al2O3','Fe2O3','CaO','MgO','SO3'
X = df[['CaCO3','SiO2','Al2O3','Fe2O3','CaO','MgO','SO3'
]
]
y = df['SO3']
print (y)
```

Ln: 1 Col: 0

Appendix E

The Emission of Pollutants from the Chimney of the Kirkuk Cement Plant

Appendix F

Validation of 3D Gaussian Plume Model

Table 1 : Statistical of Validation between Modeled and Calculated Seasonal Pollution Concentration 2020 on Kirkuk City Using 3D Gaussian Plume Model

Season	**NMSE**	**Geometric Mean**	**Standard deviation**	**R^2**	**Bias**
Spring	0.044612	2.71E-07	0.009966	1	-0.171%
Summer	0.009885	2.21E-07	0.007397	1	-0.147%
Autumn	1.375085	0.114541	1.027655	0.999	2.815%
Winter	1.298534	0.114203	0.97005	1	2.549%

Table 2 : Statistical of Validation between Modeled and Calculated Seasonal Pollution Concentration 2020 on Laylan District Using 3D Gaussian Plume Model

	NMSE	**Geometric Mean**	**Standard deviation**	**R^2**	**Bias**
Spring	0.044072	2.64E-07	0.009845	1	-0.170%
Summer	0.009723	2.14E-07	0.007276	1	-0.147%
Autumn	1.380631	0.114119	1.031743	1	2.837%
Winter	1.305208	0.113861	0.974965	1	2.572%

BIODATA OF STUDENT

Qayssar Mahmood Ajaj was born in Kirkuk, Iraq in 04^{th} of March 1980. He obtained his Bachelor of Surveying Engineering, from Technical Engineering College, Kirkuk in 2003. He obtained his Master Degree in Remote Semsing and GIS from University Putra Malaysia in 2016. In 2020, he enrolled in PhD Degree of GIS, University Putra Malaysia.

LIST OF PUBLICATIONS

Ajaj, Q. M., Shafri, H. Z. M., Wayayok, A., & Ramli, M. F. (2023). Assessing the Impact of Kirkuk Cement Plant Emissions on Land cover by Modelling Gaussian Plume with Python and QGIS. *The Egyptian Journal of Remote Sensing and Space Science*, *26*(1), 1-16.

Ajaj, Q. M., Mohd Shafri, H. Z., Ramli, M. F., & Wayayok, A. (2023). Prediction of Air Pollutants Concentration Emitted from Kirkuk Cement Plant Based on Deep Learning and Gaussian Equation Outputs. *Pollution*, *9*(2), 810-820.

Ajaj, Q. M., Shafri, H. Z. M., & Ramli, A. W. A. F. Common Analysis Methods for Gaseous and Solid Contaminants Emitted from Different Pollution Sources: A Review Paper.